The Dissertation Committee for Yao Peng Certifies that this is the approved version of the following dissertation:

Study of Methane Hydrate Formation and Distribution in Arctic Regions: from Pore Scale to Field Scale

Committee:

Steven L. Bryant, Supervisor

Maša Prodanović, Co-Supervisor

David DiCarlo

Mukul M. Sharma

Peter Flemings

Study of Methane Hydrate Formation and Distribution in Arctic Regions: from Pore Scale to Field Scale

by

Yao Peng, B.E; M.E.

Dissertation

Presented to the Faculty of the Graduate School of

The University of Texas at Austin

in Partial Fulfillment

of the Requirements

for the Degree of

Doctor of Philosophy

The University of Texas at Austin

August, 2011

Dedication

To my family

Acknowledgements

I would like to thank Dr. Bryant and Dr. Prodanovic for their support in my Ph.D. None of these achievements would be possible without their guidance. It has been a really enjoyable experience to work under their supervision. Their profound knowledge, enthusiasm for science and encouragement guided me through these years.

I also would like to extend my appreciation to my other committee members: Dr. DiCarlo, Dr. Flemings and Dr. Sharma, for their support and useful suggestion and comments in the dissertation and the final defense.

Special thanks are also due to my colleague Javad Behseresht, who has been working and sharing knowledge with me. I was really inspired by the discussion with him.

Tim Guinn and Roger Terzian were always there when I had software issues. I would like to show my acknowledgement as well.

Last but not least, this project is supported by Department of Energy for funding this project (DE-FC26-06NT43067).

Study of Methane Hydrate Formation and Distribution in Arctic Regions: from Pore Scale to Field Scale

Publication No._____

Yao Peng, PhD.

The University of Texas at Austin, 2011

Supervisor: Steven L. Bryant

Co-Supervisor: Maša Prodanović

We study hydrate formation and distribution in two scales. Pore-scale network modeling for drainage and imbibition and 1D field-scale sedimentological model are proposed for such purpose. The network modeling is applied in a novel way to obtain the possible hydrate and fluid saturations in the porous medium. The sedimentological model later uses these results to predict field-scale hydrate distribution.

In the model proposed by (Behseresht et al., 2009a), gas charge in the reservoir firstly takes place when BGHSZ (Base of Gas Hydrate Stability Zone) is still above the reservoir. Methane gas migrates from deep source and is contained in the reservoir by the capillary barrier. The gas saturation distribution is determined by gas/water capillary pressure, and is modeled by network modeling of drainage.

When gas charge is complete, the gas column in the reservoir is assumed to be disconnected from the deep source, and BGHSZ begins to descend. Hydrate formation is

assumed to occur only at BGHSZ. At the microscopic scale it first occurs at the methane/water interface. A review of the possible modes of growth leads to the assumption that hydrate grows into the gaseous phase. It is assumed that the hydrate formation at the pore scale follows the path of imbibition process (displacement of gas phase by aqueous phase), and can be predicted by the network modeling of imbibition. Two scenarios, corresponding to slow and fast influx of water to the BGHSZ, are proposed to give the maximum and minimum hydrate saturations, respectively. The volume of hydrate is smaller than the total volume of gas and water that are converted at fixed temperature and pressure. Therefore, vacancy is created to draw free gas from below the BGHSZ and water into the BGHSZ.

BGHSZ keeps descending and converting all the gas at BGHSZ into hydrate. The final hydrate profile has a characteristic pattern, in which a region of high hydrate saturation sits on top of a region with low hydrate saturation. This pattern agrees with the observation in Mount Elbert and Mallik sites. The low hydrate saturation in certain regions with good lithology shows that hydrate distribution is not only controlled by the quality of lithology, but also the gas redistribution during hydrate formation.

Table of Contents

List of Tables

List of Figures

1. Introduction

1.1 THE SIGNIFICANCE OF METHANE HYDRATE RESEARCH

Gas hydrate is a natural form of clathrate where gas molecule (guest) is encaged in the center of the crystalline lattice created by water molecules (Figure 1.1). Even the most conservative estimate suggests that the energy stored in the gas hydrate is possibly twice as much as all the fossil fuels combined (Sloan, 2003). A large amount exists in the form of methane hydrate, where methane is the most abundant guest molecule in the hydrate clathrate. Therefore, we use methane hydrate as the representative form in our research. The ideal environment for methane hydrate formation is the deep ocean floor and beneath permafrost (Zatsepina and Buffett, 1997; Judd et al., 2002), where high pressure and low temperature satisfy the formation requirements (Kvenvolden, 1988; 1993; 2002).

Figure 1.2 shows the regions of hydrate stability and instability as a function of temperature and pressure. Only above the curve can hydrate be stably maintained.

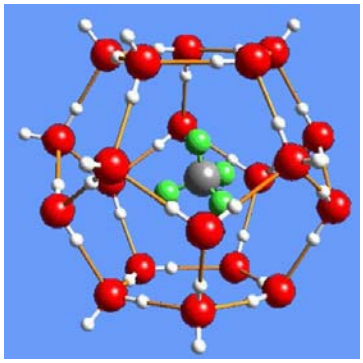

Figure 1.1: The structure of methane hydrate. A methane molecule is centered in a lattice built water molecules.

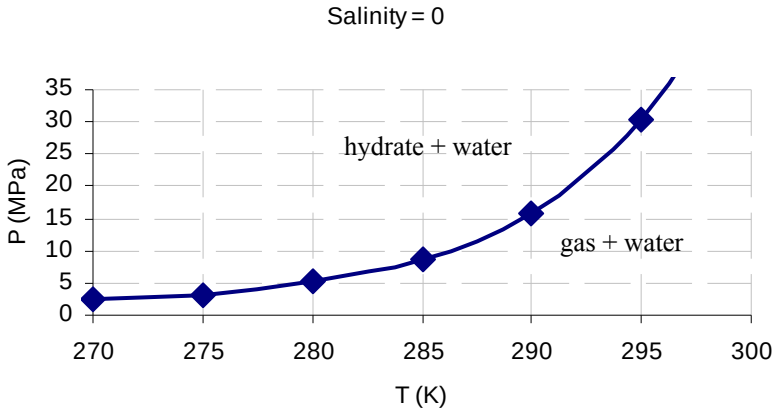

Figure 1.2: Boundary between hydrate-water stable region and gas-water stable region. In this case water salinity is zero. Cases of other salinity values can be found in Figure 4.3.

The vast abundance of gas hydrate has been recognized since 1960's. However, its importance as a potential energy resource has not been recognized until recently. Due to its high energy density (Sloan, 2003) and less green house effect, gas hydrate has drawn people's attention. The research in general examines the subjects described in the following sections.

1.1.1 Potential energy resource

Simple calculation shows that 1 m^3 of methane hydrate ($CH_4 \cdot 5.75H_2O$, with the density of 910 kg/m^3, from Sloan, 2003) contains 121.8 kg of methane gas; that is, 172.4 m^3 in standard conditions. This is equivalent to 1 m^3 of highly compressed gas at 13.5 MPa and 273 K. Such energy density, combined with its worldwide availability (Figure 1.3) and abundance, makes methane hydrate an intriguing energy resource for the next generation.

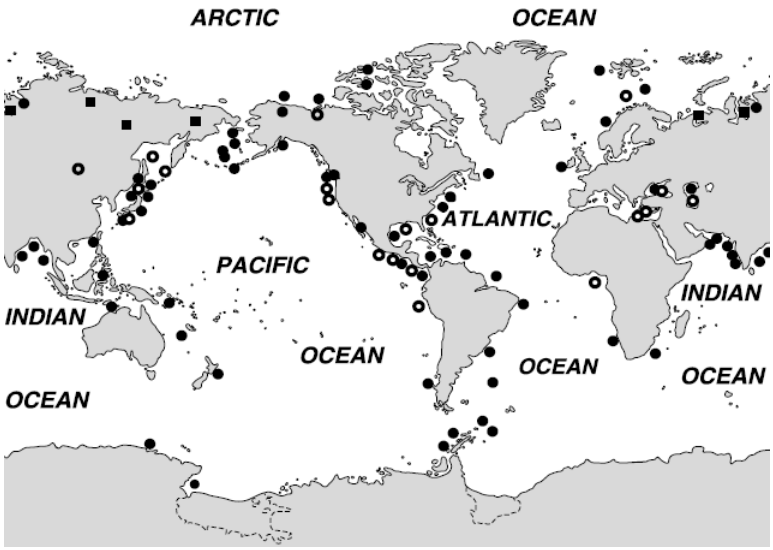

Figure 1.3: Potential gas hydrate distribution in the world. Open circle indicated sites where hydrate samples have been retrieved. Filled circles indicate inferred locations where gas hydrate possibly exists. From (Kvenvolden, 2002).

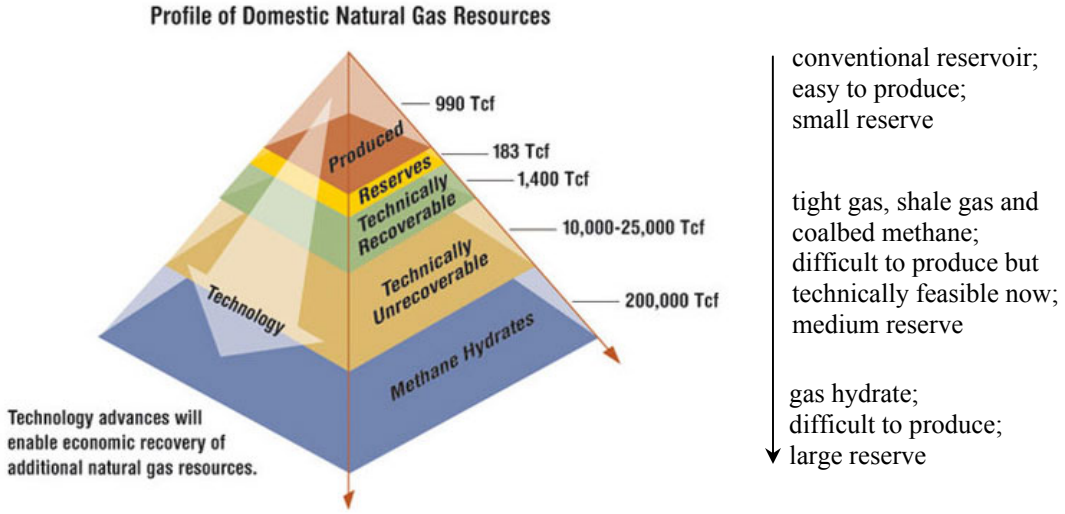

Figure 1.4: Gas resource pyramid showing the general trend of availability and accessibility of worldwide gas reservoirs. From (http://www.netl.doe.gov/KeyIssues/secure_energy3b.html).

The production of gas hydrate often employs thermal methods such as in-situ combustion (Schicks et al., 2010) or hot water injection (Nengkoda et al., 2010). However, these technologies are either premature or economically unfeasible, due to the fact that most of the reservoirs have low hydrate concentration. The environmental and geological issues involved (addressed in more detail in the next section) might also limit the application. Finally, the technology breakthrough (e.g. multistage hydraulic fracturing of horizontal wells) enables the production of other unconventional gas resources (tight gas, shale gas and coal-bed methane), which are less abundant but relatively easier to produce (Figure 1.4). These factors combined have a negative influence on the development of new technologies for gas hydrate production.

1.1.2 Impact on the geological stability

Gas hydrate commonly exists in the shallow sediments below the seafloor of the continental margins, where low temperature and high pressure provide ideal environment for hydrate stabilization. The proper temperatures, pressures, and fluid salinity create a so-called Gas Hydrate Stability Zone (GHSZ), in which gas hydrate is stably sustained. Moving out from GHSZ, either due to pressure decrement (moving from above to below the curve in Figure 1.2) or temperature increment (moving from left to right hand side of the curve in Figure 1.2), destabilizes gas hydrate, and therefore induces hydrate dissociation. As the volume of gas and water released from hydrate is much greater than hydrate itself (refer to Section 4.2.1 for detail), the pore pressure increases, and might cause massive and hazardous submarine landslides (Sultan, 2007). The pressure reduction can also destabilize gas hydrate (that is, moving from above to below the curve in Figure 1.2

Figure 1.2), and is a possible cause for the dissociation of the gas hydrate in marine sediments. One mechanism for pressure reduction is the falling sea level, which reduces the pore pressure. When the pore pressure reduces from above to below the curve in Figure 1.2, hydrate dissociation happens. Another mechanism is the sediment failure on top of the hydrate reservoirs. When the sediment layers collapse and move down the slope during this process, the overburden pressure decreases and causes gas hydrate to dissociate (Maslin et al., 2010).

The hydrate stability in the arctic region is also affected by the similar factors. Studies suggest that the continued global warming has flooded warm water into the cold permafrost regions, which not only raises the sea level but also increases the sediment temperature, a factor that could also trigger hydrate dissociation (Paull et al., 2007).

1.1.3 Impact on the global warming and carbon cycle

Gas hydrate dissociation might release methane gas into the atmosphere. Since methane is a greenhouse gas much more effective than carbon dioxide, the impact of widespread dissociation on the global warming could be significant. The clathrate gun hypothesis, as proposed by (Kennett, 2002), suggests a correlation between the methane release record and global temperature variation over geological time. With the falling sea level (global cooling) or rising temperature (regional or global warming), methane gas is released into the atmosphere, and further increases the temperature because of the green house effect. If the hydrate dissociation is due to the rising temperature, the releasing of methane gas becomes a vicious feedback. This worsens the global warming and is believed to be one of the causes for the massive extinction of species at the Permian-Triassic boundary (Erwin, 1993; Padden et al., 2001; Krull and Retallack, 2000).

Gas hydrate association and dissociation might also have a large contribution to the global carbon cycle (Dickens, 2003). The simulation results by considering three carbon reservoirs (dissolved gas, free gas and gas hydrate) match with the observation of global $\delta^{13}C$ excursion (Zachos, 2001), which suggests the gas hydrate dissociation in the ocean sediment should be included in the carbon cycle model. This shows the release of methane gas from the clathrate is an important step of this cycle.

The impacts of gas hydrate to the regional and global temperature variation and continental slope stability should not be considered as isolated processes (Archer, 2007; Bangs et al., 2010). When gas hydrate is dissociated due to the temperature rising or pressure falling in the continental margin, regional landslide might take place as the increasing pore pressure fractures the sediments. The gas then migrates from gas hydrate reservoir to the dissolved or free gas reservoirs. If it enters atmosphere, this would strengthen the global warming and might increase the pace of releasing gas from the clathrate as a feedback.

1.2 GAS HYDRATE FORMATION AND DISTRIBUTION

A very fundamental question to be answered is how gas hydrate distributes in the reservoir and why it distributes the way it does. A conceptual model is usually applied to identify the gas hydrate location in the field (Dickens, 2001; 2003). Gas, either biogenetic or thermogenetic, originates in the deeper sediments (Figure 1.5). Individual gas bubbles merge into large gas columns. When the buoyancy exceeds the capillary displacement pressure of the sediments, free gas migrates upwards. The temperature cools down as gas bubble moves to the shallower sediments. When the temperature is low enough, gas hydrate will form from gas and water, and remain stable under favorable temperature and pressure. The region where hydrate is thermodynamically stable is called Gas Hydrate Stability Zone (GHSZ, Figure 1.6). The base of this region is referred to as Base of Gas Hydrate Stability Zone (BGHSZ).

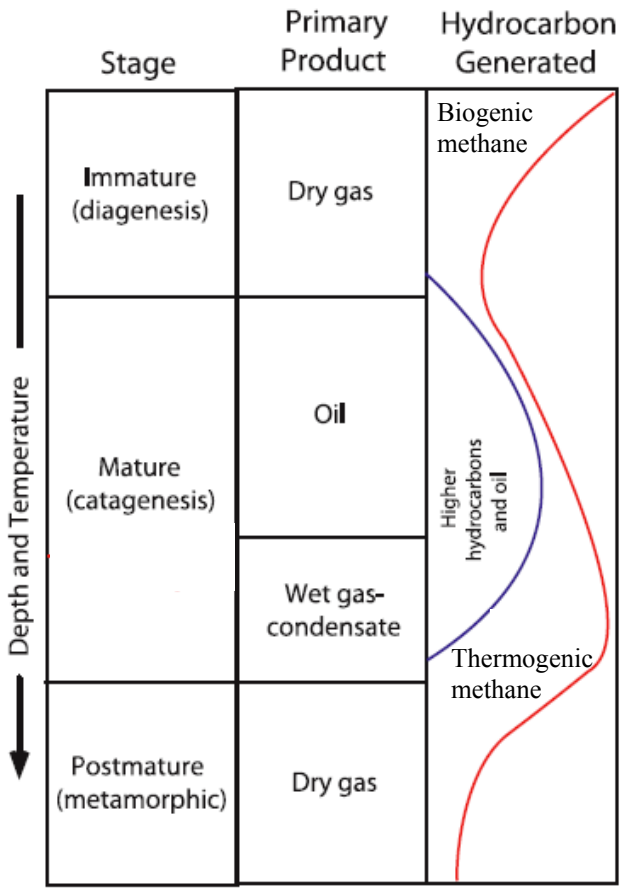

Figure 1.5: A schematic of gas generation showing the depth and temperature effects. The depth varies with the geothermal gradient. Biogenic methane is due to the microbial degradation of organic matter in the shallow sediments, and thermogenic methane, usually occurring below 1000 m, comes from thermal degradation of organic matter in the deeper sediments. From (Collett et al., 2010).

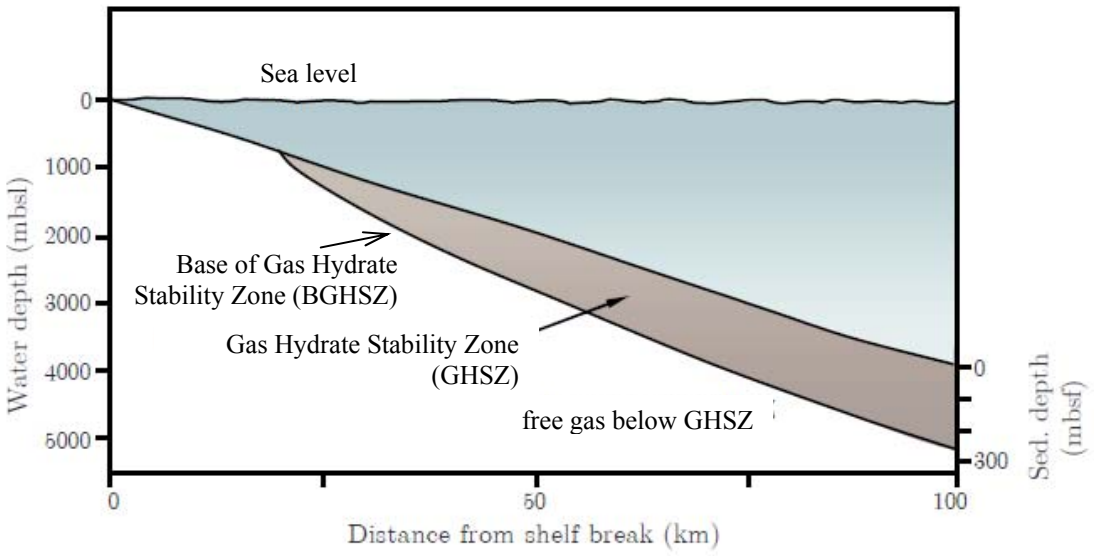

Figure 1.6: An idealized model of Gas Hydrate Stability Zone (GHSZ) in the continental shelf. Free gas exists beneath GHSZ. Base of Gas Hydrate Stability Zone (BGHSZ) is the boundary that separates the region where hydrate can or cannot be stably sustained. Although the concept of GHSZ is from the ocean environment, the same idea can also be applied to the arctic regions such as Mount Elbert and Mallik hydrate reservoirs. After (Dickens, 2003).

It has been proved by experiments (Tohidi et al., 2001; Katsuki et al., 2007; Katsuki et al., 2006; Ohmura et al., 2005; Teng et al., 1995; Shindo et al., 1995) that hydrate formation can take place either from a single phase (gas-saturated aqueous phase) or two phases (gaseous and aqueous phases). In fact, the initial hydrate nucleation requires low energy region, where the interface, either between gas and water or solid (grain) and water, provides such an environment. When hydrate forms on the solid (grain)/water interface, experiments in (Katsuki et al., 2007) show it is forming inside the saturated aqueous phase. In this work, we assume methane hydrate formation as a process that occurs only on the gas/water interface. This is due to the fact that the solubility of methane in water is very low under the reservoir environment. (Handa, 1990) suggests

only 0.004 kg methane can be dissolved in 1 kg of water, at 20 MPa and 278 K. This amount of gas only gives 0.031 kg of methane hydrate, which corresponds to only 3% hydrate saturation. This is much less than the observation from the field. To obtain more hydrate, it is required that the methane molecules diffuse into the aqueous phase from the methane gas. Such process inevitably passes methane molecules through the gas/water interface, where hydrate is being formed as well. These molecules are likely to be converted into hydrate on the gas/water interface, instead of being dissolved in the aqueous phase. Consequently in our work, a two phase system (gaseous and aqueous phases) is assumed, and methane hydrate is formed at the gas/water interface (Figure 1.7).

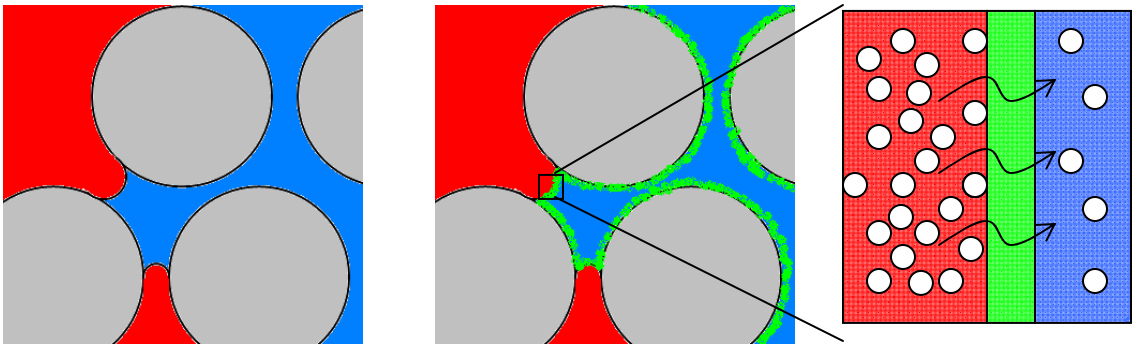

A. methane gas (red) and water (blue) saturated with methane coexist in the sediment.

B. After methane molecules in the water are converted to hydrate (green shell coating the gas/water interface and grain surface), gas molecules from the gaseous phase need to diffuse through the gas /water interface to form more hydrate.

C. During the diffusion, most methane molecules (hollow disks) will be converted to hydrate at the gas/water interface, rather than enters the bulk aqueous phase.

Figure 1.7: Schematic of hydrate formation in the porous medium. The red region represents methane gas and blue region represents water, either saturated or depleted of methane. The green region represents hydrate.

A lot of factors play a role in the hydrate formation and distribution. First, the amount of hydrate in the reservoir is controlled by the amount of the available gas and water. Since the generated hydrate volume is much less than the combined volume of gas and water consumed (Kneafsey et al., 2007), the pressure within each reservoir layer drops during the formation process. In nature, gas and water from other layers of sediments flow into this layer to fill the vacancy. Such process changes the gas and water distribution profile, and therefore affects the hydrate distribution the field scale. Second, salinity limits the hydrate saturation as well (Husebø et al., 2009; Dickens and Quinby-Hunt, 1994). Only the water molecules are used for gas hydrate crystallization, while salt ions are expelled from the hydrate clathrate. The local salt ion accumulation would take place if the hydrate formation rate is much greater than the ion diffusion rate. Thermodynamic models have been proposed to compute the critical salinity at different temperature and pressure (Sun and Duan, 2007). If the salinity accumulation is above the critical salinity, hydrate formation is inhibited; otherwise more hydrate can be formed. Finally, temperature and pressure create Gas Hydrate stability Zone (GHSZ), inside which gas hydrate is stable Figure 1.6. All these factors will be studied in this work.

In general, hydrate formation is a complex process that is controlled by both the local parameters, such as temperature, pressure, salinity; and also the regional ones, such as the available amount of gas and water. It is necessary to focus on both the pore and field scales in order to address the effects of different parameters separately. Researches on these two scales are not isolated. The final hydrate distribution is a combined effect of both scales.

1.2.1 Gas hydrate formation in the pore scale

Although the scientific understanding of gas hydrate formation in the porous medium has been largely improved over the decades, the answers to a lot of fundamental questions remain unknown, and open to the scientific debate.

The experimental study of gas hydrate formation goes back to (Tohidi et al., 2001). The authors used three different gases (tetrahydrofuran, methane and carbon dioxide) to experimentally investigate gas hydrate formation in an artificial porous medium, which was built from etched glass plates. In the experiments on free methane and water, the authors observed that with the proper temperature and pressure, hydrate first formed at the interface between methane and water as a thin layer. The layer later expanded into the gaseous phase, and finally filled up the space originally taken up by gas. Further, a water film coating the grain surface was always present, even when the whole pore was filled by gas.

A similar experiment was performed by (Katsuki et al., 2007). The porous medium was represented by a regular lattice of tubes, with an average tube radius of 100 microns. Instead of spreading at the methane-water interface, hydrate first nucleated inside the methane-saturated liquid, and moved towards the gaseous phase. Hydrate eventually took up the gaseous space. This observation suggests that hydrate formation takes place where interface exist (either gas-water or solid-water). Hydrate morphology variation was observed at different subcoolings, with a constant environment pressure.

A more delicate experiment was performed by (Ohmura et al., 2005) to observe hydrate formation in an even smaller scale (Figure 1.8). Without introducing a porous medium, the whole experiment was performed inside a chamber, which was filled by methane gas and methane-saturated water (Figure 1.8). Hydrate crystallization started from the liquid-gas interface, with variation in morphology at different pressures (the temperature effect

is not clear, as the experimental temperature was kept at around 273 K). Instead of moving into the gaseous phase as in (Tohidi et al., 2001), hydrate crystal invaded the aqueous phase. The experiment also showed that hydrate crystal can form at the glass wall of the chamber, where no free methane was present. Such observation also conflicts with that of (Tohidi et al., 2001), which observed no hydrate formed from the solid wall.

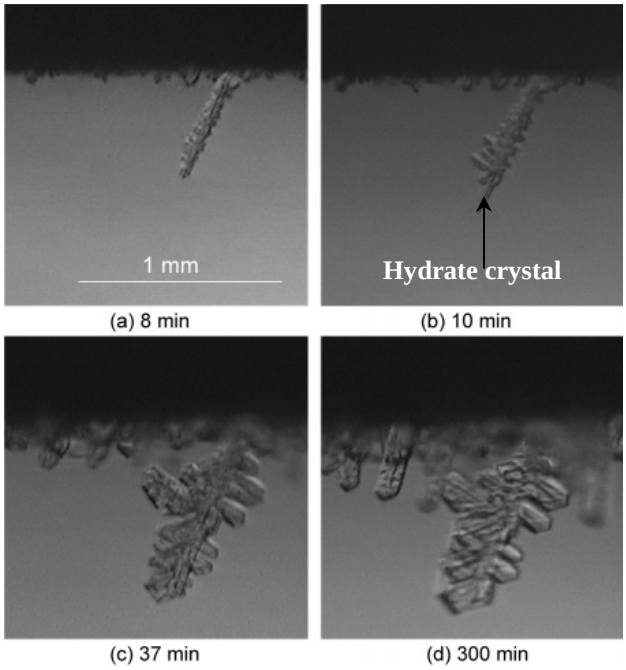

Figure 1.8: Hydrate crystallization at the interface between free methane (black) and methane-saturated water (gray). The experiment was under the condition of 8.3 MPa and 273.7 K. Hydrate invades into the aqueous phase as time increases. The hydrate morphology varies from 'needle' to 'Christmas tree' as pressure increases (6.9 MPa to 9.7 MPa), with a relatively constant temperature (~273 K). From (Ohmura et al., 2005).

(Dong Lee et al., 2005) tested the hydrate formation in a free gas (methane or ethane)-water droplet system (Figure 1.9). In this system, water is the limiting phase. Similarly to lots of other experiments, hydrate begins to form at the gas-water interface. Since from Figure 1.9(a) to (c) the volume of the droplet does not change, we conclude

that hydrate formation invades the aqueous phases, the same observation as in (Ohmura et al., 2005). The white arrows in (c) indicate the inward collapse of hydrate. This shows that low pressure zones inside the gas bubble are generated during hydrate formation. The unbalanced pressure difference causes the hydrate collapse. It can be inferred that under the experimental pressure and temperature, the volume of hydrate is smaller than the volumes of gas and water that are converted. This is an important observation since it indicates that hydrate formation will lead to fluid movement, and therefore redistribute fluids from their original state.

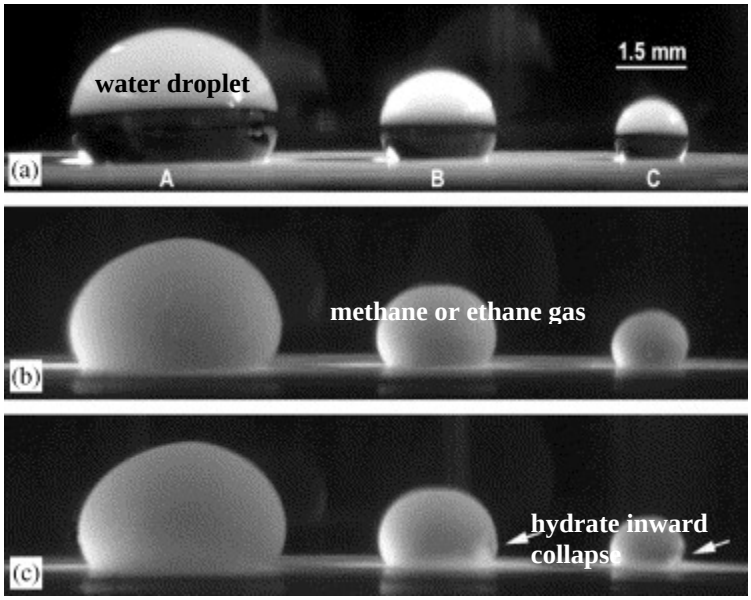

Figure 1.9: hydrate formation from the water droplet surface. The experiment was at 5.1 MPa and 273.85 K. (a) the beginning of experiment, three droplets of different sizes are used in the experiments. (b) 10 min after the beginning of nucleation. Hydrate formed at the gas-water interface. (c) 24 hrs after the beginning of nucleation. Compared to the size of the water droplet, the size of hydrate droplet does not change, indicating that no hydrate grows into the gaseous phase.

Other than gas-water interface, the grain surface, coated by the gas-saturated water, can also be the active hydrate nucleation site. (Katsuki et al., 2006) used carbon dioxide as the guest molecule, and compared the hydrate formation in 1) carbon dioxide-saturated water only and 2) free carbon dioxide and water, with the same experiment apparatus as in (Katsuki et al., 2007). In both cases hydrate formation were observed. In the case of water only, hydrate appears to form at the tube wall, and spreads into the aqueous phase. In the free gas case no direct evidence shows where hydrate is originated. Hydrate later invades into the gaseous phase. When the hydrate formation is complete, both hydrate and water takes up the space that was originally filled by carbon dioxide. This is another indication that the volume of hydrate formation is less than the consumed volume of carbon dioxide, so that free water imbibed to fill the vacancies.

As shown from the above literatures, numerous experiments showed that hydrate nucleation can take place where interface (either gas-water or water-solid surface) exists. However, the mechanism governing this process is not clear, which imposes difficulties in determining the direction of hydrate crystallization. Models have been developed to study the hydrate formation in a gas/water system. Carbon dioxide (CO_2), instead of methane, is often used as the guest molecule to form the gas hydrate.

(Shindo et al., 1995; Lund et al., 1994; Teng et al., 1995) developed models based on the concept that hydrate film is formed at the carbon dioxide (liquid) – water interface. The discrepancy among these models is the direction of hydrate growth. (Shindo et al., 1995) argued that hydrate grows into water, so that gas molecules are required to diffuse through the hydrate layer and contact with the water molecules so that new hydrate can be formed. A straightforward extension of this model was proposed by (Lund et al., 1994): after the initial nucleation, hydrate would grow into both liquids (carbon dioxide and water). Both water and carbon dioxide molecules would diffuse through the hydrate

layer in the opposite directions. However, (Teng et al., 1995) suggested that in the situation of a carbon dioxide liquid droplet resides in the bulk water, hydrate should form into the carbon dioxide. In this case, water molecules would diffuse through the hydrate layers and associate with water to form new hydrate. A demonstration of these models can be found in Figure 1.10.

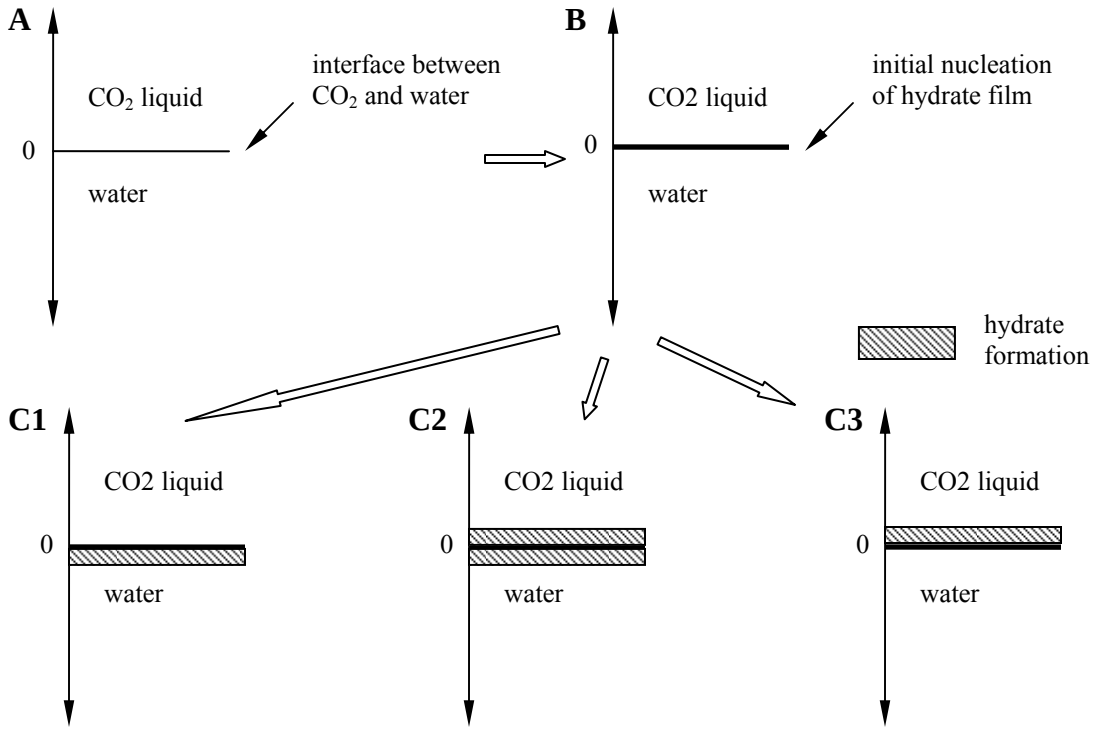

Figure 1.10: A demonstration of different models concerning hydrate formation directions. (A) the system contains CO_2 liquid and water. (B) hydrate nucleation initializes at 0. At this stage, only a thin film of hydrate is formed, whose thickness can be ignored. (C1) hydrate forms and grows into water. CO_2 molecules diffuse through the hydrate film to maintain the hydrate formation towards the water (Shindo et al., 1995). (C2) hydrate grows into water and CO_2 liquid. Both water and CO_2 molecules would diffuse to the opposite directions so as to maintain the hydrate formation in both directions (Lund et al., 1994). (C3) hydrate grows into CO_2 liquid. Water molecules diffuse through the hydrate film (Teng et al., 1995).

The direct application of these models to the methane/water system might be problematic in several aspects. First, all these models were developed in the CO_2 liquid – water system, while methane is a different component and generally a gaseous phase in subsurface. Second, these models reached different and even contradictory conclusions. However, they are all based on the experimental observations. This reveals there is still lack of the understanding of the mechanism that determines the direction of hydrate growth. Therefore the model might yield ambiguous results, which will be unreliable and might give wrong information of the hydrate formation in pore scale.

A closer scrutiny of hydrate film between CO_2 liquid and water gives us some insights into how methane or water is transferred through the hydrate film. (Hirai et al., 1996) assumed that hydrate grows into water and explained the CO_2 diffusion through the hydrate film. The hydrate layer is considered to be a porous medium where tortuous conduits model void space within the crystal structure. CO_2 diffuses through those conduits and is driven by the concentration difference of CO_2 molecules in liquid CO_2 and water.

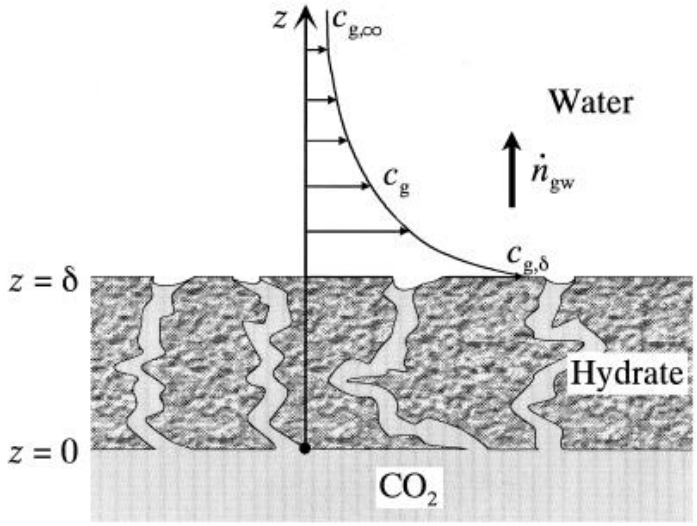

Figure 1.11: CO_2 diffusion through hydrate film during hydrate formation. Hydrate film is considered to be a permeable layer with tortuous conduits connecting water and CO_2 liquid. The diffusion is driven by the CO_2 concentration gradient between CO_2 liquid and water, as well as within the water. (Hirai et al., 1996).

The models developed by (Mori and Mochizuki, 1997), on the other hand, suggested a different mass transport mechanism, of which water is sucked into the conduits and transported through the hydrate layer. This model uses the same concept as in (Hirai et al., 1996), but does not specify the guest phase (compared to the aqueous phase) or component. Therefore, it is a fair assumption that methane gas can also be the guest. Similarly, hydrate is formed at the interface between hydrate and methane, and dissociated at the interface between hydrate and water (Figure 1.12). By doing so, hydrate thickness is kept constant. Since water is a wetting phase and gas is a nonwetting phase, capillarity is the driving force that imbibes water into the conduits. New hydrate is formed at the gas-water interface (at the mouth of the conduits). This is the mechanism that transports both water and methane through the hydrate layer.

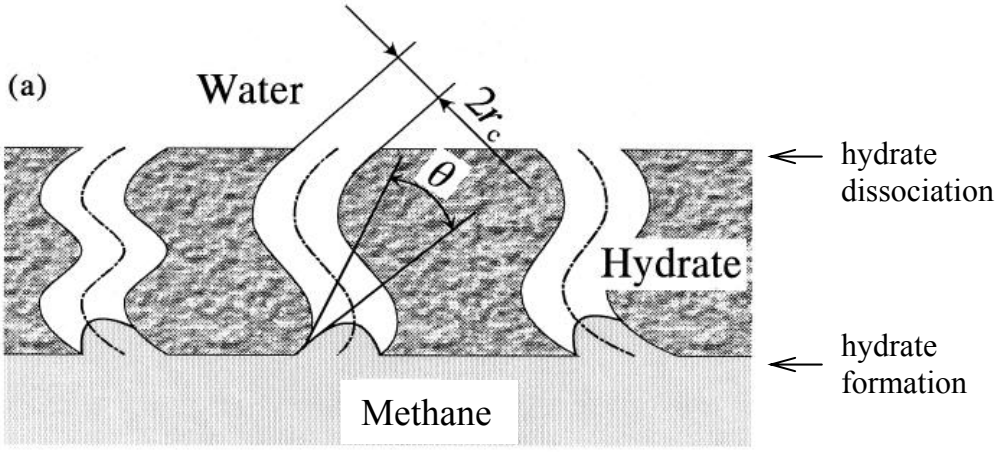

Figure 1.12: A demonstration of methane and water transportation during hydrate formation. Hydrate forms a permeable layer with tortuous conduits (crystal defects). Water imbibes into the conduit due to the capillary force, and contacts with methane at the mouth of those conduits, where new hydrate forms. Hydrate dissociation takes place at the water-hydrate interface. This process releases methane into the aqueous phase. The hydrate thickness is kept constant during this process (Mori and Mochizuki, 1997).

Although most of the above literatures used CO_2 liquid as the guest phase, a similar extension could be applied to methane-water. The review suggests the current scientific debates over the hydrate formation and fluid transport mechanisms (for example, which phase hydrate grows into, and the transport mechanism of the guest molecules through the hydrate layer). Questions concerning where hydrate is preferentially formed (fluid-fluid surface or fluid-solid surface) and which direction hydrate grows into (water-ward or gas-ward) are still open to discussion.

The numerical simulation of hydrate formation usually focuses on two scenarios. One is that hydrate forms in the single phase (aqueous phase). The simulations in molecular scale usually assume such scenario (BáEz and Clancy, 1994; Jiang et al., 2007; Kang, 2004). This is beyond the scope of this dissertation. The other scenario is that hydrate forms at the gas-hydrate interface. At the pore scale, this is a common

assumption due to fact that gas and water coexist in the porous medium. Based on this assumption, the thickness of hydrate film and the speed of hydrate film growth are studied, and are compared with the experimental data.

(Mori, 2001) developed a 2D model to investigate the speed of hydrate film expansion along the gas-water interface (Figure 1.13A). The expansion speed was controlled by the heat transfer at the hydrate-forming front, where hydrate, water and the guest substance (either gas or liquid) coexist. The hydrate edge profile was assumed to be circular, which is a first order approximation considering the fact that hydrate morphology varies in different environments (Ohmura et al., 2005). By assuming a constant hydrate film thickness, the correlation between growth speed and the driving force (temperature difference between three-phase equilibrium and simulation setup) was developed. The hydrate thickness is an unknown; however, it can be estimated by using the trial-and-error process. That is, the simulation results were compared with the experimental data by assuming a thickness, and the thickness was adjusted accordingly. A direct modification of this model was performed by (Mochizuki and Mori, 2006). In this study, hydrate front profile was assumed to be either circular or square (Figure 1.13B), and both water and guest substance are moveable during the hydrate formation. Similarly, the hydrate thickness was estimated from the comparison with the experimental data.

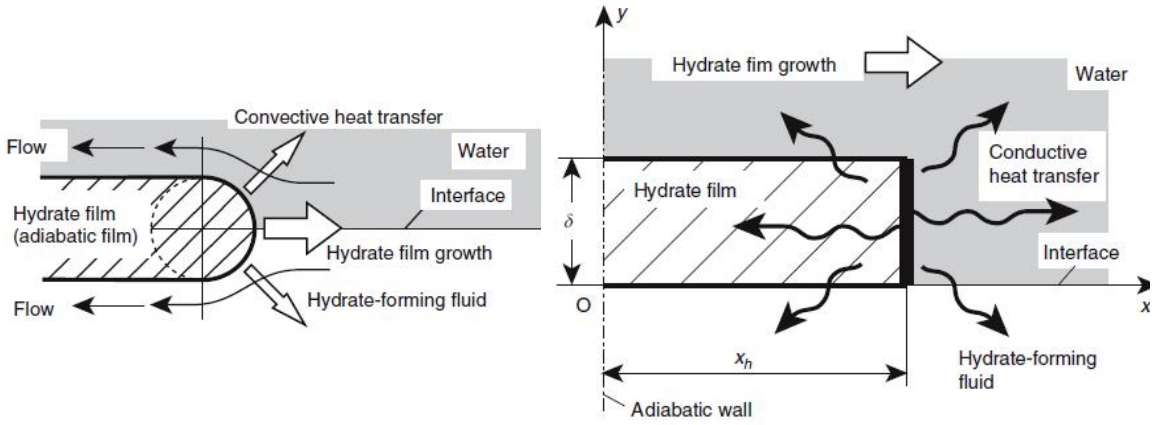

A. (Mori, 2001; Mochizuki and Mori, 2006) B. (Mochizuki and Mori, 2006)

Figure 1.13: A comparison between two 2D models for hydrate expansion. Hydrate film expands along the interface between water (gray) and guest substance (white). The speed is controlled by the heat transfer at the front of the hydrate film. (A) assumes the front has a circular shape, and (B) assumes the front has the square shape. Both models estimate the hydrate film thickness from a trial-and-error process.

(Peng et al., 2007) re-formulated the model of (Mori, 2001) by assuming the hydrate thickness is inversely proportional to the driving force. This assumption enabled the direct calculation of hydrate film thickness and comparison with the measurements. The study allowed the hydrate growth in both phases, but with different computed thicknesses. Moreover, the simulation suggested a faster film growth at higher driving force, which qualitatively agreed with the experimental observation.

Despite the large amount of work on numerical prediction of the hydrate film growth, little research has been done to estimate the hydrate saturation in the porous medium from the numerical approach, due to our limiting understanding of the formation mechanism. Analytical models based on the thermodynamics perspective were proposed for this purpose. Those models lack the description of gas-water (interface) distribution in the porous medium, as well as the detailed explanation of hydrate formation; however,

they introduced the effect of pore size to the hydrate formation, and correlated hydrate saturation with parameters like temperature, pressure, and pore size distribution.

The original model was to describe the ice formation inside a tube. (Everett, 1961) proposed that when the water molecules are transferred through the ice-water interface to form new ice, water molecules are entering the high chemical potential, which requires extra work. The work *w*, from thermodynamics, is

$$dw = \left(P^s - P^b\right)dV^s - \left(P^l - P^b\right)dV^l \tag{1.1}$$

where superscript *s*, *l* refer to solid and liquid in the capillary tube. *b* represents the bulk properties when the entire system is only filled by water, and ice formation has not started.

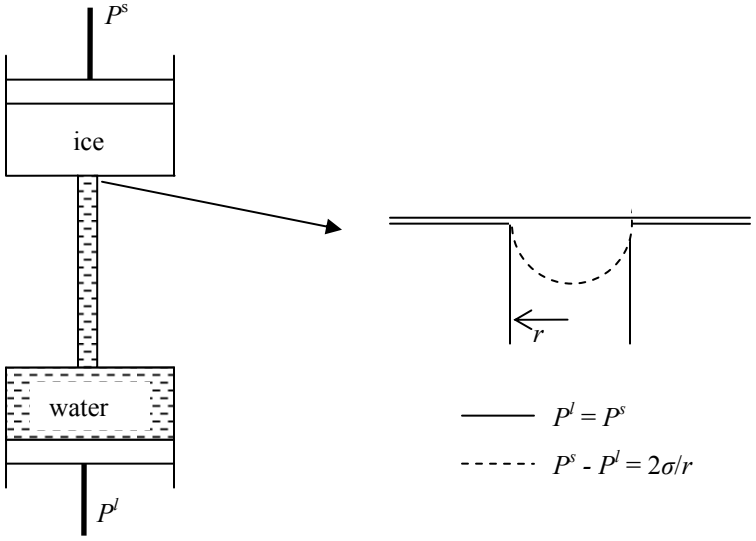

Figure 1.14: A schematic of the system used by (Everett, 1961).

For a reversible transfer of one mole of water through the capillarity, the work *w* becomes

$$w = \Delta P^s v^s - \Delta P^l v^l \tag{1.2}$$

w is equal to the change of Gibbs energy in the system, and v^s and v^l are the molar volume of solid and liquid, respectively. If pressure change is ignored, equation (1.2)becomes

$$\Delta T_f = -\frac{\Delta P^s v^s - \Delta P^l v^l}{S} \tag{1.3}$$

where S is the molar entropy of ice fusion and ΔT_f is the difference between ice formation temperature and bulk fluid temperature. Also this can be correlated with the molar enthalpy, which shows

$$H = ST_f \tag{1.4}$$

where H is the molar enthalpy of the ice fusion. From equation (1.3) and (1.4), we obtain

$$\frac{\Delta T_f}{T_f} = \frac{1}{H}\left(\Delta P^s v^s - \Delta P^l v^l\right) \tag{1.5}$$

Note that

$$\Delta P^s - \Delta P^l = \frac{2\sigma}{r} \tag{1.6}$$

where the symbol Δ means the pressure difference between the phase pressure and bulk pressure. Substitute equation (1.6) into (1.5), and assume that the water pressure is the bulk pressure, we have

$$\frac{\Delta T_f}{T_{f,bulk}} = \frac{2\sigma_{iw}}{r}\frac{v^s}{H_{f,i}} \tag{1.7}$$

which is the basic form of Everett's model. This model can be used to calculate the required temperature drop ΔT_f for ice formation in the tube as a function of bulk temperature $T_{f,bulk}$, ice-water interfacial tension σ_{iw}, ice-water interface curvature $2/r$ in the tube, ice molar volume v_s, and the molar enthalpy of ice fusion $H_{f,i}$.

A modified model was presented by (Ben Clennell et al., 1999), who applied Everett's model to the porous medium. Similarly, this model only considers the ice-water system, without the presence of free gas. Here only the final equation is shown.

$$\Delta T_{i,pore} = \frac{2\sigma_{iw} T_{i,bulk} \cos\theta_{iw}}{\rho_l \Delta H_{f,i} r_e} \tag{1.8}$$

In this model, r_e is the effective radius of the pore, and it spatially varies in the porous medium. The other parameters are generally considered to be constants in a static system. Therefore, in smaller pores, higher temperature depression ($\Delta T_{f,pore}$) is required for the ice formation than the bigger pores.

A later modification enables a similar model to solve for both hydrate clathrate formation and dissociation (Anderson et al., 2003). The authors argued that Everett's model can be applied to any clathrate, as long as the parameters are changed according to different substances. Moreover, the model is also capable of calculating the temperature increment due to the hydrate dissociation. The formulations are shown below.

$$\frac{\Delta T^d_{f,pore}}{T_{f,bulk}} = -\kappa \left(\frac{\gamma_{sl} \cos\theta}{\rho_l \Delta H_{f,i}} \right) \tag{1.9}$$

$$\frac{\Delta T^i_{f,pore}}{T_{f,bulk}} = \kappa \left(\frac{\gamma_{sl} \cos\theta}{\rho_s \Delta H_{f,i}} \right) \tag{1.10}$$

κ is the curvature of hydrate-water interface. Equation (1.9) is the governing equation that computes the temperature depression ($\Delta T^d_{f,pore}$) at hydrate formation by using the liquid density ρ_l. Equation (1.10) is the governing equation that computes the temperature increment ($\Delta T^i_{f,pore}$) at hydrate dissociation by using the hydrate density ρ_s. Since water is usually denser than hydrate, the temperature depression (Equation (1.9)) is smaller than increment (Equation (1.10)). This qualitatively agrees with theoretical analysis and experimental observation of hydrate formation and dissociation hysteresis (Lekvam and Ruoff, 1997).

Although our understanding of methane hydrate has improved over the past decades, the research on this area mostly employs experimental and theoretical approaches. The experimental results are limited and affected by the availability of the

experimental apparatus and conditions. Most of the experimental results are either 1D or 2D, while 3D data are rare. Most of the theoretical approaches were originally developed from other systems (CO_2 liquid and water, or ice and water), and the direct extension to the methane-water system might be problematic. Moreover, different theoretical explanations introduce contradictory assumptions, which are not yet justified because of the lack of fundamental understanding of mechanisms.

Compared with experimental and theoretical studies, numerical investigation of hydrate growth in the porous medium is very rare, due to the imperfection of our theoretical models. However, in a relatively static system, the hydrate saturation is predictable given the gas and water distributions. In this dissertation, we apply pore-scale models (elaborated in Chapters 2 to 4) to predict the hydrate saturation in the porous medium, which will be later used for the estimation of the field-scale hydrate distribution.

1.2.2 Gas hydrate formation and distribution in the field scale

Gas hydrate reservoirs have been discovered worldwide. In North America, the hydrate resource locates either in offshore shallow sediments below the seafloor (Wood et al., 2008; Holbrook, 2001; Bohrmann et al., 2007)., or onshore arctic regions below the permafrost (Dallimore and Collett, 2005; Rose et al., 2011). For the former case, in many sites researchers still observe active gas seepage on the seafloor, and active hydrate formation and dissociation are still taking place nowadays. The latter case is more passive. There is no strong evidence of the ongoing phase change in the system.

The hydrate distribution in the vertical direction varies among different sites. Two basic patterns can be identified from field data. Figure 1.15A shows the hydrate saturation profile from Blake Ridge, which locates offshore North Carolina. In most

depths, the hydrate saturation in this reservoir is lower than 10%, and the saturation increases from shallower to deeper depth. It is a continuous distribution over a long depth. Another offshore hydrate site, Hydrate Ridge, also has the similar hydrate distribution (Torres et al., 2004). However, due to the higher gas flux in this reservoir, the average hydrate saturation is higher than Blake Ridge (Davie and Buffett; Bohrmann and Torres, 2006).

Figure 1.15B shows a typical hydrate distribution in the arctic regions: layers with high hydrate saturation are separated by the layers with low hydrate saturation. In this type of reservoir, the hydrate saturation can reach up to 80%, and reduce to as low as less than 5%. There is a sharp transition between these two regions. Compared to Figure 1.15A, Figure 1.15B unambiguously differentiates the reservoir into different regions.

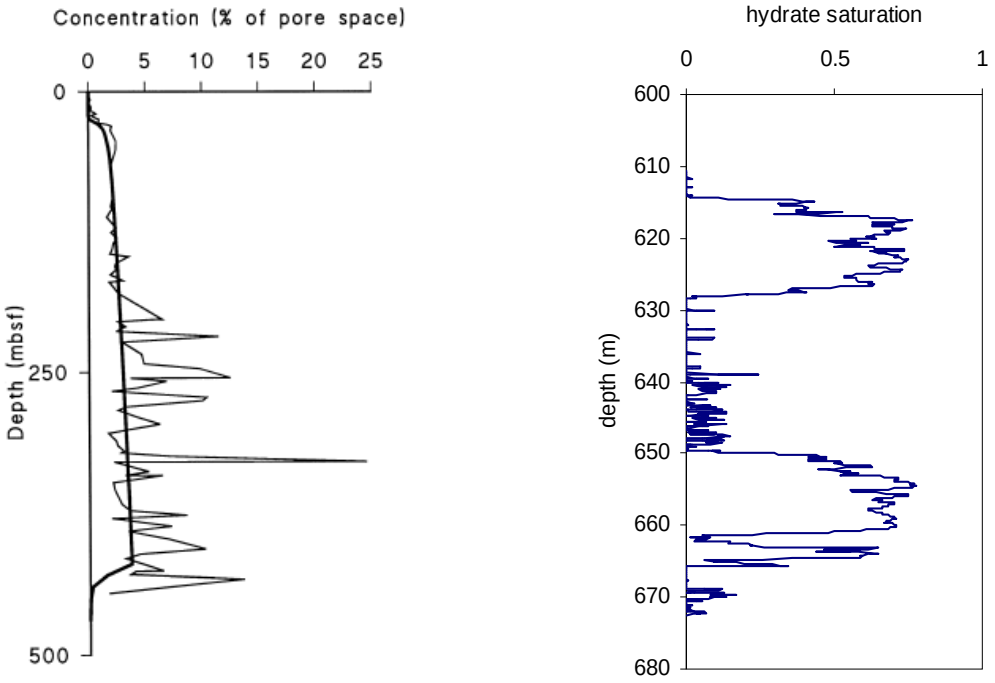

A. Hydrate distribution at ODP site 977, Blake ridge, offshore North Carolina (Egeberg and Dickens, 1999). The curves represent the hydrate saturation based on different models.

B. Hydrate distribution Mount Elbert hydrate reservoir, Alaska North Slope (Lee and Collett, 2011)

Figure 1.15: Hydrate distribution in two different types of hydrate reservoirs.

Hydrate distribution in the offshore ocean sediments

(Hyndman and Spence, 1992; Xu and Ruppel, 1999) proposed a model to explain the hydrate distribution pattern shown in Figure 1.15A. Since only the dissolved methane in the water is not enough to produce the amount of hydrate observed the ocean sediments, it is believed that water saturated with methane molecules migrates upwards from the deep gas reservoir. The migration is through the permeable conduits, such as faults and fractures. When the flow enters the GHSZ, if the mass fraction in water exceeds the gas solubility of that depth, free gas comes out and hydrate formation occurs.

There is a thin layer of free gas accumulation beneath BGHSZ. Since hydrate saturation is directly related to the amount of free gas in the sediments (Xu and Ruppel, 1999), the hydrate saturation decreases as moving farther away from BGHSZ. Figure 1.16 demonstrates such process.

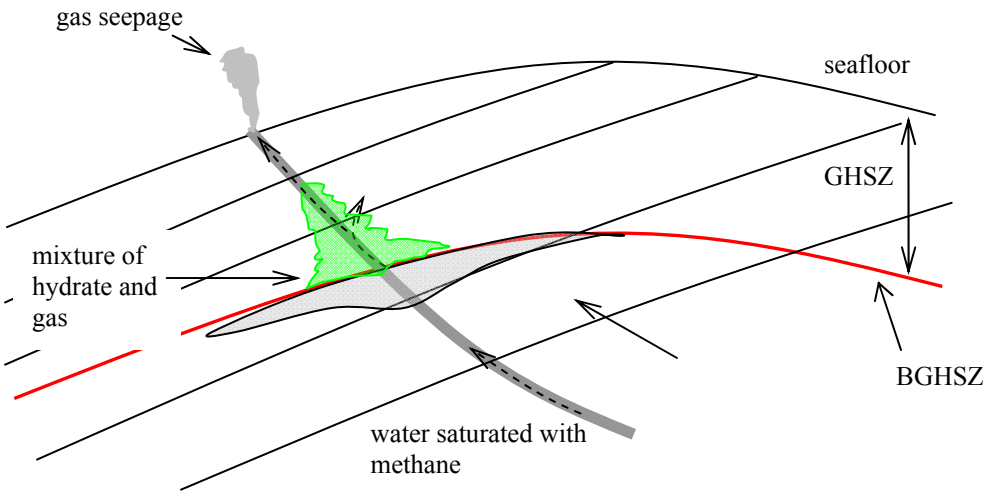

Figure 1.16: A scenario of water migration and hydrate formation in the ocean sediments. The water is saturated with methane molecules. It migrates upwards from the deep gas reservoir. Gas hydrate formation takes place when the flow enters GHSZ. The hydrate saturation has a direct relationship with the available gas (Xu and Ruppel, 1999), and therefore higher hydrate saturation is observed on top of BGHSZ where a free gas layer locates below BGHSZ. The hydrate saturation is lower in the shallower sediments. The extra gas that is not used for hydrate formation leaks on the seafloor and into the ocean (gas seepage).

An important modification of this model is proposed by (Tréhu et al., 2004; Liu and Flemings, 2006; 2007). The new model features the free gas migration through the conduits rather than the water flow saturated with methane molecules. This modification better explains the regions with high hydrate saturation (>50%) in Hydrate Ridge, as well as the very active gas seepage observed on the seafloor.

Several hydrate reservoirs in the ocean sediments have been discovered in North America. Blake Ridge, locating offshore southeastern North Carolina, is one of the reservoirs that have been extensively studied. Seismic study (Holbrook et al., 1996) shows the coexistence of methane and methane hydrate in the reservoir, and also relatively low average hydrate saturation (5%-7%). Such observation is consistent with the well logging readings, where resistivity log was used to estimate the hydrate saturation in several test wells. These readings suggest that hydrate occupies 2%-10% pore volume. Along with the volume of the reservoir, (Collett and Ladd, 2000) estimated that the total gas in place from only methane hydrate is 57 trillion m^3. Both of the above approaches estimate the hydrate saturation from the interpretation of other related data. The accuracy of the estimation is affected by lots of factors. A direct measurement from the cores is probably the most reliable method. However, it was believed that most hydrate dissociated and methane was lost during the core retrieving (Paull et al., 2006). Only a limited amount of cores are successfully retrieved by using PCS (Pressure Core Sampler). Although these cores were extremely valuable for the in-situ information, the measurements are insufficient to reconstruct the hydrate saturation profile in the reservoir.

Hydrate Ridge locates at Cascadian margin, offshore Oregon. Similar to Blake Ridge, methane and methane hydrate coexist in the reservoir (Torres et al., 2004). Very high gas saturation (~90%) exists beneath BGHSZ, and the capillary pressure between gas and water enables gas to pass through GHSZ (Tréhu et al., 2004). PCS was also applied and 18 cores from 3 test wells were obtained (Milkov et al., 2003). On average, 11% hydrate saturation and 4% gas saturation were measured in the in-situ condition. Gas venting is inferred from the observation, and a 1D model was proposed to estimate the chloride and gas hydrate saturation in GHSZ (Torres et al., 2004). (Liu and Flemings,

2006) proposed that the driving force for the upward gas migration is the elevated pore water salinity, and the 2D model based on this hypothesis was established as well (Liu and Flemings, 2007).

Another system that is being studied recently is at Atwater valley and Keathley canyon sites, northern Gulf of Mexico (Ruppel et al., 2008). For both sites, numerous different approaches are used to study the petrophysical and geochemical features of the hydrate system. These approaches include 3D seismic imaging (Dai et al., 2008; Dai et al., 2008), well logging (Lee and Collett, 2008; Cook et al., 2008), and lab-based core measurements (Lorenson et al., 2008; Winters et al., 2008). All these measurements suggest relatively higher hydrate saturation (on average, 30%) than Blake Ridge or Hydrate Ridge. Moreover, the hydrate saturation in the sediments has some correlation with the porosity: the higher porosity usually corresponds to higher hydrate saturation as well. Such observation suggests that, as argued by (Cook et al., 2008), hydrate formation fractures the sediments and therefore increases the porosity. The fractures also become the conduits for gas chimney in the reservoir. Gas venting is also observed in these two sites (Wood et al., 2008) , indicating the coexistence of gas and hydrate in GHSZ.

Hydrate distribution in the onshore arctic regions

Hydrate distribution below permafrost often exhibits a characteristic pattern (Figure 1.15B), where sediments with high hydrate saturation are separated by the layers of little to none hydrate (Dallimore and Collett, 2005; Rose et al., 2011). It is not surprising to see the hydrate saturation reaches up to more than 80% in the sediments. Moreover, no free gas is observed in the system. These distinct features suggest a totally different governing mechanism for the hydrate saturation.

The scenario in Figure 1.16 is no longer valid. First, the hydrate reservoir usually locates below the permafrost in the arctic region, and no gas seepage is observed. Second, from the field measurement, neither free gas is present in the hydrate reservoir, nor the hydrate formation and dissociation processes. We (Behseresht et al., 2009a) have therefore proposed a different scenario that could explain the observations in the field (Figure 1.15). The validity of such scenario will be tested in this work.

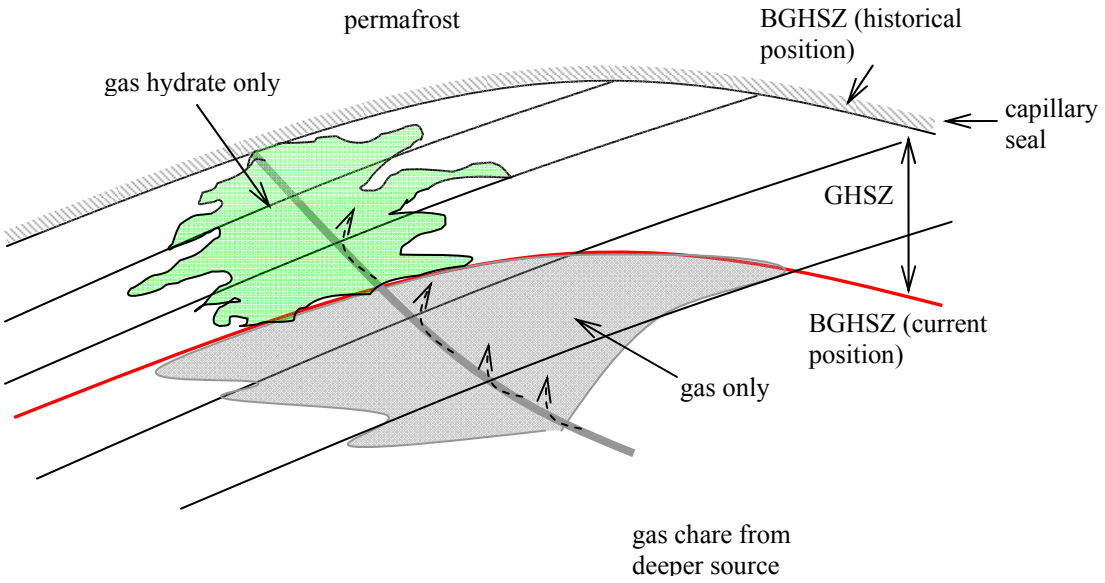

Figure 1.17: A scenario of gas migration and hydrate formation in the arctic sediments. Before BGHSZ descended (at the historical position), gas feeding from the faults and fractures invaded the sediments. Gas feeding completed later when the reservoir (include the green hydrate region and the gray gas region) was saturated with gas. That is, originally the entire reservoir was saturated by gas (gray). Over the geological time, BGHSZ descended, and gas and water were turned into gas hydrate at BGHSZ. The current BGHSZ stops at a position, which separates the hydrate-saturated region and the gas-saturated region. Note that this is only a conceptual scenario. Whether the reservoir is saturated by the gas or hydrate depends on lots of factors, which will be discussed in this work.

This scenario contains three stages (Figure 1.17). At the first stage the BGHSZ is above the sediments that will become the hydrate reservoir. Gas generated from the deep

sediments migrated upwards through the conduits (faults and fractures). When the capillary pressure between gas and water exceeds the entry pressure of the sediments, gas invasion took place. The gas saturation in the reservoir is controlled by capillarity. On top of the gas reservoir, the capillary seal contains the gas column. The seal could be clay-rich silts or shale. We assume this gas column only has a limited communication with the deeper gas resource, and can be considered as an isolated one during hydrate formation. Therefore, compared with the formation water, gas becomes the limiting phase. At the second stage the BGHSZ started to descend, and gas hydrate began to form at BGHSZ. The hydrate volume is smaller than the volumes of gas and water consumed, given that temperature and pressure being constant. Therefore, fluid redistribution in the reservoir occurred. All gas was converted into hydrate and no gaseous phase is observed in GHSZ. Only hydrate and water coexist in GHSZ. Nowadays (third stage), BGHSZ separates the hydrate-saturated region from the gas-saturated region. It should be noted it is also possible that the region below BGHSZ is already depleted of gas (this could due to the upward migration of free gas during hydrate formation at shallower sediments). Therefore, even the further descent of BGHSZ would not produce more hydrate in the reservoir.

The initial gas saturation and distribution in the reservoir becomes extremely important to determine the amount of hydrate. Figure 1.18 demonstrates how the capillary pressure between gas and water at different depths determines the water and gas saturations. At the free water level (FWL) the capillary pressure P_c between water and gas is equal to zero. P_c increases with height above the FWL in a linear fashion. P_c might get to a value that exceeds the capillary entry pressure of the sediment (P_c^{entry}), so that drainage can take place. As shown from the right panel of the figure, the initial water saturation, as well as the gas saturation, is determined by ΔP_c: the higher ΔP_c becomes

the lower water saturation is. ΔP_c is the difference between the capillary pressure between gas and water (P_c) and the capillary entry pressure of the sediments (P_c^{entry}). Only when the gas invades the sediment can hydrate subsequently be formed from the gas/water system (after BGHSZ descends) and get to a noticeable saturation. Moreover, as higher gas saturation provides more available gas for hydrate formation, the different gas saturation in the sediments has an important effect on the hydrate saturation.

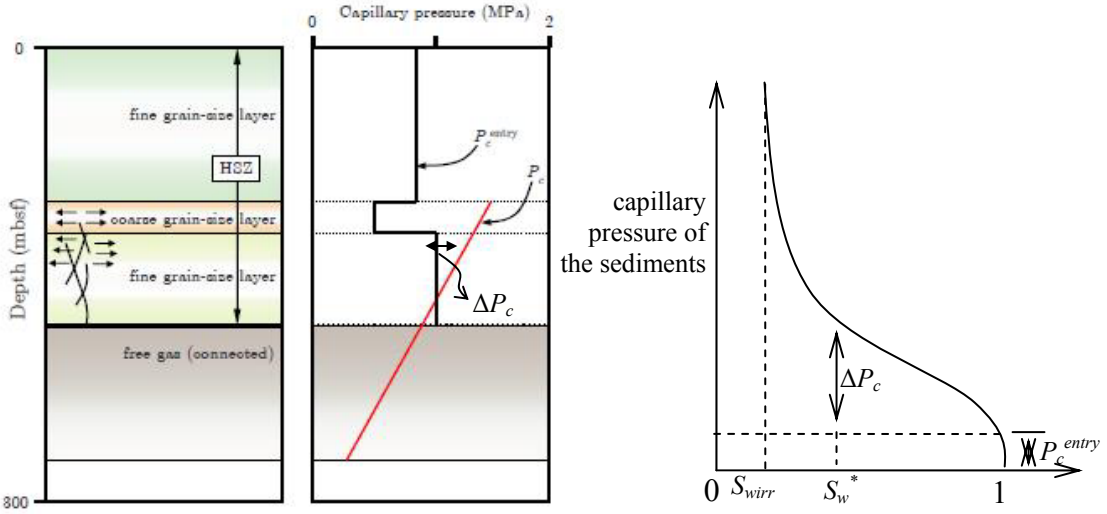

Figure 1.18: A conceptual model that shows pore level events determine the initial gas saturation in sediments that will subsequently be in the GHSZ. **Left**: an idealized 1D reservoir which contains layers of different reservoir facies. **Center**: the comparison between capillary entry pressure P_c^{entry} (or displacement pressure, percolation pressure) of the sediments and the capillary pressure P_c between gas and water. When P_c is smaller than P_c^{entry}, at the base of the sediments (the case shown here) gas cannot displace water from the sediments. When P_c is greater than P_c^{entry}, gas can displace water. The final water and gas saturation in the sediments is determined from the capillary pressure of the sediment P_c^{sed}. **Right**: a typical curve of P_c^{sed} versus water saturation. ΔP_c, which is the difference between P_c and P_c^{entry} from the centered figure, is reproduced in the right figure. From ΔP_c the corresponding water saturation S_w^* can be determined. As ΔP_c is increasing from the bottom to the top of the sediments, initial water and gas saturation varies vertically.

Two important hydrate reservoirs are under extensive studies. Mount Elbert Hydrate reservoir locates at the Alaska North Slope (Hunter et al., 2011). While BGHSZ (Base of Gas Hydrate Stability Zone) is at 1100 m, the gas hydrate (measured from one well) only extends to less than 680 m. Different approaches were employed to cross-verify each other (Winters et al., 2011) and estimate the hydrate saturation (Lee and Collett, 2011). Two regions of high hydrate saturation were identified, with an average

hydrate saturation of 60% (Figure 1.15B). Below each of these regions, sediments with low hydrate saturation (less than 10%) were observed. This highly concentrated hydrate distribution allows for the possible production of natural gas from the hydrate. Both test production and numerical simulation were performed to analyze the production potential (Pooladi-Darvish and Hong, 2011; Kurihara et al., 2011; Anderson et al., 2011).

The Mallik hydrate reservoir locates on the coast of Beaufort Sea, northwest Canada. Gas hydrate is usually found 300 m to 700 m below the permafrost. Four test wells were drilled for the hydrate research, among which 5L-38 well was extensively studied. Seismic, well logging and core-analysis are all used to analyze the petrophysical, geochemical features and production potentials. The results were turned into over 60 scientific papers, which can be found at (Dallimore and Collett, 2005). Similar hydrate distribution pattern as Figure 1.15B was also observed in 5L-38. Hydrate is found in about 200 m of sediments, where the high saturation regions are separated by the low saturation regions. Tests were also performed to analyze the possible hydrate production in an economical way (Moridis et al., 2004; Moridis, 2004).

1.3 MODEL DESCRIPTION AND OBJECTIVES

Gas hydrate is a natural clathrate with methane molecules encaged in the water lattice. It deserves a thorough investigation due to its potential role as an energy source, in geological hazards, and in global carbon cycle and global warming. Methane hydrate, owing to its abundance in the gas hydrate family, becomes the representative clathrate in our research. In this work, we consider the scenario of the coexistence of methane gas and water. That is, the system contains two phases before hydrate formation, rather than a single phase system where methane is dissolved in the aqueous phase.

Compared to the hydrate reservoirs in the ocean sediments, where theoretical and numerical models have been proposed to analyze the hydrate distribution in the field scale, to our best knowledge there is no model available for the reservoirs in the arctic region. However, the importance of these reservoirs should not be underestimated. The concentration of gas hydrate (can reach up to 80%) make it a more attractive potential reservoir for gas production than those in ocean sediments (hydrate usually has a lower concentration). Consequently, models are needed to better explain the hydrate formation and distribution in the arctic regions.

Methane hydrate formation (from methane and water to methane hydrate) leads to the hydrate volume much smaller than methane and water volume combined. The reduction of the fluid-occupied volume becomes a driving force for the fluid movement in the local porous medium. The fluid movement in turn changes the capillary equilibrium in the reservoir. This leads to a larger scale (field scale) fluid redistribution, and as a feedback, alters the local fluid distribution and saturation as well.

We employ models from both pore and field scales. First, we describe the methane hydrate formation at the level of gas/liquid interfaces in the porous medium,

where capillarity-dominated drainage and imbibition are the governing processes. Several models are proposed to study the effect of temperature, pressure, salinity, pore and throat size distributions on hydrate distribution and saturation. One is the pore network modeling based on model sediments (Chapter 2). This model gives the fluid distribution in the porous medium during the capillary-controlled events, which the crucial information to estimate the hydrate saturation. The other one is Level Set Method Progressive Quasi Static algorithm (LSMPQS, Chapter 2), a numerical method introduced as a benchmark to test the correctness of network modeling. The last one is a thermodynamic model that analyzes the effect of salinity, temperature and pressure (Chapter 4). Knowledge from the above models provides crucial information for the hydrate distribution in the field scale. Second, a field-scale sedimentological model is developed (Chapter 5). It employs the information from the pore-scale, and takes into consideration the regional environment. The model helps reveal the mechanism affecting the field-scale hydrate distribution, and predicts the hydrate distribution in the reservoir.

As discussed previously, we focus on the hydrate formation within gas accumulations in permafrost regions. In this system, hydrate formation takes place at a slow pace and no drastic macroscopic gas and water movements are associated with it. Based on this environmental setting, models combining both scales are developed and applied to predict the hydrate distributions.

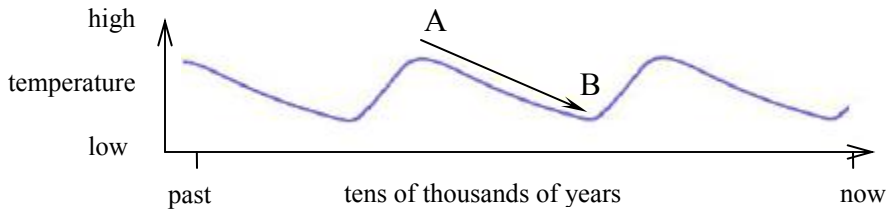

Figure 1.19: Qualitative arctic temperature cycle during the past several tens of thousands of years. The arrow indicates that within one cycle, temperature dropped with time. The Base of Gas Hydrate Stability Zone (BGHSZ, as shown in Figure 1.6) in the permafrost regions fell as well.

Figure 1.19 shows several cycles of arctic temperature variation. Within each cycle, the Base of Gas Hydrate Stability Zone (BGHSZ, above which gas hydrate can stably sustained) moves upwards during the warming, and downwards during cooling. The process happens in such a slow pace that there is sufficient time for possible methane hydrate formation. As BGHSZ moves downwards (temperature drops), the methane and water system that was originally below BGHSZ starts to form hydrate. When BGHSZ moves upwards, methane hydrate dissociates into water and methane gas because the temperature in the formation no longer provide an environment for hydrate stability, that is, conditions in the formation move across the boundary between hydrate and water as the stable phases to gas and water as the stable phases (Figure 1.2). We focus on the hydrate formation when BGHSZ moves downwards, while the hydrate dissociation is beyond our interests in this work.

The field observation from Mallik reservoir suggests that methane hydrate saturation exhibits lateral continuity; therefore, we propose a 1D model to investigate the hydrate distribution in the vertical direction. In this model, water is only allowed to invade from above and below the reservoir, and methane supply from outside the reservoir is not permitted. Figure 1.20 shows the coexistence of gas and water when

BGHSZ is above the reservoir. This corresponds to the early stage of the arrow (point A in Figure 1.19), when the global temperature is at a large value. In a static system, we assume that a gas column has accumulated below BGHSZ, and stabilized by the capillary equilibrium between gas and water. The initial gas and water saturation along the vertical direction can be determined by using our network modeling for drainage: for example, at a depth above the Free Water Level (FWL), capillary pressure P_c^* can be calculated (Figure 1.20B). This value is substituted to the capillary curve (Figure 1.20C), which is obtained from the drainage simulation based on the network modeling of the model sediments. The corresponding saturation S_w^* can therefore be determined.

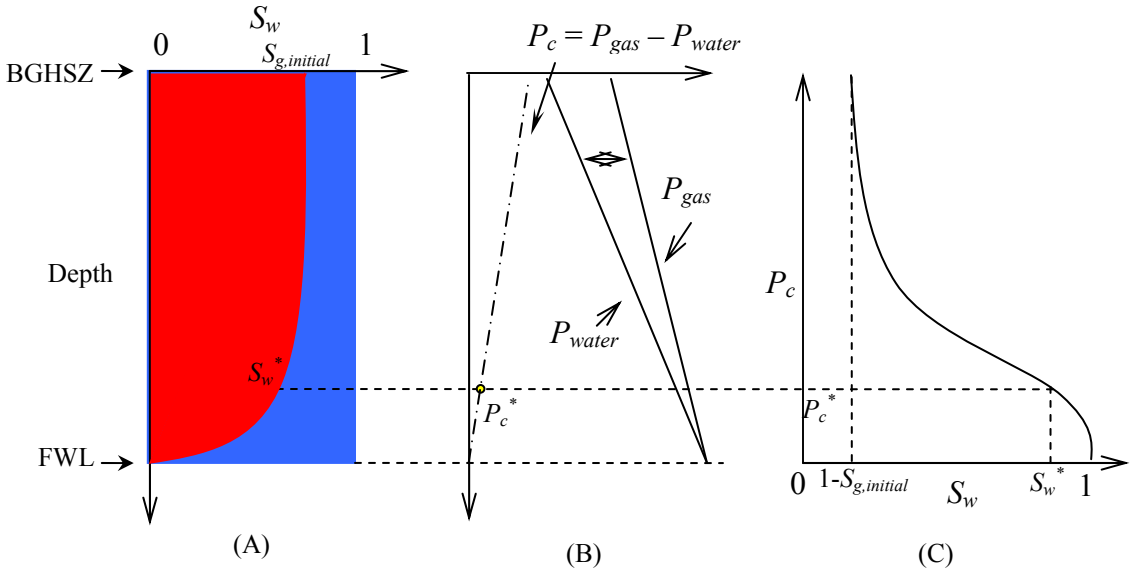

Figure 1.20: Gas (red) and water (blue) distribution before hydrate formation takes place. (A) shows BGHSZ is at the top of the gas column and Free Water Level (FWL) is at the bottom where the porous medium is saturated with water. (B) gives the capillary pressure (P_c) distribution in the system. P_c ($P_{gas} - P_{water}$) is zero at FWL, and increases upwards in an approximately linear fashion. (C) shows the capillary pressure vs. water saturation. In the real reservoir, different facies have different capillary curves. However for an illustration, we use a single curve as the representative.

When BGHSZ is moving down, hydrate is formed. Keeping temperature and pressure constant, the volume of hydrate is smaller than the volume of consumed water and methane. This is the driving force that sucks water and gas into the void space. When the gas and water contact again, new hydrate will form. This positive feedback maintains hydrate growth until no more gas is available.

The elements of this model, including the effect of sedimentological variation with depth, were outlined in (Behseresht et al., 2009a). The implications of the model for large scale fluid movement during BGHSZ descent were examined in (Behseresht and Bryant, 2011). In this work the pore scale basis for the model of hydrate growth is examined. We assume that hydrate forms at the gas-water interface, and moves into the gaseous phase (Figure 1.21). This assumption is based on both the experimental observation in microscale (that is, we assume gas is the limiting phase and water is the presumed available) and theoretical analysis of capillary equilibrium along the gas-water interface. Also in this work, the implications of the model for pore-scale fluid transport are examined. As hydrate continues to grow, two possible hydrate formation scenarios are proposed. They correspond to different water supply rates to form the hydrate: if the water supply rate is much greater than the hydrate formation rate, we argue that the minimum hydrate saturation will be obtained in the porous medium. On the other hand, if the water supply rate is much lower than hydrate formation rate, we suggest this leads to in the maximum hydrate saturation. Thus the model should bracket the range of hydrate saturations observed in the field. An important assertion in the pore-level model is that both scenarios resemble the imbibition process in the porous medium, with gas phase being replaced by aqueous phase and/or hydrate phase. Consequently, the imbibition results from both our network modeling and the simulation based on level set method

progressive quasi-static algorithm (LSMPQS) become the powerful tool to investigate the fluid migration and redistribution during this process.

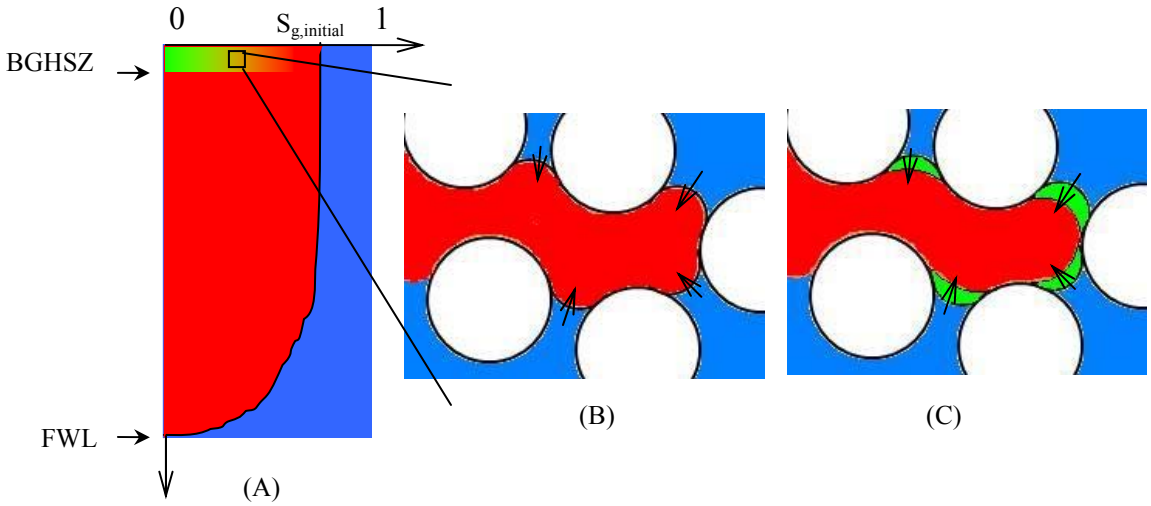

Figure 1.21: Hydrate is formed when BGHSZ moves downwards. (A) shows hydrate (green) formation at BGHSZ, and takes up the spaces that was originally occupied by gas (red). In this process, water invasion also occurs. (B) shows a demonstration of the gas (red) and water (blue) distribution in the porous medium before hydrate formation. Hydrate is formed from the gas-water interface, and moves towards the gaseous phase (C). The volume decrease associated with hydrate formation reduces the gas phase pressure, causing water to be sucked through microscopic defects in the hydrate layer to form new hydrate at the gas side. Hydrate formation ends when no more free gas is available. At this endpoint, the space formerly occupied by gas phase is filled by either hydrate alone, or by a combination of hydrate and aqueous phases, depending on the rate of aqueous phase invasion through the hydrate layer.

The formation of methane hydrate creates vacancies in the porous medium, which sucks both gas and water to fill in. Gas from the bottom of gas column will flow upwards to fill the vacancy. This generates low pressure region at the bottom, where water

invasion will take place. Figure 1.22 shows this situation. Between Gas Water Transition Point (GWTP, above which gas saturation starts to increase from the residual value) and FWL, a region of residual gas saturation arises due to the imbibition process. The free gas that originally exists in this region migrates upward to the hydrate-forming region, and provides the methane for continued hydrate formation there. As BGHSZ keeps moving down, GWTP rises accordingly, until GWTP and BGHSZ converge. This means that no free gas can move up for further hydrate formation.

GWTP keeps rising when BGHSZ continues to move down. Between GWTP and FWL, only the residual gas is available to convert into hydrate, which gives a very small hydrate saturation region at the bottom. The hydrate formation, therefore, alters the distribution of hydrate-aqueous phase saturations compared to the initial gaseous-aqueous phase saturations. The altered distribution agrees with the field observation.

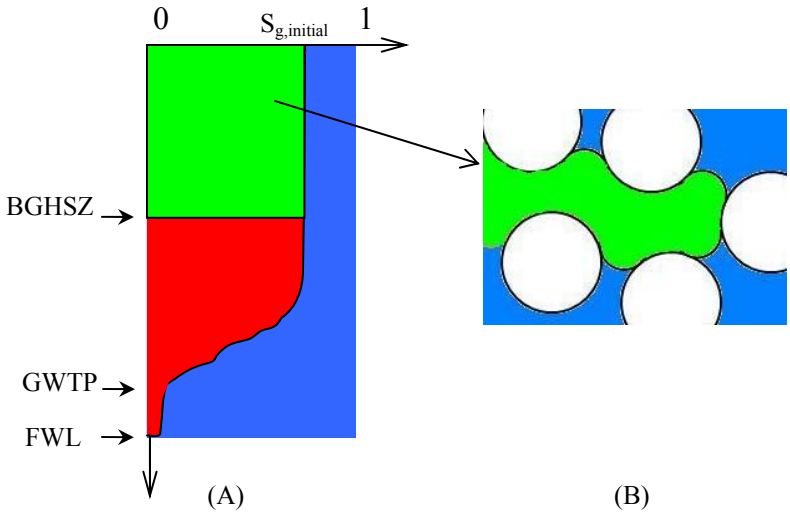

Figure 1.22: The maximum hydrate saturation in the porous medium after formation is complete. We only show one scenario to give a general idea of the model. (A) shows the field scale hydrate saturation. GWTP, originally very close to FWL before hydrate formation, now moves upwards as imbibition takes place at the bottom of the gas column. The gas saturation between GWTP and FWL is reduced to the residual value. The free gas moves upwards to form hydrate. (B) gives a schematic of the hydrate distribution in the porous medium.

The model proposed to estimate hydrate distribution in reservoir requires the understanding of hydrate formation in the pore level and fluid distribution in the field level. In the pore level, we use our pore-network modeling on model sediments to predict the drainage and imbibition behavior. The drainage simulation gives the initial gas saturation in the sediments before the hydrate formation, while the imbibition simulation predicts the hydrate saturation based on different scenarios. LSMPQS is employed to ensure the reliability of the network modeling: LSMPQS captures the basic physics and is able to model fluid/fluid interface movement in the porous medium with great detail. In the field scale, a 1D sedimentological model is developed. It incorporates the results from the pore level, and accounts for the fluid redistribution by using global material balance.

These models allow us to give a reasonable prediction of the hydrate distribution in a passive hydrate system.

1.4 HYPOTHESES TO BE TESTED IN THE RESEARCH

Three important hypotheses are introduced in this dissertation.

The first hypothesis is that network modeling is capable of predicting the correct individual drainage and imbibition events in the porous medium (Chapter 2 and 3). This hypothesis can be justified by comparing the network simulation results with those from LSMPQS. LSMPQS can directly simulate the fluid interface movement in the porous medium without any geometry simplification (Section 2.2), and is considered as the benchmark when the experimental data are not available in the pore level.

The second hypothesis follows the first one, which argues that the network modeling based on the periodic boundary conditions gives a better estimate of irreducible wetting phase saturation (S_{wirr}) and residual nonwetting phase saturation (S_{nwr}) in the field scale. The periodic boundary condition eliminates the boundary effects on the fluid distribution (Behseresht et al., 2009b), which resembles the conditions in the reservoir: the local porous medium is not affected by the reservoir boundaries that are usually miles away. The validity of this hypothesis for $S_{w,irr}$ was studied by (Behseresht et al., 2009b). In this work we test the simulation results with the field observations of residual oil saturation from field-scale Tracer Tests (either single well or two well test), and a good agreement would justify this hypothesis.

The last hypothesis (that is, the vertical hydrate profile in the hydrate reservoirs of the arctic regions has a characteristic pattern that is the natural consequence of BGHSZ descending through a pre-existing gas accumulation) involves several premises. An isolated gas column is established before BGHSZ moves downwards from above the reservoir. When hydrate forms at BGHSZ, a thin layer of hydrate is first generated at the gas/water interface, and then hydrate grows into the gaseous phase. We further assume

hydrate formation follows the imbibition pathway, and different imbibition events would result in different hydrate saturations in the porous medium. The local hydrate formation creates vacancy in the porous medium, which is the driving force to redistribute fluid in the reservoir. After BGHSZ moves to the bottom of the reservoir, the hydrate profile yields a characteristic pattern. The hydrate profile from the model prediction is compared with the field observation to validate this hypothesis.

1.5 THESIS SUMMARY

Chapter 2 focuses on the drainage and imbibition simulation by network models. The physically representative network is established from the model sediments (dense, disordered sphere packs). By using the new imbibition criteria, we are able to predict the drainage and imbibition events. The network model is justified against the results from the LSMPQS algorithm (Prodanovic and Bryant, 2006). We compare not only the macroscopic properties (drainage and imbibition curves) but also the pore-scale properties (filling status of individual pores). Using the tested drainage and imbibition criteria, we next improve our saturation prediction by applying periodic boundary condition (Behseresht et al., 2009). This novel boundary condition minimizes the boundary effect, so that the irreducible wetting phase saturation and the residual nonwetting phase saturation are representative of the reservoir values, which are the key parameters for the field-scale hydrate saturation prediction.

Chapter 3 studies drainage and imbibition in the real rock samples. Presently, this chapter showcases the generality of our fluid displacement simulation methods. While gas hydrate has thus far been found in the oceanic or arctic sediments, we should not exclude the possibility of hydrate existence in the rocks. Therefore, knowing the fluid distribution in the rock becomes important. Digitized rock samples from multiple sources are used to generate the network, by using *3DMA-Rock* software (Lindquist, 2008). New drainage and imbibition criteria are proposed, and the simulation results are compared with those from LSMPQS. The pore-by-pore comparison is also introduced to compare the filling status of the pores.

In Chapter 4 we introduce two different approaches to estimate the hydrate saturation in the pore scale. The first approach employs mass conservation in a 1D box.

We investigate the possible hydrate saturation at different initial methane and water saturation, temperature, pressure and initial water salinity. The system volume change is significant resulting from converting methane and water into hydrate, which in nature is the driving force to redistribute gas and water in the field scale. The second approach studies the hydrate saturation by using the imbibition simulation of network modeling. We assume the hydrate crystal growth follows the path of conventional imbibition process. Different imbibition events (incremental movement and Melrose jump) can either promote or inhibit hydrate formation, and therefore we estimate the upper and lower bounds of the hydrate saturation in the porous medium.

In Chapter 5 we develop a 1D sedimentological model to estimate hydrate distribution in the vertical direction. This model only focuses on the hydrate system in arctic regions. It incorporates the pore-scale models and the corresponding results, regional mass conservation and also the environment change (for example, the decrement BGHSZ). The predicted hydrate distribution is compared with the field observation (Mallik and Mount Elbert hydrate reservoirs), where a satisfactory agreement is obtained.

Chapter 6 summarizes the dissertation. Conclusions and future work are presented in this chapter.

2. Network modeling of drainage and imbibition in the model sediments

Drainage and imbibition govern the fluid distribution and availability, and thus are important processes for hydrate formation and distribution in the porous medium. The initial methane distribution in the field is determined by the capillary equilibrium between gas and water, which extends from the GWC (Gas Water Contact) to the seal that contains the gas column. Our network simulation for drainage is capable of modeling the gas saturation at different capillary pressures, which can be applied to estimate the initial gas distribution in the reservoir. With BGHSZ moving downwards into the gas reservoir, hydrate formation takes place. The formation process involves gas and water consumption, as well as water invasion (which will be elaborated in Chapter 4), and therefore mimics the imbibition process. Moreover, we assume the imbibition events control the hydrate saturation, and therefore the imbibition simulation by network modeling is important.

In this chapter, we propose a new approach – pore-by-pore comparison – to test the correctness of network modeling, along with the newly-developed C_1 imbibition criterion. This approach checks the pore filling status (that is, the pore is filled by wetting or nonwetting phase in both simulations) in individual pores at each step of drainage and imbibition. The comparison shows good agreement between the two simulations, and thus justifies the network modeling. The periodic boundary condition is later applied to eliminate the boundary effect, so that our results from the network modeling can be used to represent the true fluid distribution in the sediments in the reservoir. We then elaborate in details of the importance of network modeling to the methane hydrate research in this work.

2.1 INTRODUCTION

Since its introduction by (Fatt, 1956a; 1956b; 1956c), pore throat network modeling has become a powerful tool to investigate the microscopic behavior of fluid displacement in the porous media (Blunt, 2001; Valvatne and Blunt, 2004; Valvatne et al., 2005; van Dijke and Sorbie, 2003). Network modeling provides an approach other than the lab-based experiments to investigate the petrophysical properties of the porous medium, which are the crucial input for a field-scale reservoir simulation.

Network modeling is capable of simulating flow of single and multiphase fluids. For single phase flow, by solving the pressure difference between the inlet and outlet of the network, permeability can be computed. The similar idea can also be applied to the electrical current flow in the porous medium, to obtain the electrical resistivity and conductivity, both of which are important properties for resistivity log. The model can also be used to investigate the flow behavior of the non-Newtonian flow (Pearson and Tardy, 2002). For two phase flow, network models are widely used for drainage and imbibition simulations, and are naturally extended to compute the two-phase relative permeabilities (Bryant and Blunt, 1992a; Gladkikh, 2005; Jerauld and Salter, 1990; Valvatne and Blunt, 2004). Other factors, such as the effects of wettability, mix-wet medium and capillary number on relative permeability, are also investigated (Øren et al., 1997; Patzek, 2001; Knudsen and Hansen, 2002; Aker et al., 1998; Singh and Mohanty, 2003; Mogensen and Stenby, 1998; Al-Raoush and Willson, 2005; Al-Gharbi and Blunt, 2005; Mason and Mellor, 1995; Motealleh, 2009). The calculation of the relative permeability is widely studied to understand the fluid displacement in a three-phase system (Mani and Mohanty, 1997; Blunt, 2001; Mani and Mohanty, 1997; Pearson and Tardy, 2002; Valvatne et al., 2005). This gives a better understanding of the fluid

displacement that happens during enhanced oil recovery (for example, WAG injection, water-alternating-gas injection), and therefore important as well (van Dijke and Sorbie, 2003). Moreover, the mix-wet medium is commonly observed in the reservoir, and thus deserves investigation as well (van Dijke and Sorbie, 2003).

To use the network model, complicated void space of a porous rock is simplified to a network of geometrically simple pores (openings) and throats (constrictions). Historically, the first pore-level description of a porous medium was as bundle of isolated capillary tubes. The tubes, with different sizes, represent both pores and throats (Figure 2.1A). (Fatt, 1956a; 1956b; 1956c) developed the structured pore-throat network model to account for the interconnectivity in the porous medium (Figure 2.1B). This model, either 2D or 3D, introduces connections between junctions (pores) through bonds (throats) on a regular lattice. Pore and throat sizes, often extracted from experimental measurements, need to be assigned to each unit. The usual procedure is to perform the assignment randomly. Such treatment usually results in large variation of the sizes at the neighboring units, which violates the fact that the neighboring pores and throats are correlated (Bryant et al., 1993) and therefore should share the similar sizes.

We use 3D network models (Figure 2.1C) that extract and retain the interconnectivity and physical parameters (volumes, areas) of the original porous medium (real rock sample or model sediment). The algorithms to extract the network from different types of porous media will be described later. Compared to the other two models shown in Figure 2.1A and B, this network is derived from the real porous medium, and therefore better represents the pore-level geometry and its influence on physics.

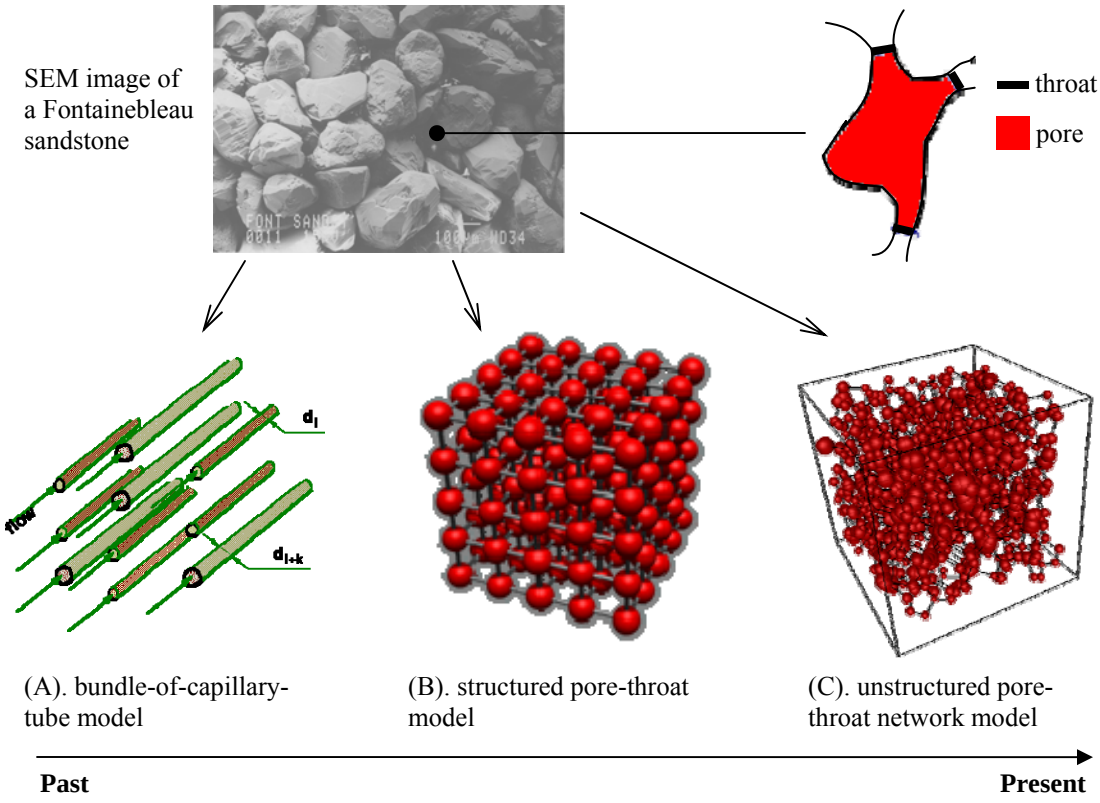

Figure 2.1: A brief history of networks for the flow simulation. All the networks are developed to mimic the real porous medium, where the void spaces are differentiated as pores (open space, junctions) and throats (narrow space, bonds). The earliest and simplest network is the bundle-of-capillary-tubes model where tubes running across the volume are not interconnected (A). A later modification (B, structured pore-throat model) separates pores and throats, and also accounts for the interconnectivity in 2D or 3D; however it ignores intercorrelation among the neighboring pores and throats. Modern network models extract the network directly from the porous medium and thus retain topology of the original medium (C).

Physically representative network (PRN) was originally developed to model the physical process (e.g. fluid flow or electrical current flow) in the unconsolidated porous medium. The simplest version of PRN is derived from model sediments created by mimicking natural sedimentological processes. A sediment is simplified as a dense,

disordered sphere packing, where spheres represent the real grains (Figure 2.2A and B). Using Delaunay tessellation of the sphere centers (Ripley, 2004), the packing is divided into individual, tetrahedral units (Mason and Mellor, 1995). Each tetrahedron is constructed by centers of the four neighboring spheres and its void part defines a pore (Figure 2.2C). Each tetrahedron shares 4 faces (throats) with four neighboring tetrahedra (pores, Figure 2.2D), so that fluid can move from one tetrahedron to another. The resulting network preserves the key characteristics of the porous medium. For example, pores and throats are interconnected and randomly positioned, and the sizes of the neighboring pores and throats spatially correlated (Bryant et al., 1993). We therefore refer to this network model as Physically Representative Network Model (PRNM). This model has a broad use in estimating the relative permeabilities (Bryant and Blunt, 1992), permeability (Bryant et al., 1993) and electrical resistivity (Motealleh et al., 2007), as well as simulating the capillary-controlled fluid displacement in porous media (Behseresht et al., 2009b; Gladkikh and Bryant, 2003; Gladkikh, 2005).

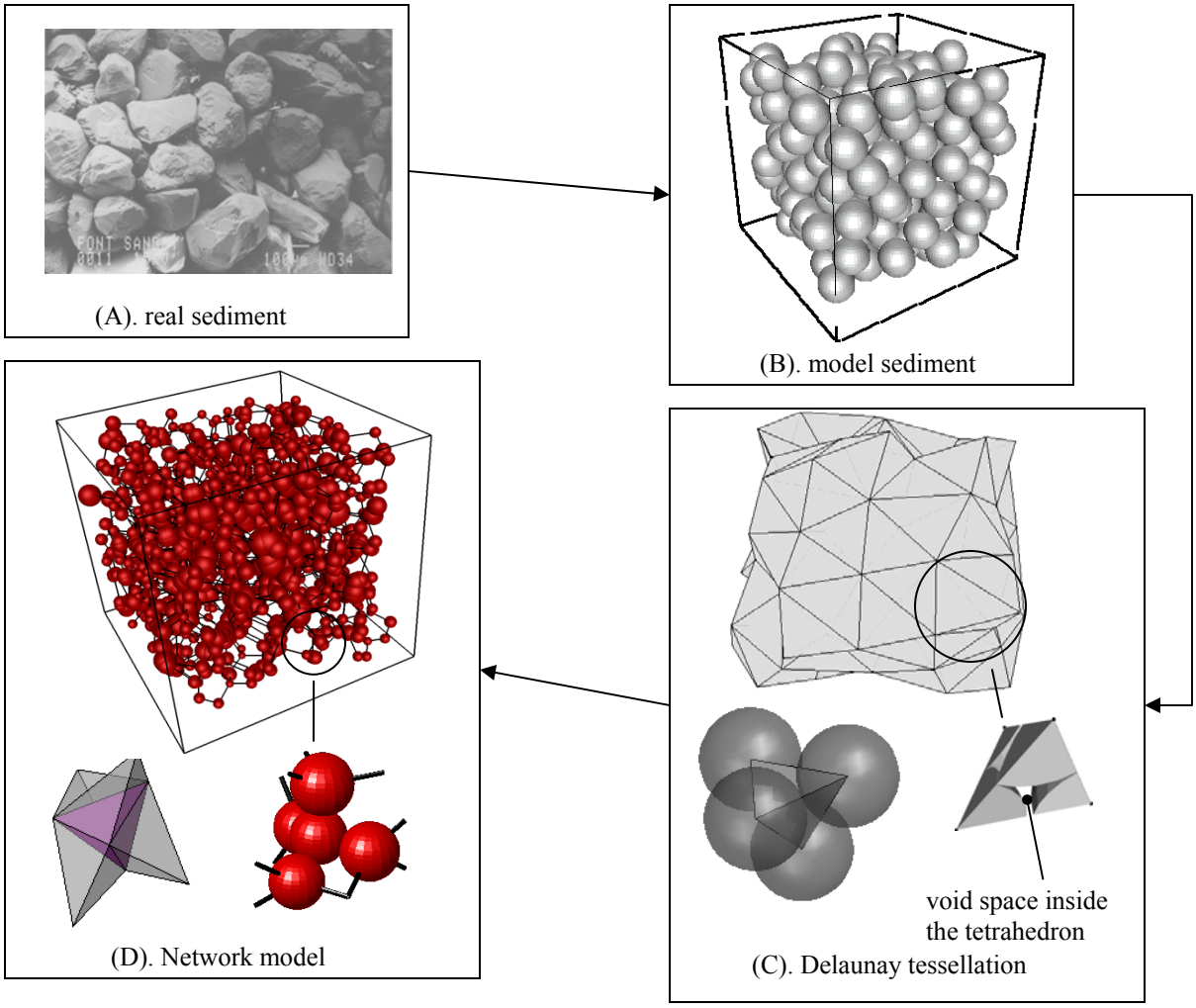

Figure 2.2: The procedure (A to D) to generate a network from the model rock sample. (A) shows a Fontainebleau rock sample, and (B) is the model sediment. Gray spheres in B are used to represent the grains in A as a first order approximation. Delaunay tessellation is employed to subdivide the sphere packing (B) into individual tetrahedron units (C). Every tetrahedron is constructed by the centers of four neighboring spheres. The void space inside the tetrahedron is the pore, and the void area at each face of a tetrahedron is the throat. As shown in D, the magenta tetrahedron is connected to the neighboring tetrahedra (gray) through its faces, this is equivalent to that each pore (red spheres) is connected to its four neighboring pores through its four throats (black bonds) (D). The entire network is also shown in (D).

Most common boundary conditions in network flow simulation are those where inlet and outlet face is assigned to let fluid flow in and out, with other faces sealed. (Behseresht et al., 2009b) have recently implemented periodic boundary conditions - referred to as infinite acting PRNM (iPRNM) - in order to alleviate boundary and finite size effects and make predictions more applicable in the field. Both the model sediment and the resulting network are disordered, yet periodic in all directions. We thus distinguish finite PRNM (fPRNM, which is based on the conventional boundary conditions), as opposed to infinite acting PRNM (iPRNM), where periodic boundary condition is applied. We study drainage and imbibition based on each set of boundary conditions, and compare their results with the available data.

2.2 LEVEL SET METHOD PROGRESSIVE QUASI STATIC ALGORITHM (LSMPQS)

We here introduce another numerical method – Level Set Method Progressive Quasi Static algorithm (LSMPQS). The purpose of using this method in our work is to provide a benchmark for two-phase flow, where no experimental data are available to test the correctness of the network modeling at the pore scale. LSMPQS accounts for the basic physics governing the multiphase flow displacement driven by capillarity, and is capably of tracking interface movement in a complex geometry without any simplification. The simulation results have been compared with the experimental data, where satisfactory results are achieved (Prodanovic and Bryant, 2006; Prodanovic et al., 2008). This method is used in Chapter 2, 3 and 4 to verify the results of network modeling.

The level set method was initially introduced by (Osher and Sethian, 1988), and has gained application in numerous areas (Osher and Fedkiw, 2002). Its capability of tracking complex interface evolution under curvature enables the application in predicting the capillary displacement process in porous media.

The zero level set of a function ϕ is used to represent the position of interface at all times. In our case, $\phi < 0$ denotes wetting phase and $\phi > 0$ denotes nonwetting phase and solid grain together. The differentiation of $\phi = 0$ with respect to time and space gives:

$$\frac{\partial \phi}{\partial t} + F\left|\nabla \phi\left(\vec{x}(t), t\right)\right| = 0 \tag{2.1}$$

Equation (2.1) governs the evolution of function ϕ in space during a period of time, so the interface of interest is at all times embedded as the zero level set. F is the interface movement speed, with the assumption of F normal to the interface. In LSMPQS algorithm, F reflects the influence of difference between capillary pressure and fluid/fluid

curvatures scaled by interfacial tension. At the initial step of drainage, F is determined by:

$$F(\vec{x},t) = a_0 \exp\left[f\left(1 - \frac{V(t)}{V_m}\right)\right] - b_0\kappa(\vec{x},t) \tag{2.2}$$

The first term on the right hand side represent the influence of capillary pressure, where a_0 is a reference pressure, f is the dimensionless bulk modulus, and V_m and $V(t)$ are the target volume and the phase volume inside the boundary, respectively. The second term reflects the surface energy, where b_0 is the surface tension and $\kappa(\vec{x},t)$ is twice the average curvature of the interface. At steady state, the fluid/fluid interface is stabilized, so that F is zero everywhere in the computational domain. Capillary pressure and surface tension are balanced under this condition.

After the initial stage, we increase the curvature by $\Delta\kappa$, and evaluate the following speed function

$$F(\vec{x},t) = a_0 - b_0\kappa(\vec{x},t) \tag{2.3}$$

to get the new steady state, at which the capillary pressure and surface tension is balanced again. Fluid configurations, such as fluid distribution and interface, can be easily computed.

The boundary of the computational domain is defined by introducing the fixed level set function ψ (called 'mask'), where the pore-grain boundary is described by $\psi = 0$, and the level set function in the pore space satisfies $\phi(\vec{x},t) \le \psi$. We enforce the mask after every step thus preventing the fluid/fluid interface from entering into the grains. Furthermore, it results in a zero contact angle (without explicitly solving for it). More details can be found in (Prodanovic et al., 2006). Software package LSMPQS based on this algorithm and used in this work is freely available (Prodanovic, 2009).

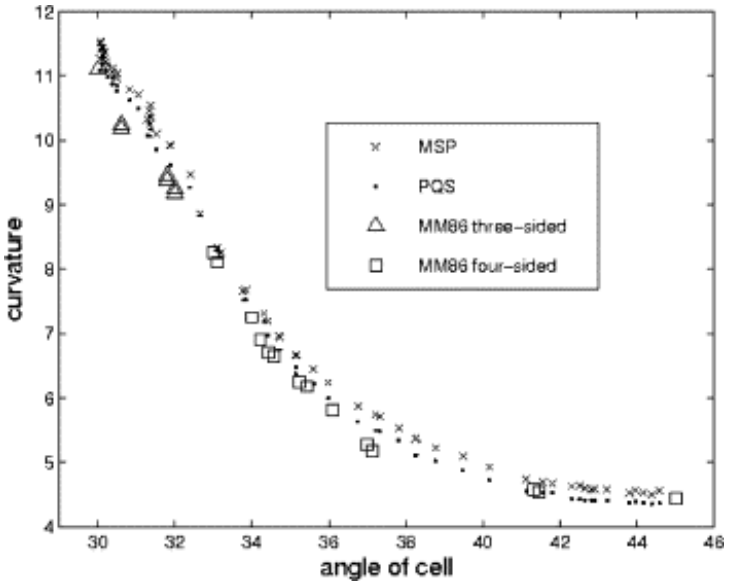

(A). Drainage critical curvature comparison with experiments (Prodanovic and Bryant, 2006)

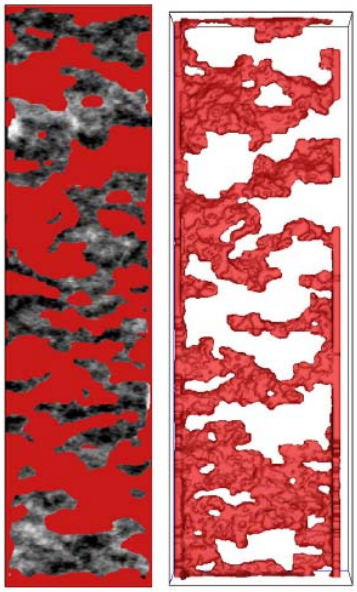

(B). Oil blobs (red) comparison with the experimental image (Prodanovic et al., 2008)

Figure 2.3: Comparison between LSMPQS and experimental results. (A) is the critical curvature comparison from 58 Finney pack throats. (B) is the image comparison of the oil blobs trapped in a fracture after the water flooding.

LSMPQS has been validated by comparing its results with experiments (Figure 2.3). The comparison includes the fluid displacement within single pores (Prodanovic et al., 2006) and within a fracture (Prodanovic et al., 2008). Reasonable agreement can be obtained in both cases. when the pore scale information in experiments is intractable, LSMPQS becomes a useful approach to measure the appropriate fluid configurations. Thus the validation of the pore network model can be done on microscale level, as opposed to comparing macroscopic information such as capillary pressure-saturation relationship.

2.3 DRAINAGE AND IMBIBITION SIMULATIONS WITH THE CONVENTIONAL BOUNDARY CONDITIONS

An important, and yet to be answered question is the correctness of network modeling in predicting drainage and imbibition. The conventional approach is to compare the capillary curves (P_c vs. S_w) between modeling and experiments, and the network modeling results are considered to be reliable once the two curves agree with each other. However, we argue that this is an important and yet insufficient justification. The capillary curve only reflects the global average of the fluid distribution in the porous medium. The agreement of the curves does not yield any information of the pore-level events, since different fluid distributions can lead to identical point on the capillary curve. It is possible that our network prediction produce false fluid distribution but correct capillary curve.

The reason for comparing only the capillary pressure curve is that experiment-based pore-level visualization is not available. In this work, we avoid that problem and are consequently able to compare pore level events. A new numerical technique, Level Set Method Progressive Quasi Static algorithm (LSMPQS), is introduced to address this problem. This technique is capable of modeling the correct physics in the porous medium without employing any tunable parameters. Moreover, unlike network modeling that simplifies the geometries of pores and throats, no simplification is required in LSMPQS. The comparison with the experimental data suggests satisfactory agreement, and thus such technique can be used as the substitute when the experimental data are not available.

2.3.1 Drainage and imbibition criteria

Drainage criterion

We focus on capillary-controlled (quasi-static) drainage and imbibition processes. A quasi-static process assumes the activity occurs very slowly and it is always at equilibrium. The fluid menisci in porous media are known to be the surface, satisfying Young-Laplace equation:

$$P_c = \sigma C \tag{2.4}$$

where P_c is the capillary pressure between two fluids and σ is the fluid-fluid interfacial tension. σ is almost a constant within the range of pressure and temperature in our study (in the hydrate reservoir, the pressure ranges from 6 to 9 MPa, and temperature from 275 to 280 K). C equals twice the curvature of the interface, which is calculated as:

$$C = \frac{1}{R_1} + \frac{1}{R_2} \tag{2.5}$$

R_1 and R_2 are the principal radii of the curvature measured in any two orthogonal directions. P_c and C are proportional to each other, and therefore can be used interchangeably. In a capillarity-dominated process, equation (2.5) is justified to model the curvature of interface as it evolves through a series of drainage and imbibition stages. During the modeling, we apply a curvature (or capillary pressure) to the network. Whether we increase or decrease the applied curvature depends on whether we are simulating drainage or imbibition. At each simulation step, the simulator compares the applied curvature and the critical curvature of a throat (for drainage) or a pore (for imbibition) to determine whether drainage or imbibition can take place in that throat or pore.

During drainage, throats locally determine sequence of displacement events. All neighboring throats of an already drained pore are examined if the can “hold” the fluid-fluid interface at an applied curvature or not: if the applied curvature is greater than the

throat critical curvature, drainage takes place (i.e. neighboring pore is drained, and its throat examined), otherwise not. Thus throat critical curvatures need to be known in advance. For the drainage in sphere packing, two models have been proposed to estimate the critical curvature: Haines inscribed sphere approximation (Haines, 1930) along with Mason and Mellor modification (Mason and Mellor, 1995), and MS-P approach (Mayer and Stowe, 1965; Princen, 1969; 1970). Mason and Mellor model is an *a priori* estimation, of which the critical curvature for every throat in the network is calculated before drainage simulation is performed. On the other hand, MS-P model checks the interface stability on the throat during drainage simulation, and drainage only happens when interface becomes unstable. However, MS-P was developed for 2D scenario, and involves only simple geometries, compared to the fact that Mason and Mellor criterion is more adaptable to more complex geometries.

The practical difference between MS-P and Mason and Mellor criteria for sphere packing is minor. We choose Mason and Mellor criterion in the simulation because it is a much simpler calculation that MS-P, and therefore computational efficient. A typical calculation of the critical curvature in a 5000 sphere pack suggest that Mason and Mellor criterion takes less than half of the time required by MS-P criterion. Mason and Mellor criterion gives:

$$C^*_{drainage} = \frac{2R_{avg}}{R_{thr\_ins}} - 1.6 \tag{2.6}$$

where $C^*_{drainage}$ is the dimensionless drainage critical curvature for a throat. R_{thr_ins} is the radius of the inscribed sphere of the throat. R_{avg} is the average sphere radius of the sphere packing. The constant -1.6 was introduced by Mason and Mellor to match the experimental results (also note that Mason and Mellor used a mono-dispersed packing so

R_{avg} was not necessary). Equation (2.6) is in the dimensionless form; therefore, the simulation results are independent of the sphere size of the packing.

Imbibition criterion

Imbibition on the other hand, is controlled by pore events. Wetting phase displaces nonwetting phase during imbibition and the concept of critical curvature for pore imbibition is used (even though we will see it is not as straightforward as for throat drainage). Of the numerous imbibition criteria proposed to compute the critical curvature (Jerauld and Salter, 1990; Melrose, 1965; Mason and Mellor, 1995; Gladkikh and Bryant, 2003), we are interested in the ones proposed by (Mason and Mellor, 1995) and (Melrose, 1965). Mason and Mellor criterion for imbibition is also an *a priori* estimate, which has the following form.

$$C^*_{imbibition} = \frac{2R_{avg}}{R_{pore\_ins}} - 1.6 \qquad (2.7)$$

The above equation has exactly the same form as equation (2.6). $C^*_{imbibition}$ is the imbibition critical curvature for a pore. R_{pore_ins} in this equation is the radius of the inscribed sphere of the pore (as opposed to throat), which in general is larger than that in equation (2.6). Correction of -1.6 was introduced to maintain the imbibition hysteresis (and match the experimental results). This criterion was inspired by Haines, who observed in the experiments that right before imbibition happens the fluid-fluid interface has the shape of a sphere a sphere inscribed to the pore. However, the application of this criterion to model other than monodisperse sphere packings is not satisfactory. First, it neglects the experimental and theoretical evidence that having more throats containing menisci enables a pore to imbibe at a larger curvature. Second, the choice of throats containing interfaces and the presence of pendular rings at grain contacts might prompt

snap-off event in the imbibition and subsequent trapping of nonwetting phase inside the pore (Prodanovic and Bryant, 2008; Prodanovic et al., 2008), which cannot be captured by using this criterion. Finally, the curvatures computed by this model are also physically questionable: it gives negative critical curvatures when R_{avg} is much smaller than R_{pore_ins}, contrary to the fact that all the critical curvatures should be positive in a spontaneous process.

Melrose criterion (Melrose, 1965), on the other hand, reflects the fact that imbibition happens when two separate menisci come into contact. Although this is physically realistic, it is difficult to track interfaces in practice. Short of tracking interfaces in the detailed pore space (Prodanovic and Bryant, 2006), it can only be computed by idealizing the interface as locally spherical (Gladkikh and Bryant, 2003). We propose a simple and yet accurate imbibition model is proposed in this work.

Our novel imbibition criterion aims to give a satisfactory prediction of the imbibition critical curvature, as well as to employ more physical basis than Mason and Mellor criterion. Figure 2.4 shows a comparison between the imbibition critical curvature by Haines criterion (Haines, 1930) and LSMPQS. C_1 and C_2 are the largest and 2nd largest critical curvatures for imbibition that could happen in a pore, respectively. These values are obtained from direct LSMPQS simulation in individual pores (Prodanovic and Bryant, 2006), starting from different drainage endpoints within the pores (Figure 2.5). LSMPQS invariably shows imbibition will occur when two interfaces come into contact on a grain surface (confirming Melrose criterion). This is the reason different critical curvatures are possible: the value depends on the starting arrangement of menisci and pendular rings in the pore. When there are more menisci existing in the throats, there are more opportunities for interfaces to come into contact when decreasing the applied curvatures. C_1 and C_2 correspond to the cases where more menisci are present, and

therefore imbibition has a better chance to happen at C_1 and C_2 than the other smaller curvatures.

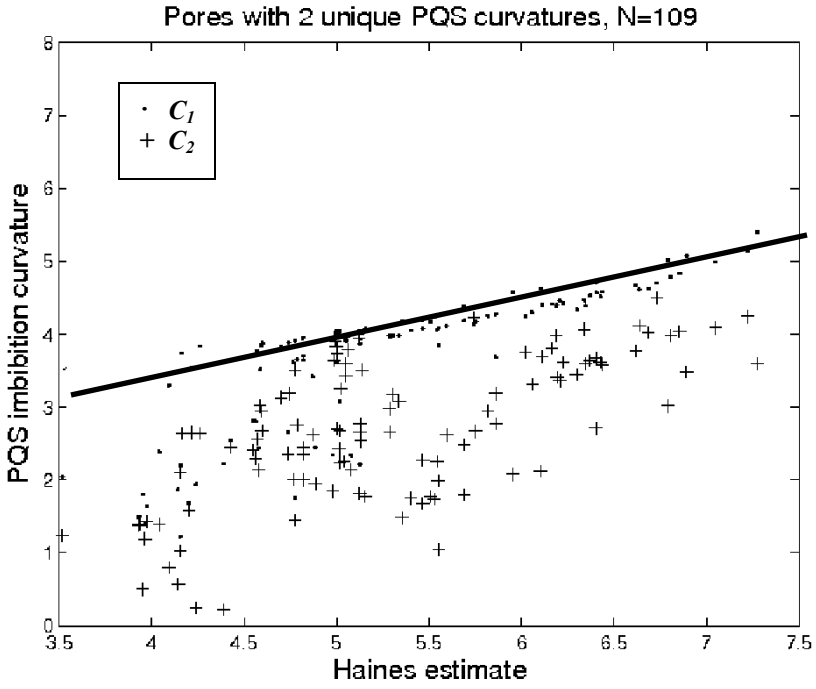

Figure 2.4: The largest two imbibition critical curvatures (C_1 and C_2) that could happen to individual pores by using LSMPQS (Prodanovic and Bryant, 2006), plotted against Haines criterion (Haines, 1930). Haines estimates the critical curvature by using $C^*_{Haines} = 2R_{avg}/R_{inscribed}$, similar to Mason/Mellor criterion (equation (2.7)) but without -1.6. The total number of pores tested is 109. For a single pore, C_1 is the largest critical curvature, and C_2 is the 2nd largest one. The black line shows a linear approximation of C_1 as a function of Haines estimate. From (Prodanovic and Bryant, 2006).

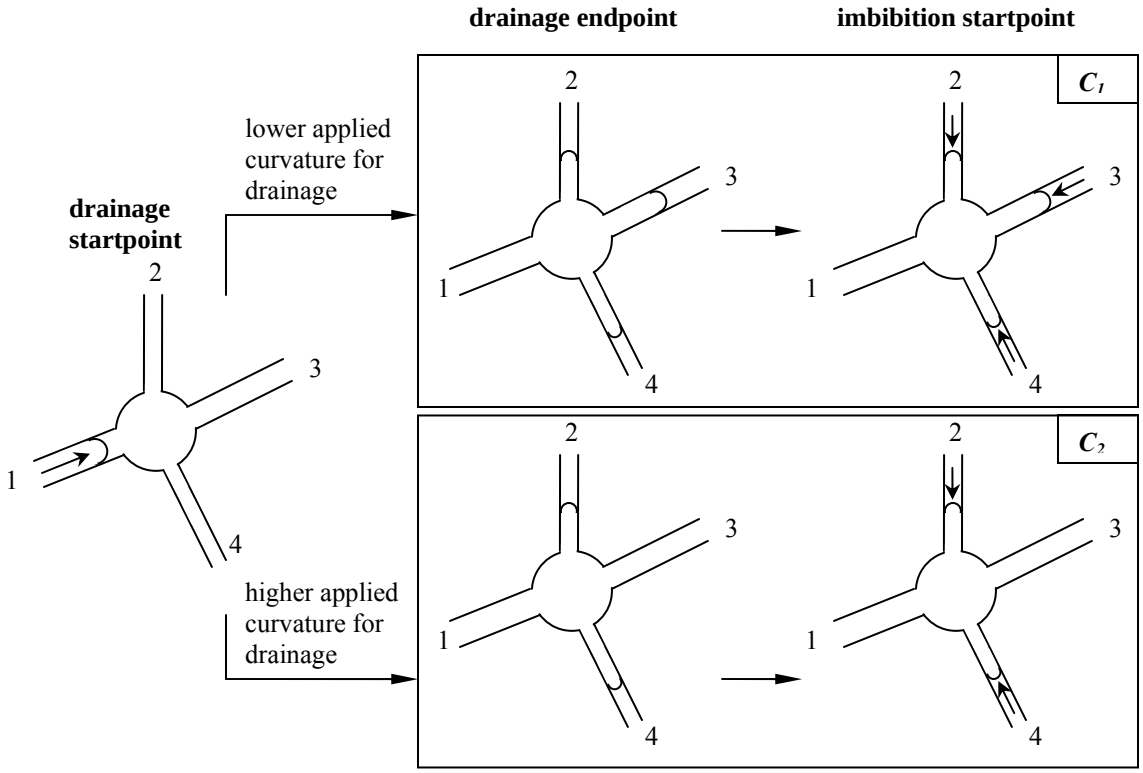

Figure 2.5: A comparison between the two scenarios that cause imbibition to happen at the largest (C_1) and 2nd largest (C_2) imbibition curvatures for a single pore. Both cases start from the same interface configuration, where throat 1 is drained. **Top panel:** At a lower drainage applied curvature, drainage is stopped when all the other throats (2, 3 and 4) are filled by two phases. When imbibition is started from this point, the pore can be imbibed without greatly reducing the applied curvature, since the menisci at each throat can easily merge together, thus triggering Melrose's physical condition for imbibition. **Bottom panel:** At a higher drainage applied curvature, throat 3 is totally drained. Menisci at throat 2 and 4 must merge for imbibition to occur only at applied curvature lower than the previous case. The top panel corresponds to the highest imbibition curvature C_1, and the bottom panel to the 2nd highest imbibition curvature C_2. Here only a 2D pore is shown; however, the same concept applies in 3D.

A perfect match of the critical curvatures predicted by Haines and those observed in LSMPQS would yield a linear relationship. However in Figure 2.4, large deviation is observed, and the values estimated by LSMPQS are smaller than Haines, that is,

imbibition happens at a lower curvature in the simulations by LSMPQS. C_1 values have a narrower range that C_2, and we can approximate them approximated by the black line. We use this line to construct a simple linear relationship for estimating C_1 from the pore geometry in this class of pores (that is, pores in a dense disordered packing of equal spheres):

$$C_1 = \frac{1.25R_{avg}}{R_{pore\_ins}} + 0.8 = 0.625C^*_{Haines} + 0.8 \qquad (2.8)$$

where R_{pore_ins} is the sphere radius that could be inscribed into the void space in the pore. Henceforth we use C_1 as the critical curvature. Thus we ignore the contribution of C_2 and other smaller curvatures, and assume all imbibition should occur at C_1.

The correlation in equation (2.8) gives an *a priori* estimation from a more accurate calculation by LSMPQS. We denote this as the C_1 criterion.

2.3.2 Simulation settings

Our network model simulation starts with drainage of porous medium filled with wetting phase. We increase the applied curvature at each drainage step, and check whether the throats can be drained. Then the curvature will be increased again. Drainage simulation stops when all the remaining pores that are filled by wetting phase are trapped (in accessible from inlet or outlet via main wetting phase). Imbibition starts from the drainage endpoint. Contrary to drainage, the applied curvature will be decreased at each imbibition step. We also check whether at each step the pores can be imbibed. The applied curvature will be further reduced if no more pores can be imbibed at this step. Imbibition continues until all the pores that are filled by nonwetting phase are trapped. Several technical details are elaborated below.

Model sediments

In the simulation, two types of model sediments are used (Figure 2.6). The first one comes from a subset of Finney pack (Finney, 1968), with only around 100 spheres both to reduce the simulation time and to be able to manually visualize/process the results. By doing this we can justify the correctness of network modeling and drainage and imbibition criteria. The second model sediment set involves 76 packings of spheres with various size distributions. Each packing contains 5,000 spheres. Those packings are generated by mimicking the sedimentological process and are periodic, meaning the shape of the opposite boundary should match with each other (a detailed explanation can be found later in this chapter). All of the packings have the shape of a cube to facilitate the application of boundary conditions. All the sphere packings used in the simulation are dimensionless, that is, the sizes of the spheres or the entire packing are normalized. Therefore the results can be easily applied to the sediments with different grain sizes.

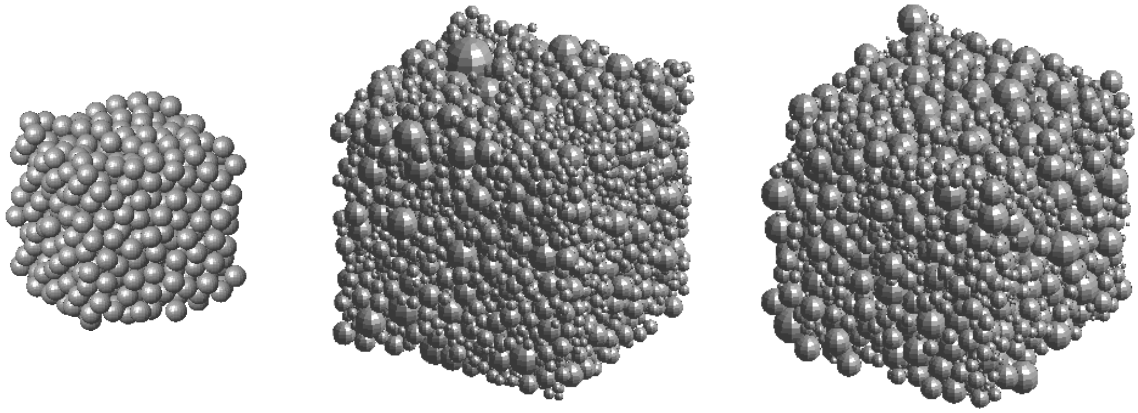

A. A subset of Finney packing

B. model sediment #14
Sorting index 1.31

C. model sediment #71
Sorting index 2.12

Figure 2.6: Three examples of model sediments. Since all the packings are dimensionless, the sphere size comparison among different packings does not necessarily reflect the real sizes. However, the sphere size variation within a packing show the relative sizes of the spheres. The sorting index is defined as $\sqrt{d_{75}/d_{25}}$, where d_{75} is the grain size that is larger than 75% of all grains, and d_{25} is the grain size larger than 25% of all grains. The summary of the properties of all 76 packings can be found in Appendix A.

Delaunay Tessellation

A good Delaunay cell based on the sphere packing has similar length of all its 6 edges. However, a Delaunay tessellation on a finite sphere packing inevitably generates cells with bad quality close to the boundary. Two examples are illustrated in Figure 2.7. Both cells are 'flat', with all the sphere centers almost lying on the same plane.

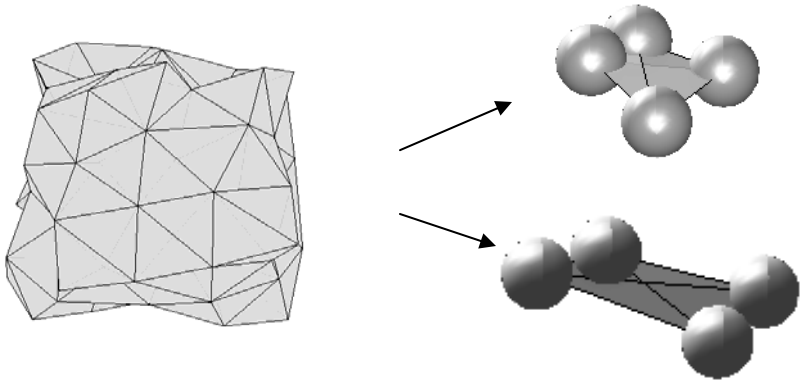

Figure 2.7: Two examples of Delaunay cells on the packing boundary. Both examples show the cells are 'flat', with all the sphere centers almost in the same plane. Simulations based on these cells would result in local errors when calculating the quantities.

The quality of the cells can be improved by diminishing the boundary effects. Two techniques are used. For the case of the subset of Finney packing (Figure 2.6A), a larger packing is first used to generate the Delaunay cells. Then we exclude the cells on the boundary (bad quality ones) and only keep the cells at the center (good quality ones). For the case of the 76 packings (Figure 2.6B, C), the packings are periodic, which enables us to maintain the quality of the Delaunay cells without removing the boundary cells.

Entry and exit pores

The entry pores are the source for one fluid displacing the other fluid in the pack, and the displaced fluid leaves the pack through the exit pores. At drainage, a sharp percolation threshold can only be achieved with a high sample size number ratio, defined as the total number of pores divided by the number of entry pores (Mason and Mellor, 1995). Selecting all the pores on a face as the entry pores in the drainage simulation gives

a much smaller ratio than a sample core in experiments, and thus results in a smooth transition instead of a percolation threshold typical for drainage. For a sphere packing of 5000 spheres, roughly 20 entry pores will give a sharp percolation. Therefore, a random selection of 20 pores on a face is taken as the entry pores for drainage simulation, and that face is referred to as 'entry face'. The selection of exit pores, on the other hand, has no significant effect to the final results. We take all the pores on the opposite of the entry face as the exit pores to match with the experimental condition.

Imbibition starts from the drainage endpoint, where wetting phase is allowed to displace nonwetting phases by growing from the trapped pores and pendular rings. This is based on the assumption that wetting phase is connected in the entire medium through the wetting film coating the grain surfaces. Therefore, a natural choice of the entry pore for imbibition is the trapped pores at drainage endpoint. Also to maintain the percolation threshold, 20 pores are randomly selected. For the exit pores, however, we consider all the pores on the pack surface as the exit pores for imbibition.

Wetting and nonwetting phase connectivity

At each step of drainage, the wetting phase can only be displaced when it belongs to a continuous cluster of wetting phase that contains at least one of the exit pores. It is the same with imbibition, but with nonwetting phase instead. Three types of connectivity are available for wetting phase: through pores, pendular rings and wetting film coating the sphere surfaces (Bryant and Johnson, 2003). Only the first two types are the effective ones in the range of time that most of the experiments allow and give the best match with the experimental results, while the last type is only important given an elongated time. In the simulation, we assume pore and pendular ring connections for wetting phase. This

ignores the possible contribution of wetting thin film connectivity through the sphere surface, which is often too thin to have a noticeable effect within the usual time scale of interest (Dullien et al., 1989).

The connectivity of nonwetting phase only occurs only through the pores. No connectivity through pendular ring and thin film is available for nonwetting phase as it stays at the center of the pore and cannot wet the grain surface.

Wetting and nonwetting phase trapping

Once a fluid is not connected to any of the continuous clusters mentioned above, this fluid is trapped. The pore connection terminates when the pore no longer connect through the continuous clusters. For pendular ring, the connectivity is broken due to the breaks of pendular ring under higher applied curvatures (Gladkikh and Bryant, 2005).

The trapped wetting phase exists in two forms: pores and pendular rings, both of which contribute to the irreducible wetting phase saturation (S_{wirr}). Isolated pores or pendular rings, or a combination of them are often observed. The nonwetting phase can be trapped only within bypassed pores. Similarly, both isolated pores and pore clusters are observed. The trapped nonwetting phase is known as the residual fluid at imbibition endpoint.

2.3.3 Simulation procedure

At every step of simulation, the simulator needs to check whether a fluid (A) inside a pore can be displaced by the other fluid (B), in both drainage and simulation. Fluid A can be displaced only if the follow 3 conditions are satisfied.

1. Fluid A has at least one neighboring pore filled by fluid B, which guarantees the displacing source.
2. The displacement criterion is satisfied. For drainage, the applied curvature should be greater than the critical curvature of the throat that connects fluid A and B. For imbibition, the applied curvature must be smaller than the critical curvature of the pore containing fluid A.
3. Fluid A must belong to the continuous cluster that connects fluid A to the exit pores. For drainage, fluid A is the wetting phase and the continuous cluster can be a combination of wetting-filled pore and pendular rings. For imbibition, fluid A is the nonwetting phase and the cluster is a combination of nonwetting-filled pores.

The sequence to do the above checking is not important. In practice, the first two conditions are checked, and the last condition is checked when the first two are satisfied.

At each step of drainage or imbibition, the above three checks are done for the entire packing. The applied curvature will increase (in drainage) or decrease (in imbibition) to the next value and the simulator will perform the above procedure again. The simulation terminates when all continuous clusters disappear.

2.4 COMPARISON WITH EXPERIMENTAL DATA

The drainage and imbibition capillary curves are compared between our network simulation results and the experimental data by (Haines, 1930) (Figure 2.8). The simulation is performed in a sphere packing of 7000 randomly positioned equal spheres, which is comparable to the packing of similar glass beads used in the experiment. Both the simulation and experiment start from drainage. We used 20 pores on one of the boundaries as the entry pores. Such choice gives us similar drainage percolation threshold with the experiment. Discrepancy is observed towards drainage endpoint, where the drainage critical curvatures from experiment are greater than the values Mason and Mellor proposed (equation (2.6)). Both simulation and experiment finish at the similar drainage endpoint. This suggests network modeling captures the correct trapping saturation for drainage.

Imbibibition starts from the drainage endpoint. We randomly choose 20 trapped pores as the entry pores for imbibition. A satisfactory agreement is obtained for percolation threshold. At the end of imbibition, network simulation achieves much higher (by about ten saturation percentage points) residual saturation than experiment.

Multiple causes might contribute to this deviation. First, in the simulation the contact angle between water and sphere surface is set to be zero. This is not likely the case in the experiment as the contact angle is affected by smoothness of the sphere surface, the materials of spheres, temperature, etc., and therefore subject to large variations. When contact angle gets larger, (Gladkikh, 2005) suggested that the network simulation gives a smaller residual saturation in imbibition, which would reduce the difference in Figure 2.8. Second, the simulation condition is not identical to that in the experiment. In simulation, imbibition starts from the randomly-selected trapped wetting

phase at drainage endpoint, which is in the form of isolated pores and pendular rings spotted in the porous medium. As previously discussed, this treatment allows us to have a sharp percolation. If the pores on the entire face are selected as the entry pores (which is the choice in experiment), we expect the percolation would happen at much higher applied curvature than (Figure 2.8). The different residual saturations might also be due to the different choices of entry pores/faces between network modeling and experiment. Finally, our new imbibition C_1 criterion only accounts for the most probable imbibition event that could happen in a pore. Other imbibition curvatures at which imbibition event can take place is not considered in C_1 criterion. For example, if imbibition happens at C_2 (Figure 2.4), a percolation could take place, corresponding to different trapped pores. The ignorance of the other less likely events can also lead to the difference.

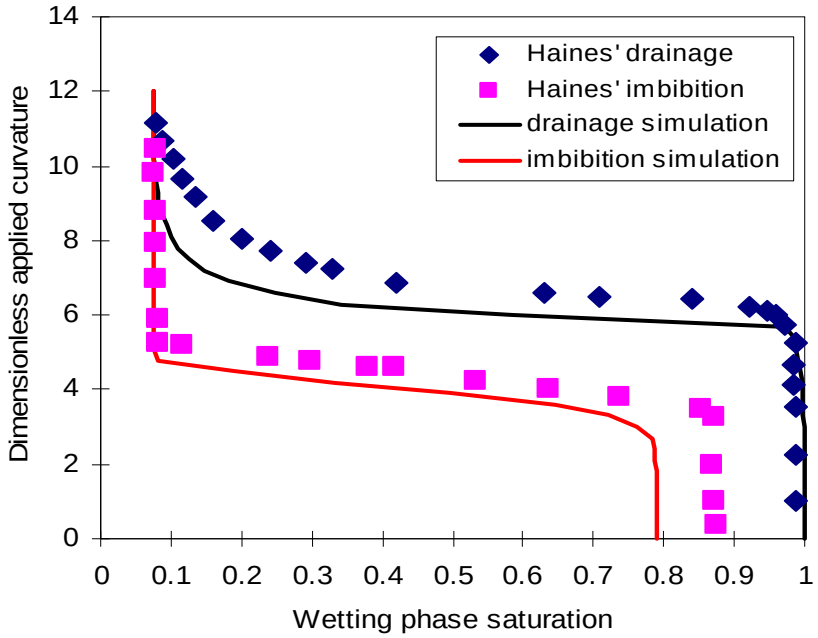

Figure 2.8: Comparison between the network simulation and experimental measurements.

The comparison gives a reasonable comparison between the model prediction and experimental measurements. However, Figure 2.8 only shows the global average of fluid saturation versus applied curvature. It does not reflect the events happening in the individual pores, and therefore it is an insufficient approach to check the correctness of the network modeling. For example, a saturation of 50% in both simulation and experiment at the same applied curvature does not necessarily indicate our network model predict the correct capillary event, because the filling status of individual pores (meaning whether the pore is filled by wetting or nonwetting phase) can be totally mismatched in simulation and experiment, but statistically still give the same saturation value. Consequently, a comparison of the individual events between simulation and experiment is crucial to validate the network modeling.

2.5 COMPARISON OF NETWORK MODELING AND LSMPQS RESULTS

The comparison is performed in two scales. Macroscopically, the curves of applied curvature versus wetting phase saturation are compared between the two simulations. This is the statistical results and only reflects the cumulative filling status of individual pores. We also check the filling status in the pore scale. Such comparison enables us to test whether the pore-level events in both models are happening in a similar fashion. Obtaining such information from the experiment is not plausible with current technologies. Instead, the results from LSMPQS are used as the substitutes.

The size of the model sediments used for the comparison is considerably smaller than in the previous section. This is because (1) simulation based on LSMPQS is computationally expensive. For a packing of 100 spheres, a LSMPQS simulation of a full drainage and imbibition cycle takes a week, while network modeling only takes seconds. (2) 3D visualization of fluid distribution is unclear for a large sample. Because of these, a subset of Finney pack (Finney, 1968) is used, which contains about 100 spheres (Figure 2.9).

2.5.1 Different treatments for model sediment

Although the model sediment (sphere packing) should be identical for network modeling and LSMPQS, some implementation differences are inevitable. First, partial spheres commonly exist on the surface of the sphere packing for LSMPQS (Figure 2.9A) as cut by a flat boundary, where a non-curved fluid/fluid interface is initialized. Network modeling cannot work with partial spheres, and only complete spheres are allowed (Figure 2.9B), resulting in an uneven boundary. The boundary difference influences the calculation of the pore volume: since partial spheres only yield partial pores. The pore

volume on the boundary of LSMPQS is smaller than those of complete spheres in network modeling (demonstrated by Pore A and A' in Figure 2.10). Ultimately, the difference should be negligible as the portion of those pores is small compared to the whole pack.

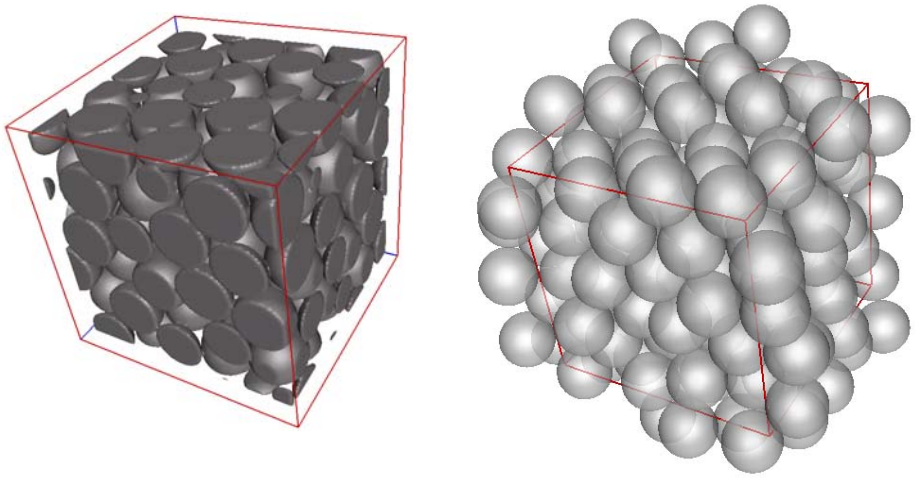

A. LSMPQS B. Network model

Figure 2.9: The cubic sphere packs used for network model (right) and LSMPQS (left). Both sphere packs are the same subset of a larger Finney Pack. The left pack is cut along the red frame from the right pack. Therefore, lots of partial spheres exist at the boundary of the left pack.

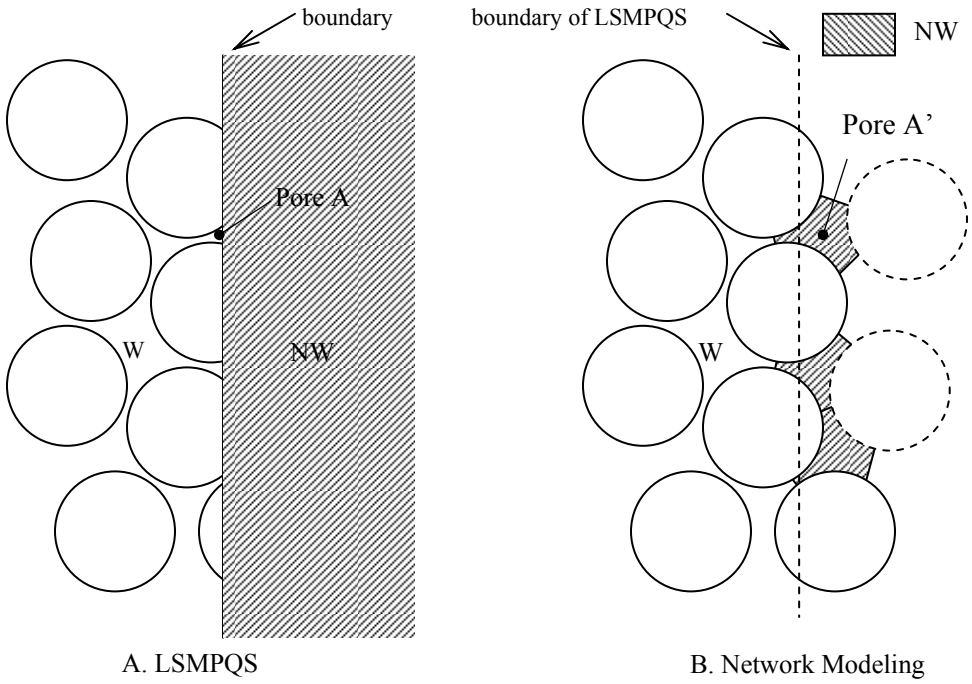

Figure 2.10: A 2D schematic of the treatment of boundaries on the sphere packing used for LSMPQS and network simulations. For better visualization and demonstration, 2D sphere pack is applied instead in this figure, although in simulation only 3D sphere pack is used. At the drainage initialization, the fluid/fluid interface overlaps the sphere pack boundary for LSMPQS (A), and nonwetting phase can move into the porous media from the right side of the boundary. For network modeling, nonwetting phase can only be initialized to fill the pores right to the boundary of LSMPQS (B). More spheres, as denoted by the dashed circles, are needed to generate the tetrahedron (in 2D case, it reduces to triangle). Nonwetting phase starts from these pores and goes to their neighboring pores, and in this fashion drainage takes places.

Second, to enable the same initialization of network modeling as LSMPQS and to enable better quality of Delaunay tessellation, we place an extra layer of spheres on the boundary of the Finney subset. The addition of extra spheres makes a bigger pack. Figure 2.10 provides a 2D schematic of the initialization at the drainage startpoint. For LSMPQS, the nonwetting (shaded) and wetting (white) phases are isolated by the flat

boundary, and thus the interface overlaps the boundary. However for network modeling, at least one pore should be filled with nonwetting phase in order to provide the drainage source or entry pore. To obtain an initial interface position similar to that of LSMPQS, extra spheres (dashed circles in this 2D demonstration) are added to the original sphere pack, so as to form extra tetrahedra (triangles in this 2D demonstration) beyond the boundary. In contrast with the flat interface in LSMPQS, a zigzag interface shape is obtained.

For those two reasons, the sphere pack used for network modeling is larger than LSMPQS, but the pores within the Finney subset are identical. In the pore-by-pore comparison, only the pores present in both packing are taken into account.

2.5.2 Filling status identification

The filling status of each pore reflects whether this pore is filled by wetting or nonwetting phase. This is the basic value to be checked in the pore-by-pore comparison. While the filling status can be easily obtained from network modeling as the pore is well defined (Figure 2.2), the determination of this value induces some difficulty in LSMPQS. Due to the continuous evolution of the interface in LSMPQS, a 'pore' could be partially filled with both wetting and nonwetting phases (Figure 2.11). Consequently, a mapping technique is developed to find the corresponding pores between the network modeling and LSMPQS. We let the center of a network model pore (location decided by the arithmetic average of coordinates of the spheres constructing the tetrahedron for LSMPQS) represent the whole pore. The center is shown as the black dot in Figure 2.11. The spatial coordinates of the center are communicated to LSMPQS, within which a simple calculation determines whether the center is inside the wetting or nonwetting

phase. The filling status of the corresponding 'pore' in LSMPQS is taken to be the same as the status of this point. This approximation only applies for the filling status determination; when calculating the phase saturation, we use actual volumes computed with LSMPQS.

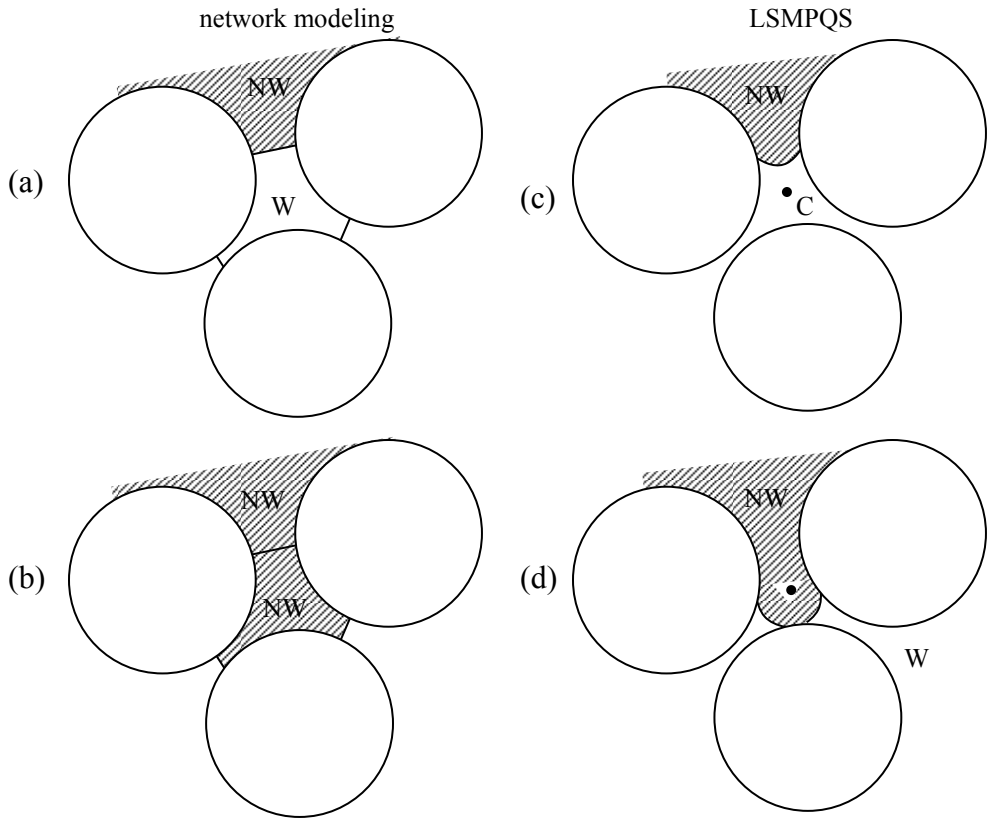

Figure 2.11: A 2D demonstration of the filling status of a pore for network modeling ((a) and (b)) and LSMPQS ((c) and (d)). Only drainage event are shown here. For network modeling, nonwetting phase totally displaces wetting phases from the pore (from (a) to (b)) if the drainage criterion is met. The filling status is thus easily determined. For LSMPQS, the fluid displacement is a gradual process. When drainage occurs in the pore, it does not necessarily drain the entire pore (from (c) to (d)). In some cases, the pore will contain two fluids at the same time (d), which impedes our determination of filling status. We suggest that the center of the pore C is representative of the whole pore. The filling status in LSMPQS therefore is decided by which fluid C is soaked in.

2.5.3 Drainage and imbibition curves

We begin with the traditional comparison of macroscopic properties, in this case drainage and imbibition curves. The computed curvature-saturation curves match well for network modeling and LSMPQS (Figure 2.12). We use the same drainage/imbibition steps (increments/decrements in curvature) for both simulations. The drainage data are available for applied curvature greater than 5.8, below which nonwetting phase does not enter the Finney subset and the wetting phase saturation (S_w) remains close to 1. During drainage, S_w for network modeling is constantly smaller at a given curvature than LSMPQS, except for the last few steps. Thus at a given curvature more pores have been drained by network modeling, and network modeling percolates at a smaller curvature than LSMPQS. The observation shows that Mason and Mellor drainage criterion slightly underestimates the critical curvature. At the last few steps, the difference between these two approaches is minimized, and the endpoints are essentially the same.

No appreciable difference in the imbibition curves for the approaches can be observed at the initial steps (Figure 2.12). Not much imbibition takes place until the applied curvature reduces to 4.8. The increase of S_w before the imbibition percolation, as C^* decreases from 11 to 5, is due to the expansion of pendular rings, where wetting phase is supplied through the thin film coating the grain surface. In order to match with the settings of LSMPQS, we allow all pendular rings to expand. By doing this we assume the thin film coating the grain surface provides the pathway to transport wetting phase through the entire packing. During percolation, network modeling shows a larger increase in S_w than LSMPQS for the same decrement in curvature, as indicated by the gray square on Figure 2.12. This is attributed to the overestimation of the critical imbibition curvature

by the C_1 criterion. The actual curvature at which imbibition takes place is a dynamic value that depends on which throats contain menisci and which grain contacts hold pendular rings. Applying the C_1 criterion presumes that the configuration needed for the C_1 event actually exists in each pore. If that configuration does not arise, however, the pore necessarily imbibes at a smaller curvature, e.g. when events labeled C_2 in Figure 2.4 occur. The fact that the imbibition curve predicted using the C_1 criterion provides a very good estimate of the percolation threshold indicates that C_1 events correspond to the imbibition event actually occurring in most pores.

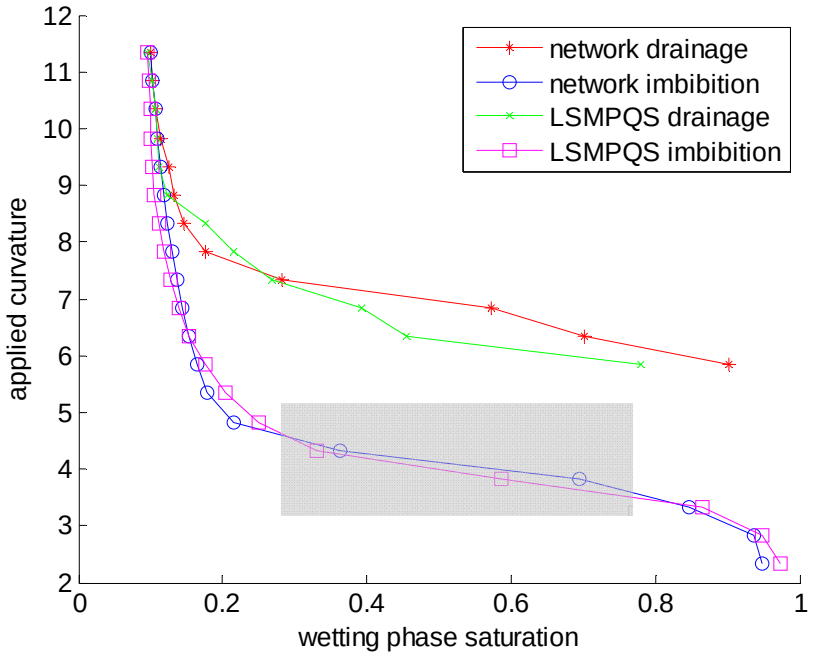

Figure 2.12: Drainage/imbibition comparison between network modeling and LSMPQS. The simulation starts with drainage of a packing filled with wetting phase, and imbibition follows from the drainage endpoint. The calculation of wetting phase saturation includes the volumes of pores and pendular rings in network modeling, and is by counting the voxels filled with wetting phase in LSMPQS.

2.5.4 Pore-by-pore comparison for drainage

We now turn to a more detailed analysis, namely comparing the filling status of individual pores in network modeling and LSMPQS. This is a much stronger test compared to the capillary-pressure comparison between network modeling and LSMPQS. Figure 2.13 plots the fraction of pores that have the same status in both simulations at each value of curvature. The first step (curvature = 5.8) maintains a very high number fraction. The poorest pore-by-pore agreement is during the percolation (curvature = 6.3), where a great amount of pores in both simulations are drained. As can be seen from Figure 2.12, network modeling predicts smaller S_{nw} (1-S_w) than LSMPQS at this step, and the ratio of the two S_{nw} values at C = 6.3 explains the 13% agreement in filling status.

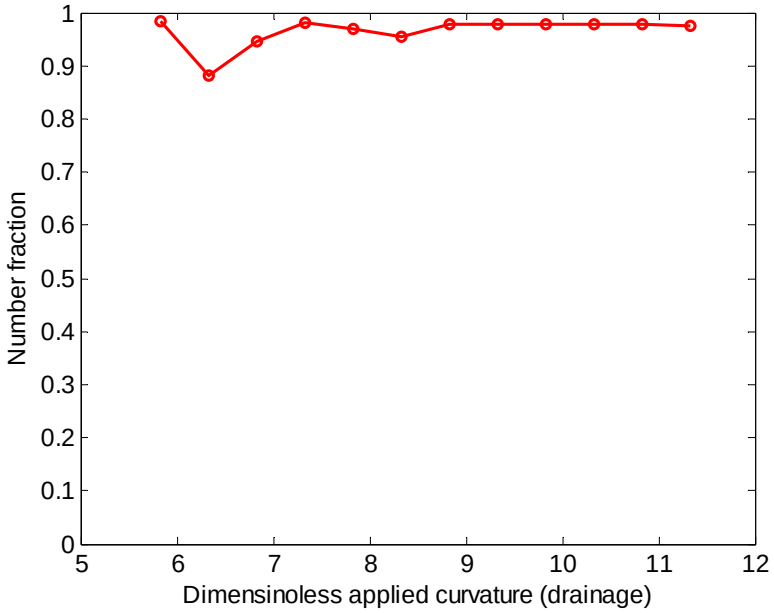

Figure 2.13. The number fraction of pores that have the same filling status during network and LSMPQS simulations of drainage compared to the total number of pores at different applied curvatures of drainage simulation. When the number fraction is 1, the filling status of all the pores is exactly the same for both simulations.

A visual comparison of filling status is provided in Figure 2.14. For clarity only the filling status of nonwetting phase is shown. Each image is constructed at a given curvature. The blue spheres show the pores that are drained (contain nonwetting phase) in both the simulations. Red spheres correspond to pores drained in network model but not in LSMPQS. The yellow spheres show pores drained in LSMPQS but not in network model. At curvature = 5.8, the region of blue spheres in Figure 2.14A shows that drainage still concentrates at the entry boundary (the right boundary), and no pores have been drained in the center or close to the exit boundary (left boundary).

Figure 2.14B suggest two simulations still maintain similar behaviors in draining the pores. The pore scale visualization shows that the blue spheres percolate to the middle of the packing, which corresponds to the large variation of saturation value in Figure 2.12. We also observe both yellow and red spheres in the domain, with more yellow spheres than red spheres. This indicates LSMPQS drains more pores than network modeling at the applied curvature, and the summation of all the yellow and red spheres corresponds to about 13% of the total number of pores (Figure 2.13 at curvature = 6.3). Finally, at the drainage endpoint (curvature = 11.3, Figure 2.14C), after all pore-filling events have ended and S_w decreases only because pendular rings are shrinking, almost all the spheres are blue. We conclude that the Mason/Mellor criterion slightly underestimates the critical curvature for drainage, and that the network modeling matches the sequence of pore-filling drainage events obtained in the LSMPQS simulation.

(A) Drainage step 1, applied curvature 5.8

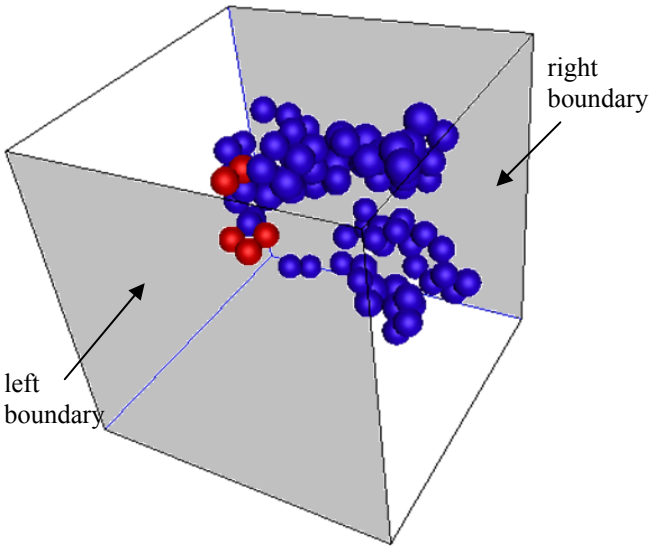

(B) Drainage step 2, applied curvature 6.3

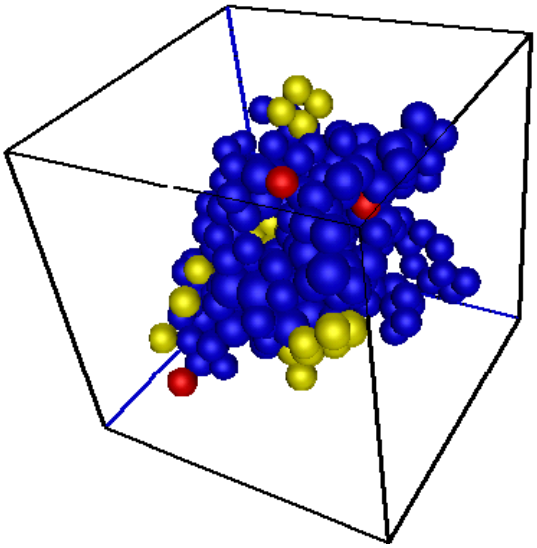

continued on next page

(C) Drainage step 12, applied curvature 11.3

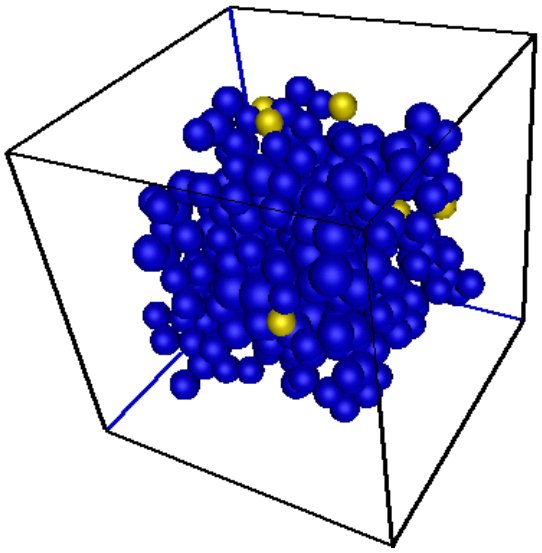

Figure 2.14: Comparison of filling status during drainage for network modeling and LSMPQS. The filling status of a pore shows whether a pore is filled with wetting or nonwetting phase (refer to Figure 2.11 for detail). The spheres represent individual pores, the locations of which are the centers of the pores. All the spheres shown in the figure are filled by nonwetting phase. The blue spheres are filled by nonwetting phase in both simulations. The red spheres are filled in network model but not LSMPQS, while the yellow spheres are filled in LSMPQS but not network model. All pores on the right boundary are selected as the entry pores, and the pores on the left boundary are the exit pores. All the other boundaries are sealed to prevent fluids from leaving the model rock. Drainage starts from the right boundary of the sphere pack, so that the pores on the right side are firstly drained. Both simulations have roughly the same invasion at the first step (A), with more pores invaded in network modeling. The invasion of LSMPQS later overtakes network modeling, giving more pores drained by LSMPQS (B). At the endpoint, both simulations converge to similar filling status, with LSMPQS drains slightly more pores (C).

Confirming the visual assessment, the agreement in Figure 2.13 improves to above 98% at larger applied curvatures, meaning less than 10 pores have different filling status out of a total of around 300 pores.

2.5.5 Pore-by-pore comparison for imbibition

Imbibition does not percolate until curvature decreases below 4.8 (Figure 2.12). At this curvature, 90% of the pores have the same filling status in network modeling and LSMPQS. The fraction of pores with the same filling status is less than 70% at curvature = 3.8. Fewer pores have been imbibed in LSMPQS than network modeling at this curvature, giving lower S_w (Figure 2.12). Figure 2.16 gives the similar information as Figure 2.14, where the filling status of individual pores are shown and compared between two simulations. The blue spheres indicate the pores that are not imbibed in both simulations. The red spheres are the pores only imbibed in LSMPQS but not in network modeling, while the yellow spheres have the opposite meaning. Figure 2.16A shows the step at curvature = 4.8, where still a relatively high number fraction (90%) is achieved. The 10% mismatch in the filling status corresponds to the yellow and red spheres spreading in the domain. During the percolation (step 16), a large number of yellow spheres emerge in the porous medium, the number of which are comparable to that of the blue spheres. This is consistent with the preceding discussion of the C_1 criterion overestimating the critical curvature for imbibition. Therefore at an applied curvature, more pores in network simulation will be imbibed than LSMPQS, corresponding to yellow spheres. Close to the imbibition endpoint, the match returns to 85%, as in Figure 2.15. This suggests that many of the pores not yet imbibed in LSMPQS at C = 3.8 later imbibe at smaller curvatures. Nevertheless the number of yellow and red dots in Figure 2.16C (imbibition endpoint) is large, indicating a different sequence of pore-filling events occurred in the simulations.

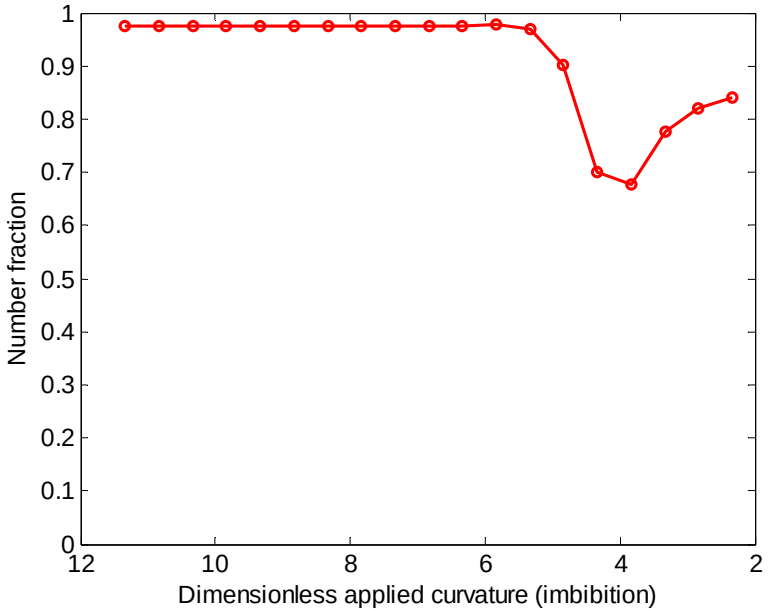

Figure 2.15: The number fraction of pores that have the same filling status during network and LSMPQS simulations of imbibition. The sets of imbibed pores are very similar until applied curvature = 4.5, where imbibition starts to occur. Also, about a third of the pores are different due to different imbibition speeds predicted by two models. But the filling status becomes similar towards imbibition endpoint.

(A) Imbibition step 14, applied curvature 4.8

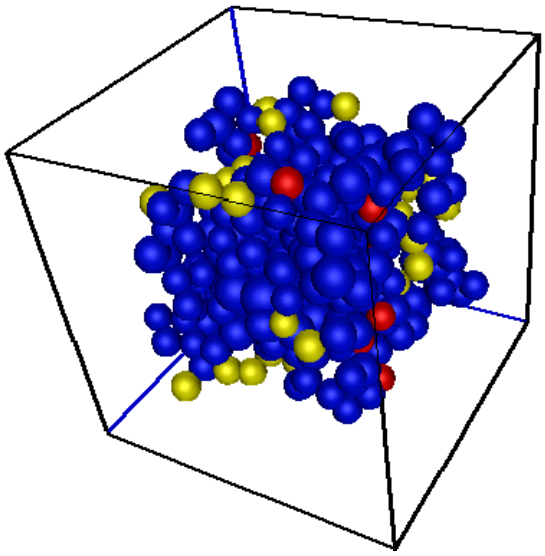

(B) Imbibition step 16, applied curvature 3.8

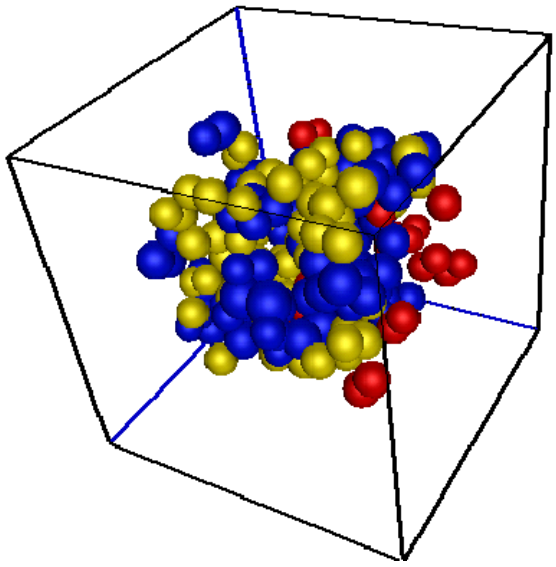

Continued on next page

(C) Imbibition step 19, applied curvature 2.3

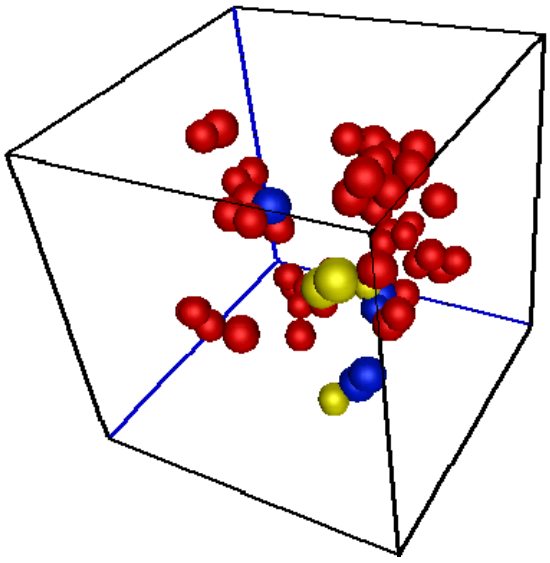

Figure 2.16: The filling status comparison of imbibition for network modeling and LSMPQS. The definition of spheres and colors are identical as in Figure 2.14. The right and left boundaries are set as the exit faces from which fluid can leave the model rock, and the other boundaries are sealed. Rather than supplying displacing fluid from the right boundary as in drainage, the displacing fluid (wetting phase) for imbibition is supplied from the trapped wetting phase in the pores. Before step 14, no pores are imbibed, and the filling status is the same as the drainage endpoint. Imbibition occurs faster in network modeling. In (B), the massive yellow spheres and few red spheres indicate imbibition of network modeling happens all over the model rock, compared to only several pores imbibed in LSMPQS. However at the imbibition endpoints (C), more pores have been imbibed for LSMPQS, leaving some pores still filled with nonwetting phase in network modeling (red spheres).

The imbibition endpoint does not show as good pore-by-pore agreement as the drainage endpoint: more pores are mismatched (yellow and red) than matched (blue). This microscale discrepancy arises because the C_1 criterion does not account for certain classes of pore-filling events that occur in nature and in the LSMPQS. LSMPQS tracks detailed interfaces and confirms the Melrose criterion: imbibition in granular media

happens either when a pendular ring and a meniscus in a pore throat come into contact, or when two pendular rings come into contact and coalesce. The C_1 criterion attempts to represent the former event (meniscus/pendular ring merger), but it does not account for the latter (coalescence). Since coalescence creates new menisci, it can thus yield a different sequence of imbibition events. Moreover, we use C_1 to be representative of the critical curvature of the whole pore, but leave out the other smaller and yet possible critical curvatures. Consequently, the network model using C_1 criterion provides good but not perfect pore-by-pore agreement with LSMPQS for imbibition.

2.6 DRAINAGE AND IMBIBITION SIMULATION BASED ON CONVENTIONAL BOUNDARY CONDITION

The pore-by-pore comparison applies a stricter rule than the conventional macroscopic comparison to test the correctness of network modeling for drainage and imbibibition, as well as the associated criteria. The preceding tests and comparisons suggest that network modeling is a reliable tool to predict the fluid movement in the porous medium. Consequently, we further apply the same models in much larger model sediments (76 samples of different grain size distributions) and their drainage and imbibition behaviors.

76 packings are generated to cover large different grain size distributions. Appendix A shows the properties of these packings, similar to Table 2-1. In the network simulation, problems are encountered when calculating the properties associated with these packings. First, a Delaunay cell (from Delaunay tessellation, Figure 2.2) containing spheres with large size variations would yield misleading inscribed spheres for both pore and throat, that is, the inscribed sphere cannot correctly represent the position and size of the pores and throats (Figure 2.17). Second, the sphere size variation might also cause the miscalculation of porosity. The approach for porosity calculation in the network modeling is done on each tetrahedron: the volume of the void space is computed by the volume of tetrahedron minus the volume of partial spheres cut off by the tetrahedron (Figure 2.2C), and then porosity is computed as the summation of the individual void spaces divided by the total volume of the packing. The validity of this approach relies on the prerequisite that no other spheres exist inside the pore except for the ones constructing the tetrahedron. In a packing with large grain size distribution, however, this is often not the case (Figure 2.18), and thus leads to large error in calculating the

porosity. Finally, the calculation of the shapes of fluid-fluid interface (pendular rings and menisci) is affected by the sphere size variation.

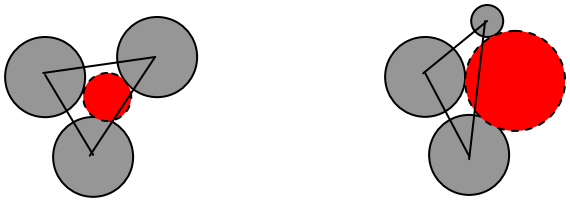

A. The inscribed sphere of a typical pore in a packing of narrow grain size distribution

B. The inscribed sphere of a typical pore in a packing of wide grain size distribution

Figure 2.17: A 2D schematic of the inscribed spheres of a pore. In 2D, a Delaunay cell is constructed by 3 spheres. With a narrow grain size distribution (A), the inscribed sphere (red) correctly represents the pore, and thus its radius is used to compute the drainage criterion. A wide grain size distribution is more likely to lead to an irregular pore (B). In this example, the inscribed sphere is already outside the pore, and the sphere size is also much larger than the pore size.

A. Two cells in a packing of narrow grain size distribution

B. Two cells in a packing of wide grain size distribution

Figure 2.18: Two adjacent Delaunay cells in the packing of narrow and wide grain size distributions, respectively. For the case of narrow grain size distribution (A), each cell only contains spheres that construct itself. For the case of wide grain size distribution (B), part of the cell is also filled by the large sphere, which does not contribute to construct cell 1.

Most of these problems are fixable by removing the small spheres from the original model sediments (referred to as the 'truncated' packing in the appendix). Since only a few spheres are removed, this treatment does not largely affect the grain size distribution, but improves the quality of the simulation results significantly. However from packing 19 to 34, this treatment does not fix the problem even though a large amount of spheres are removed. We neither include these packings in the following analysis, nor in the complete list of the drainage and simulation results in Appendix B and C. We compare the drainage and imbibibition curves for model sediments with different grain size distributions. Mason and Mellor criterion is used to compute the drainage critical curvatures for each packing, while C_1 imbibition criterion is used to compute the imbibition critical curvatures. Several representative packings are selected, with their basic properties listed in Table 2-1(note that none of them are from packing 19 to 34). These packings are grouped by grain size distribution patterns (normal distribution and log-normal distribution), and compared separately with respect to the groups. The definition of sorting index can be found in Figure 2.6.

Figure 2.20 shows the drainage curve comparison for both groups. We observe significant variations in drainage percolation behavior. With larger grain size distribution, a more gradual percolation is observed. This the due to the throat sizes in the packing. A larger grain size distribution also leads to a larger throat size distribution, which allows the drainage to occur over a greater range of the applied curvature. To the contrary, when the throat size has a relatively uniform distribution, all the drainage would take place over a small range of curvature, and yield a sharp percolation.

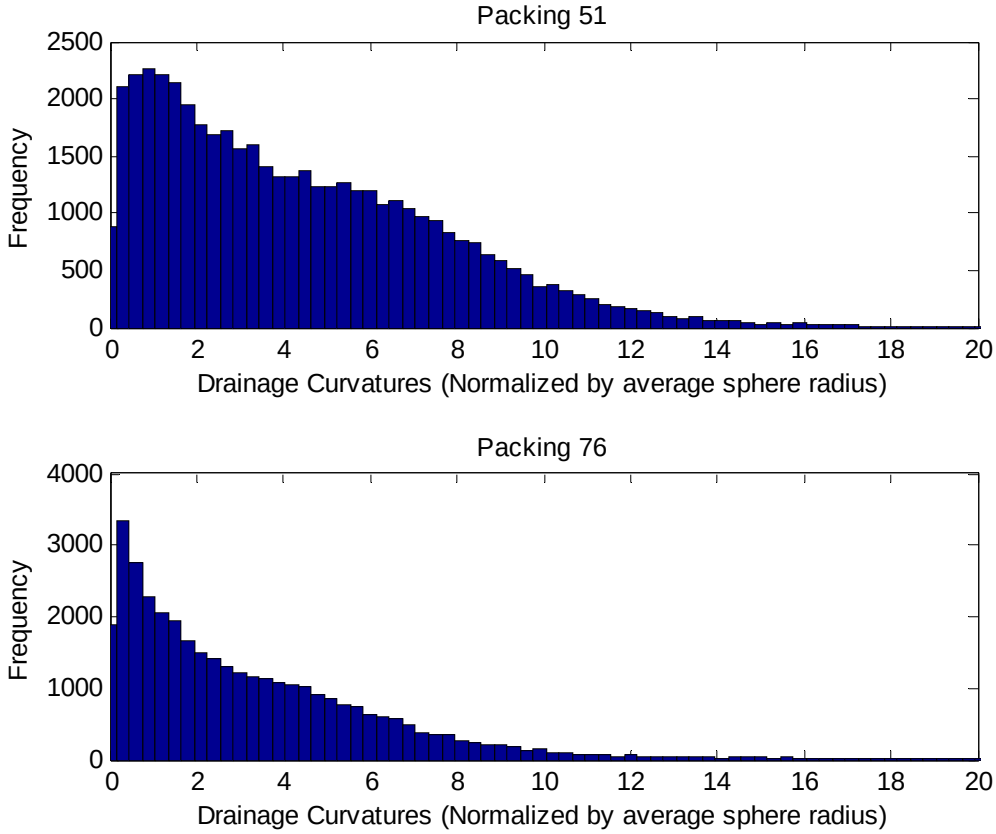

Figure 2.19: The histograms of the critical curvatures in packing 51 and 76. Mason and Mellor criterion (equation (2.6)) is used to calculate the critical curvatures. Packing 76 has a wider grain size distribution than Packing 1 Packing 76 gives a wider range of the curvature values from close to 0 to 20, while same value ranges only from 0.5 to less than 14 for packing 1.

The percolation threshold is also affected by the grain size distribution. For the packings with narrow grain size distribution (Packing 1, 7, 12, 39, 43), percolation threshold is close to 7. Increasing the width of grain size distribution lowers the percolation threshold. For example, the value drops to 4 for packing 14, and almost 0 for packing 38, in the log-normal panel; and 4 for packing 51 and 0.5 for packing 76, in the normal panel. This is a straightforward consequence of the grain size distribution: with wider distribution, the

throat size distribution becomes larger as well. Figure 2.19 shows the comparison between packing 51 and 76. Since packing 76 has a wider grain size distribution, we see more larger grains and throats, and therefore greater portion of smaller critical curvature compared to packing 51. A comparison between packing 51 and 76 (Figure 2.19) suggests that there is a distinct shift of the critical drainage curvature to the lower values, which causes a lower percolation threshold as shown in Figure 2.20

Figure 2.20.

The residual nonwetting phase saturation, however, does not behave differently with different grain size distributions. About 7% to 8% residual saturation is obtained for all the simulations. This suggests that only the grain size variation does not have a strong effect on this value. Although smaller grains generate narrow corners, and therefore might be able to trap more wetting phase, there are comparable amount of larger grains inside the packing. They create only the larger pores and the wetting phase trapping within these pores are less likely to happen. The overall trapping effect is the compromise between the larger and smaller grains (and of course pores), and is of not much difference from the packing with narrow grain size distribution.

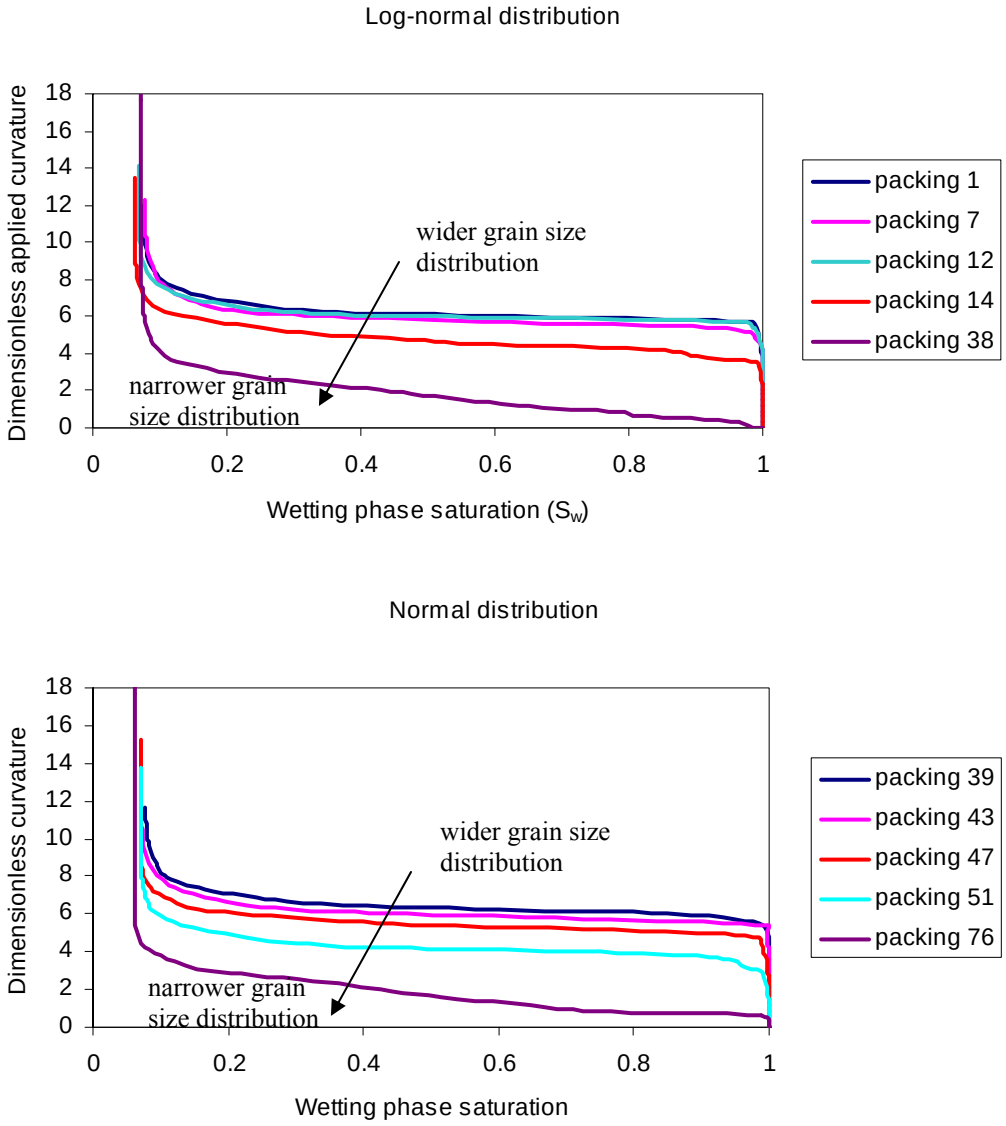

Figure 2.20: Drainage curves for model sediments with different grain size distributions. The model sediments are grouped as log-normal and normal grain size distributions. The percolation threshold declines as increasing the grain size distribution.

Table 2-1: The properties of selected packings (model sediments)

Packing No.	Minimum Radius	Maximum radius	Arithmetic mean radius	Standard deviation of grain size	Porosity	Sorting index* (number fraction based)	Notes
1	0.32	2.58	2.18	0.11	0.37	1.04	LN (log normal distribution)
7	1.50	3.08	2.16	0.22	0.36	1.07	LN
12	1.07	4.49	2.11	0.42	0.35	1.14	LN
14	4.24E-03	7.05	1.90	0.80	0.32	1.31	LN
38	3.98E-03	9.41	1.60	1.05	0.27	1.51	LN
39	1.97	2.40	2.19	0.07	0.34	1.02	N (normal distribution)
43	1.07	3.20	2.14	0.35	0.36	1.12	N
47	5.64E-05	4.01	2.01	0.68	0.34	1.27	N
51	1.27E-03	4.59	1.85	0.90	0.32	1.42	N
76	7.35E-04	5.52	1.53	1.20	0.32	2.23	N

* The sorting index is defined as $\sqrt{d_{75}/d_{25}}$, where d_{75} is the grain size that is larger than 75% of all grains, and d_{25} is the grain size larger than 25% of all grains.

Imbibition curves are also simulated for the different groups. One important different treatment from Section 2.5 is that the pendular expansion is only allowed when pendular ring is connecting to the bulk wetting phase. In Section 2.5, pendular ring expansion is in the entire domain to match simulation setting with LSMPQS. The percolation threshold for packings with wider grain size distribution has a lower value than those with narrower distribution, due to the different critical curvature distributions. This is observed in both log-normal and normal groups (Figure 2.22). Figure 2.21 shows the critical curvature distribution of Packing 51 (narrower grain size distribution) and 76 (wider grain size distribution), which are computed by using C_1 imbibition criterion (equation (2.8)). An obvious shift of the mode to the smaller value is observed for Packing 76, which reduces the percolation threshold. The imbibition curves are all parallel for different packings. This is evident from Figure 2.21, where the ranges of

critical curvatures for both packing are almost the same (0.8~7 for packing 51, and 0.8 to 6 for packing 76).

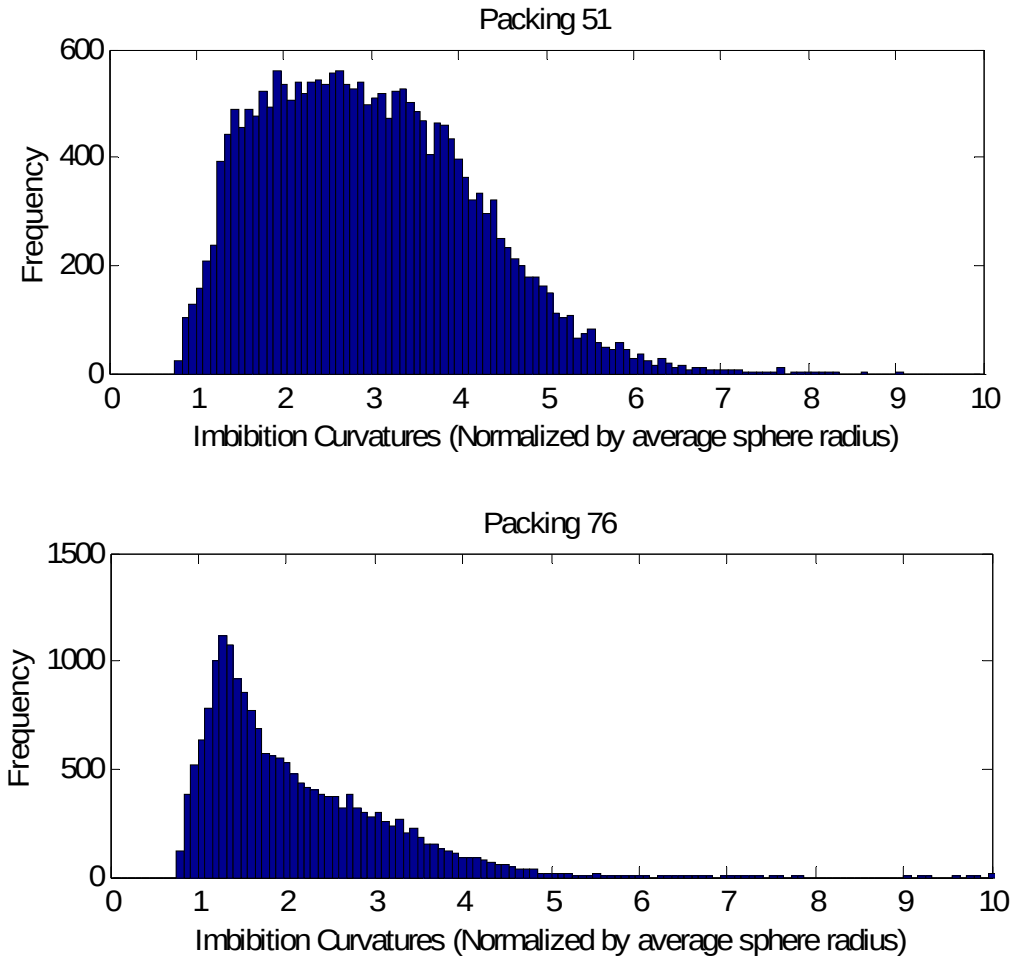

Figure 2.21: The imbibition critical curvature distribution for packing 1 and 76. C_1 imbibition criterion (equation (2.8)) is used to calculation the critical curvatures. Both packings have similar range of critical curvatures.

In imbibition, the residual nonwetting phase saturation varies for different packings. In general, wide grain size distribution yields smaller residual saturation, while narrow grain size distribution gives the opposite. Similar behavior is observed in both groups. This is a significant difference with the drainage result, where different model

sediments share similar irreducible saturation (Figure 2.22). We argue that such behavior is due to the different connectivities of wetting and nonwetting phases. In imbibition, the nonwetting phase displacement is through pore connectivity, that is, a pore can be imbibed only if the nonwetting phase inside is connecting to the exit faces via the continuous pore clusters filled by nonwetting phase. Such connectivity can be easily disconnected during the percolation, as the wetting phase imbibes a great amount of pores in the porous medium. In a packing with wide grain size distribution, at each applied curvature only a small amount of pores can be imbibed, and the continuous clusters that ensure imbibibition maintain even at very low applied curvatures. Therefore, less trapping occurs. On the other hand, a great number of pores are imbibed at percolation for a packing with narrow grain size distribution, which terminates most of the clusters and results in more trapping.

The wetting phase has two types of connectivities: pore connection and pendular ring connection. The latter plays an important role towards drainage endpoint, which enables the displacement of wetting phase. Therefore, different packings finish with at the similar residual saturation in drainage.

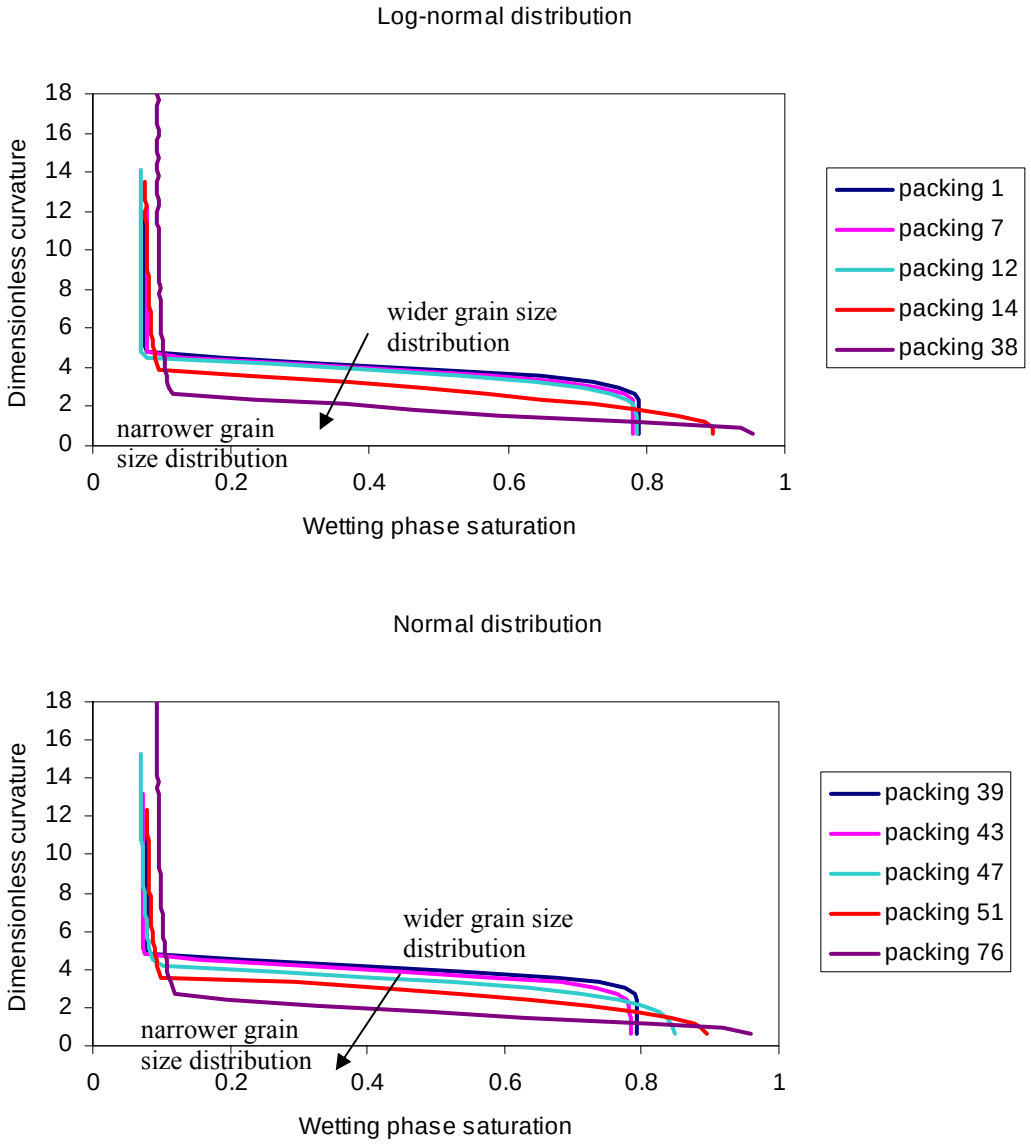

Figure 2.22: Imbibition curves for model sediments with different grain size distributions. The model sediments are grouped as log-normal and normal grain size distributions. The percolation threshold declines as increasing the width of grain size distribution.

2.7 DRAINAGE AND IMBIBITION SIMULATIONS BASED ON PERIODIC BOUNDARY CONDITION

A new treatment of boundary condition is used to eliminate the boundary effects. By doing this, the drainage and imbibition results are more applicable to the larger scale, which is later confirmed by the comparison with the field data. 60 model sediments are used for the drainage and imbibition simulations. Different behaviors for both drainage and imbibition are observed compared to the simulation results with the conventional boundary conditions. We refer to this model as the infinite-acting physically representative network model, or iPRNM, as opposed to the network models with conventional boundary conditions, which is referred to as finite physically representative network model, or fPRNM.

2.7.1 Model description

The boundary effect is one of the problems that arise when applying network modeling to predict petrophysical properties. For example, trapping is underestimated due to the presence of boundaries. The pores have better access to the exit faces in a small sample, and thus both wetting and nonwetting fluids are less likely to be trapped. Although this is a similar boundary condition for the core-based experiments (therefore the network modeling and experimental results can have a reasonable match, as in Figure 2.8), in the reservoir the condition is totally different. In the reservoir, whether the fluids are trapped is only determined by fluid connectivity in the porous medium. The effect of the reservoir boundary to the local porous medium is insignificant, owing to the distance between them. Consequently, the removal of boundary effect from the network

simulation is significant as it allows us to have a more reasonable prediction of the fluid distribution and saturation in the reservoir conditions.

A common approach to eliminate the boundary effect is by imposing the periodic boundary conditions. For example, if we have a cubic domain, applying the periodic boundary condition ensures that each point on one boundary has its corresponding point on the opposite boundary, which can communicate with each other. Such communication, for fluid flow, means that when the fluid leaves from a point on one boundary, it re-enters the domain from the opposite boundary through the corresponding point. By using the periodic boundary condition, the domain is wrapped around in all directions, and becomes boundaryless.

When it gets to our model sediments, a more complex treatment is required to apply the periodic boundary condition. The model sediments must be generated by considering the periodicity, in such a way that the spheres near one face of the boundary cell are in contact with the spheres at the opposite face. Figure 2.23 shows a demonstration in 2D. For instance, when the left boundary in Figure 2.23A is concave, the corresponding right boundary should be convex. Therefore, no boundaries are observable when duplicates are put alongside to each other (Figure 2.23B). The same concept is used in 3D model sediments, although a much more complex geometry is encountered.

We still need to subdivide the model sediments into individual units to generate the network. Delaunay tessellation is used for this purpose. In this example, we demonstrate Delaunay tessellation only in x direction. The domain only includes the original packing A and its two duplicates on the left and right hand sides of it. Delaunay tessellation does not differentiate individual packings, but performs the calculation for the entire domain (this case includes packing A and its two duplicates). Triangles *i* and *ii* are

the two cells on the boundaries that contains spheres from both Packing A and its duplicates (as in Figure 2.23B).

Triangles *i* and *ii* are geometrically identical as they are constructed by spheres with the same relative locations, although the actual spheres appear in different parts of the domain. Every triangle on one of the boundaries has a duplicate on the opposite boundary. Thus when fluids flow through triangle *ii* and leave packing A, it is equivalent to the same fluids coming back from the other side through triangle *i*, and re-entering packing A. This 'wrap-around' feature eliminates boundaries in *x* direction, and thus the packing can be considered as infinite in *x* direction.

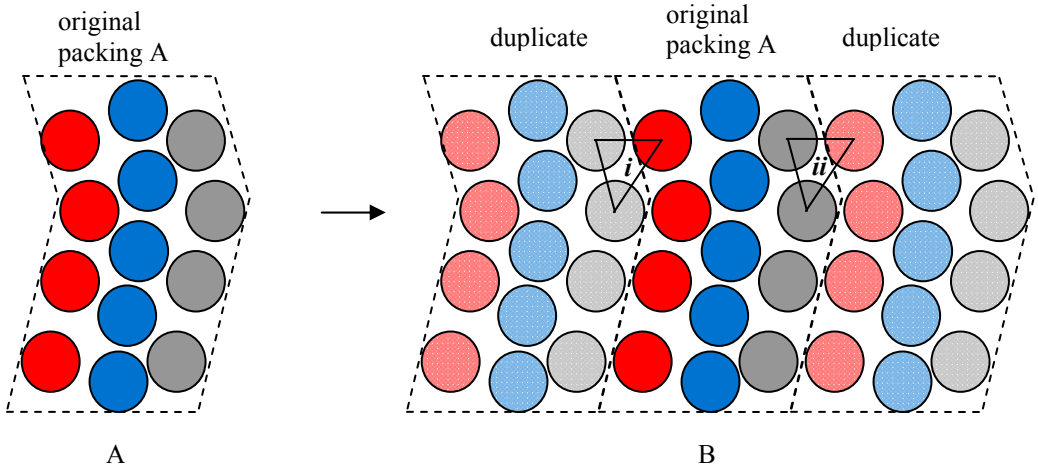

Figure 2.23: A 2D demonstration to apply a periodic boundary condition to a model sediment (the colorful disks are the grains in the model sediment, the partially transparent disks are the duplicates of the model). On the left hand side (A) shows the original packing A. When its duplicates are placed next to A, the boundaries between A and the duplicates become unnoticeable. Triangle *i* and *ii* belong to the opposite boundaries. However, they are the identical triangles constructed by the disks with the same relative locations.

The 3D treatment is similar to the preceding description. Following the implementation of (Behseresht et al., 2009b), a total of 26 duplicates should be placed

next to the original packing A in the coordinate axis directions. Therefore, a domain (cube) containing 27 packings (3 by 3 by 3) are generated. Delaunay tessellation is performed for the entire domain. The corresponding tetrahedra on the opposite boundaries of the central 'unit cell' are identified, which allows the fluid transportation to 'wrap-around' on the opposite boundaries of the unit cell. The extra tetrahedra with no sphere belonging to Packing A are removed from the domain. The remaining domain contains the original Packing A and an layer of spheres from the duplicates (these spheres are contained in the tetrahedra on the boundaries). Physically, the implementation of the periodic boundary condition represents the case that the identical sediment sample duplicates itself in all the directions infinitely, and creates a homogeneous porous medium. This technique enables the using of finite sphere packing to model the fluid flow in an infinite domain, and thus the network model is referred to as the infinite-acting physically representative network model (iPRNM).

Due to the elimination of boundaries, the original trapping criterion, which checks if the pores are still connecting to the exit face through the continuous cluster (Figure 2.24A), is not applicable. (Behseresht, 2008) proposed the concept of infinite and finite clusters to determine whether the trapping happens. A 2D example is shown in Figure 2.24B. An infinite cluster is the one that virtually has infinite size, and therefore the fluid in that cluster is displaceable (Figure 2.24B1). On the other hand, a finite cluster has finite size. It can extend through several copies of the unit cell, but ultimately it has distinct tips (Figure 2.24B2). Fluid in the pores of this type of cluster is trapped, and cannot be drained or imbibed.

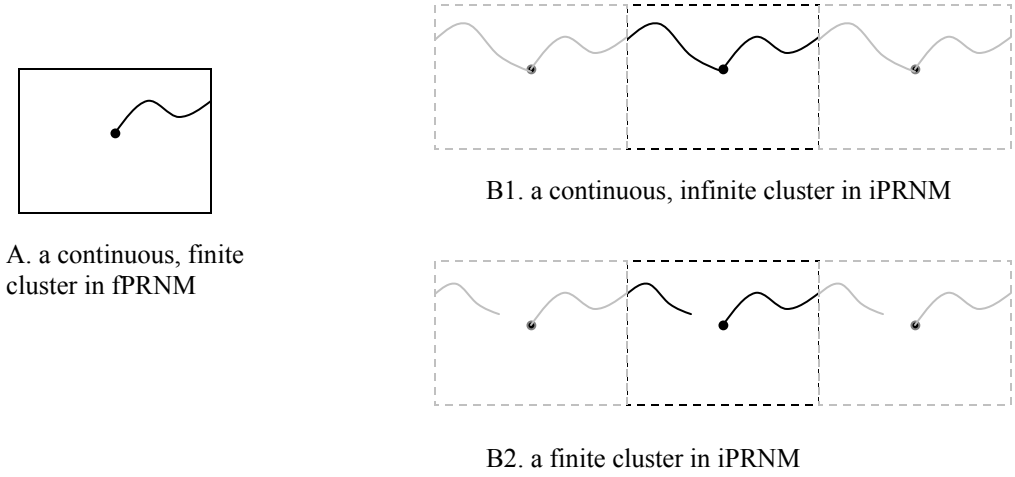

Figure 2.24: A 2D demonstration of the clusters in both fPRNM (left panel) and iPRNM (right column). The black dot represents a candidate pore, in which the fluid would be displaced by drainage or by imbibition. The curve represents a cluster of pores that have the same fluid as the candidate pore. In the left panel (fPRNM), the curve connects the candidate pore to the exit boundary, and thus drainage or imbibition events can happen in the pore. In the right panel (iPRNM), (B1) shows the cluster wraps around the left and right periodic boundaries and eventually returns to the candidate pore from the opposite side. In (B2), the cluster also wraps around but terminates somewhere inside the domain, and results in a broken cluster. The former case shows an infinite cluster, as indicated by the continuous curve spanning the unit cell and adjacent duplicates (gray). Fluid inside the pores in an infinite cluster is capable of being drained or imbibed. The latter case shows a finite (or "broken") cluster of pores (no continuous path exists in the unit cell plus adjacent duplicates). Fluid in the pores belonging to the broken clusters cannot be displaced and thus is trapped.

In fPRNM, the entry pores are usually the random selection of several pores on one of the boundaries. As no boundary exists in iPRNM, the entry pores are randomly chosen in the entire domain. Our tests (not shown) confirm that the drainage and imbibition results are not sensitive to the different combinations of the entry pores, only the number of pores would vary the drainage percolation. To maintain the similarities

between iPRNM and fPRNM, we keep the number of entry pores the same for both simulations, while the locations of these pores are insignificant.

Other than the above differences, the settings in iPRNM are the same as the fPRNM.

2.7.2 Comparison between iPRNM and fPRNM

Figure 2.25 shows the comparison between iPRNM and fPRNM based on Packing 1. The radii of the spheres range from 0.32 to 2.58 (arbitrary units), with a mean value of 2.18 and a sorting index of 1.04. The simulations based on other packings have the similar results, and therefore the analysis can be applied as well. For drainage, two models give the identical curves at the beginning of drainage, and percolation happens at curvature = 6 for both simulations. This suggests that different boundary conditions do not play noticeable role at the first half of the drainage simulation. At this stage, none of the pores are trapped in either of the simulations, otherwise two curves would diverge. After the percolation, the drainage curve for iPRNM stops at the end of percolation, with S_{wirr} = 15.4% and curvature = 7.2. On the other hand, fPRNM shows a different behavior. Few pores are drained at very high curvatures, forming a 'tail' towards the drainage endpoint.

The major difference between these two models is the 'tail' part of drainage that occurs in fPRNM. It corresponds to the case of draining a few small pores by using large capillary pressures. At this stage of drainage, in fPRNM the few remaining continuous clusters ('continuous' here means only connecting to the exit face, as in Figure 2.24A) still allow the drainage events. However as suggested by Figure 2.24B, the periodic boundary condition imposes a stricter rule to check the fluid connectivity. That is, only a

'wrapped-around' cluster is considered as the 'continuous' one in this case. This requirement becomes more difficult to satisfy towards the drainage endpoint than that in fPRNM. This becomes the reason that iPRNM traps more wetting phase pores in the drainage simulation.

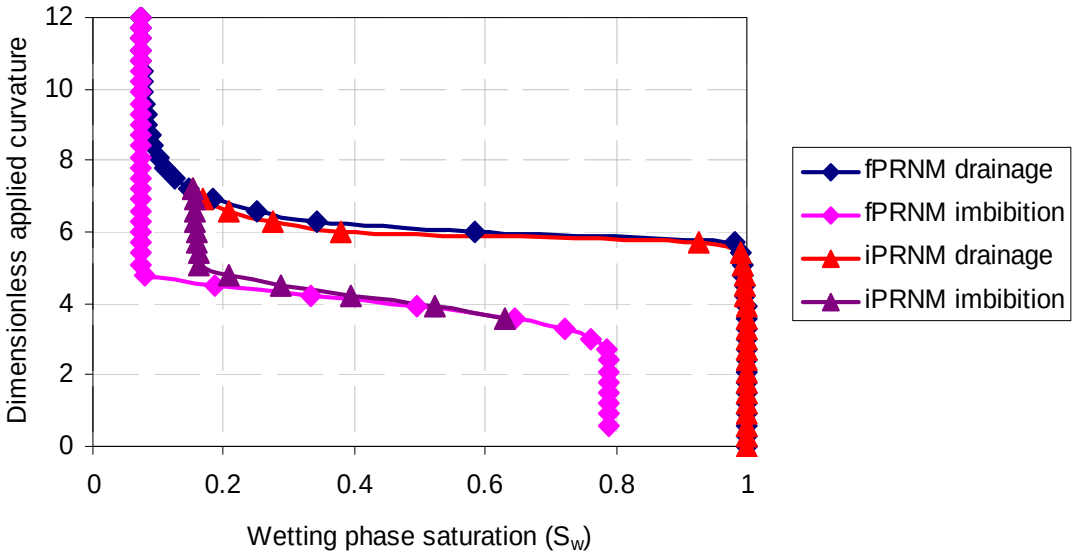

Figure 2.25: The comparison of the drainage and imbibition curves between iPRNM and fPRNM. Both models use the same model sediment (Packing 1), which is a dense, disordered packing of 5000 spheres with narrow grain size distribution. The boundary conditions are different for these two models, and the other conditions are kept the same.

Imbibition starts at the representative drainage endpoints. The beginning of imbibition shows no saturation change with decreasing the curvature, showing no imbibition events yet take place above curvature = 4.5. Following that, the percolation happens at the same curvature for both simulations. Similar to drainage, different boundary conditions does not have noticeable effect during the percolation. Two curves converge during the percolation. The imbibition curve for iPRNM stops at S_w = 62.5%

and curvature = 3.6, while the curve for fPRNM continues to much larger saturation and lower curvature values, which builds up a 'tail' for imbibition.

This 'tail' part in fPRNM suggests that the last few large pores that can still be imbibed in fPRNM with very small curvatures are all trapped in iPRNM. This indicates that while these pores are still in the continuous clusters of fPRNM (Figure 2.24A), they already belong to already broken clusters in iPRNM (Figure 2.24B2), and therefore cannot be displaced. In this simulation, the total volume of these pores contributes to 15% saturation units.

In both simulations, more trapping occurs at imbibition endpoint than drainage endpoint. Both iPRNM and fPRNM suggest such behavior. For instance, fPRNM gives 7.4% S_{wirr} and 21.2% S_{nwr}; iPRNM gives 15.4% S_{wirr} and 37.1% S_{nwr}. The difference between S_{wirr} and S_{nwr} is controlled by the wettability setting in the simulation. The model rock is considered as 100% wetting phase wet, with the contact angle being 0. With this setting, the wetting phase is capable of connecting through pores and pendular rings, while only the pore connection is available for nonwetting phase. The pendular ring connection plays an important role towards the drainage endpoint to maintain the continuous cluster. Consequently, the displacement of wetting phase is much easier than nonwetting phase, yielding more nonwetting phase trapping.

2.7.3 Comparison between S_{or} from iPRNM and tracer tests

The residual oil saturation in the reservoir, either after primary or secondary recovery, is an important value for the industry. The amount of residual oil is the primary factor that determines whether an EOR treatment is economic for the further production. The single well tracer test (SWTT) and two well tracer test (TWTT) are widely accepted

techniques to determine the residual oil in the reservoir (S_{or}). Field data from (Causin et al., 1990; Deans and Majoros, 1980; Lichtenberger, 1991) shows the successful application of these techniques in the sandstone reservoirs, which are also our data source in this section.

Our simulations based on the infinite acting physically representative network (iPRNM) and finite physically representative network (fPRNM) are used to predict the residual oil saturation. Compared to fPRNM, iPRNM eliminates the boundary conditions, which is believed to have a better agreement with the reservoir conditions. Strictly speaking, S_{or} predicted from the imbibition simulation only represents the value of primary recovery, which might not always be the case in the field observation.

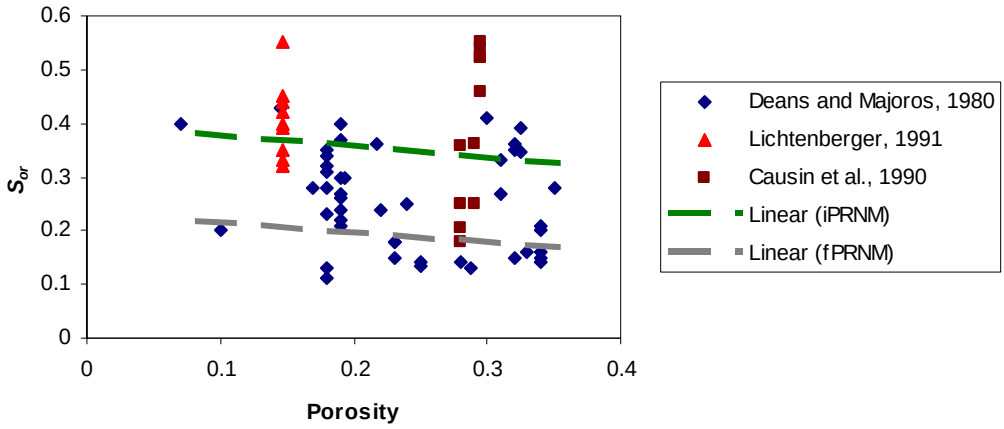

Figure 2.26: The residual oil saturation (S_{or}) comparison between the iPRNM (upper dashed line)/fPRNM (lower dashed line) predictions and field data from tracer tests (sandstone reservoirs). The simulation results are computed at larger porosities (>15%), and extrapolate to the smaller values. Packing 1 is used for both simulations.

Figure 2.26 shows the field measurement of residual oil saturation (S_{or}) from different sources. The field data have a very wide range of porosity and S_{or}. The residual oil saturation from the field data range from 10% to 55%, and there is no a clear

correlation with the porosity. It should be pointed out that there is no report of the reservoir production history from (Deans and Majoros, 1980). That is, we do not know if waterflooding has been performed before SWTT. If waterflooding has been performed, S_{or} would be lower than that after the primary recovery. On the other hand, the other two sources (Causin et al., 1990; Lichtenberger, 1991) are all based on tracer tests after the primary recovery.

We apply both the iPRNM and fPRNM imbibition simulations to model sediments with different porosities, obtained by increasing the radii of the spheres in the packing without moving their centers. This mimics the growth of epitaxial cement on grains and reduces the porosity of the packing (Bryant et al., 1993). A maximum of 10% radius was increased to reduce the porosity to 18%. For both simulations, almost linear relationship between porosity and S_{or} are obtained. We can therefore extrapolate the computed data at higher porosity to predict S_{or} at lower porosity. The comparison indicates that fPRNM predicts lower S_{or} (20%~25%, the lower dashed line), while the prediction by iPRNM gives a range of 40%~45% (higher dashed line), 20% increase compared to fPRNM.

The comparison with the field data suggest that results predicted by fPRNM roughly gives a lower bound of S_{or} measured from tracer tests, while iPRNM prediction has a better agreement in terms of the average S_{or} of each porosity. As discussed precedingly, data from (Deans and Majoros, 1980) might give lower S_{or} than the primary recovery. If this is true, in Figure 2.26 S_{or} after the primary recovery would shift upwards, which better agree with iPRNM prediction.

It should be noted that the residual saturation varies from different model sediments. This variation is a function of the grain size distribution (please see the next section, Section 2.7.4). In other words, by using different packings the residual saturation

value would shift (Figure 2.26, the dashed line). However, comparison between iPRNM and fPRNM is not affected, that is, iPRNM always predicts much higher residual saturation than fPRNM, and thus yields a better agreement with the field observation.

Overall, iPRNM has at least the similar agreement with fPRNM when compared with the field observation, if not better. However, iPRNM is based on a boundary condition that is more physically reasonable than the conventional boundary conditions in predicting the fluid distribution in the field scale. The results based on iPRNM (S_{wirr} and S_{nwr}) are therefore used for the methane hydrate saturation prediction, which are elaborated in Chapters 4 and 5.

2.7.4 Drainage and imbibition simulation based on iPRNM

We compare the simulation results based on different model sediments. The complete results are listed in Appendix C. We choose the identical packings as in

Table 2-1 for the simulation. The simulation settings are identical to fPRNM, except for that the periodic boundary condition is used instead of the conventional one.

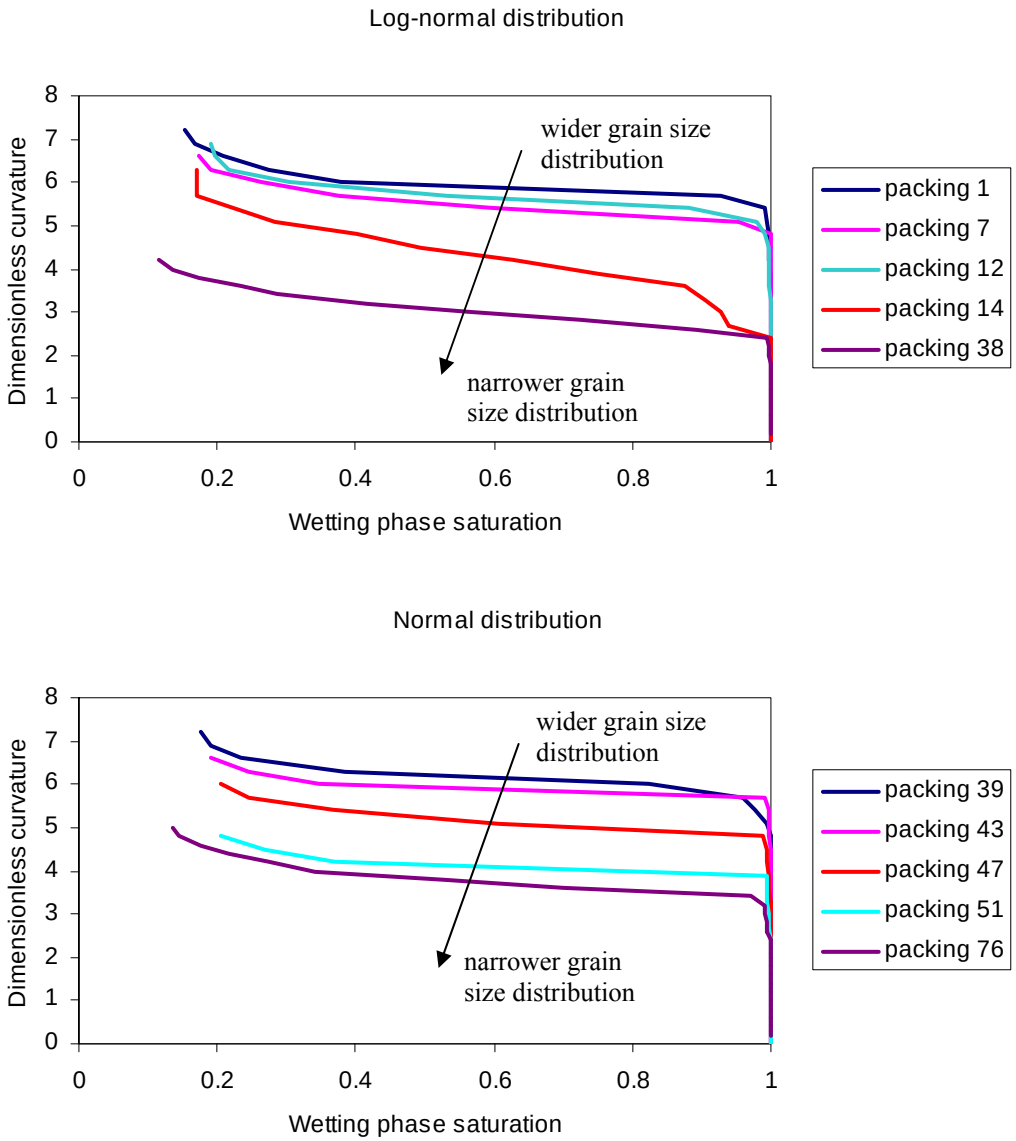

Figure 2.27: Drainage curve comparison for different model sediments, from iPRNM. The results are grouped as log-normal and normal distributions of grain sizes. Increasing the grain size distribution reduces the percolation threshold for drainage.

Figure 2.27 shows the drainage results for 10 selected model sediments based on iPRNM. A distinct shift of percolation threshold is observed as the grain size distribution gets wider. For the case of log-normal distribution, Packing 1 percolates at curvature ≈ 6, with the sorting index being 1.04. The sorting index increases to 1.31 for Packing 14, and thus declines the percolation curvature to 4. A further increment of the sorting index (1.51 for Packing 38) further reduces the percolation curvature to 3. Similar behavior is also observed for the case of normal distribution. From Packing 39, 47 to 76, the sorting index increases from 1.02, 1.27 and 2.23, and the corresponding percolation curvatures drop from 6, 4.5 to 4.

Per the preceding discussion, the boundary conditions have limited influence on the percolation. Percolation is only a function of the network topology and of spatial correlation of the geometric attributes on the network. Moreover, we do not observe large differences among S_{wirr} in Figure 2.27. Since for all the simulations, the settings for different simulations are the same except for the grain size distributions, the result suggests that S_{wirr} is a weak function of the grain size distribution. This observation is similar to the drainage results based on conventional boundary conditions (Figure 2.20), where S_{wirr} are similar for different packings as well. Consequently, we argue that the wetting phase connectivity does not vary significantly for different grain size distributions in both boundary conditions.

For the imbibition simulation, at the beginning there is only a small increment of the wetting phase saturation. At this stage, no imbibition events in the pores have yet taken place, and the expansion of few pendular rings contributes to that small increment (unlike Section 2.4 where pendular expansion is allowed in the entire domain to match the simulation setting of LSMPQS, in Section 2.6 and 2.7 pendular ring only expands when it is connecting to the bulk wetting phase). The percolation thresholds for different model

sediments have distinct behaviors from each other. Narrower grain size distribution, which also yields narrower pore size distributions, has a higher percolation threshold, while wider grain size distribution results in a much lower percolation.

Figure 2.28 shows that from Packing 1, 12 to 38, the percolation threshold drops from 5, 4, to 3 (the determination of the percolation threshold for imbibibition simulation, however, is much more difficult than drainage, as the wetting phase expansion smears the sharpness of percolation threshold), and the similar pattern is obtained for Packing 39, 51 to 76 as well.

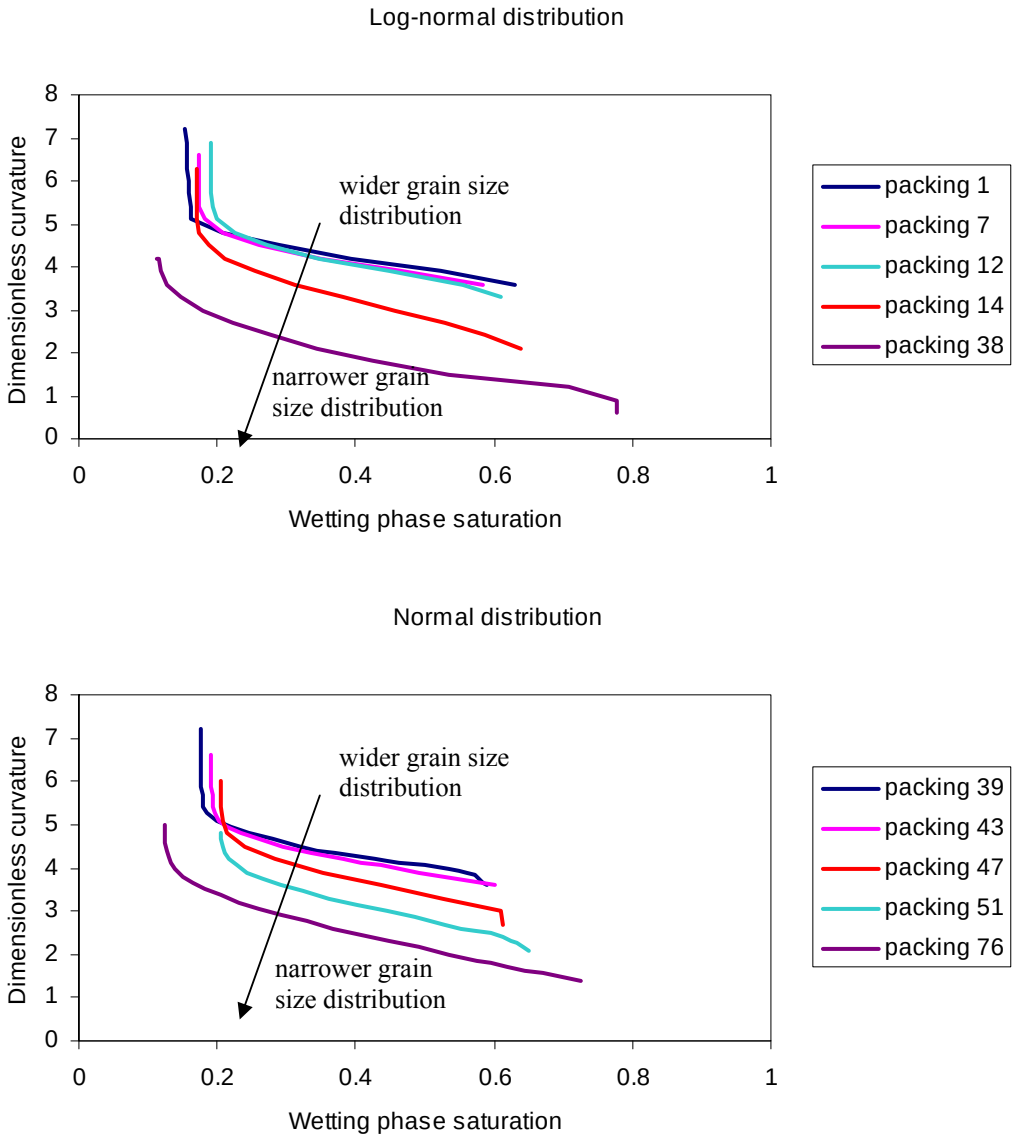

Figure 2.28: Imbibition curve comparison for different model sediments, from iPRNM. These packings are grouped as log-normal and normal grain size distributions. Increasing the grain size distribution reduces the percolation threshold for imbibition.

Unlike the results of drainage simulation, the residual saturation at imbibition endpoint is affected by the grain size distribution. The general trend shows that with wider grain size distribution, S_{nwr} decreases accordingly. In our network modeling, whether the pore can be imbibed depends on if that pore belongs to the continuous cluster. Breaking the cluster yields the trapping of the wetting phase in the pore. The critical curvatures have a narrow range with narrow grain size distribution. Imbibition therefore experiences an abrupt breaking of all the connecting clusters within a small range of applied curvatures. On the other hand, the wider grain size distribution gives wider range of critical curvatures. With the same variation of applied curvature, connecting clusters remain for the latter case, which makes fluid displacement possible for smaller curvatures. Consequently, S_{nwr} decreases with increasing the width of grain size distribution.

As shown in Figure 2.27, S_{wirr} does not have significant variations. This is because for wetting phase, it can also connect through pendular rings other than pores. The former type stays at the narrow spaces of the porous medium until high applied curvatures break it. For different packings, the pendular rings can nevertheless maintain the connection to the exit faces (fPRNM) or as infinite clusters (iPRNM), even though the pore connection might be terminated at the early or late stage of drainage, owing to the curvature distributions. Therefore, we obtain the similar S_{wirr} at drainage endpoint.

2.8 THE IMPLICATION OF DRAINAGE AND IMBIBITION SIMULATION TO THE FIELD-SCALE METHANE HYDRATE DISTRIBUTION

Methane hydrate distribution in the field scale is largely affected by the local mechanisms of methane hydrate formation. When hydrate is formed from existing gas accumulation, the pore-scale phenomena are very important: they not only determine the initial gas saturation, but also affect the global gas and water distribution.

Our hydrate formation model in the field scale, which is outlined in chapter 1 and will be elaborated in Chapter 5, assumes the following gas charge and hydrate formation steps. First, gas migrates upwards, and displaces water in the reservoir. The gas saturation in each layer is dependent on the capillary equilibrium. At this stage, BGHSZ is at an arbitrary location above the gas reservoir. Second, BGHSZ moves downwards. Methane and water begin to be converted into hydrate at BGHSZ. The amount of hydrate that can be produced is the function of many factors, e.g., temperature and pressure (Chapter 4), salinity (Chapter 4), and the availability of methane and water (Chapter 4 and 5).

The drainage and imbibition are significant processes in the hydrate formation. The initial formation of the gas column is a process of nonwetting phase displacing wetting phase. This is the drainage process that can be simulated by using the network models. The simulation gives us the information of the gas and water distribution and saturation at different stages of drainage for model sediments. For our purpose, such information can be directly translated as the initial fluid distributions at different vertical distances. Moreover, our iPRNM simulation eliminates the boundary effect, so that the initial gas saturation predicted from the network modeling is more applicable to the field-scale problem. For example, on average the iPRNM drainage simulation (Figure 2.27) shows 15%~20% S_{wirr} at drainage endpoint, whereas lab-scale measurements yield $S_{w,irr}<$ 10% due the boundary effect (Behseresht et al., 2009). Such result indicates that the

initial gas saturation has a maximum value of 75%~80%, which is an important value for the stoichiometric calculation of hydrate saturation.

Hydrate forms at BGHSZ, where vacant space is created because the volume of hydrate formed is much smaller than the volume of gas and water consumed, assuming constant temperature and pressure during formation. This leads to the conclusion that hydrate, free water and free gas all invade into the gaseous phase (a detailed elaboration can be found in Chapter 4 and 5). The hydrate and water invasion follows the path of imbibition. The free gas migration draws the gas from the bottom of the reservoir, where water invasion consequently occurs. We argue that both cases (hydrate formation at BGHSZ and water invasion at the bottom of the reservoir) follows the path of imbibition, and therefore our network modeling based on the periodic boundary condition can be applied to predict the imbibition events and also the residual gas saturation. For example, iPRNM simulation predicts an average of 32% S_{nwr} in the model sediments. This value gives the lower bound of the gas that exists in the reservoir sediments, which limits the amount of free gas that can be supplied to fill the vacant spaces at BGHSZ. For these reasons, network modeling for imbibition is also an important tool for the hydrate saturation prediction in the local porous medium or the distribution in the reservoir.

2.9 CONCLUSIONS

We use the critical curvatures previously computed by Level Set Method Progressive Quasi-Static algorithm (LSMPQS) in individual pores to develop a new criterion to estimate imbibition critical curvatures (C_I criterion). This criterion has the simple form of Mason/Mellor criterion. Employing it in Physically Representative Network Model (PRNM) simulations yields a percolation threshold for imbibition that agrees well with LSMPQS predictions and with experiments.

A pore-by-pore comparison of network simulations to LSMPQS simulations enables a more rigorous verification of the C_I imbibition criterion and Mason/Mellor drainage criterion, and the underlying premise of all network modeling: that networks can capture pore-scale physics. This is a more detailed analysis than the usual macro-scale comparison of the capillary pressure-saturation curves. It is an important step toward eventual validation against experiment, which will require not-yet-available resolution of pore-filling events in space and in time. While we only verify two specific network models/media, the pore-by-pore comparison with LSMPQS simulation can provide an independent verification of any network model provided that the detailed map of the original pore space exists (so that LSMPQS method can be used).

The sequence of pore-filling events during drainage is very similar in fPRNM and in LSMPQS. Events occur at slightly different curvature, but fPRNM is able to capture the essential physics of pore-scale displacement. This checks the correctness of Mason/Mellor criterion in fPRNM. The sequence of pore-filling events during imbibition differs somewhat between fPRNM and LSMPQS. One reason for the discrepancy is that the C_I criterion does not account for coalescence of pendular rings. Another is that the C_I criterion presumes that configuration of menisci and pendular rings needed for a C_I event

in a pore is always present. In reality the configuration of menisci in an individual pore is determined dynamically, and the C_1 event may be precluded. Thus fPRNM with the C_1 criterion is capable of predicting the macroscopic properties, but inclusion of additional physics is needed to capture the correct sequence of pore-filling events.

The predictions of drainage/imbibition from large fPRNM and iPRNM are compared with experiment and field data. fPRNM is applicable to lab-scale experimental results. The key characteristics, e.g., percolation thresholds and S_{wirr}, are correctly reflected, while some differences of S_{nwr} are observed with the experimental observation. iPRNM is aiming to mimic a large scale, e.g. the field, where boundary effects are negligible. S_{or} from iPRNM predictions are consistent with the values inferred from tracer tests reported in the literature. The values are substantially larger than in usual lab-scale experiments, indicating nontrivial boundary effect and also that iPRNM can provide valuable insights into the fluid saturation in the field. Similar result is also obtained in drainage that S_{wirr} from iPRNM is much higher than from fPRNM.

A wider grain size distribution leads to a wider pore and throat size distributions, and more importantly, shifts the modes of pore and throat sizes to smaller values. This yields a decrement of percolation thresholds in both drainage and imbibition, as the critical curvatures for these events are inversely proportional to the pore size (imbibibition) and throat size (drainage). Such observation is available in both fPRNM and iPRNM, showing that different boundary conditions have no significant effects on the percolation.

In general, S_{wirr} at drainage endpoint has lower values than S_{nwr} at imbibition endpoints. This is due to the different connectivities of wetting and nonwetting phases. The wetting phase connectivity is through both pores and pendular rings, while the nonwetting phase has only the pore connections. The breaking of most of the pore

connectivity does not necessarily trap the wetting phase if the connected clusters of pendular rings are still available. However, nonwetting phase trapping will take place once the pore connection is terminated. This is also one of the reasons that similar S_{wirr} is obtained for all of the packings, but not S_{nwr}: the pendular ring connectivity is not significantly affected by the grain size variations, and therefore allows the wetting phase displacement at higher applied curvatures.

3. Network modeling of drainage and imbibition in real rock

The simulations based on the model sediments presented in Chapter 2 shows the drainage and imbibition behaviors with both conventional and periodic boundary conditions. The model sediments are idealized approximations of the real unconsolidated porous media. The application of the model sediments (sphere packing) might be restricted because the grains in reality are angular and irregular and real sediments will have undergone compaction during burial. The model sediments do not represent rocks which have undergone geologic processes that reduce their porosity. Model sediments usually have a porosity of around 36%, while the porosity in clean rock, depending on the degree of compaction and cementation, is much less than this value. Therefore, it is a natural extension to apply the concepts developed in Chapter 2 to the real rock cases, and study the drainage and imbibition events.

The hydrate stability zone often exists in the sediments rather than the rocks. However, we do not preclude the possibility of hydrate existence in the rock, that is, a much compacted and cemented irregular porous medium. This is based on the understanding that our knowledge of gas hydrate is still limited by the current scope of investigation, and therefore, environments with such rocks are still potential candidates for hydrate reserve. Moreover, it is a common belief that the models developed for a specific problem should broaden their applications into other fields. For these purposes, we extend the network modeling, along with the pore-by-pore comparison technique, to the real rock cases.

Three sandstone samples are used to test the reliability of network modeling of drainage and imbibition: Fontainebleau, Berea and Castlegate sandstones. These are the benchmark porous media usually applied in the lab tests. They can be simplified by using

model rock, a porous medium derived from the model sediment in Chapter 2 by compaction and grain growth. It has been proved as long as their porosities are the same the model rock and real rock would have the same permeability (Bryant et al., 1993).

However, when network is directly built upon the topology and geometry of the real rocks, we probably cannot simply extend the models developed in Chapter 2 to this case: the highly irregular void spaces in the real rock require more attention than the simple geometry in the model sediments. Furthermore, no periodic boundary conditions can be applied to the network models derived from the real rocks. Using periodic boundary condition requires taking periodicity into consideration when generating the porous medium (as in Chapter 2), a condition that cannot be readily satisfied in the real rock case. In this chapter, we only use conventional boundary conditions for simulation, that is, only two opposite faces are used as the entry and exit faces, and the other four faces are all sealed.

Despite the above differences, network models based on model sediments and real rocks share lots of similarities. We only describe the unique treatments in real rock, while the rest can be found in Chapter 2.

By comparing the drainage and imbibition results of network modeling and LSMPQS, we test the correctness of the network modeling, as well as the newly developed drainage and imbibition criteria. Similar to Chapter 2, the comparison is also based on the macroscopic (curves of applied curvature vs. saturation) and microscopic (pore-by-pore comparison) scales.

3.1 INTRODUCTION

A general procedure to create network model from a real porous medium involves the following steps. First, a small real rock sample needs to be scanned and digitized, and its 3D data for topology and geometry are stored in the computer. Second, numerical technique is employed to subdivide the void space into pore and throat units. For the network modeling, simplifications are also introduced to approximate the shapes of pores and throats. Third, the relationship among pores and throats is established, based on which a network model is built. Finally for drainage and imbibition, models controlling the events in pores and throats are developed.

X-ray computed microtomography (Flannery et al., 1987) is a widely accepted technique to generate the 3D geometric and topological data of the porous medium in micron scale within a relatively short time. Although the technology now allows for a resolution up to 3nm (Sisk et al., 2010), in most practice a resolution of microns is enough for a representation of the clean lithology (e.g. sandstone) without losing important information that affects the fluid flows. Such technique is also applied in visualizing multiphase distribution (Seright et al., 2003; Prodanovic et al., 2006; Turner et al., 2004), other than partitioning the solid grain and void space of the porous medium.

Many numerical methods have been developed to analyze the microstructure of the digitized rock samples, and in most cases identify pore and throat units. These approaches include multiorientational scanning (Zhao et al., 1994), a variant of morphological thinning (Baldwin et al., 1996), medial axis skeletonization (Lindquist and Venkatarangan, 1999; Lindquist et al., 1996), and quantitative morphology (Vogel and Roth, 2001). Except for the first method, the other three also establish the pore and throat

geometries and the relationship between them, all of which are essential for building the pore-throat networks.

The pores and throats in the real porous medium have extremely irregular geometries. For a practical application of network models of displacement, the shapes of pores and throats need to be simplified so that the criteria for pore-level events can be developed. The simplest and yet still widely-used method is to assume spherical pores and cylindrical throats. However, this treatment precludes corners (narrow spaces) in the network model, while such spatial constriction is observed in the real porous medium. More complex and advanced shapes include triangular- or square-shaped pores and throats (Mason and Morrow, 1991; Valvatne and Blunt, 2004; Patzek, 2001). It has the same shape factor with the real porous medium. The corners of triangle and square are able to hold certain amount of wetting phase depending on the capillary pressure. Further development uses a more physically-based shape: the cross-section of space constriction of touching grains (Kagan and Pinczewski, 2000; Mani and Mohanty, 1997; Man and Jing, 1999; Valvatne and Blunt, 2004), which captures the features of the throat shape in a model sediment.

The criteria are developed to determine at which applied capillary pressure (or curvature) the drainage and imbibition events could take place. The shape factor G (defined as $G = A/P^2$, where A is the area of pore or throat cross section and P is the wetting perimeter) is often employed to develop the criteria (Øren et al., 1997; Patzek, 2001; Mason and Morrow, 1991). These criteria require the calculation of fluid interface movement (for instance, interface movement, merging and separation) to determine the occurrence of drainage or imbibition events, while an *a priori* criterion, such as Mason and Mellor criterion and C_1 imbibition criterion, does not have such requirements.

In this chapter, we model the drainage and imbibition based on the existing geometric and topological data of three sandstone samples. The algorithm developed by (Lindquist and Venkatarangan, 1999) is applied to generate the pore-throat network. Simple, *a priori* criteria for drainage and imbibition are proposed for the pore-level events. Results based on the network are also verified by comparing with LSMPQS, where both macroscopic (applied curvature-saturation curves) and microscopic (pore-by-pore check) approaches are applied.

3.2 NETWORK DESCRIPTION

We obtain the digitized rock samples from different sources. The Berea sample is from (Prodanovic et al., 2007), the Castlegate sandstone sample is from (http://xct.anu.edu.au/network_comparison/), and the Fontainebleau sandstone sample is from (Kumar, 2009).

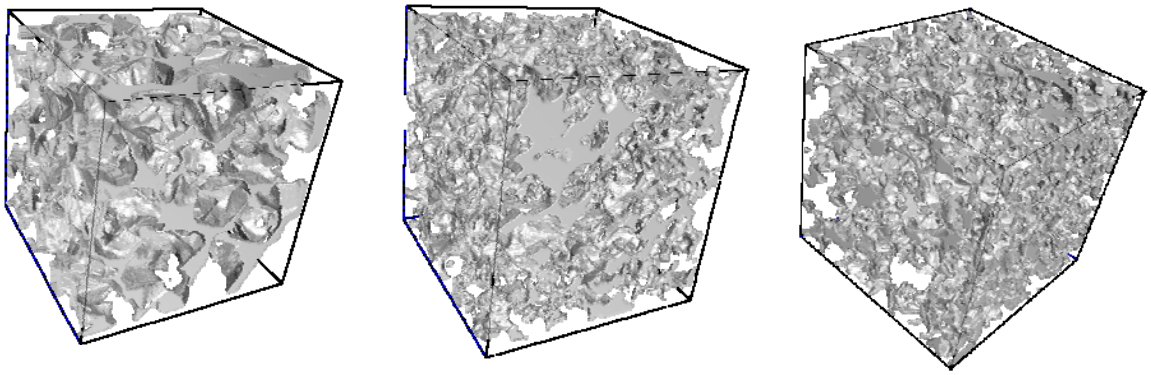

A. Fontainebleu sandstone
Porosity: 19.3%
Sample size: 768 by 768 by 768 μm^3
Resolution: 3 μm/voxel

B. Berea sandstone
Porosity: 16.9%
Sample size: 1262 by 1262 by 1262 μm^3
Resolution: 4.93 microns/voxel

C. Castlegate sandstone
Porosity: 19.8%
Sample size: 1434 by 1434 by 1434 μm^3
Resolution: 5.6 microns/voxel

Figure 3.1: Schematics of the grain surfaces of three different rock samples. All the samples are 256 by 256 by 256 voxels.

A total of three samples are used in this chapter. Each of them comes from a different outcrop, with grain size (diameter) between 100 to 200 μm. The grain surface is shown in gray in Figure 3.1. The resolution of the CT scan ranges from 3 μm to 5.6 μm. With this resolution, the geometric data preserve the important features that determine the fluid flows. LSMPQS simulation is directly run on the geometry in Figure 3.1 without any geometry simplification. All the samples contain 256 by 256 by 256 voxels, so that an entire cycle of drainage and imbibition simulation by LSMPQS can be completed within a manageable scale of time. Approximations are introduced for network modeling,

and simple, quasi-static models are developed. A much faster simulation can be done by network modeling, without computing the detailed interface movement as LSMPQS.

The network is generated by using *3DMA-Rock*, a free software available online (http://www.ams.sunysb.edu/~lindquis/3dma/3dma_rock/3dma_rock.html). It analyzes the 3D geometries based on the method proposed by (Lee et al., 1994), who employed a thinning algorithm to extract the medial axes of a 3D object. Pores and throats are later characterized from the medial axis information. The general procedure starts with identifying the throats, which have the minimum local cross-sectional area. These throats are not necessarily 2D planes, but curved surfaces (Figure 3.2). Pores are identified by using the marching cube algorithm (Bloomenthal, 1988; Lorensen and Cline, 1987) as the spaces encaged inside the throat and grain surfaces. Figure 3.2 shows an example of the medial axis of a 3D pore. Despite of the irregularity, medial axis correctly finds the skeleton of the 3D geometry, based on which topological network can be identified. In the output of the software, the pores and throats are numbered, which are also cross-indexed with their neighbors. For example, the information of each pore contains the indices of the pores and throats connecting to it, while the information of each throat contains the indices of the pores connecting to it. The relationship of the pore-throat interconnectivity provides the necessary information to build the network. Figure 3.3 gives a graphical demonstration of the process to generate the network in a digitized rock sample. The entire clusters of medial axis (Figure 3.3B) is obtained for the digitized sample (Figure 3.3A). For the medial axis within a pore (Figure 3.3C), the joint is treated as a pore (has the pore volume), and the clusters of medial axis become the throat (has no volume). The network is finally established based on the topological information of the rock (Figure 3.3D).

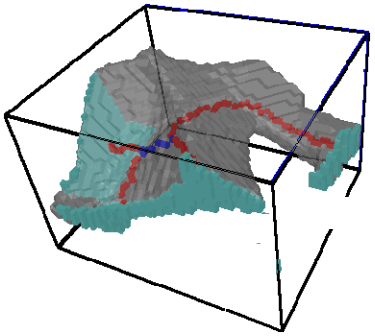

Figure 3.2: The medial axis of an irregular pore extracted from the Fontainebleau sandstone sample. The gray surface is the surface of the pore, and the continuous voxel cluster (blue and red voxels) represents the medial axis. The different colors in the medial axis indicate the distance to the nearest grain voxels. The light blue, curved surfaces are the throats.

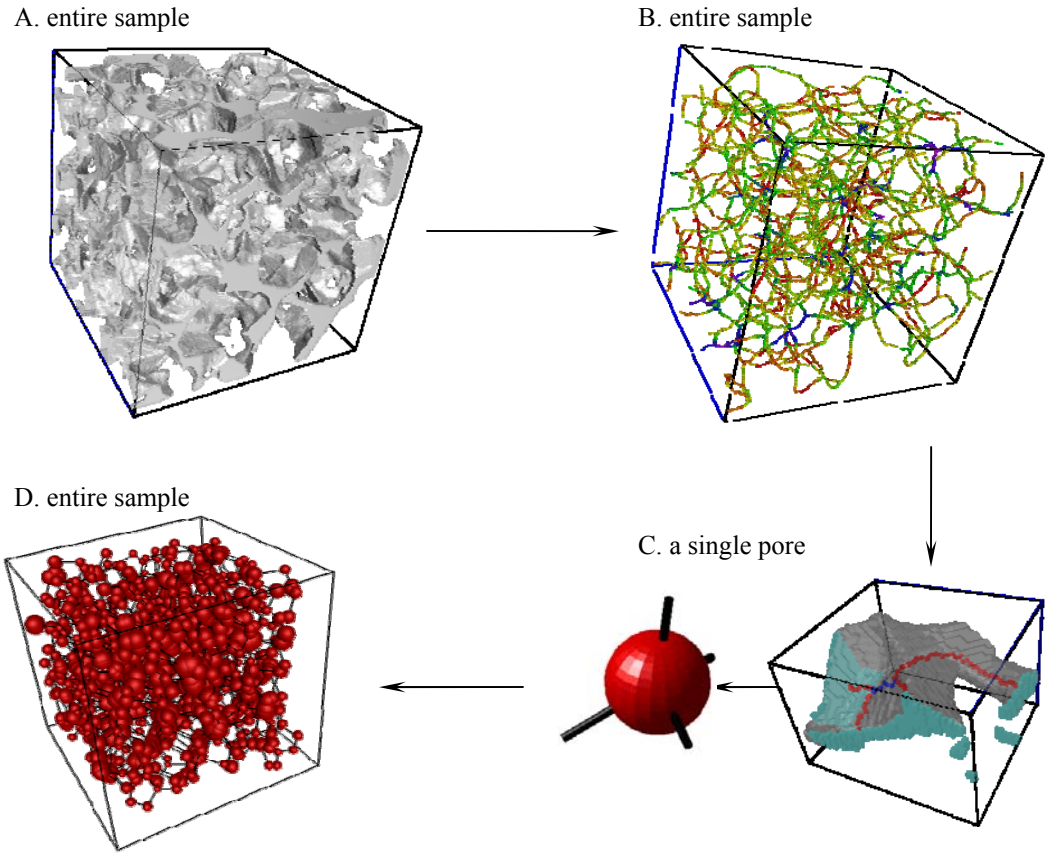

Figure 3.3: The procedure to generate a network from the real rock sample. (A) The grain surface (gray) is obtained from the micro CT scan. (B) The skeleton of the porous medium is characterized by using the medial axis. The rainbow color suggests the distance from the medial axis to the nearest grain surface. (C) Pores and throats are identified from the medial axis, both of which are highly irregular. We use the red spheres to represent the pores and black cylinders to represent the throats. The pore volume is totally assigned to the 'pores' (red sphere), while the throats have no volume. (D) Pores connect through the throats and generate the network.

This new network model (referred to as RRNM, Real Rock Network Model, and the corresponding network modeling is based on conventional boundary condition) has some unique features other than the network derived from the model sediments (finite

Physically Representative Network Model, fPRNM; and infinite-acting Physically Representative Network Model, iPRNM). First, due to the complex geometry in the real rock, it is no longer reasonable to keep the number of neighbors (or coordination number) for each pore to a constant 4. For the rock samples investigated, the coordination number for the pores in RRNM ranges from 1 to more than 20. In fPRNM, the model rock is subdivided into tetrahedron units, based on which pore bodies and throats are characterized. Each tetrahedron has 4 faces, and they are considered as the throats.

Second, the relatively simple geometry allows for the calculation of pendular rings in fPRNM and iPRNM, and thus we can consider the pendular ring connectivity in these models. RRNM is based on a much more complex geometry, and problems rise when concerning pendular rings. The calculation of pendular ring directly from the digitized images is difficult. RRNM simplifies the pore as a sphere and the throat as a cylindrical tube. This simplification still makes it a nontrivial attempt to consider pendular rings. Therefore, we do not consider pendular ring existence in RRNM. The negligence of pendular ring also affects the wetting phase connectivity. This effect will be elaborated later.

Third, it might not be suitable to use the idea of 'inscribed sphere' to develop drainage and imbibition in the real rock cases. This point will be analyzed in detail in the next section. For a simple analysis, our development is based on the experimental observation that before drainage or imbibition takes place, the fluid/fluid menisci resembles a spherical shape, which can be approximated by using an inscribed sphere. Although it is also true that even in the real rock, the local sphericity is also observed before the occurrence of drainage or imbibition, using an inscribed sphere to represent this shape might give a more curved surface than the observation. This is because the angularity in the pores or throats creates narrow spaces, which restricts the size of the

inscribed sphere. Therefore, we need to develop new drainage and imbibition criteria according to the observations.

3.3 DRAINAGE AND IMBIBITION CRITERIA FOR REAL ROCK NETWORK MODEL (RRNM)

The drainage and imbibition criteria applied for fPRNM and iPRNM rely on the inscribed spheres of pores (imbibition criterion) and throats (drainage criterion). The development of these criteria is based on the observation. Figure 3.4 shows a 2D demonstration of the fluid interfaces at critical moments of drainage (A) and imbibition (B) in a granular medium. For drainage, the critical moment means that a tiny increment of capillary pressure would lead to Haines jump (Haines, 1930) of the nonwetting phase through the throat. For imbibition, it means that a tiny decrement of capillary pressure would lead to Melrose jump (Melrose, 1965) of the wetting phase into the pore. The shape of the fluid/fluid interface at the critical moment is well represented by a dashed circle in the grain geometries of Figure 5. Similar behavior is also observed in the 3D glass-bead packing. (Haines, 1930) used the results of this observation and developed the criteria based on the radius of inscribed sphere. In practice, a constant is often introduced in the criteria to match with the experimental data.

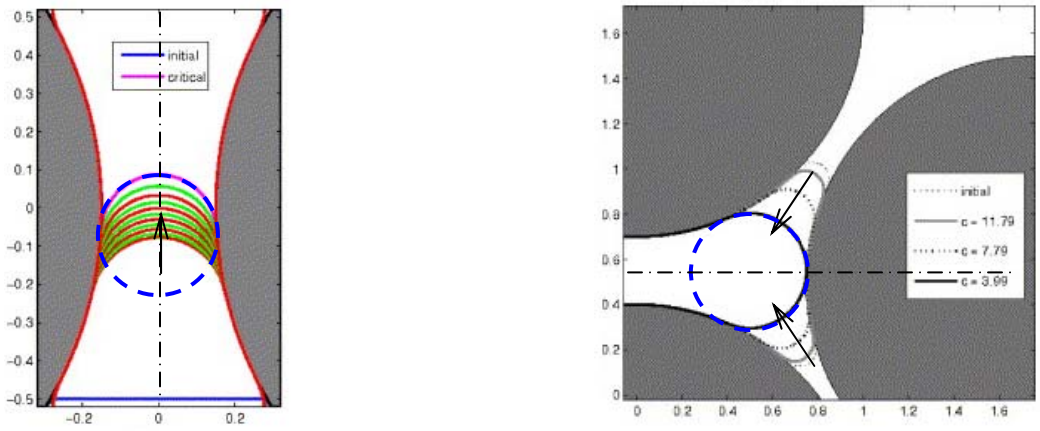

A. drainage B. imbibition

Figure 3.4: LSMPQS simulations of drainage and imbibition in simple 2D granular medium. The arrows indicate the movement of the fluid/fluid interface. At the critical moment (purple curve for drainage and black curve for imbibition), the shape of the interface agrees with the shape of the inscribed circle (dashed blue). This is the visual basis for using the radius of inscribed sphere to compute the drainage and imbibition criteria in fPRNM and iPRNM. The red and green curves on the left panel and the dashed curves on the right panel are the intermediate fluid/fluid interface at different steps of drainage (left) and imbibition (right). From (Prodanovic and Bryant, 2006).

The observation of spherical menisci is not only restricted to granular medium. In the real porous medium, the spherical menisci are also observed before drainage and imbibition take place. Figure 3.5 shows the menisci (red surface) morphology before (we refer to moment as the critical moment) and after the events. The images are obtained from a single throat (for drainage) and a pore (for imbibition) of the simulation by LSMPQS, in the Fontainebleau sample. At the drainage critical moment (Figure 3.5A), the zoom-in figure (in the green circle) shows that the meniscus does present a spherical shape, although the entire meniscus are somewhat irregular because of the throat cross-section. At the imbibition critical moment (Figure 3.5C), the arrows in Figure 3.5 all indicates the local sphericity. The concave part, shown by the green circle, is caused by

the angular pore space, where the grain surface extends into the pore space and pushes back the fluid/fluid interface. This random angularity in the pore space is the leading factor for the irregular shape of several locations on the meniscus.

It can be concluded from Figure 3.5 that local spherical meniscus is a common observation for both drainage and imbibition in the real rock case. This agrees well with the observation in the granular medium, where local spherical menisci exist. This is the basis of using throat and pore inscribed radii to develop drainage and imbibition criteria (Equation (2.6) and (2.8)). The constants in those equations are an adjustment of the menisci at the critical moment not being exactly spherical.

Another premise of the validity of Equation (2.6) and (2.8) is the symmetric geometry. Although in 2D the shape of the menisci is irrelevant to the geometry symmetry, in 3D when the symmetry is broken, the fluid/fluid menisci cannot be approximated by the surface of the inscribed spheres at the drainage and imbibition critical moments. In a sphere packing with wide grain size distribution, each pore might contain spheres with large differences in size. In this case, using the inscribed sphere to represent the shape of menisci at the drainage and imbibition critical moments might give inaccurate results, as indicated by Figure 2.17.

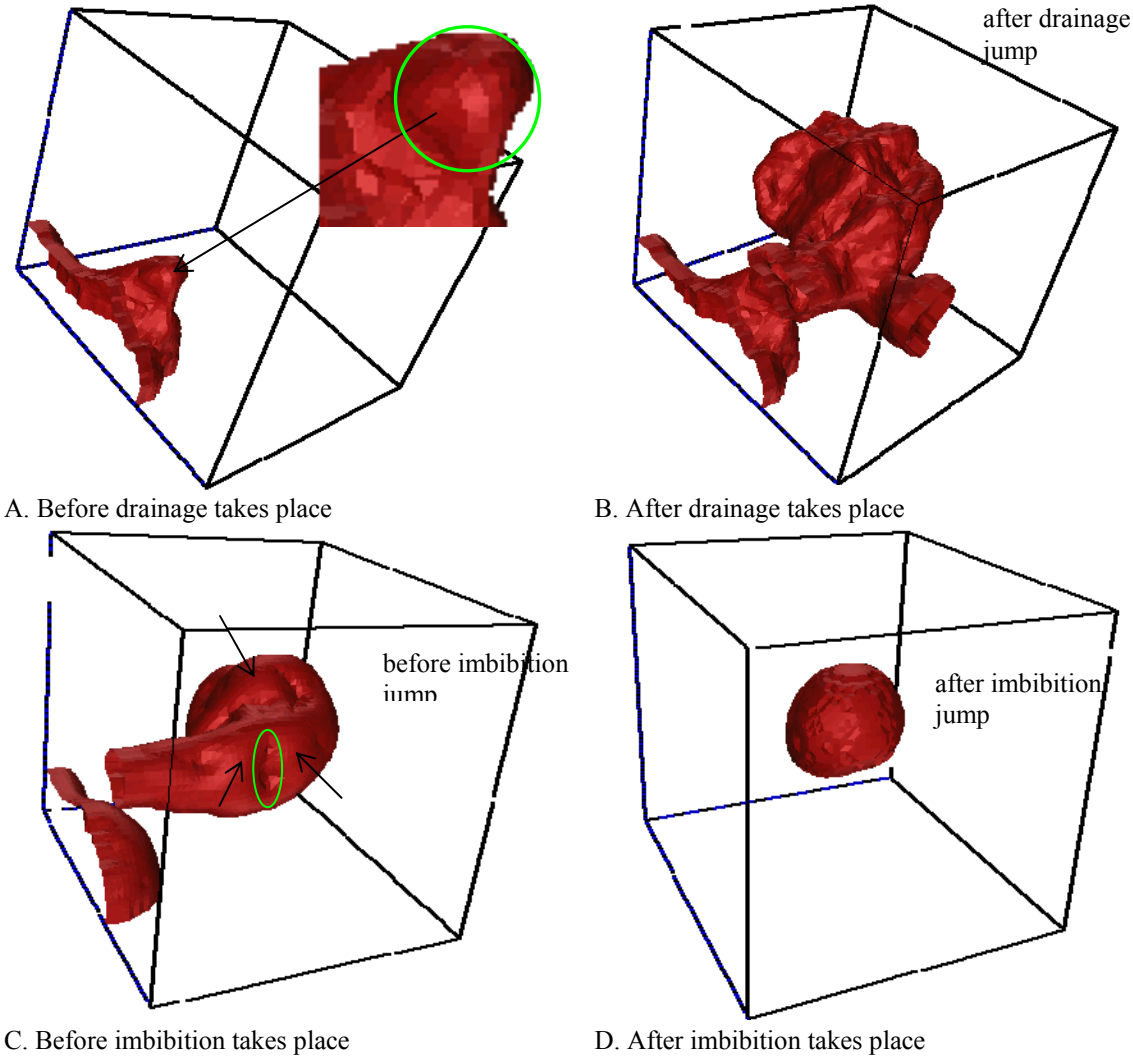

Figure 3.5: The fluid interface in a single pore before and after the drainage and imbibition events. The fluid/fluid menisci are from the LSMPQS simulation based on the Fontainebleau sample. For drainage, we only show the meniscus in a single throat; and for imbibition, the meniscus in a single pore is shown. For drainage (the first row). The surface of the throat or pore is not shown for a better visualization. The green circle indicates the interface configuration in the throat before the drainage takes place. Imbibition (the second row) shows a similar behavior. Although local spherical shape is observed at several locations (black arrows), it is not appropriate

Based on the above analysis, even though the locally spherical menisci exist in the real rock, we probably cannot directly extend the idea of 'inscribed sphere' to develop the drainage and imbibition criteria for the real rock. To confirm this argument, we still use Mason and Mellor drainage criterion and C_1 imbibition criterion for the drainage and imbibition simulations (both of which use the inscribed sphere). The comparison with LSMPQS (not shown here) confirms that due to the irregular and asymmetric shapes of the throats and pores, we often obtain a very small inscribed sphere, and therefore much larger critical curvatures for drainage and imbibition. The simulation based on these critical curvatures gives a much higher percolation threshold than LSMPQS, for both drainage and imbibition.

Another attempt to develop the new drainage and imbibition criteria is based on the area of the throat (A_{thr}) for drainage, and the volume of the pore (V) for imbibition. The effective radii for pores and throats are defined by the following equations.

$$r_{thr\_eff} = \sqrt{A_{thr} / \pi} \tag{3.1}$$

$$r_{pore\_eff} = \sqrt[3]{\frac{3V}{4\pi}} \tag{3.2}$$

where r_{thr_eff} is the effective radius of the throat and r_{pore_eff} is the effective radius of the pore. Then the critical curvatures for drainage and imbibition are computed as follows.

$$C_{drainage} = 2 / r_{thr\_eff} \tag{3.3}$$

$$C_{imbibition} = 2 / r_{pore\_eff} \tag{3.4}$$

This new approach assumes the spherical shape of pores and the circular shape of throat cross sections, whose sizes are defined by r_{thr_eff} and r_{pore_eff}, respectively. Compared to the results by LSMPQS (not shown here), this approach significantly underestimates the percolation threshold for drainage and imbibition. This is because the assumption of spherical-shaped pores or throats gives the minimum aspect ratio (1:1) and also no corners, and thus the lowest drainage and imbibition critical curvatures. In the

real geometry, however, the local narrow restrictions require more energy for nonwetting phase displacing wetting phase (thus higher drainage critical curvature), and less energy for the opposite displacement (thus higher imbibition critical curvature).

Our last attempt to develop the drainage and imbibition criteria involves the perimeter (P) and area (A_{thr}) of the throat, and surface area (A_{pore}) and volume (V) of the pore. For drainage, we propose the following criterion for the critical curvature:

$$C_{drainage} = \frac{P}{A_{thr}} \tag{3.5}$$

3DMA-rock calculates the perimeter and area by counting the number of voxels forming the throat. For a circular throat with the radius of r', the perimeter and throat area can be written as $P = 2\pi r'$ and $A_{throat} = \pi r'^2$, Equation (3.5) therefore reduces to $C_{drainage} = 2/r'$, which is the Haines criterion (Haines, 1930). This shows that equation (3.5) gives the correct prediction for a simple geometry. Moreover, it indicates equation (3.5) still uses the concept that an equivalent sphere can be used to 'fit' the fluid/fluid meniscus at the drainage critical moment, although in this case the 'equivalent sphere' is more of an abstract identity, defined by some effective radius. And the final critical curvature is calculated by using the effective radius of the equivalent sphere.

The geometry information is contained in both P and A_{thr}, and therefore $C_{drainage}$ by equation (3.5) reflects the irregularity of the geometry. For instance, the analytical solution for the drainage critical curvature in a slit (width d and length L, $d << L$) gives $C_{drainage} = 2/d$, while equation (3.5) yields $C_{drainage} = 2(L+d)/(Ld)$, which boils down to the analytical solution by imposing the condition $d << L$. We refer to this new drainage criterion as ERdrainage criterion, an abbreviation of Effective Radius drainage criterion.

We propose *a priori* imbibition criterion for real rock,

$$C_{imbibition} = \frac{2A_{pore}}{3V} \tag{3.6}$$

where A_{pore} and V are the internal area and the volume of a pore, respectively. Similarly, those values are obtained by counting the voxels in the individual pores. For a spherical pore with the radius of r'', we can rewrite A_{pore} and V as $A_{pore} = 4\pi r''^2$ and $V = 4/3\pi r''^3$, and thus by applying equation (3.6) we obtain $C_{imbibition} = 2/r''$, which is also the Haines criterion. Similar to ERdrainage criterion, this new imbibition criterion is still based on the concept of equivalent sphere, but in this case, of the pore. The critical curvature is also a simple function of the radius of the equivalent sphere. For other complex shapes, equation (3.6) is capable of estimating the critical imbibition curvatures robustly. This new imbibition criterion is referred to as ERimbibition criterion, an abbreviation of Effective Radius imbibition criterion.

Similar to C_1 criterion for the model sediments, ERimbibition criterion also predicts only one imbibition curvature of a pore. Although multiple imbibition curvatures are available due to different fluid configurations, we hope that ERimbibition criterion predicts the most probable imbibition curvature in the pore, and therefore can correctly capture the imbibition events. By using this *a priori* criterion, no interface locations are computed, which are necessary for other criteria (e.g., the one proposed by (Jerauld and Salter, 1990; Gladkikh and Bryant, 2005)) but also time-consuming. This criterion would effectively reduce the computational time but still yield reasonable results.

Equation (3.5) and (3.6) give *a priori* estimates of the critical curvature for drainage and imbibition, respectively. Since the effective radius for a throat is usually smaller than the effective radius of a pore, the critical curvature for drainage becomes greater than that for imbibition. Therefore, the capillary hysteresis is well preserved by using the new criteria. In the following sections, we test the correctness of the network model along with these criteria by comparing the results with LSMPQS.

We now can generalize the criteria used for both model sediments and real rocks. Criteria developed for both porous media are based on the concept of equivalent spheres. That is, an equivalent sphere can be used to represent the shape of menisci at the critical moments of either drainage or imbibition. On one hand, for the model sediment with narrow width of grain size distribution, this equivalent sphere becomes the inscribed sphere of the pore or throat, due to the symmetric and smooth geometry, which enables the development of the criteria by using the inscribed spheres. The inscribed sphere, however, might not be a good representation when the geometry symmetry is damaged, for example, in a sphere packing with wider grain size distribution. On the other hand, the void space in the real rock does not hold symmetric geometry, and also the angular grains restrict the development of an entire spherical meniscus inside pore or throat. Only isolated locally spherical shape exists. In this case, the equivalent sphere is an abstract identity, whose size is determined by both of the throat perimeter and cross-section area, if for the throat; or by both of the pore surface area and volume, if for the pore. Equations (3.5) and (3.6) are developed based on this idea.

3.4 RESULTS AND DISCUSSION

Each of three rock samples contains the same voxels (256 by 256 by 256), but has different resolutions. Thus the physical size of the Berea sample is twice as much as the Fontainebleau sample. The network generated from the Berea sample contains more pores and throats than the other two samples. We use several different settings of simulation in RRNM (Real Rock Network Model) than in fPRNM and iPRNM (finite and infinite acting Physically Representative Network Model).

First, the trapping mechanism for drainage is not well captured in RRNM drainage. RRNM uses simple geometry (spheres and cylinders) to represent both pores and throats. The trapped phase at the corners of narrow spaces (one example is pendular ring) cannot be properly estimated. This prevents us from getting the correct irreducible wetting phase saturation at the drainage endpoint. On the other hand, fPRNM (as well as iPRNM) is an advanced and more complete model, which is capable of computing the configuration of fluids in the actual porous medium, not just in the network. The volume of the trapped wetting phase can be estimated by using the analytical solutions. For example, we can solve for the system of nonlinear equations to gain the volume of pendular rings.

Without the proper estimation of the nonwetting phase at the corners, wetting phase connectivity is altered in RRNM. RRNM inevitably predicts more trapping than LSMPQS, which can automatically capture the correct wetting phase connectivity. A simple and yet effective way to solve the conflict is to turn off the trapping in both simulations. This gives different consequences in RRNM and LSMPQS: In RRNM, if drainage continues to the endpoint, no pores will be trapped and the wetting phase saturation drops to zero. However in LSMPQS, turning off the trapping only means that

no pores are allowed to be trapped. Wetting phase can still be trapped in the corners of pores and throats (Figure 3.6). This type of wetting phase only contributes to a small saturation.

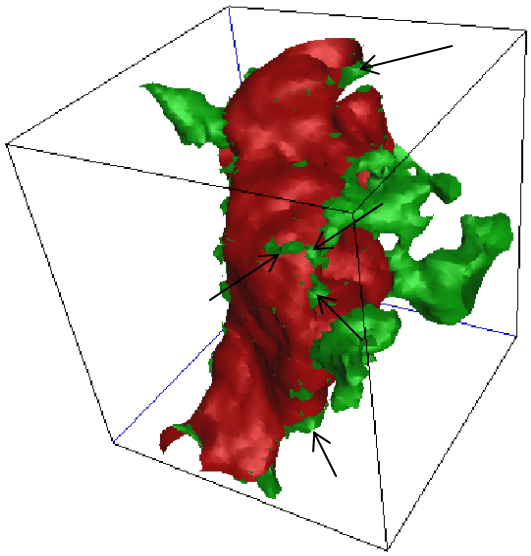

Figure 3.6: Wetting (green) and nonwetting (red) phases coexist in a pore. The arrows indicate some of the wetting patches that are trapped in the corners.

Second, it is a natural choice to start imbibition from the trapped wetting phase at the drainage endpoint. By doing this we are able to match the saturations of imbibition startpoint and drainage endpoint. However in RRNM this choice is problematic: as suggested previously, we turned off the option for wetting trapping in the network modeling for drainage. We have to use the pores that are not yet drained in RRNM to be the imbibition source. As we set the drainage curvature for RRNM the same as LSMPQS (LSMPQS simulation determines the range of applied curvature), in RRNM there are still pores filled by wetting phase at the drainage endpoint, which can be drained at very high curvatures beyond the available curvatures. These pores are our candidates to start imbibition. In order to maintain the sharp percolation, we randomly choose several of

these pores as the source pores. This treatment only allows imbibition happen from the selected pores in RRNM.

LSMPQS simulation checks the movement of fluid-fluid interface in the entire porous medium. It is impossible to constrain the movement in the selected pores. This becomes the reason for the different imbibition initial conditions between LSMPQS and RRNM. Such difference also contributes to the final discrepancy in the imbibition endpoint.

In imbibition, both simulations capture the major trapping mechanism: pores containing nonwetting phase are trapped when disconnected from the continuous clusters attaching to the exit faces or pores. LSMPQS also accounts for the menisci snap-off, another mechanism for trapping towards the end of imbibition. The different mechanisms also yield different trappings and imbibition endpoint.

RRNM and fPRNM share the similarities in other aspects. For example, one face of the model is treated as the entry face and the opposite one as the exit face in drainage, with the other faces sealed. Imbibition starts from drainage endpoint without entry face specified, the entry and exit faces in drainage are turned into exit faces in imbibition. We also consider capillarity-dominated processes, where quasi-static models are used, etc.

We still use results from LSMPQS simulation to check the correctness of RRNM. Few experimental data for drainage and imbibition curves are available (Bourbie and Zinszner, 1985) for only the Fontainebleau sandstone with the similar porosity, but not the pore-by-pore comparison data. However, with the reasonable agreement between LSMPQS and the experimental data from both single pores and fractures (Figure 2.3), the reliability of this technique is well accepted and its results can be the benchmark for the drainage and imbibition events.

3.4.1 Fontainebleau sandstone sample

Figure 3.7 shows the applied curvature and saturation relationships for Fontainebleau sandstone sample. The applied curvatures on the *y* axis, unlike those in Chapter 2, are dimensional in this figure and rest of this chapter, because all the samples we use have a physical size (Figure 3.1). The applied curvature reflects the sizes of pore and throat. For example at the drainage percolation the applied curvature is 0.13 μm^{-1}, which from equation (3.5) gives an equivalent throat radius of 15 μm. The percolation for imbibition happens at 0.075 μm^{-1}, and thus gives an equivalent pore radius of 27 μm.

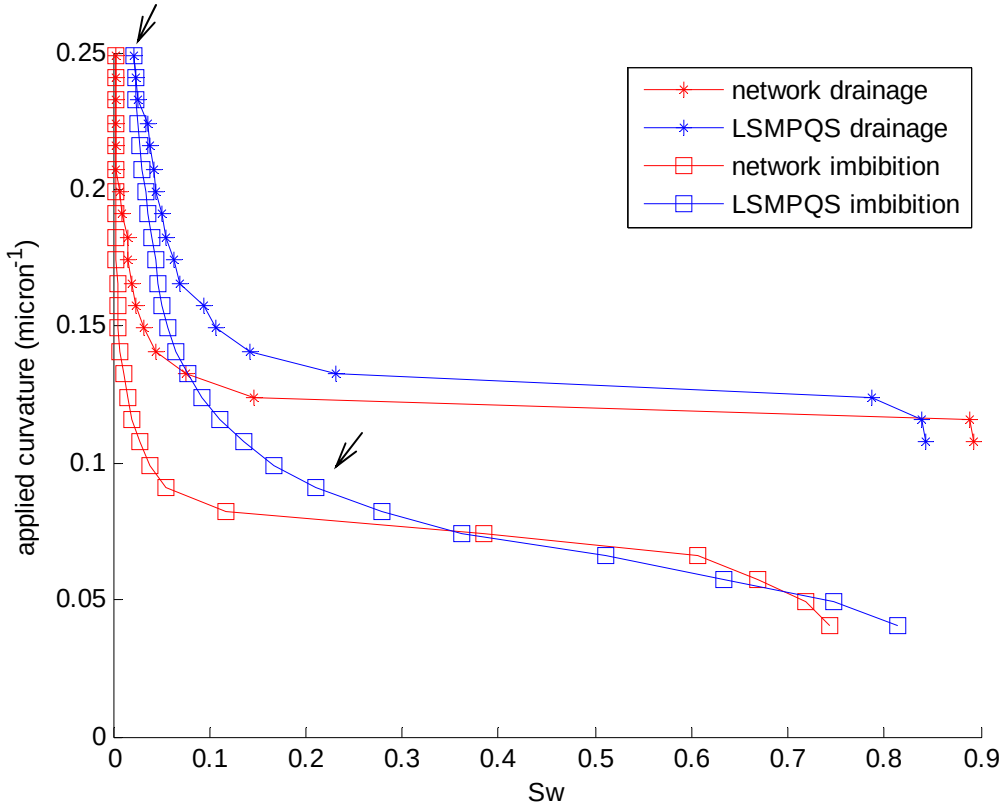

Figure 3.7: Drainage and imbibition curves for a sample of Fontainebleau sandstone. Porosity: 19.3%. RRNM and LSMPQS results are compared. Both simulations use the same drainage and imbibition curvature steps (from LSMPQS simulation).

The applied curvature for drainage starts from 0.12 μm^{-1}, below which no pores are drained. With trapping option turned off, the saturation in RRNM for drainage reaches almost zero at drainage endpoint (the reason for not being zero is that the applied curvature is not high enough to drain the remaining several small pores). The irreducible wetting phase saturation (S_{wirr}) from the LSMPQS simulation gives about 3%, which is all due to the trapped wetting phase in the corners of grain surfaces.

In drainage, the percolations for both simulations happen at the similar curvature, with ERdrainage criterion slightly underestimating the critical curvature by LSMPQS simulation. It indicates that the new drainage criterion, which features the concept of effective radius, is capable of reasonably predicting the drainage events. A difference towards the end of drainage (S_w = 0.1 ~ 0.2) between two simulations is observed, although there is no sign of large mismatch in the filling status of the pores (Figure 3.10A). This is the reflection of the rough estimate of the phase saturation in RRNM. We use a simple approach to compute the saturation in RRNM: the pore is always totally filled by wetting or nonwetting phase, and the partial filling, that is, a pore is filled by wetting and nonwetting simultaneously, is not allowed. LSMPQS simulation suggests that partial filling is commonly observed towards the end of drainage (Figure 3.6), and the volume of wetting and nonwetting phases can also be computed by counting the voxels. The difference is minimized at drainage endpoint as all pores have been drained in both simulations. The only trapped wetting phase in LSMPQS exists in the space constrictions of the porous medium. It should also be noted that in fPRNM and iPRNM (models used in chapter 2), the volume of pendular rings (the only configuration of trapped wetting phase besides the blobs in the pore) can be estimated. This gives a more accurate prediction of saturation than RRNM, and thus we obtain a better agreement as shown in Chapter 2.

Imbibition starts from the drainage endpoint. Before the percolation, the difference between two simulations increases as the applied curvature decreases. Before the percolation, the major imbibition event in LSMPQS is the slow expansion of trapped wetting phase, while the Melrose jump rarely occurs. A comparison of two steps at the beginning of LSMPQS simulation (Figure 3.8) clearly indicates that the slow expansion, rather than the Melrose jump, is the major contributor that changes the saturation before the percolation in Figure 3.7. As RRNM neglects this phenomenon, the wetting saturation from RRNM is therefore lower than LSMPQS.

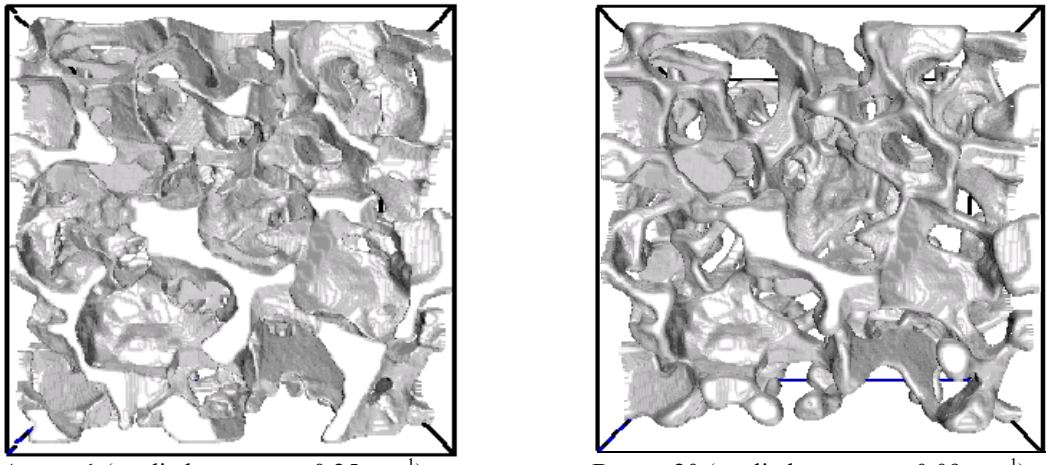

A. step 1 (applied curvature: 0.25 μm^{-1})

B. step 20 (applied curvature: 0.09 μm^{-1})

Figure 3.8: A comparison of the fluid/fluid interface at steps 1 and 20 (each is indicated by the arrows in Figure 3.7) of imbibition simulation by LSMPQS. The Melrose jump corresponds to the invasion of wetting phase in one or several pores, therefore results in a sudden, large variation of the fluid-fluid interface. On the other hand, the slow expansion of interface is a continuous and smooth change. Between step 1 and 20 although the applied curvature drops from 0.25 to 0.09 μm^{-1}, the imbibition events are dominated by the slow expansion of trapped wetting phase.

The imbibition percolation happens at the same curvature for both simulations. This shows that our new imbibition criterion (ERimbibition criterion) predicts the correct

imbibition events when Melrose jumps take place. The mismatch of the data points during the percolation (Figure 3.10B) suggests a slight shift of the percolation for two simulations, although the imbibition sequences are essentially similar. About 7% residual nonwetting phase saturation (S_{nwr}) difference is observed at imbibition endpoint, with the value of RRNM lower than LSMPQS. This is the consequence of two possible causes: first, ERimbibition does not capture the correct trapping mechanism. Second, even for the correct trapping, RRNM does not compute the partial saturation in a single pore (as shown in Figure 3.9), but treats it as fully saturated by either of the fluids. This also yields the incorrect saturation in RRNM.

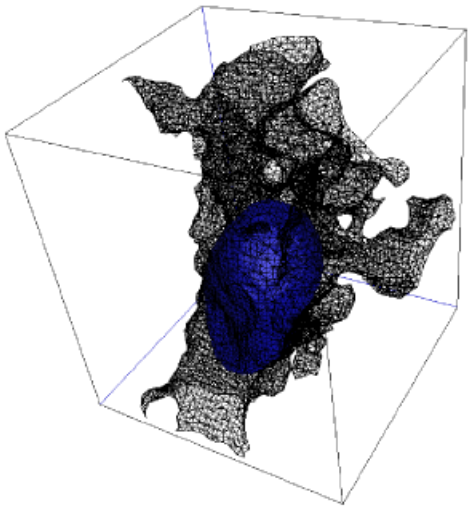

Figure 3.9: A nonwetting phase blob (blue surface) is trapped in a pore (black mesh). The pore was obtained from the Fontainebleau sandstone sample. The blob only occupies the center of the pore, where the major part (mostly narrow regions) is filled by wetting phase (not shown in the figure).

Because of the latter reason, saturation is not a reliable parameter for the comparison. The microscopic pore-by-pore comparison is therefore employed to show whether the individual pores of two simulations have the same filling status. This helps

us obtain a better understanding of the drainage and imbibition sequences happening in these pores.

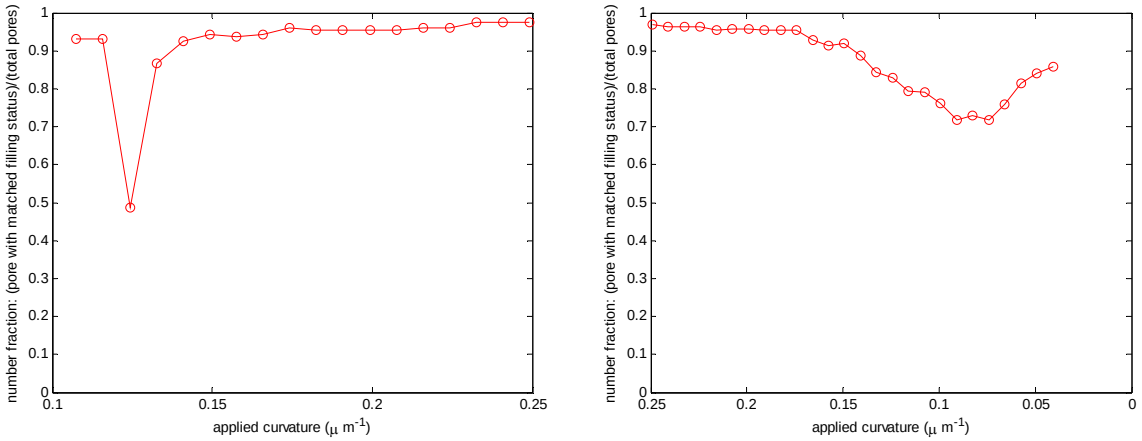

A. Drainage B. Imbibition

Figure 3.10: The filling status for drainage and imbibition of the Fontainebleau sandstone sample. The *x* axis is the drainage and imbibition applied curvatures, and the *y* axis is the fraction of the number of pores having the same filling status in both simulations compared with the total number of pores. Fraction = 1 means in both simulations the filling status of individual pores are identical, while fraction = 0 means none of the pores have the same filling status in both simulations. We use the same method as in Chapter 2 to determine filling status.

Figure 3.10 gives the filling status fraction for both drainage and imbibition. Very few drainage events, due to isolated invasions into the pores, happen at the first two steps. The 3rd step corresponds to the percolation threshold, where the Haines jump occurs all over the sample. The fraction drops from the 92% to 50%. RRNM by applying ERdrainage criterion drains more pores in the entire rock sample, while the percolation in LSMPQS simulation has not yet started (Figure 3.11A). The low fraction only stays for one step. It returns to 88% in the following step (step 4), showing that LSMPQS percolation occurs in the pores that are only drained by RRNM in step 3 (Figure 3.11B).

The fraction keeps improving for the rest of drainage, and the value is above 95% at the drainage endpoint.

The applied curvatures in Figure 3.10B decrease from left to right. The fraction for imbibition inherits from the drainage endpoint (95%). This value maintains above 88% until the applied curvature decreases to the percolation threshold (0.11 μm^{-1}). Between curvature = 0.05 and 0.11 μm^{-1} (percolation), the fraction reduces to 70%, the lowest value of the entire imbibition simulation. The filling status comparison later improves as decreasing the applied curvatures. At the end of imbibition, the fraction returns to 86%. This is 14% mismatch in filling status, but only corresponds to about 7% difference in saturation (Figure 3.7). Such observation further indicates that the rudimentary saturation calculation in RRNM still needs improvement. Moreover, it also suggests that ERimbibition criterion does not yield the same trapped pores as LSMPQS. The different startpoints of two simulations might contribute to the different trapped pores. The similar behavior is also observed in the comparison between fPRNM and LSMPQS (Figure 2.15), where a 15% mismatch in pore filling status is observed at imbibition endpoint.

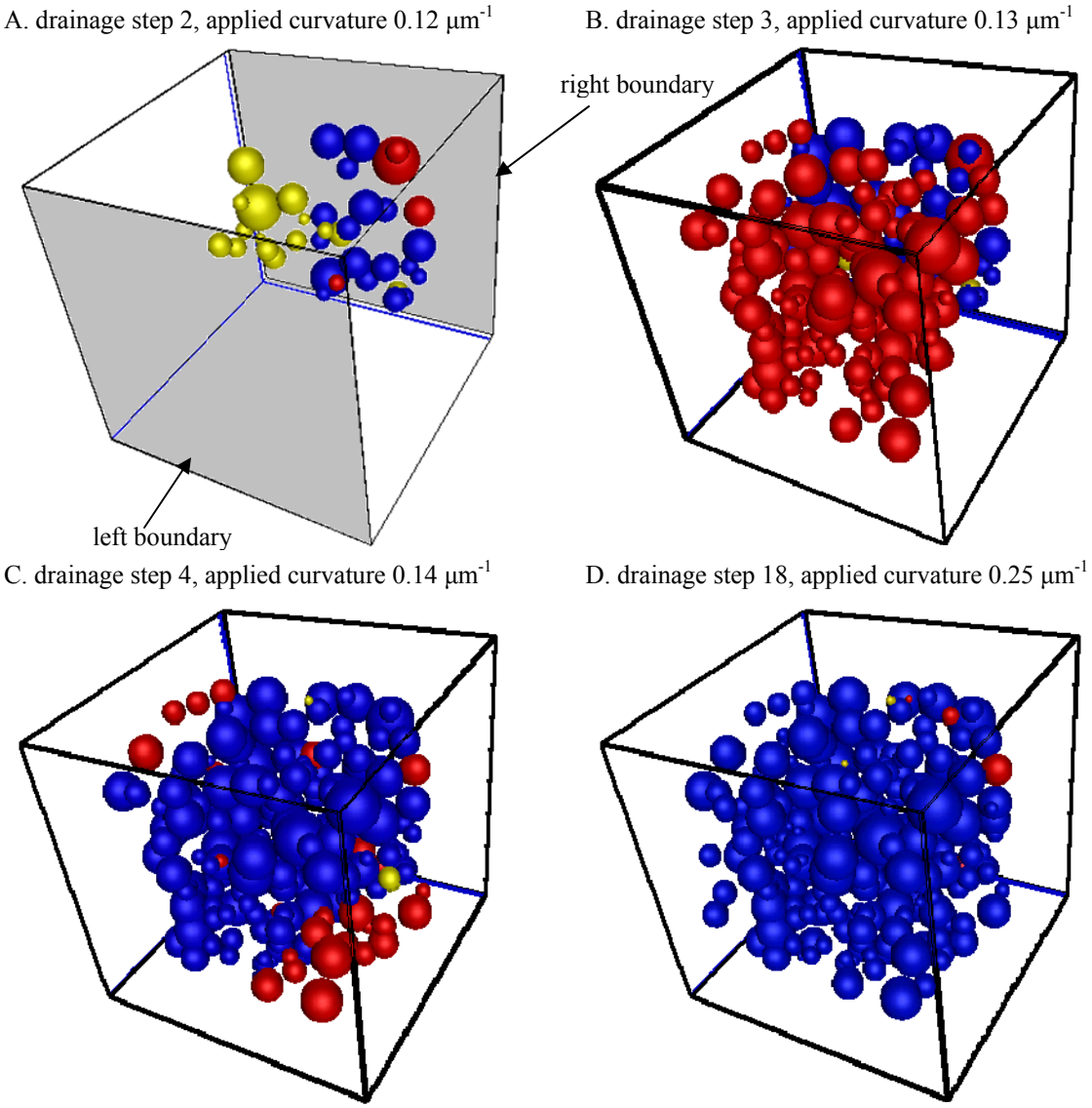

Figure 3.11: The filling status comparison between RRNM and LSMPQS for drainage, Fontainebleau sandstone sample. The right face (right boundary) is set to be the entry face for LSMPQS. 7 pores are randomly chosen as the entry pore for RRNM to maintain the sharp percolation. The left face (left boundary) is the exit face for both simulations. Only the pores filled by nonwetting phase are shown in spheres of different colors. Blue spheres: pores drained in both simulations. Red spheres: pores are drained only by RRNM, but not LSMPQS. Yellow spheres: pores are drained only LSMPQS, but not RRNM.

Figure 3.11 shows the 3D visualization of the filling status during drainage simulation. Only the pores filled by wetting phase are shown. The locations of spheres represent the center of individual pores, while the pore sizes indicate the pore volume. 4 representative steps are chosen for the demonstration. Figure 3.11A shows the step (curvature = 0.12 μm^{-1}, step 3) before percolation threshold takes place. All of the spheres concentrate at the entry phase, showing that the invasion has not reached to the center of the porous medium. Besides the blue spheres, we also observe the similar amount of yellow spheres, which are the pores only drained by LSMPQS. The reason for such mismatch at the beginning of simulation is due to the different initial conditions. For LSMPQS, the entire boundary is treated as the entry face, and therefore nonwetting fluid initially already fills up the pores at to the entry face. On the other hand, only several pores are randomly chosen to be the entry pores at the entry face in network modeling. Consequently, more pores are filled by nonwetting phase before the percolation in LSMPQS than network modeling. The mismatched pores only contribute to a 7% of the total amount of pores, shown in Figure 3.10A.

The red spheres (meaning pores only drained by network modeling) dominate the domain at step 4, lowering the agreement fraction to less than 50% (Figure 3.10). The yellow spheres from last step are also drained by network modeling. Pores drained by both simulations still concentrate close the entry face, showing that the percolation for LSMPQS has not yet started at this step. The comparison shows that ERdrainage criterion predicts a lower critical curvature for the throat than LSMPQS. Curvature = 0.13 μm^{-1} (step 4) is greater than most of the critical curvatures by ERdrainage criterion, and thus leads to the percolation. But this value is lower than the critical curvature by LSMPQS.

At step 4, most of those red spheres turn into blue. The drainage events in LSMPQS catch up with RRNM in a similar drainage footprint, that is, both simulations

drain in the same sequence of pores but at slightly different curvatures. With most of the pores having the same filling status, the fraction also returns to 85% in Figure 3.10. However, red spheres still exist, especially close to the boundary. Such mismatch explains the remaining 15% of pores that are only drained by the network modeling. For the rest of drainage steps, the fraction slowly increases with the applied curvatures. At the last step (step 18), 98% of the pores have the same filling status in both simulations. The blue spheres dominate the domain and only a few red spheres can be seen in Figure 3.11D.

Based on the simulation settings, it is not surprising to see few yellow spheres at the drainage endpoint. Since the RRNM drainage uses the applied curvature from LSMPQS so that two simulation results can be compared step by step, it is possible that a few pores in RRNM simulation are not yet drained at the last applied curvature. As we do not consider trapping, those pores will be drained in a much higher applied curvature, which is beyond our interests and out of the scope of the applied curvatures we use.

The red spheres (meaning pores are only drained by RRNM but not LSMPQS) suggest some wetting phase is trapped in LSMPQS. This observation does not agree with our setting that no pores are allowed to be trapped in LSMPQS. Figure 3.12 shows several trapped wetting blobs at the drainage endpoint. These blobs are attaching to the sealed boundaries, which, along with the nearby grains, provide the narrow spaces to trap the wetting phase. Some of the trapped fluid extends to the center of the pores, a situation that satisfies our criterion for pore filling: a pore is considered to be filled once the center of the pore is filled by that phase. Consequently, pores close to the sealed boundaries are possibly to be considered as the ‘trapped pores’ although the pore-trapping option is turned off in the simulation.

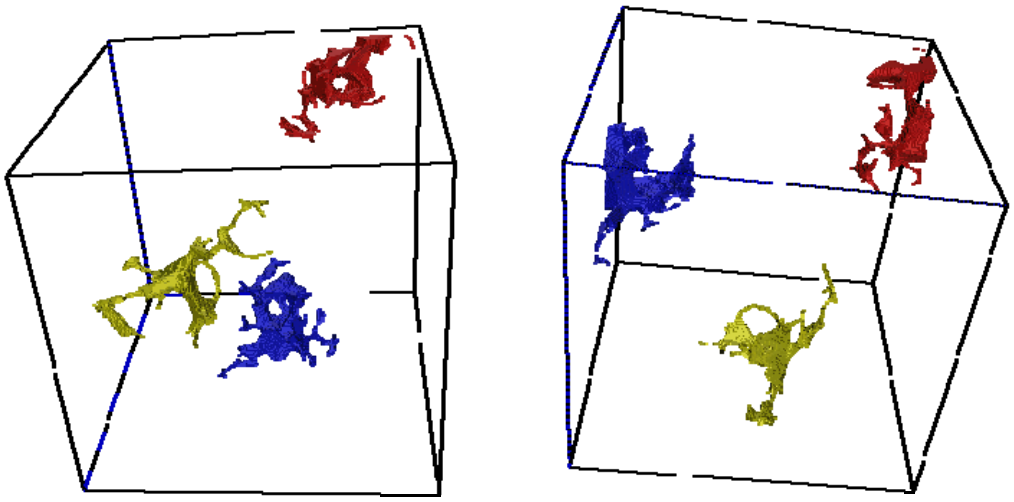

Figure 3.12: Several trapped blobs at drainage endpoints of LSMPQS, viewed from two different angles. Different blobs are demonstrated by using different colors. These colors are only for demonstration and are irrelevant to the colors used in the pore-by-pore comparison. The wetting blobs are all close to the sealed boundaries. The wetting phase attaches to the surface of the grains, and extend to the center of the pore.

For LSMPQS, all the trapped wetting phase is the source for imbibition, while for RRNM imbibition we only start from several source pores to maintain a sharp percolation. These pores are selected from the pores that are not yet drained at the drainage endpoint. The different treatments of the imbibition startpoint accumulate during the imbibition and inevitably affect the results. Figure 3.13 shows the pore-by-pore comparison of different imbibition steps. Figure 3.13A and B are two intermediate steps during the imbibition percolation. With the curvature decreasing from A to B, not much discrepancy is observed in the pore filling status. Most of the pores are still filled by nonwetting phase in both simulations. Yellow spheres emerge in the porous medium, showing that RRNM imbibes at a higher curvature than LSMPQS. At the step where the lowest fraction is achieved (Figure 3.13C), a noticeable amount of yellow spheres are observed, while few red sphere are present. This is a further proof that LSMPQS

imbibition follows the path of network modeling (otherwise comparable amount of red and yellow spheres will emerge), but imbibes at a lower applied curvature. In other words, ERimbibition criterion predicts a higher critical curvature than observed in LSMPQS. The lack of preferential direction during imbibition simulation yields the scatting yellow spheres all over the porous medium (drainage, however, has a preferential direction from the right boundary to the left).

A. imbibition step 13, applied curvature 0. 15 μm^{-1}

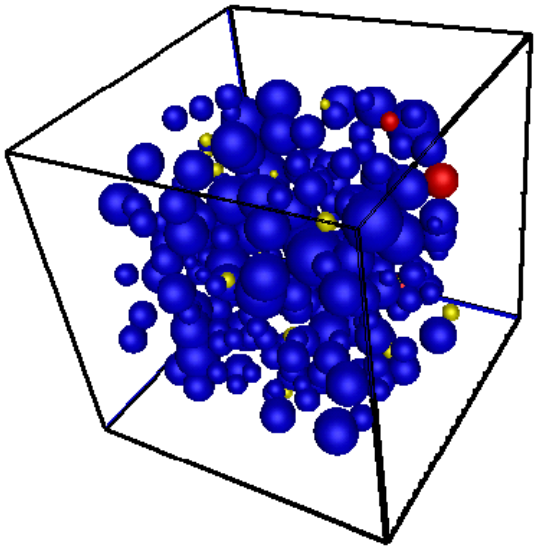

B. imbibition step 16, applied curvature 0. 12 μm^{-1}

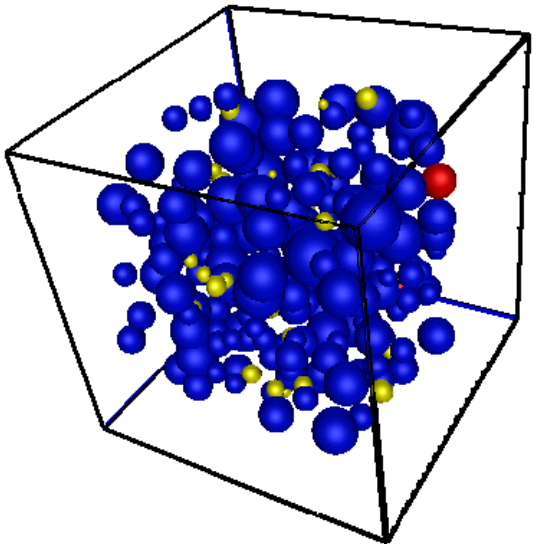

C. imbibition step 22, applied curvature 0. 07 μm^{-1}

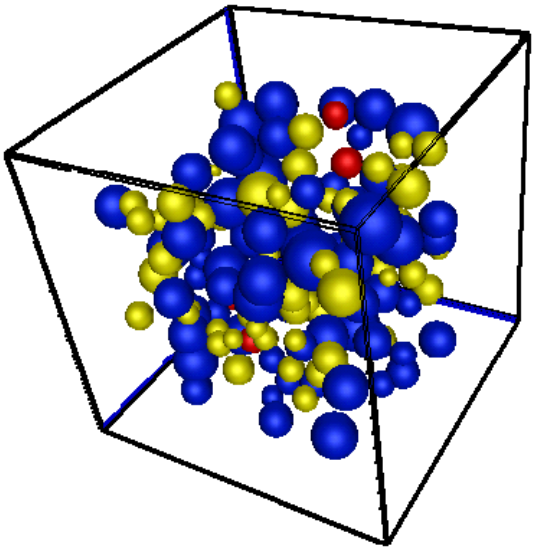

D. imbibition step 26, applied curvature 0. 04 μm^{-1}

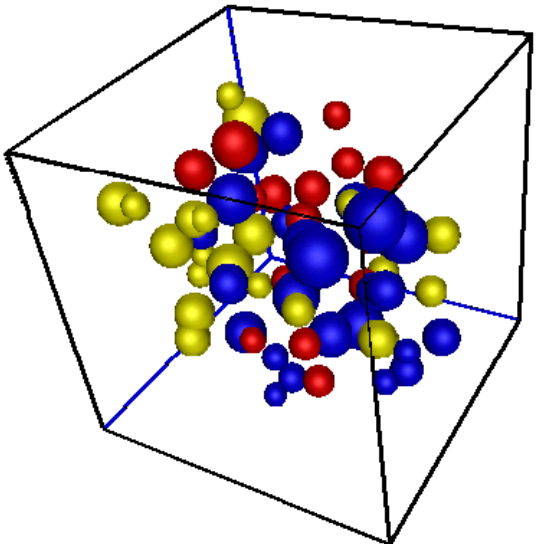

Figure 3.13: The filling status comparison between RRNM and LSMPQS for imbibition of a Fontainebleau sandstone sample. The boundary setup and the color scheme are the same as in Figure 3.11. Only the pores filled with nonwetting phase is shown.

The filling status of imbibition endpoint is shown in Figure 3.13D. The red and blue spheres combined give the pores filled by nonwetting phase in RRNM. This could possibly be trapped pores and pores that are not yet imbibed at the last step. The last applied curvature, from LSMPQS, is 0.04 μm^{-1}. It is possible that the remaining pores can be imbibed at a lower curvature, which is not available in the curvature list. Comparable amounts of yellow and red spheres are observed in Figure 3.13D, showing that RRNM and LSMPQS trap similar amount of pores, but with different identities. RRNM does not satisfactorily capture the correct trapping mechanism: a perfect match would yield pure blue dots. This criterion is an *a priori* estimate of the critical curvature and only one critical curvature is predicted for each pore. This criterion ignores the fact that the different meniscus configurations in the throats affect the occurrence of imbibition events (the Melrose criterion of merging menisci), and thus multiple critical curvatures are available. At an applied curvature, imbibition event could take place at another curvature other than predicted by ERimbibition criterion, which leads to the discrepancy eventually. Another possible cause is the snap-off events that might happen approaching the imbibition endpoint. The physics-driven interface movement in LSMPQS is capable of capturing this event, while RRNM lacks the details of interface and ignores this event.

3.4.2 Berea sandstone sample

We apply RRNM along with ERdrainage and ERimbibition criteria to predict drainage and imbibition events in a Berea sandstone sample, and compare the results with those from LSMPQS. This sample contains 550 pores, which doubles the size of the Fontainebleau sample (281 pores). Due to the lower resolution of the geometry, the

details of pores and throat might not be as well preserved as the Fontainebleau sandstone sample.

The simulation settings and procedures are similar to the previous case. Both drainage and imbibition are analyzed in terms of macroscopic curves and pore-by-pore comparisons. Figure 3.14 shows the relationship between saturations and applied curvatures for drainage and imbibition. Results from both simulations are compared. Before the percolation threshold, drainage occurs in a few, separated pores, which does not significantly vary the saturation. RRNM predicts a lower percolation threshold than LSMPQS: at the same applied curvature, more pores are drained in RRNM. The discrepancy of the two simulations continues to the drainage endpoint. RRNM drains almost all the pores at drainage endpoint, leaving behind a few small pores that can only be drained at higher curvatures. LSMPQS simulation obtains more irreducible wetting phase. As we do not allow for the wetting phase trapped in pores, the only explanation is that wetting phase is trapped at the constrictions of the geometry. A similar case can be found in the Fontainebleau sandstone sample, where irreducible wetting phase is trapped and attached at the narrow spaces close to the boundary (Figure 3.12).

Imbibition simulation starts from the drainage endpoint. Only a slight change of saturation is observed before the percolation threshold, which happens at about 0.1 μm^{-1}. The percolations have a better agreement in imbibition than in drainage, showing that ERimbibition criterion yields a more reasonable prediction of the critical curvatures. In imbibition, we do not observe significant difference during the early stage of percolation. However, two curves begin to deviate when S_w is greater than 36%. LSMPQS gives a residual saturation of 35% (1-65%), while network modeling predicts a much larger value 43%. There is about 10% difference of S_{nwr} for the two simulations. However, as pointed out in the Fontainebleau sandstone case, the saturation difference might be misleading

due to the different approaches we use for computation. And the only way to justify this is by the pore-by-pore comparison.

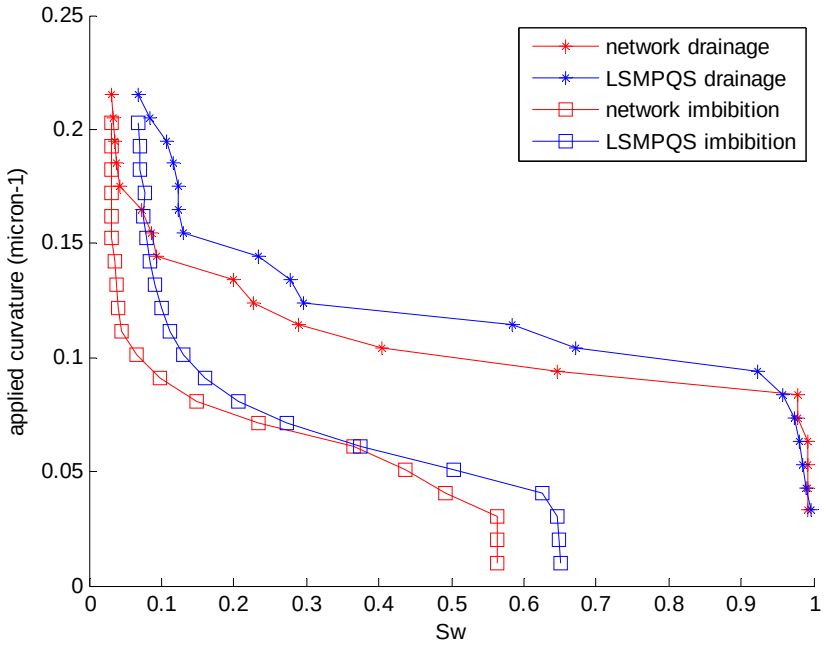

Figure 3.14: Drainage and imbibition curves for a sample of Berea sandstone. Porosity: 16.9%. RRNM and LSMPQS results are compared. Both simulations use the same drainage and imbibition curvature steps (from LSMPQS simulation).

Figure 3.15 shows the filling status comparison. The fraction in the *y* axis has the same meaning as the previous case: when fraction = 1, it means all the pores in the sample have the same filling status in both simulations; while fraction = 0 means none of the pores in two simulations match the filling status. For drainage, the percolation threshold starts at step 7, at which the corresponding fraction drops from the previous 97% to 80%. This decrement continues until reaching step 9, when the fraction has the lowest value 67%. It then slowly returns to higher values as drainage continues. At the drainage endpoint, the value returns to 90%, lower than that in the Fontainebleau sample.

Compared with the previous case, the fraction drops in a more gentle fashion in the Berea sandstone sample. This indicates that this Berea sandstone sample has a wider grain size distribution than the Fontainebleau sample, and therefore wider throat size and critical curvature distributions as well. Because of this, at the percolation threshold, the same decrement of the applied curvature (the step size of applied curvature is the same for two cases) only allows the invasion to the middle of the domain (Figure 3.16B), while for Fontainebleau case, this gives the drainage in the entire packing (Figure 3.11B).

At the first several steps of imbibition, fraction does not change with decreasing the applied curvature (Figure 3.15B). This observation confirms our conclusion that the early stage of imbibition only involves the slow expansion of the trapped wetting phase. The agreement begins to decline starting from 0.15 μm^{-1}. The decrement of the fraction is gentler compared to drainage: The agreement drops from 90% (step 6) to 73% (step 15) in 10 steps, where the lowest fraction is achieved. After that, the fraction slowly increases, and returns to 81% at the imbibition endpoint. Overall, the agreement between RRNM and LSMPQS for Berea sandstone sample is less satisfactory than the Fontainebleau sandstone case.

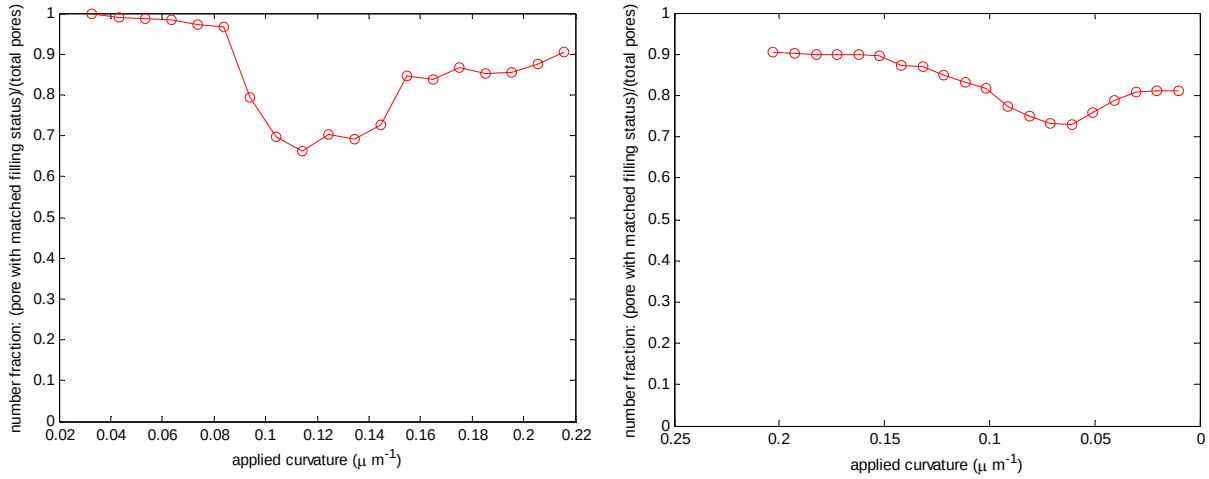

A. drainage B. imbibition

Figure 3.15: The filling status for drainage and imbibition of the Berea sandstone sample. The *x* axis is the drainage and imbibition applied curvatures, and the *y* axis is the fraction of the number of pores having the same filling status in both simulations compared with the total number of pores. Fraction = 1 means in both simulations the filling status of individual pores are identical, while fraction = 0 means none of the pores have the same filling status in both simulations. We use the same method as in Chapter 2 to determine filling status.

4 selected drainage steps are shown by using the pore-by-pore comparison technique (Figure 3.16). Figure 3.16A shows the filling status of one step before the percolation. Pores filled with nonwetting phase all concentrate close the right boundary (entry face). The mismatched pores (red and yellow) are due to the different treatments of the initial conditions. For LSMPQS the entire right boundary is treated as the entry face, and thus the pores attaching that boundary is filled by nonwetting phase in LSMPQS; in RRNM only several pores are filled with nonwetting phase initially to create a sharp percolation.

At the next step (step 7, Figure 3.16B) percolation threshold only happens in the network modeling, but not LSMPQS. Nonwetting phase percolates to the middle of the

packing in Network modeling (red spheres). However in LSMPQS, only a few more pores are drained from step 6 to 7, and all of them are still close the entry face. The limited number of pores with the same filling status concentrates close to the entry face as well. Compared to Figure 3.11B (percolation threshold for network modeling in Fontainebleau sandstone sample), the percolation at Figure 3.16B only drains the middle of the porous medium, where pores close to the other 5 boundaries are not yet touched. This shows the larger variation of the throat sizes in Berea than in Fontainebleau sample, and at the same step size only a small amount of pores can be drained in Berea case.

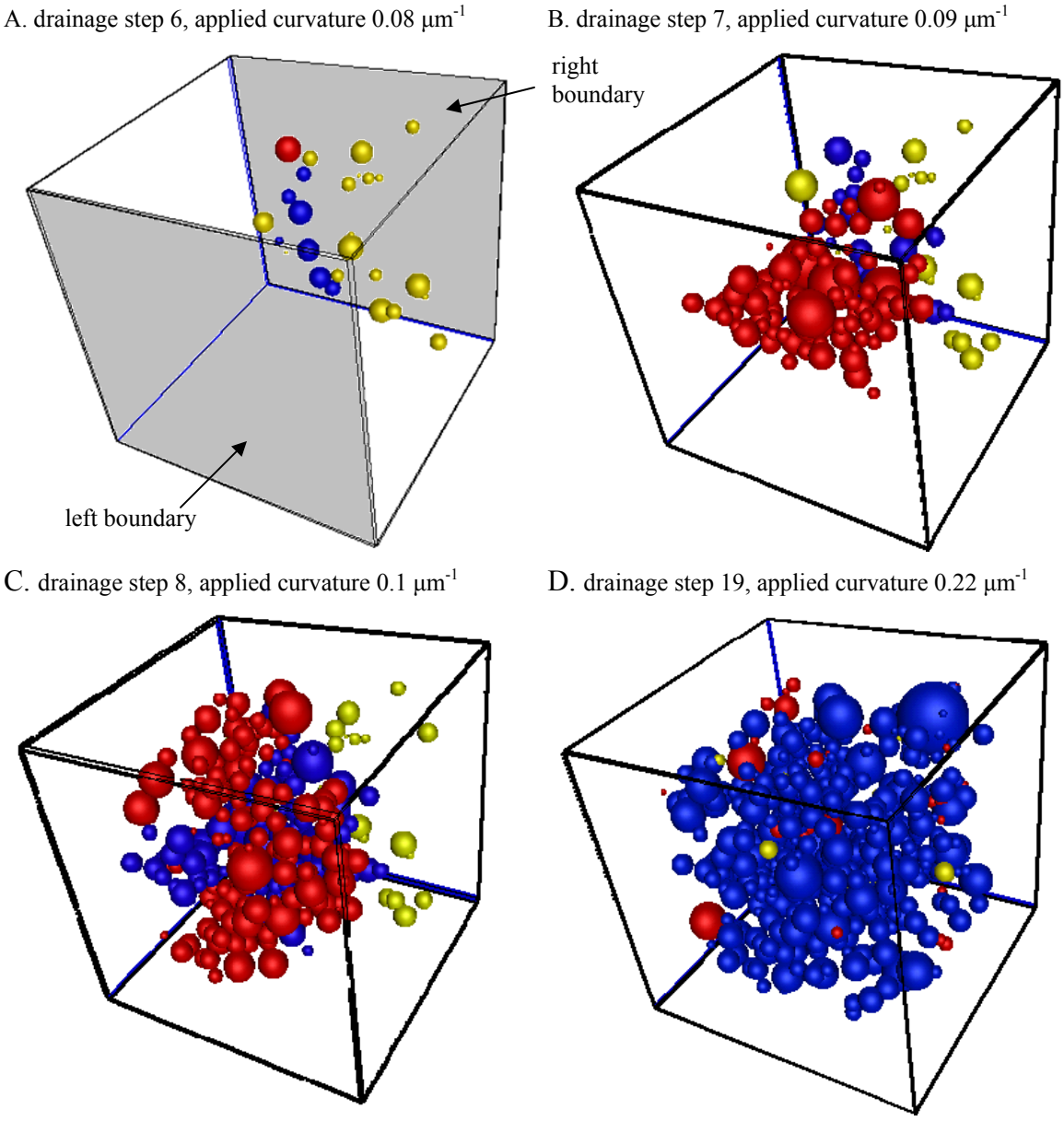

Figure 3.16: The filling status comparison between RRNM and LSMPQS for drainage, Berea sandstone sample. The boundary settings and the color scheme are the same as Figure 3.11. Only the pores filled with nonwetting phase is shown.

Most of the red spheres at step 7 (Figure 3.16B) turn into blue at step 8 (Figure 3.16C). This observation indicates that pores that are only drained in RRNM are drained

by LSMPQS at larger step. Since there are no new yellow spheres (pores drained only by LSMPQS) present in Figure 3.16C, we can also conclude that LSMPQS and RRNM drain the same sequence of pores, but at slightly different applied curvatures. At this step, we also observe lots of new red spheres expanding to the boundaries of the porous medium. It suggests ERdrainage criterion consistently predicts lower throat critical curvature than LSMPQS, so that at each applied curvature, more pores are drained in RRNM than LSMPQS. Most of these red spheres become blue at larger curvatures (Figure 3.16D), a further proof that ERdrainage criterion gives an reliable prediction of the drainage events in the pore level, with only a small underestimation o the values for all throats.

At the last step of drainage (step 19, Figure 3.16D) most of the pores share the same filling status, which are demonstrated by the blue spheres. These pores correspond to 90% of pores of the entire sample. Noticeable amount of red and yellow spheres are also observed. The presence of red spheres indicates the pores contain the trapped wetting phase in LSMPQS, most of which are small ones. The wetting phase inside is trapped in the narrow spaces and covers the geometric center of the corresponding pores. The yellows spheres (very few), on the other hand, are those pores not yet drained by RRNM at the maximum applied curvatures, rather than the trapped pores due to the disconnection from continuous clusters.

A. imbibition step 7, applied curvature 0.14 μm^{-1}

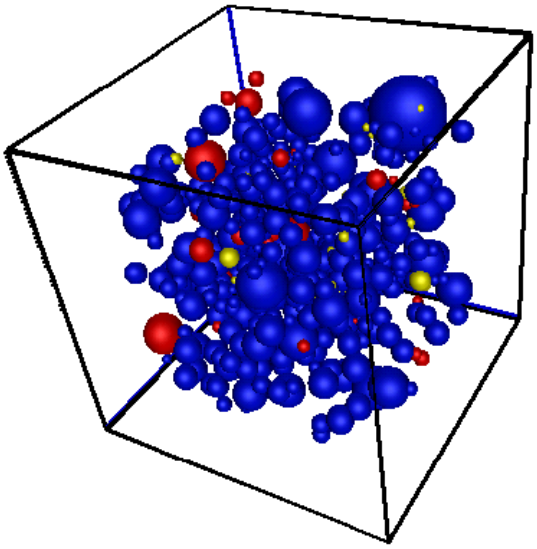

B. imbibition step 12, applied curvature 0.09 μm^{-1}

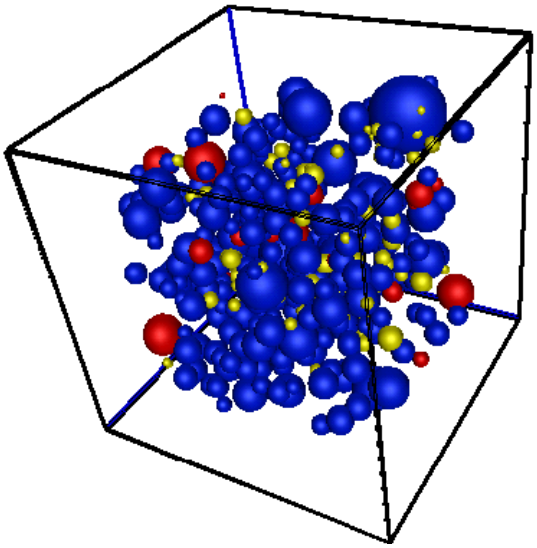

C. imbibition step 15, applied curvature 0.06 μm^{-1}

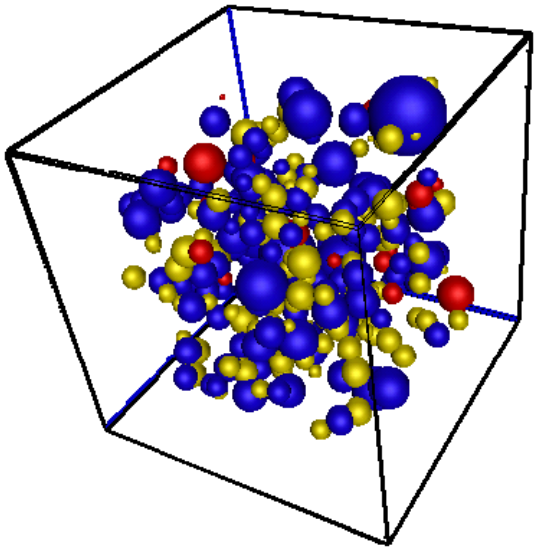

D. imbibition step 20, applied curvature 0.01 μm^{-1}

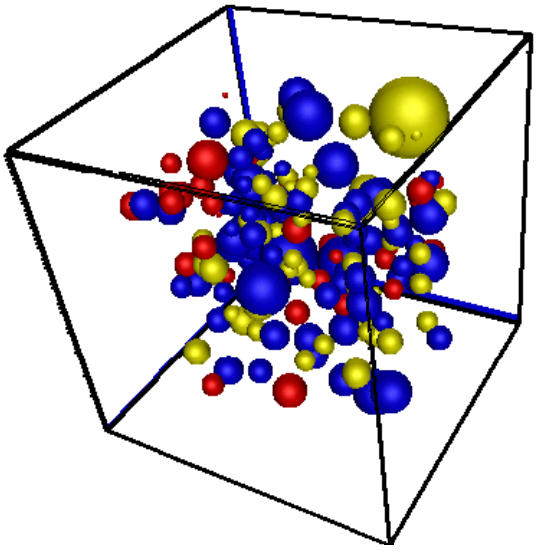

Figure 3.17: The filling status comparison between RRNM and LSMPQS for imbibition of a Berea sandstone sample. The boundary setup and the color scheme are the same as in Figure 3.11. Only the pores filled with nonwetting phase is shown.

The 3D pore-by-pore visualization for imbibition is shown in Figure 3.17 for some selected steps. Figure 3.17A shows the filling status of step 7 in imbibition, which is similar to the drainage endpoint (Figure 3.16D). Between step 1 and 7, the imbibition events happen in single and isolated pores, while the invasion of pore clusters never occurs. In fact, due to a relatively wide grain size distribution of this sample, imbibibition events take place in a gentle fashion. Step 12 (Figure 3.17B) is an intermediate step during the percolation. Compared to step 7, some blue spheres turn into yellow ones, and few red spheres disappear from the porous medium. The former observation shows RRNM imbibes more pores than LSMPQS between step 7 and 12, showing the imbibition events for both simulations happening at different applied curvatures.

The lowest fraction of agreement is obtained at step 15, where only 73% of the pores have the same filling status. Figure 3.17C shows the 3D visualization. A comparable amount of yellow spheres can be seen in the figure. This observation suggests that imbibition simulation from RRNM imbibed more pores than LSMPQS at the same applied curvature. However, the imbibition sequence is less tractable than drainage due to the lack of preferential directions. Therefore, whether or not LSMPQS follows the similar imbibition pathway as RRNM is difficult to determine. Nevertheless, some examples can still be found between step 15 and step 20 (the last step of imbibition, Figure 3.17D). A large number of yellow spheres disappear at the last step, showing that the same pores in LSMPQS are imbibed at lower applied curvature than RRNM.

Figure 3.17D is the filling status at the imbibition endpoint. Compared with Figure 3.17C, most of the yellow spheres close to the left and right boundaries (exit faces) disappear. Since the pores at the center of the porous medium are farther away from the boundary, trapping is more likely to happen: the trapped pores tend to stay in the center, away from the exit faces. LSMPQS seems to impose a stricter trapping criterion

(more yellow spheres than blue spheres present). One of the causes could be the snap-off events in LSMPQS, which trap the nonwetting phase in the pore center due to the coalescence of menisci in the pore throats (Prodanovic and Bryant, 2006). RRNM is incapable of capturing such mechanism, and thus leads to different sets of trapped pores. Moreover, as discussed in the Fontainebleau sandstone case, our ERimbibition criterion only predicts one number of imbibition critical curvatures of the pore, while in reality multiple numbers are possible because of the menisci configuration. These disadvantages of RRNM cause the filling status fraction (Figure 3.15C) to be 81%, which is still a reasonable number considering the fact of the simplifications we employ to develop RRNM.

3.4.3 Castlegate sandstone case

The geometry data for a Castlegate sandstone sample have the lowest resolution (5.6 microns/voxel). This sample has the most number of pores (1217 pores), compared with Fontainebleau sandstone case (281 pores) and Berea sandstone case (550 pores). The porosity of this sample is 19.8%, similar to the previous two cases.

Figure 3.18 shows a comparison of the capillary curves between RRNM and LSMPQS simulations. A satisfactory agreement can be observed. RRNM still predicts a lower percolation threshold than LSMPQS; however, the difference in this case is much smaller than the previous two. Moreover, we no longer observe large difference between the two simulations towards the drainage endpoint: almost the identical drainage endpoints are obtained. For imbibition, the initial saturation discrepancy enlarges when decreasing the applied curvature. When percolation threshold starts at curvature ≈ 0.08 μm^{-1}, the discrepancy quickly diminished, and the two imbibition curves converge. This

behavior also indicates that RRNM and LSMPQS have the same imbibition critical curvatures for the majority of the pores. The agreement continues until the end of imbibition, where about 3% S_{rwr} difference is present.

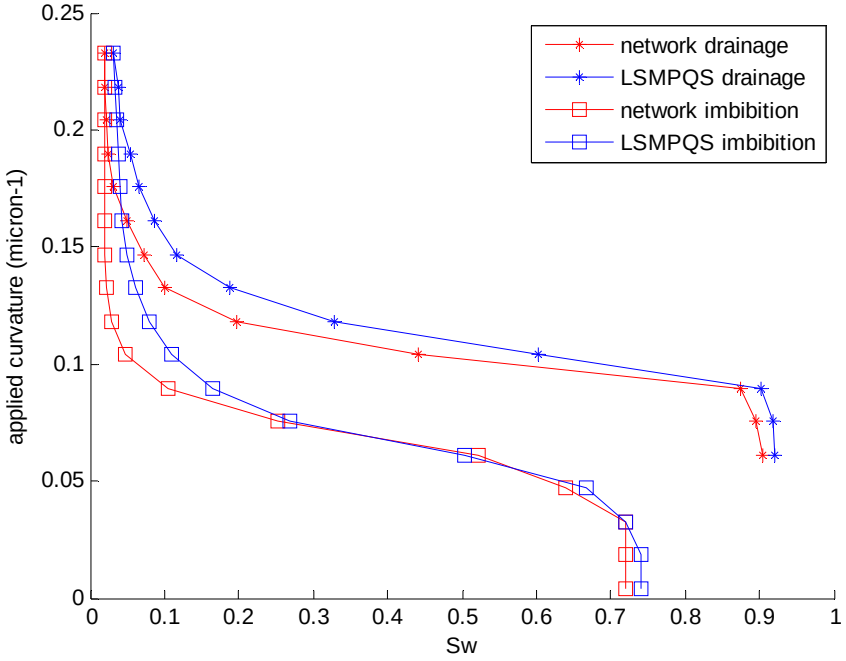

Figure 3.18: Drainage and imbibition curves for a sample of Castlegate sandstone. Porosity: 19.8%. RRNM and LSMPQS results are compared. Both simulations use the same drainage and imbibition curvature steps (from LSMPQS simulation). No drainage trapping is available for RRNM, while in LSMPQS wetting phase is still allowed to be trapped in the grain corners. Both RRNM and LSMPQS account for the nonwetting trapping in imbibition.

Figure 3.19 shows the fraction of the pores with the same filling status in both simulations to the total number of pores at different applied curvatures. For drainage (Figure 3.19A), there is not much variation before the percolation threshold. At step 4 (curvature = 0.1 μm^{-1}), the fraction drops to about 78% at step 5, indicating the drainage simulations from these two approaches predict the different percolation thresholds. This

can also be proved from Figure 3.18, where during the drainage percolation, S_w for the two simulations at the same applied curvature have about 15% difference. The fraction keeps decreasing until step 5, where is the lowest match, 75%, is obtained. For the rest of drainage, the fraction slowly returns and reaches 95% at the drainage endpoint.

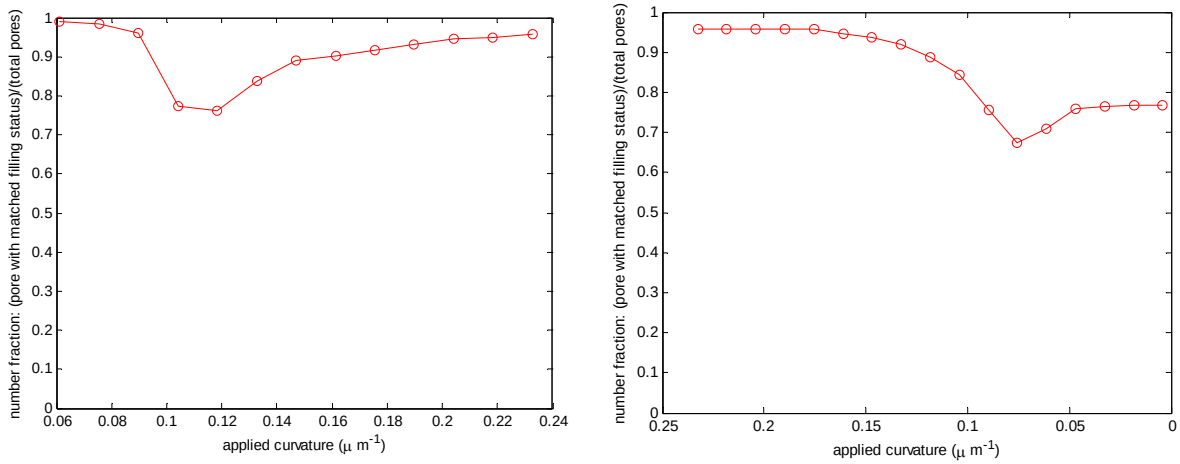

A. drainage B. imbibition

Figure 3.19: The filling status for drainage and imbibition of the Castlegate sandstone sample. The *x* axis is the drainage and imbibition applied curvatures, and the *y* axis is the fraction of the number of pores having the same filling status in both simulations compared with the total number of pores. Note that for imbibition, the applied curvature drops from left to right.

We do not observe any decrement in fraction at the first several steps of imbibition (Figure 3.19B). The imbibition percolation does not behave a 'sharp drop' as in drainage. A more gradual decrement is obtained from step 6 to 12, with the fraction drops from 95% to 65%. The rest of the imbibition steps experience slow return of the agreement. The imbibition endpoint gives a 77% of the agreement, which is the lowest among all of the three cases.

The preceding discussion suggests that, a good comparison of the macroscopic properties, e.g. the drainage and imbibition curves, does not necessarily lead to a good

agreement in the microscopic perspective. The comparison between LSMPQS and RRNM of this case gives another justification of this argument. Although a good match between the macroscopic curves is obtained (Figure 3.18), the microscopic justification (Figure 3.19) suggests that the agreement of the filling status of individual pores is not as good as what can be inferred from the macroscopic curves. An example is the imbibition endpoint, where only 3% difference in saturation unit is seen from Figure 3.18. However, Figure 3.19B indicates more than 20% pores have different filling status in the simulations. Figure 3.20 shows the pore filling status at different steps of drainage. Figure 3.20A shows the filling status at step 3, which is one step before the percolation. All the spheres concentrate close to the entry. Although only 7 pores are selected as the entry pores in RRNM, at step 3 the number of blue and red spheres indicate drainage already takes place in a small scale for RRNM, and only focuses on the pores close to the entry. LSMPQS, on the other hand, assumes the entire face as the entry.

Percolation for both simulations happens at step 4 (curvature = 0.1 μm^{-1}). Both simulations percolate through the entire domain. However, RRNM drains more pores than LSMPQS, with red spheres spreading at the center and close to the exit face. Although yellow spheres are also present, most of them still concentrate at the entry face, and the number of them is much less than the red spheres. This indicates ERdrainage criterion predicts lower critical curvatures, similar to the previous two cases.

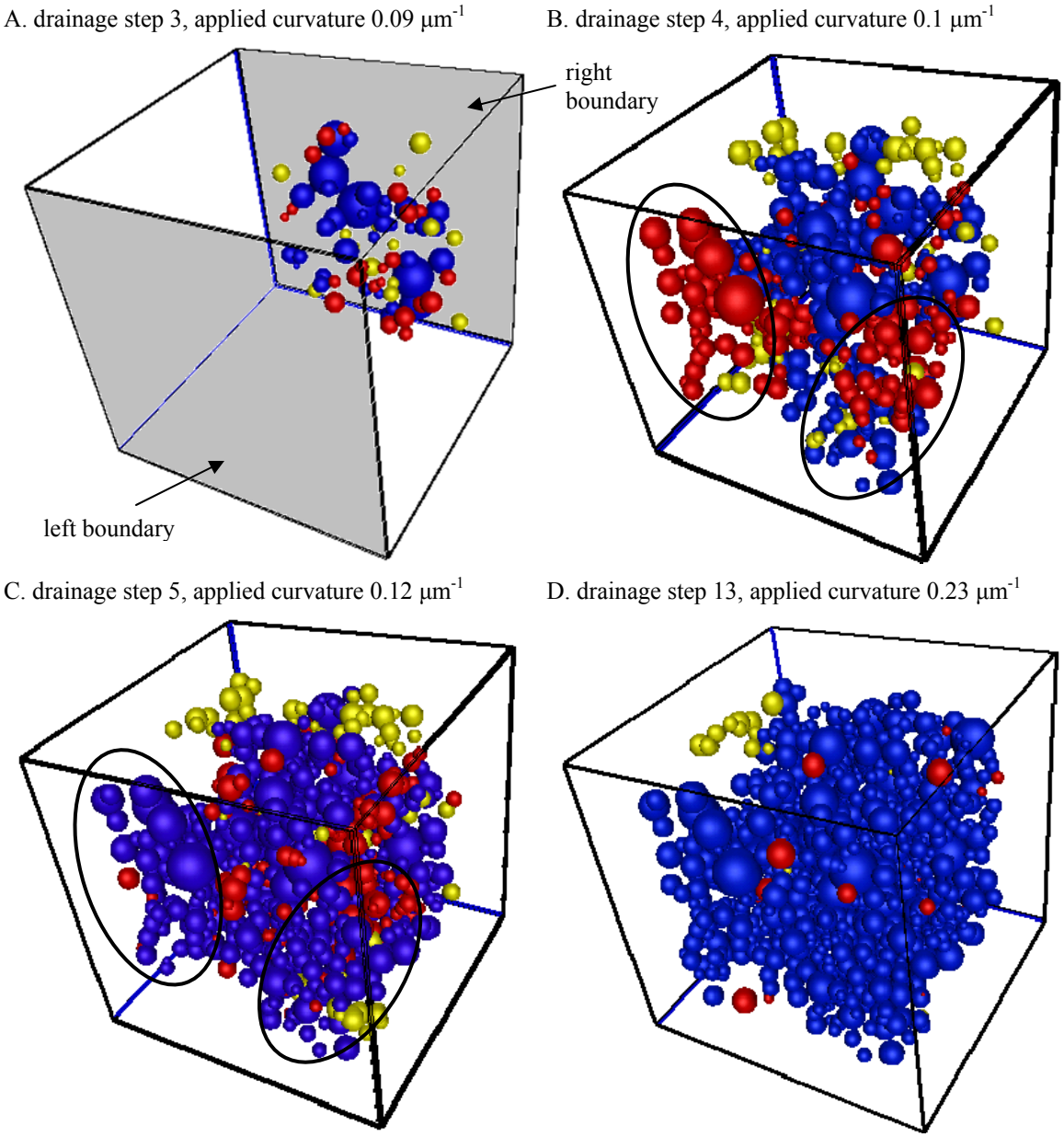

Figure 3.20: The filling status comparison between RRNM and LSMPQS for drainage of a Castlegate sandstone sample. The boundary settings and the color scheme are the same as the previous comparisons. Only the pores filled with nonwetting phase is shown.

As shown by the circles in step 4 (Figure 3.20B) and step 5 (Figure 3.20C), the pores that are only drained at the lower applied curvature by RRNM are later drained by LSMPQS as well, with a higher applied curvature. At step 5, RRNM continues to drain more pores than LSMPQS (more red spheres emerge through the entire domain), while not many new yellow spheres are present. These observations are the direct evidences that drainage predicted by using two simulations happens at the different curvature, but follows the same sequence.

Figure 3.20D gives the last step of drainage (step 13). Most of the red and yellow spheres at step are changed into blue ones. Still, isolated red spheres can be seen throughout the domain, and a cluster of yellow spheres is at the top corner. These red spheres indicate the trapped wetting phase in the corners in LSMPQS. When the pore centers are soaked into the trapped fluid, the pore is considered as the trapped one. The study shows that the cluster of yellow spheres has only one small throat connecting to the bulk pores. The drainage of this throat requires much higher curvature, not available from our simulations.

Step 6 (Figure 3.21A) and 10 (Figure 3.21B) are two intermediate steps at percolation. These two figures are similar, with step 10 having less dense blue spheres and more yellow spheres. The imbibibition simulations by LSMPQS and RRNM all occur at the similar pace, while RRNM imbibes slightly more pores at a given applied curvatures. The difference between the two simulations enlarges between step 10 (Figure 3.21B) and 12 (Figure 3.21C). With much more pores are imbibed in RRNM than LSMPQS, we observe significant increment of the yellow spheres. Meanwhile, the number of red spheres keeps increasing as well, but not as significant as the yellow spheres. Step 12 corresponds to the lowest fraction of agreement in the entire imbibition simulation, where only 67% of the pores in both simulations have the same filling status.

Although the fraction returns to 77% at the imbibition endpoint, it is still the lowest value for all the three cases.

A. imbibition step 6, applied curvature 0.16 μm^{-1}

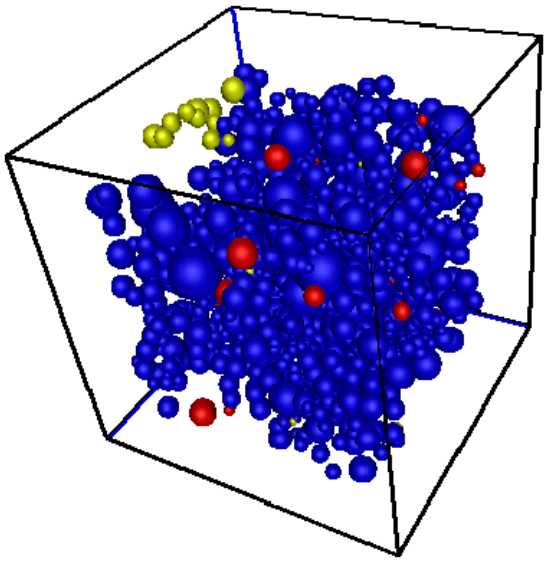

B. imbibition step 10, applied curvature 0.1 μm^{-1}

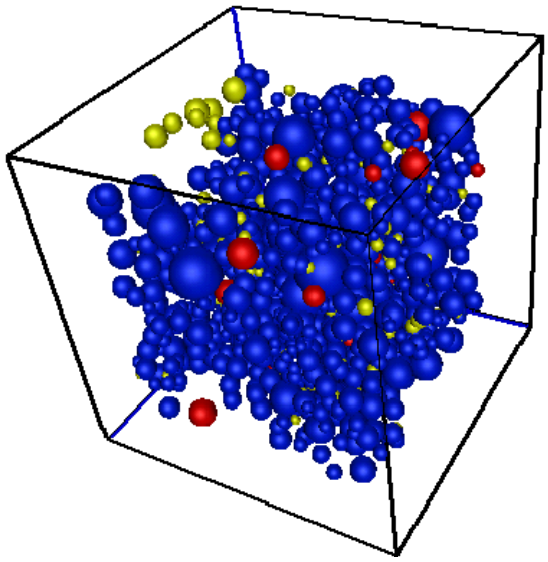

C. imbibition step 12, applied curvature 0.08 μm^{-1}

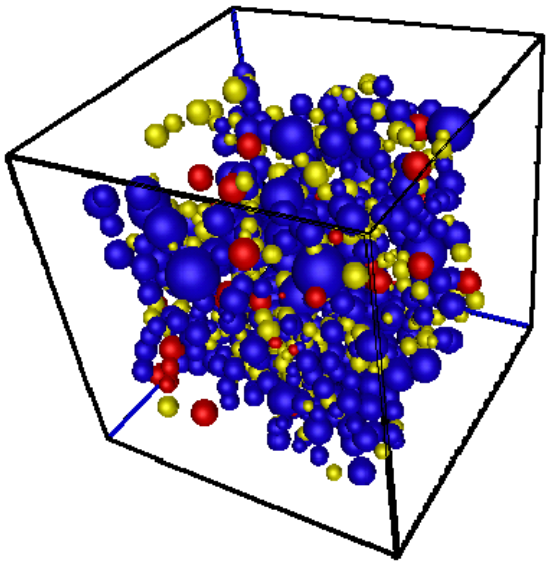

D. imbibition step 17, applied curvature 0.004 μm^{-1}

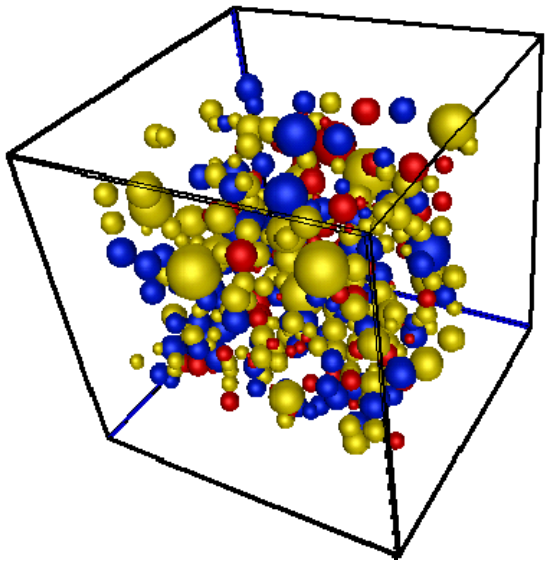

Figure 3.21: The filling status comparison between RRNM and LSMPQS for imbibition, Castlegate sandstone sample. The boundary setup and the color scheme are the same as in Figure 3.11. Only the pores filled with nonwetting phase is shown.

Figure 3.21D shows the pore filling status at imbibition endpoint. More yellow than blue spheres can be seen from the figure. This indicates more trapping happens in LSMPQS than RRNM. In RRNM, a pore can only be trapped when the pore connection is terminated due to the wetting phase invasion. This rudimentary model does not take into consideration the snap-off event. It usually happens in the narrow space (for instance, a throat): separated menisci coalescence into a whole one and block the fluid pathway. In a geometry with large ratio of open to narrow space sizes, snap-off events are more likely to happen (Prodanovic and Bryant, 2008). In the porous medium, when the sizes of the pore are much larger than the sizes of its throats, snap-off events take place at lower applied curvatures and trap the fluid in the pore. Figure 3.22 shows the histograms of all the samples, which gives the ratio of throat sizes to pore sizes. For Castlegate and Berea sandstone samples, the modes are at a small value, indicating that the pore and throat sizes have a large difference. Therefore, more snap-off events happen approaching the imbibition endpoint, and are predicted by LSMPQS. Since RRNM does not account for this event, the fractions of agreement for these two cases are lower than Fontainebleau case (fractions at imbibition endpoint: Castlegate 77% and Berea 80%, compared to Fontainebleau 87%). The ratio of throat size to pore size for Fontainebleau sample is much higher than the other two cases, so that the major trapping mechanism is the breaking of clusters due to fluid invasion into the pore. Both simulations well capture such mechanism, and thus give a better agreement than the other two cases.

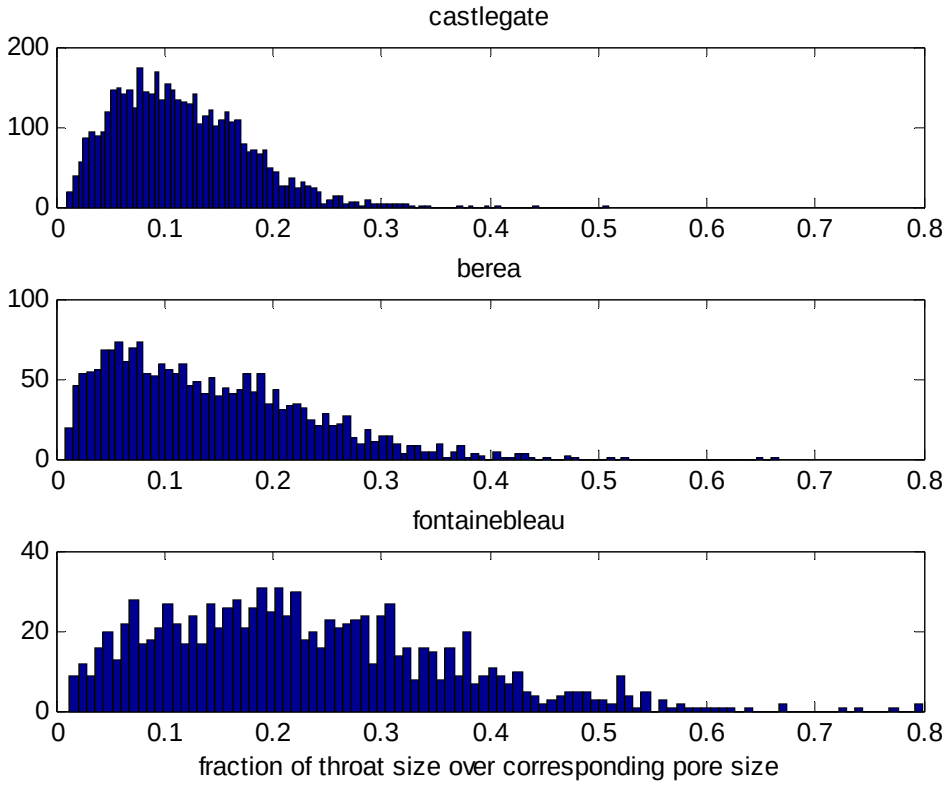

Figure 3.22: The histograms for all the samples. The *x* axis is the ratio of the throat sizes to the pore sizes to which the throats are connecting. It is calculated with effective radii of pores and throats. Smaller value indicates a larger difference between the throat and the pore.

3.5 CONCLUSIONS

We extend the application of network modeling and pore-by-pore comparison to the real rock cases. Both drainage and imbibition data are obtained, and compared with LSMPQS results. By using such technique, we check the correctness and reliability of our network with the newly-developed drainage and imbibition criteria.

All our criteria for drainage and imbibition, either developed for the model sediments or real rocks, are all based on the same concept of equivalent sphere. The inscribed sphere that we used to develop the criteria for model sediments is only special case of this concept. However, the direct application of the inscribed sphere to the real rock is not appropriate, due to the asymmetric and angular pores and throats. We therefore have developed new criteria. The equivalent sphere in this case is determined by throat parameters (for drainage) or by pore parameters (for imbibition). The critical curvature is a simple function of the radius of the equivalent sphere.

We use pore-by-pore comparison to test the simulation results by network modeling. In the absence of experimental data, results by LSMPQS are used as the drainage and imbibition benchmark. The pore drainage sequences for both simulations are similar, with the events predicted by RRNM happening at slightly smaller curvatures than LSMPQS. We observe the same behavior for all the three samples (Fontainebleau, Berea and Castlegate sandstones). This suggests that the drainage simulation based on the network modeling and the new drainage criterion correctly capture the pore level events, and therefore yields the satisfactory results in both macroscopic capillary curves and microscopic pore-level filling status.

Less satisfactory imbibition results are achieved from the imbibition simulation. We obtain a good agreement in the comparison of the imbibition curves, but

discrepancies in the pore-level filling status of two simulations. Evidences are observed that RRNM and LSMPQS still follow the similar imbibition sequence, although in a less obvious pattern than drainage. One reason is the new imbibition criterion ignores the fact that the events for individual pores can happen at multiple applied curvatures due to the different configurations of the menisci, while such behavior is well captured by LSMPQS simulation. Moreover, the drainage endpoints (from which imbibition starts) does not have the same fluid distribution for two simulations, and thus the paths for the imbibition events do not agree well.

The cross comparison of all the three samples suggests that the fraction of agreement at the imbibition endpoint decreases from Fontainebleau, to Berea and Castlegate cases. As shown by Figure 3.22, the sizes of pore and throats have a large difference in the Castlegate and Berea samples, a geometry where the snap-off events are more likely to happen. RRNM does not model the snap-off effect, while LSMPQS does. This also explains the less agreement for these two cases.

The inconsistency between the imbibition curves and the pore-level filling status suggests that the macroscopic agreement does not necessarily guarantee a perfect match microscopically. A capillary curve can correspond to multiple combinations of the fluid distribution in the pore scale. However, it is only the microscopic comparison that can promise the correctness of drainage and imbibition results from the network simulation. The technique as such has not been available until this work. This raises the question of the reliability of the network modeling approaches, which are often tested only against the capillary curves from the lab experiments.

Overall, RRNM with the newly-developed drainage and imbibition criteria provide a first order approximation of the drainage and imbibition events in the real porous medium. Because the model rudumentariness, some physical behaviors are not

accounted for in the simulation, for example, pendular rings, snap-off effects, etc. The negligence of these behaviors contributes to the larger difference at the imbibition endpoint with LSMPQS than what we have observed between fPRNM and LSMPQS. More efforts need to be invested to improve this model.

4. Methane hydrate formation in the pore scale

4.1 A STOICHIOMETRIC MODEL OF METHANE HYDRATE FORMATION

Our premise is that hydrate forms from co-existing gas and water in sediments. One important test of the premise is to assess the macroscopic consequences of the volume change associated with forming hydrate phase with components (methane and water) from the gaseous and aqueous phases. The volume change drives the pressure change and accompanying fluid displacement studied in the pore-level model (Chapter 2 and 3). At the macroscopic scale the volume change drives bulk phase fluid movement.

Here we emphasize again that we use methane hydrate to represent gas hydrate in the study, for the reason that methane hydrate is an important and most abundant existing hydrate form in nature. Methane hydrate formation is a stoichiometric process controlled by numerous factors. Temperature, pressure, salinity and the availability of methane and water all play important roles in such process. To conduct the test, we tabulate the fractional volume change as a function of temperature, pressure and salinity and identify a critical saturation of aqueous phase for hydrate conversion. We then consider implications of the limiting cases in which methane and/or water are available or not for continued hydrate formation. A simple 1D model is proposed for this purpose.

4.1.1 A simple 1D model

Figure 4.1 shows schematically a box of volume V. In this model, we only investigate the system volume change due to hydrate formation. The saturations of different phase in this section (section 4.1) means the volume fraction of box.

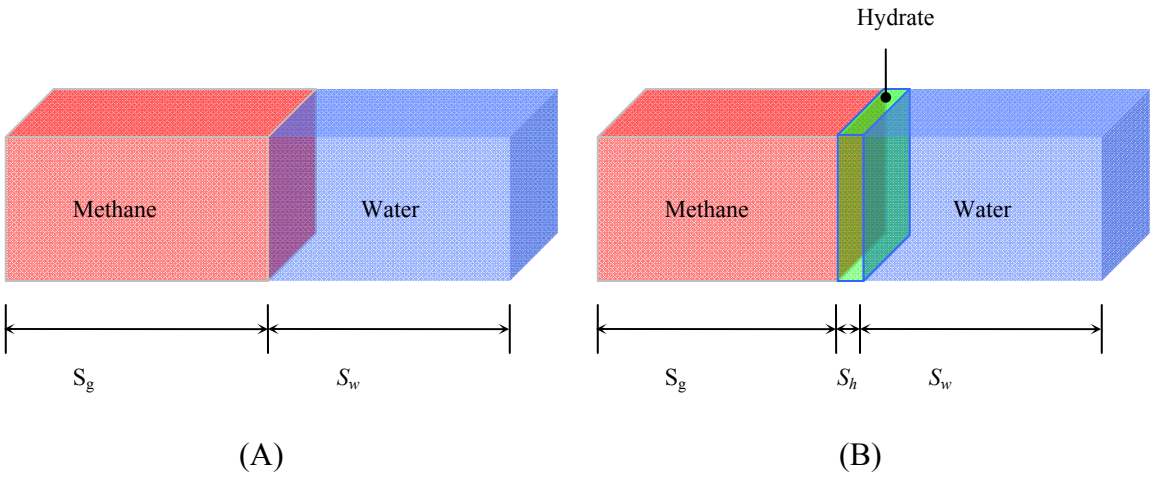

Figure 4.1: The 1D model to compute the volume change due to hydrate formation. We consider two limiting cases: no additional methane or water enters the box, and water enters the box to maintain constant S_w (S_w here means the water saturation). In section 4.1, saturation of different phases is defined as the volume fraction of the box. (A) Initially no hydrate is present, the gas saturation is fixed, and $S_w = 1 - S_g$. (B) An increment of hydrate forms at the interface between gaseous and aqueous phases.

The volume taken up by methane is denoted as VS_g, and by water as VS_w. Hydrate forms on the interface of methane and water. It occupies a volume fraction denoted as S_h. Due to the formation of hydrate, the volumes of aqueous and gaseous phases will change. In this study, we investigate the system volume change by assuming the gaseous phase is pure methane and that gas density remains constant during hydrate formation. **That is, we assume *T* and *P* do not change during hydrate formation.** This assumption says if putting this gas-water-hydrate system into the porous medium (gas, water and hydrate phases will occupies the void space of the porous medium), the sediment grains will be rearranged and/or fluid phases will enter the box as needed to maintain pressure. In this model we do not concern ourselves with the reservoir dynamics or timescales to achieve the isothermal/isobaric state.

4.1.2 Methane density calculation

The methane density, ρ_g, is an important parameter that needs to be determined before computing the hydrate conversion. We calculate this value by using the model presented by Soave, Redlich and Kwong (Sandler, 2006). The relationship between ρ_g, P and T are governed by the following system of equations:

$$P = \frac{RT}{V_m - b} - \frac{a\alpha}{V_m\left(V_m - b\right)} \tag{4.1}$$

$$a = \frac{0.42747 R^2 T_c^{\,2}}{P_c} \tag{4.2}$$

$$b = \frac{0.08664 R T_c}{P_c} \tag{4.3}$$

$$\alpha = \left(1 + \left(0.48508 + 1.55171\omega - 0.15613\omega^2\right)\left(1 - T_r^{0.5}\right)\right)^2 \tag{4.4}$$

$$T_r = \frac{T}{T_c} \tag{4.5}$$

$$\rho_g = \frac{M_g}{V_m} \tag{4.6}$$

T_c and P_c are the critical temperature and pressure, respectively. ω is the acentric factor. For methane, these values are: T_c = 190 K, P_c = 4.64×10^6 Pa, ω = 0.011. From the above system of equations, methane density is determined given the values of T and P.

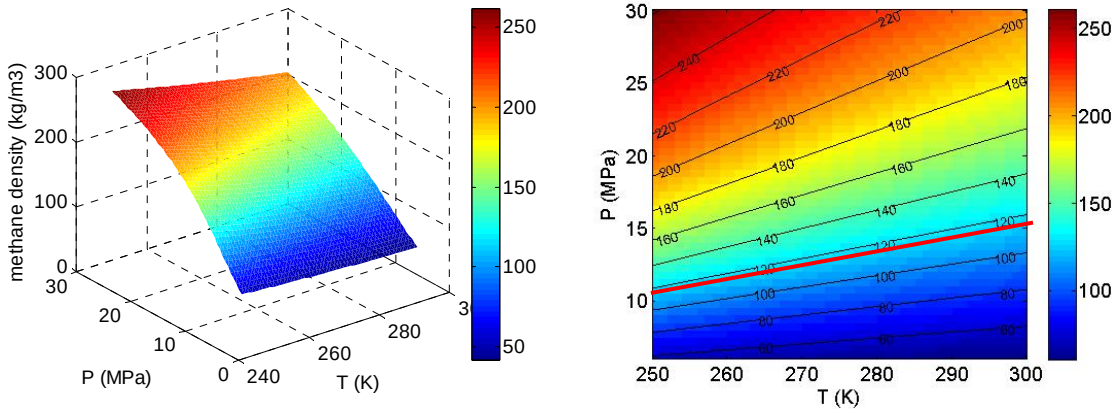

Figure 4.2: Methane density (kg/m^3) as a function of *T* and *P* (left is the surface plot and right is the contour plot). At lower pressure, methane density is a weak function of temperature over the range of interest, but a strong function of pressure. Methane density increases with increasing pressure or decreasing temperature. The red line on the contour plot is the equivalent methane density in hydrate (122 kg CH_4/m^3 hydrate, the molecular formula of methane hydrate is $CH_4 \cdot 5.75H_2O$, with the density of 910 kg/m^3, from (Sloan, 2003).

The red line in the right panel of Figure 4.2 illustrates the density of methane in the hydrate phase, i.e. the mass of methane molecules per unit volume of hydrate. If the gaseous methane density is greater than 122 kg/m^3 (region above the red line), the hydrate volume that is converted from methane will be greater than the volume of methane, assuming that *T* and *P* are kept constant. On the other hand, below the red line where the gaseous methane density is smaller than 122 kg/m^3, the opposite situation would happen. Thus system volume (methane+hydrate) change is inevitable as hydrate is generated, which leads to sediment compaction/fracture or fluid inflow/outflow in the Gas Hydrate Stability Zone (GHSZ).

4.1.3 Salinity effect on Gas Hydrate Stability Zone (GHSZ)

Salt is an inhibitor for hydrate formation. At each combination of T and P, there is a maximum water salinity, above which no hydrate can be generated and stably sustained. The maximum salinity, as well as T and P, defines the GHSZ and affects the amount of hydrate in the sediments.

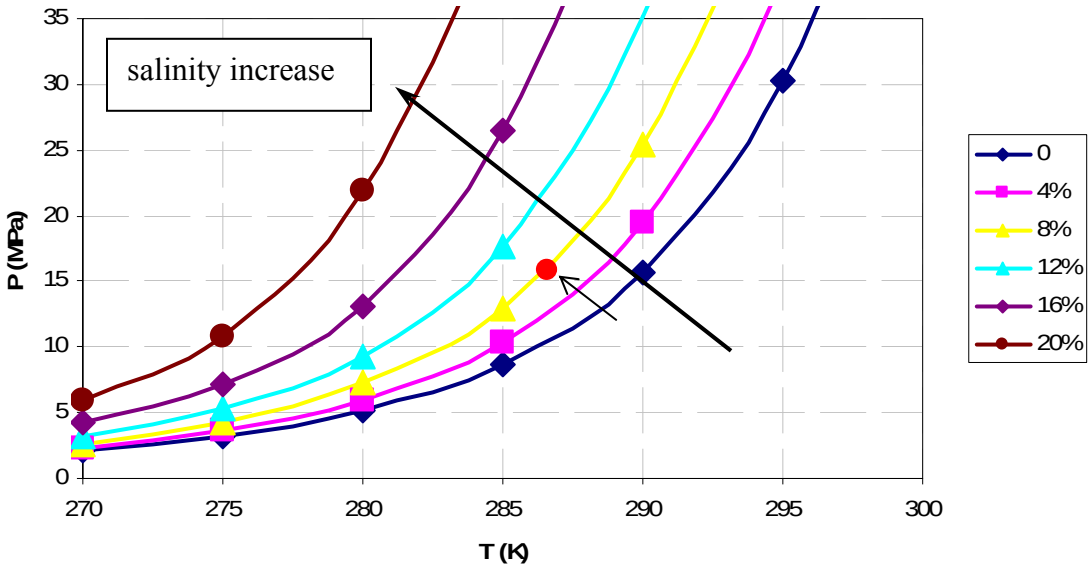

Figure 4.3: GHSZ variation due to salinity of initially present water. Contours shown for several values of wt % NaCl. Hydrate is stable above the curve, while unstable below it. That is, GHSZ is above the curve. With increasing salinity, GHSZ retreats to a region of higher P and lower T, as shown by the arrow. The values (dots in the figure) are computed from: http://www.geochem-model.org/models/ch4-sea/, whose reliability is widely tested at (Sun and Duan, 2007).

Figure 4.3 shows the salinity influence on GHSZ. The curves are the phase boundaries (gaseous and aqueous below, hydrate and gaseous or aqueous above) corresponding to various salinities. Consider for example, the curve of salinity = 4%. Hydrate is a stable phase above the curve. The salinity dependence of the phase boundary has an important implication for the formation of hydrate from co-existing aqueous and

gas phases. During hydrate formation, salt ions are excluded from the hydrate crystalline lattice and thus remained dissolved into the aqueous phase. Because water leaves the aqueous phase to become part of the hydrate, the salt concentration in the aqueous phase increases. When the water salinity becomes 8%, hydrate formation at the red point in Figure 4.3 is terminated, as now the point is on the curve of 8% salinity. The increase of salinity moves the phase boundary to higher P and lower T, which shrinks GHSZ. From salinity = 0 to 20%, a large region is lost from GHSZ, showing a significant salinity effect.

4.1.4 Formulation

In this scenario, the masses of methane and water in the box of Figure 4.1 are fixed at their initial values, that is, the box is closed after the initial saturations are set. We assume that T and P are constant when hydrate forms. The calculation uses water density as 1,000 kg/m^3, and hydrate density as 910 kg/m^3 (Sloan, 2003). The hydration number N ($CH_4 \cdot N\,H_2O$) is set to be 5.75.

With the changing of initial gas and water saturation, the amount of hydrate that can be generated varies accordingly. We define the critical water saturation (S_{wc}) as value at which both gaseous and aqueous phases are completely, stoichiometrically converted into hydrate, if it is fresh water; when the aqueous phase contains dissolved ions, critical water saturation is the value at which gas phase can be converted completely, and water phase can be converted maximally (that is, the resulting salinity from hydrate formation is the maximum salinity at which hydrate is stable at that T and P). When $S_w < S_{wc}$, methane is present in stoichiometric excess (or excess for short) and gaseous phase remains after all the water is converted; when $S_w > S_{wc}$, the pure or salted water is excess

and the aqueous phase remains after all the methane is converted. We first develop the formulation to predict S_{wc}, and then discuss the situations of excess methane and water, respectively.

Limited methane and water

In order to generate a mass m_h of hydrate, we need the following volume of gas and fresh water:

$$V_g = \frac{m_h \dfrac{M_g}{M_g + NM_w}}{\rho_g} \tag{4.7}$$

$$V_w = \frac{m_h \dfrac{NM_w}{M_g + NM_w}}{\rho_w} \tag{4.8}$$

For maximum conversion of methane, i.e. complete conversion of the methane to hydrate, we require that

$$V_g = VS_g \tag{4.9}$$

where V is the volume of the box model, and for a maximum conversion of water,

$$V_w = VS_w x \tag{4.10}$$

The coefficient x is unity if the water is fresh. Unlike the gas phase, the aqueous phase cannot be totally converted into hydrate because of the salt dissolved in it. We account for this with coefficient x, with $x = 1$ for pure water and $x < 1$ for salty water.

By the definition of initial salinity *Sal*, we have

$$\frac{u}{V_w \rho_w + u} = Sal \tag{4.11}$$

where u is the mass of salt dissolved in the aqueous phase.

As hydrate forms in this scenario, it rejects salinity ions, forcing them to remain in the water phase. Thus the salinity in the remaining water will increase as hydrate forms.

When the initial salinity increases to the maximum value for hydrate stability at the T and P of the box, none of the water remaining in the box can be used to generate hydrate (in this closed-box scenario). The maximum salinity $MSal$ is related to x, the fractional conversion of water to hydrate, by

$$\frac{u}{V_w \rho_w (1-x) + u} = MSal \tag{4.12}$$

The maximum salinity is a function of T and P, as shown in Figure 4.3.

Combining equation (4.11) and (4.12), we have

$$x = \left(1 - \frac{Sal}{MSal}\right)\left(1 + \frac{u}{V_w \rho_w}\right) \tag{4.13}$$

Also from equation (4.11), it is easy to get

$$\frac{u}{V_w \rho_w} = \frac{Sal}{1 - Sal} \tag{4.14}$$

Equation (4.13) and (4.14) yield

$$x = \left(1 - \frac{Sal}{MSal}\right)\frac{1}{1 - Sal} \tag{4.15}$$

We can combine equation (4.7), (4.8), (4.9), (4.10), (4.15) to get the critical water saturation, given the initial salinity and the temperature and pressure of box:

$$S_{wc} = 1 - \frac{1}{1 + \frac{\rho_g}{\rho_w}\frac{NM_w}{M_g}\frac{1 - Sal}{\left(1 - \frac{Sal}{MSal}\right)}} \tag{4.16}$$

When initial salinity $Sal = 0$, equation (4.16) is reduced to

$$S_{wc} = 1 - \frac{1}{1 + \frac{\rho_g}{\rho_w}\frac{NM_w}{M_g}} \tag{4.17}$$

The hydrate saturation, after the maximum conversion of gas and water under the critical water saturation (S_{wc}), is:

$$S_h = xS_{wc}\frac{\rho_w}{\rho_h}\frac{NM_w + M_g}{NM_w} \tag{4.18}$$

The water saturation after maximum conversion is zero if the initial salinity is zero; otherwise it is $(1\text{-}x)S_{wc}$.

Equation (4.18) shows hydrate saturation when $S_w = S_{wc}$ is a direct function only of initial salinity, as the other parameters are all constant at a given T and P. The volume reduction when hydrate formation is complete is the original system volume V minus the volume of hydrate VS_h formed (equation (4.18)) and volume of water remaining $(1\text{-}x)VS_{wc}$. The relative volume reduction is thus

$$\frac{dV}{V} = 1 - \left(xS_{wc}\frac{\rho_w}{\rho_h}\frac{NM_w + M_g}{NM_w} + (1-x)S_{wc} \right) \tag{4.19}$$

The maximum hydrate saturation in a closed system is obtained at $S_w = S_{wc}$ for a closed system, when all methane and the maximum amount of water are converted to make hydrate. The hydrate saturation obtained from this scenario can be used to compare with the field data to justify the validity of this closed system.

$S_w > S_{wc}$

When $S_w > S_{wc}$, water is excess. Methane is the limiting reactant in the hydrate formation, and all methane is converted to hydrate. In this case the volume change of the system (gas+water+hydrate) can be computed from initial gas saturation S_g.

Since gas is totally converted into hydrate, with V_g amount of gas ($V_g = VS_g$), we can generate the following V_h amount of hydrate.

$$V_h = \frac{VS_g\rho_g}{\rho_H}\frac{M_g + NM_w}{M_g} \tag{4.20}$$

and also require the following amount of water.

$$V_w = \frac{VS_g\rho_g}{\rho_w}\frac{NM_w}{M_g} \tag{4.21}$$

The volume change of the system is defined as

$$dV = dV_h + dV_w + dV_g \tag{4.22}$$

Because hydrate is generated, and water and methane are consumed, dV_h is positive and dV_w and dV_g are negative. The volume change of the system as fraction of the initial volume is derived from equation (4.20) and (4.21).

$$\frac{dV}{V} = S_g\left(\frac{\rho_g}{\rho_h}\frac{M_g + NM_w}{M_g} - \left(1 + \frac{\rho_g}{\rho_w}\frac{NM_w}{M_g}\right)\right) \tag{4.23}$$

where dV/V is the volume change as a fraction of the initial volume. Graphical presentation of these relationships will be discussed in section 4.2.1. It clearly indicates that gas saturation S_g determines the final volume change. The terms inside the bracket of equation (4.23), such as gas density, are constants with fixed T and P. These terms also has a first-order influence on dV/V.

$S_w < S_{wc}$

When $S_w < S_{wc}$, methane is excess. The conversion to hydrate will be limited by the availability of water and/or the salinity. The volume change of the system is thus derived in terms of the water saturation.

Because of initial salinity effect, water cannot be completely converted into hydrate. Hydrate can keep growing until the initial salinity reaches the maximum salinity at the given T and P. The volume fraction of water that can be converted into hydrate is determined by equation (4.15). The converted water volume is

$$V_w = xVS_w \tag{4.24}$$

where x is a function of initial salinity, T and P; x is computed from equation (4.15). V_w of water yield a volume V_h of hydrate according to

$$V_h = \frac{xVS_w\rho_w}{\rho_h}\frac{M_g + NM_w}{NM_w} \tag{4.25}$$

and the required gas V_g can be easily computed from the above equation

$$V_g = \frac{xVS_w\rho_w}{\rho_g}\frac{M_g}{NM_w} \tag{4.26}$$

The volume change, defined by equation (4.22), as a fraction of the initial volume is computed as

$$\frac{dV}{V} = xS_w\left(\frac{\rho_w}{\rho_h}\frac{M_g + NM_w}{NM_w} - \left(1 + \frac{\rho_w}{\rho_g}\frac{M_g}{NM_w}\right)\right) \tag{4.27}$$

Graphical presentation of these relationships will be discussed in section 4.2.1.

We have developed the formulation to determine the volume change when initial saturations of gaseous and aqueous phases are specified and neither gas nor water enter the volume. We find the critical water saturation S_{wc} (equation (4.16) and (4.17)), at which all the gas phase saturation and the maximum possible amount of the water phase are converted to hydrate. The volume change for cases of $S_w > S_{wc}$, equation (4.23), and $S_w < S_{wc}$, equation (4.27), are also derived.

At $S_w = S_{wc}$, all methane in the system is converted into hydrate, and the maximum water is also converted until the salinity in the remaining water increases to *MSal*. More system volume change can be achieved compared to the condition that $S_w \neq S_{wc}$. Both cases ($S_w = S_{wc}$ and $S_w \neq S_{wc}$) are discussed.

Limited methane and unlimited water

We now consider volume changes when the system is open to influx of water. The concept of critical water saturation is no longer relevant. We assume that water enters the box so as to keep the water saturation constant. In effect, the hydrate occupies space originally filled with gas phase. This can be regarded as the macroscopic consequence of permeable hydrate film followed by imbibition, discussed in the microscale modeling section. We also assume that the temperature and pressure in the box do not change. We further assume that the salinity remains constant, meaning that the salt buildup associated with hydrate formation diffuses away instantaneously.

The system volume change is only related to the volume of methane consumed and the volume of hydrate generated, since the volume of water is considered constant.

For V_g of methane consumed, we have V_h of hydrate:

$$V_h = VS_g \frac{\rho_g}{\rho_h} \frac{M_g + NM_w}{M_g} \tag{4.28}$$

Therefore, since all hydrate grows into the volume occupied by methane, the system volume change is:

$$\frac{dV}{V} = S_g \left(\frac{\rho_g}{\rho_h} \frac{M_g + NM_w}{M_g} - 1 \right) \tag{4.29}$$

Equation (4.29) indicates that there is a value of gas phase density at which the system volume would be unchanged after hydrate formation, i.e. $dV = 0$. This critical methane density should satisfy the following equation.

$$\rho_{gc} = \rho_h \frac{M_g}{M_g + NM_w} \tag{4.30}$$

The T and P of the system determine the gas phase density. When ρ_g is greater than critical gas density, the volume occupied by gaseous/aqueous/hydrate phases (we refer to this volume as the system volume in Section 4.1 and 4.2, as hydrate aqueous and

gaseous phases form the system we study in these two sections) will increase due to the hydrate formation. To the contrary, the same volume will decrease if ρ_g is less than the critical gas saturation. Since the right hand side of equation (4.30) consists of constants, ρ_{gc} is easily calculated.

$$\rho_{gc} = 910\frac{16}{16+5.75\times 18} = 122\ kg/m^3 \tag{4.31}$$

At the T and P characteristic of the hydrate stability zone, gas density is usually less than 100 kg/m^3; see Figure 2. This means the system volume will usually decrease in this scenario (limited methane, unlimited water). The situation that system volume increases is possible theoretically, for example in water depths greater than 1500 m with a seafloor temperature of 277 K.

4.2 RESULTS AND DISCUSSION

4.2.1 Limited methane and water

Critical water saturation

Figure 4.4 shows the contour maps of the critical water saturation (S_{wc}) as a function of T, P and salinity. When the initial water saturation in a closed volume is equal to the critical water saturation, then all the initial gas and the maximum amount of water will be converted to hydrate. When $Sal = 0$ (Figure 4, top left), S_{wc} is a strong function of pressure (large variation with changing pressure), but a weak function of temperature (small variation with changing pressure). From equation (4.17), variation of S_{wc} is driven by variation of ρ_g, as the other parameters are constants or, in the case of water density, nearly constant. Figure 4.2 shows ρ_g depends strongly on pressure but weakly on temperature. This causes the dependence feature of S_{wc} on T and P shown in Figure 4.4, $Sal = 0$ case.

At zero initial salinity, S_{wc} increases with the system pressure. Methane has a low density when pressure is low, and thus requires less volume of water to totally convert gas into hydrate. That is, the volume fraction of water initially present in the system must be smaller in order to achieve a complete conversion of both phases to hydrate. When methane density increases due to high pressure, more water is needed to convert the same volume of gas, and boosts the required initial volume fraction of water in the system.

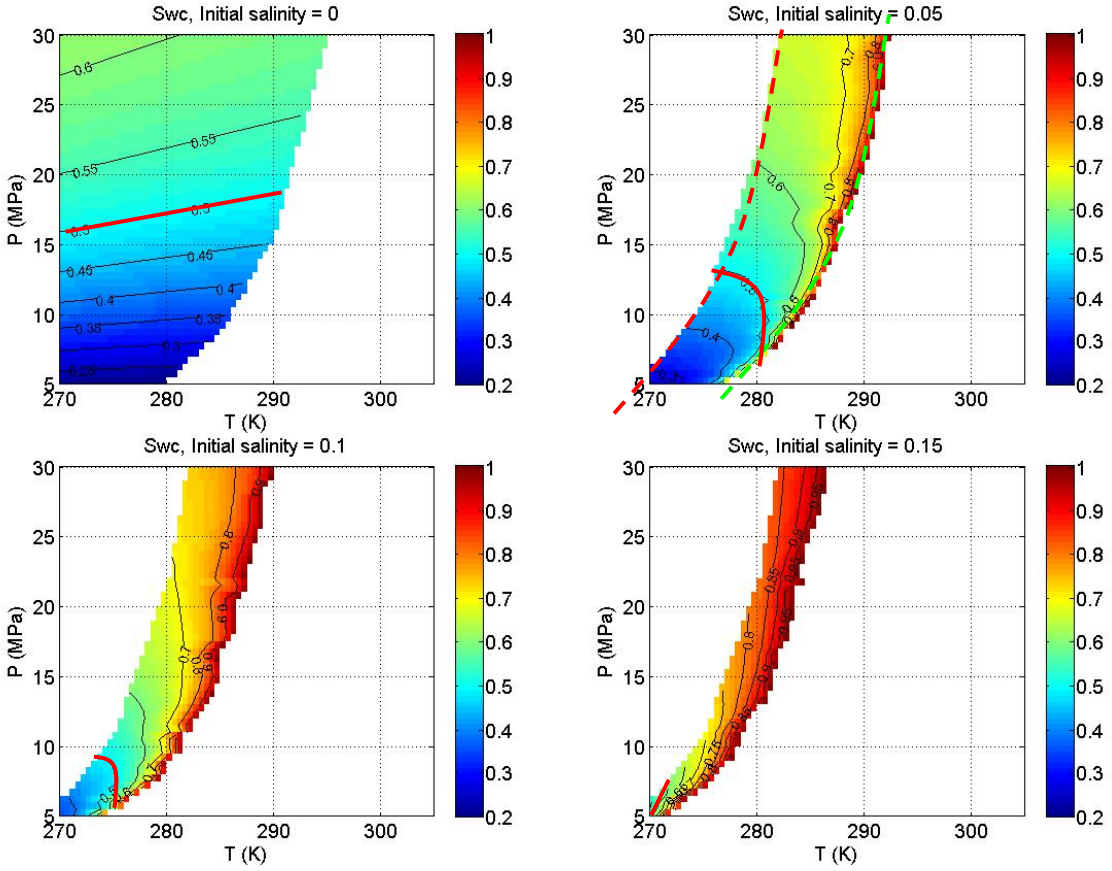

Figure 4.4: Critical water saturation (S_{wc}) as a function of T and P for four different initial salinities (Sal). This plot is based on equation (4.16), derived from a closed box. The blank region on the right hand side of each plot (boundary indicated by dashed green curve in top right panel) exists because hydrate is not stable in this region. The blank region on the left hand side of each plot (boundary indicated by dashed red curve in top right panel) is because our equation of state does not extend beyond salinity of 20%. The solid red curves shows $S_w = 0.5$.

In other cases when $Sal \neq 0$ (Figure 4, top right and bottom panels), S_{wc} behaves differently. S_{wc} increases with temperature as well as pressure. The right boundary of the domain (indicated by the blue dashed curve) separates the hydrate stability and instability zones with the current T, P and initial salinity. The left boundary (indicated by the red dashed curve) means Sal higher than 20% is simply beyond our interests: an even higher

water saturation can be computed beyond the left boundary, which corresponds to a higher maximum salinity (*MSal*) after the complete conversion to hydrate. The right boundary retreats to the upper left region with increasing *Sal*, suggesting the corresponding shrinking GHSZ. On the other hand, the left boundary is unaffected by the change of *Sal*.

For all the cases with initial salinity, the maximum S_{wc} is on the right boundary of the region. This is because close to this boundary the initial salinity of water is close to the maximum salinity for hydrate stability under that *T* and *P*. Only a small amount of fresh water in water can be converted to hydrate as the initial salinity will increase immediately to the maximum salinity. Consequently we need a large amount of water in order to convert a small amount of methane.

The general trend indicates that with higher *Sal*, S_{wc} needs to be higher so as to allow the complete conversion of methane. The amount of the available fresh water for hydrate formation in the water decreases with increasing the salinity. This yields higher water saturation in order for the compensation.

The solid red curve in Figure 4.4 indicates $S_w = 0.5$. Below this curve, methane is excess, water is the limiting component to determine hydrate saturation. Above this curve, water is excess, methane becomes the limiting component. A more detail discussion will later be combined with the presentation in Figure 4.10.

S_{wc} has a great variation at different *T* and *P*, which often ranges from 30% to 90%. This also leads to the large variation in the amount of hydrate generated. As discussed below, hydrate formation generally reduces the volume occupied by the gaseous, aqueous and hydrate phases. The manner in which this volume is filled is of great interest, because it changes the pore pressure in the sediments, which then can cause matrix instability (e.g. fracture and compaction), or fluid displacement. Any of these

events can create new gas/water interfaces, leading to a feedback loop that will influence the growth habit of hydrates. We elaborate this behavior later in this chapter.

Hydrate saturation

Figure 4.5 shows the hydrate saturation obtained when the initial water saturation equals to the critical saturation, mapped in Figure 4.4. The calculation gives the maximum hydrate saturation that could possibly be generated from limited gas and water if T and P remain constant. For example, at P = 10 MPa and T = 280 K, the maximum hydrate saturation would be 37%, if the initial salinity were 5 wt%. From Figure 4.4 we also know that at this condition S_{wc} = 48%, and therefore S_g = 52% (1-48%). The remaining water saturation (S_{wr}, the water saturation when the salinity in the aqueous phase reaches up to the maximum salinity at this condition, in this case, T = 280 K and P = 10 MPa), from Figure 4.7 (will be analyzed later) is 18%. Therefore, the volume reduction (dV/V) of the box is $1 - S_{wr} - S_h$ = 45%. It means that after hydrate formation is complete, the resulting volume of hydrate and remaining water is only 55% of the initial box volume, and the volume reduction can reach up to 45%.

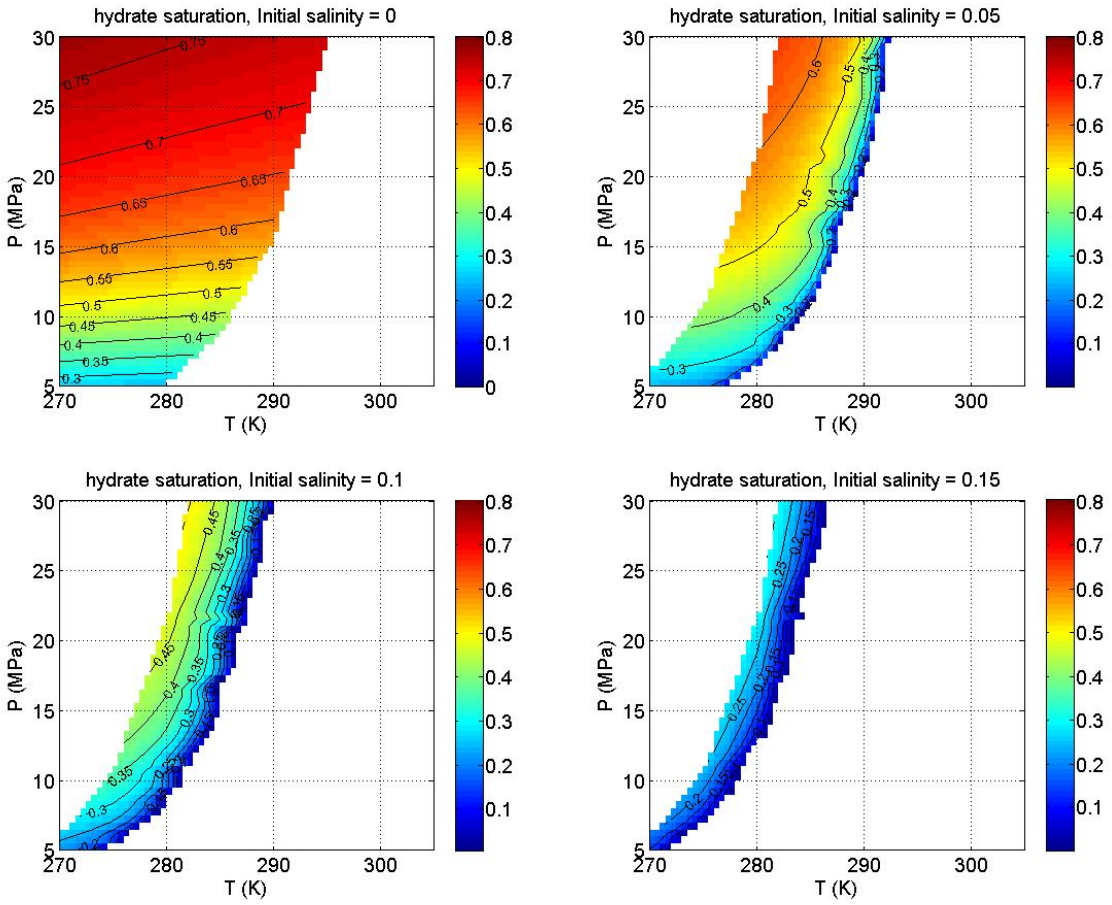

Figure 4.5: The hydrate saturation resulting from conversion of all initial gas phase at different *Sal*, *T* and *P*, when initial water saturation is equal to critical saturation of Figure 4.4. The reason for the blank regions is the same as in Figure 4.4.

At *Sal* = 0, Figure 4.5 shows similar behavior as Figure 4.4. At low pressure, we have small mass of methane gas, which leads to small hydrate saturation. At *P* = 5 MPa, Figure 4.4 suggests that S_{wc} is about 25% (at this pressure, hydrate saturation is almost independent of temperature variation). This gives 75% S_g. Because of the low density of methane, the resulting hydrate saturation is only 30%. Along with S_{wr} = 0 (no remaining water as it is the fresh water in this case), we have 70% volume reduction of the initial

box. At high pressure (25 MPa to 30 MPa), the increasing methane density reduces the requirement for water molecules. S_{wc} = 60% (S_g = 40%) corresponds to 75% hydrate saturation, a much larger value than the low pressure case. Therefore the volume reduction reduces to 25% (1 - S_h). This comparison suggests the importance of the system pressure during the hydrate formation process.

When $Sal \neq 0$, we observe a band of GHSZ, similar to those in Figure 4.4. The band is determined by the boundary of GHSZ (right boundary) and also our interest of the maximum salinity (20%, left boundary). As the preceding discussion, GHSZ withdraws to the upper left corners with increasing *Sal*, correspondingly yielding a narrower band in Figure 4.5. The general trend suggests that the hydrate saturation increases from the right to the left boundary. On the right boundary, not much hydrate can be generated because the initial water salinity is already close to the maximum salinity. While approaching the left boundary, the maximum salinity that allows for the hydrate formation increases, so that more fresh water can be used for the conversion.

From Figure 4.5, it is also a straightforward observation that higher S_h is obtained with lower *Sal* when initial S_w equals S_{wc}. water salinity plays a significant role in hydrate saturation. For example at T = 280 K and P = 15 MPa, S_h reaches 50% at initial salinity equal to 5%, while S_h is only 15% at initial salinity equal to 15%. At the same T and P, lower initial salinity always leads to higher hydrate saturation when initial S_w equals S_{wc}. This is because much more water component can be converted to produce hydrate when initial salinity is lower.

In most cases the salinity in sea water is lower than 3%. We plot the maximum hydrate saturation at salinity = 3% in Figure 4.6. It is shown that in Hydrate Ridge, Cascadia Margin, the maximum S_h ranges from 10% to 40% (Hyndman et al., 1999; Torres et al., 2004), depending on T and P. In Blake Ridge (Egeberg and Dickens, 1999;

Collett and Ladd, 2000), people observed much lower S_h (less than 10%). For Mount Elbert (M.E. Torres et al., 2011), the maximum hydrate saturation is around 80%, which is also the case in Mallik hydrate reservoir (Dallimore and Collett, 2005). The model prediction in Figure 4.6 significantly underestimates the hydrate saturation in the arctic hydrate reservoirs (Mount Elbert and Mallik), and overestimates the reservoirs in the ocean sediments (Hydrate Ridge and Blake Ridge). This indicates that this scenario is not applicable in these reservoirs.

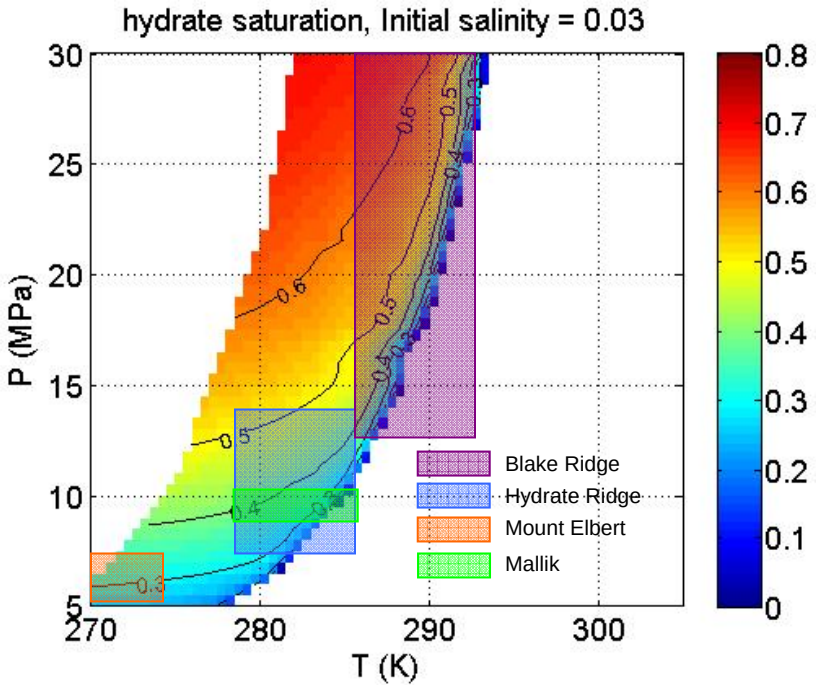

Figure 4.6: Hydrate saturation at sea water salinity (3%), at different T and P. The plot is based on the closed system, from the equation (4.19), which assumes the initial water saturation is the critical saturation S_{wc}. This setting results in the maximum hydrate saturation in the system. It also shows the $T-P$ range of several hydrate reservoirs. The region beyond the right boundary is neglected, as hydrate is not stable there.

Remaining water saturation (S_{wr})

The remaining water saturation (S_{wr}), in the limited water and gas scenario, is the water saturation when the salt concentration in the aqueous phase reaches up to the maximum value for hydrate formation at a specific T and P. S_{wr} is not simply the unity minus the hydrate saturation, since the volume of the system shrinks with the hydrate formation. That is, the total volume of hydrate and water is less than the initial system volume. It is therefore interesting to know S_{wr}.

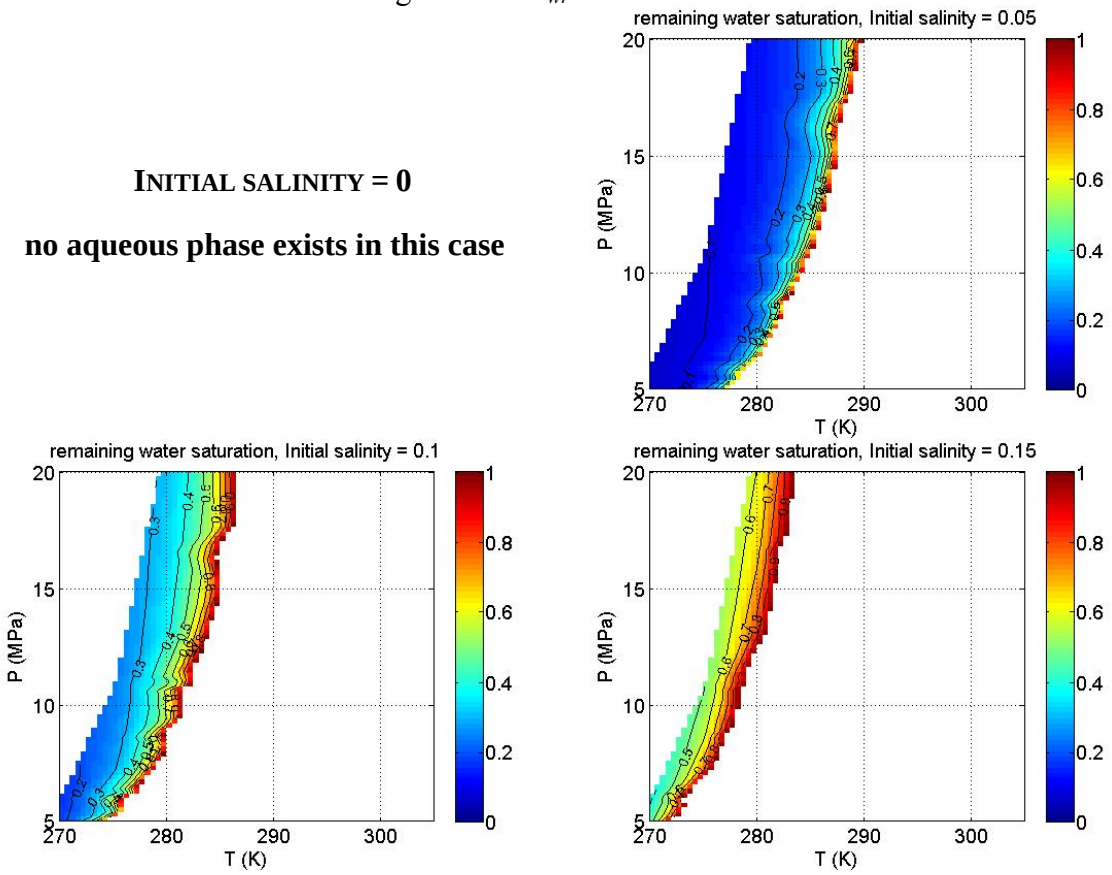

Figure 4.7: Remaining water saturation after hydrate conversion is complete, limited methane and water.

In Figure 4.7, we leave the left column, top row empty as this space corresponds to the case of Sal = 0. No water is left with a complete conversion to hydrate from S_{wc}.

For the cases with $Sal \neq 0$, S_{wr} at a specific T and P increases substantially with increasing salinity, due to the inhibitive effect of salt to hydrate formation. The highest S_{wr} is obtained at the right boundary, where the initial salinity is close to the maximum salinity that allows for the hydrate stability. This constrains the amount of fresh water to be converted, and leaves high residual water saturation at the endpoint.

S_{wr} decreases towards the left boundary, an indication that more fresh water is converted. It is interesting to notice that S_{wc} decreases towards the left boundary from Figure 4.4. The observations in Figure 4.4 and Figure 4.7 suggest that although the initial water saturation (set to be equal to S_{wc} to produce Figure 4.7) increases from left to right boundaries, less water is used for the hydrate formation. We can conclude that with sufficient amount of methane, hydrate formation does not depend on the amount of water, but on the available fresh water that can be utilized. For example, if the initial salinity is equal to the maximum salinity for hydrate formation at specific T and P combination (that is, on the right boundary), no hydrate can be generated as no water molecules are available from the water.

System volume reduction at initial $S_w = S_{wc}$

At the critical water saturation, all methane and the maximum amount of water are consumed to generate hydrate. Only two phases – hydrate and water – remain after the conversion. Consequently, the system volume change is inevitable.

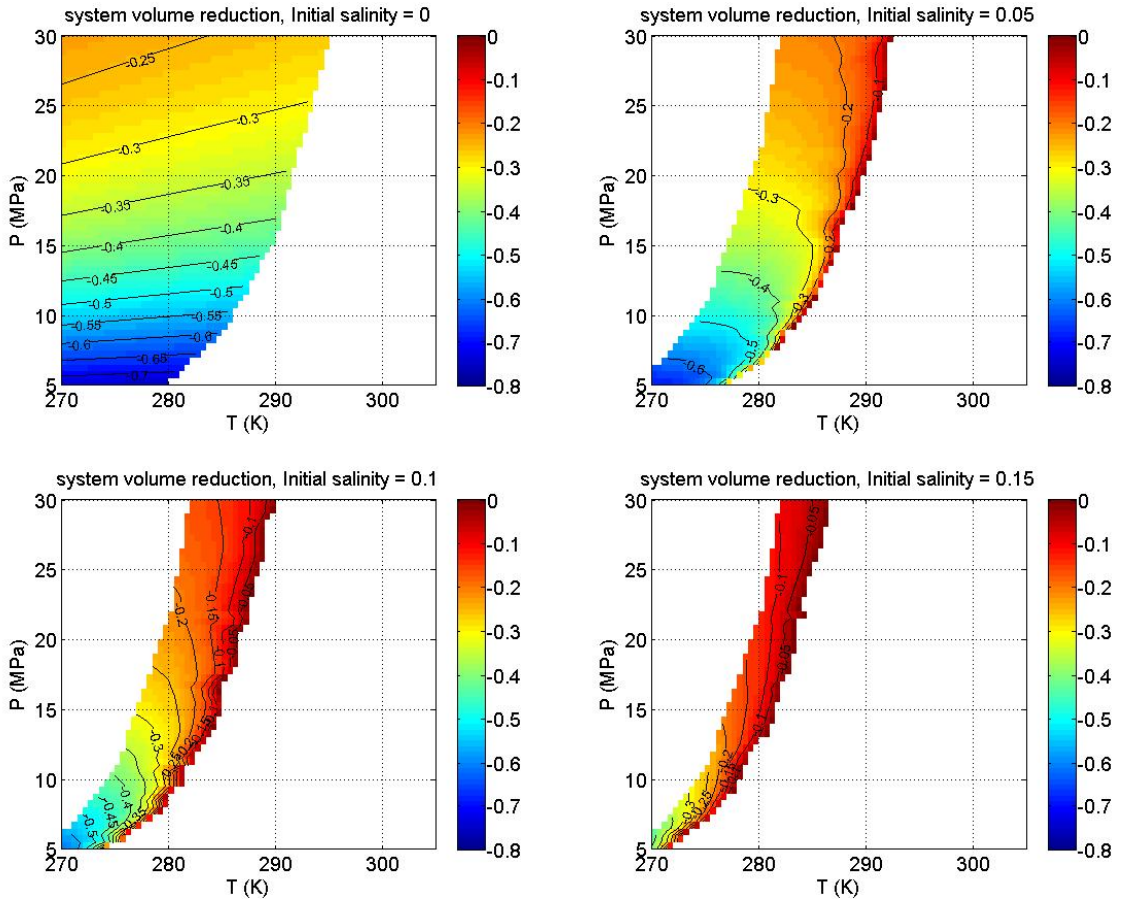

Figure 4.8: System volume reduction at S_{wc}. Note that the color bar has the negative sign, and therefore from red to blue the magnitude of volume reduction increases. The reason for the blank regions is the same as in Figure 4.4.

For all cases shown in Figure 4.8, the system volume decreases when hydrate forms from methane and water, and the initial water saturation is equal to the critical water saturation S_{wc}. The maximum reduction (>70%) happens at low pressure when *Sal* = 0, where the methane density is the lowest of the *T* and *P* regime we are interested in (*T* between 273 K and 280 K and P between 6 MPa to 9 MPa), and the fresh water is completely converted. The condition indicates that a large volume of methane is required to convert a small volume of water, but only produces a small volume of hydrate.

Therefore, the volume reduction is the biggest among all the cases studied. With increasing pressure and decreasing temperature, the methane density increases. When the gas phase gets more dense, it enables the generation of more hydrate in the system, which compensates the system volume reduction of the gas and aqueous phases. The minimum reduction (almost 0, on the right boundary) happens when the initial salinity is close to the maximum salinity, which means almost no hydrate is generated.

At a given T and P, the volume reduction decreases with increasing the salinity. This observation agrees with our preceding discussion that less fresh water can be utilized when increasing the salinity. Since volume reduction is proportional to the amount of hydrate generated, less available fresh water produces less hydrate and therefore lower volume reduction. S_{wc}, however, increases owing to higher salinity

At the low salinity condition (Sal < 5%), we observe large volume reduction (40% to 50%) at low P and T. Such condition corresponds to the hydrate reservoir in the permafrost regions. In the reservoir sediments, the vacancy corresponding to so large a volume reduction will lead to either sediment compaction or fluid displacement from elsewhere in the reservoir to the location of hydrate formation. Fluid displacement could be water in the surrounding aquifer invading the hydrate reservoir, and pore-level imbibition events will take place. On the other hand, if neither gaseous nor aqueous phases can enter the system, then sediment compaction must occur. In this dissertation, we only focus on the former possibility.

System volume reduction at $S_w \neq S_{wc}$

Given the importance of the sign of the volume change (negative means volume reduction, requiring sediment compaction if fluids cannot enter; positive means volume

increase, resulting in fracturing), it is useful to examine the behavior for a range of initial conditions such that S_w differs from the critical value S_{wc}. Figure 4.9, 10, and 11 show the results for initial S_w of 0.25, 0.5 and 0.75, respectively. Depending on the relative amounts of methane and water, the system volume reduction can be determined either by using equation (4.23) or (4.27).

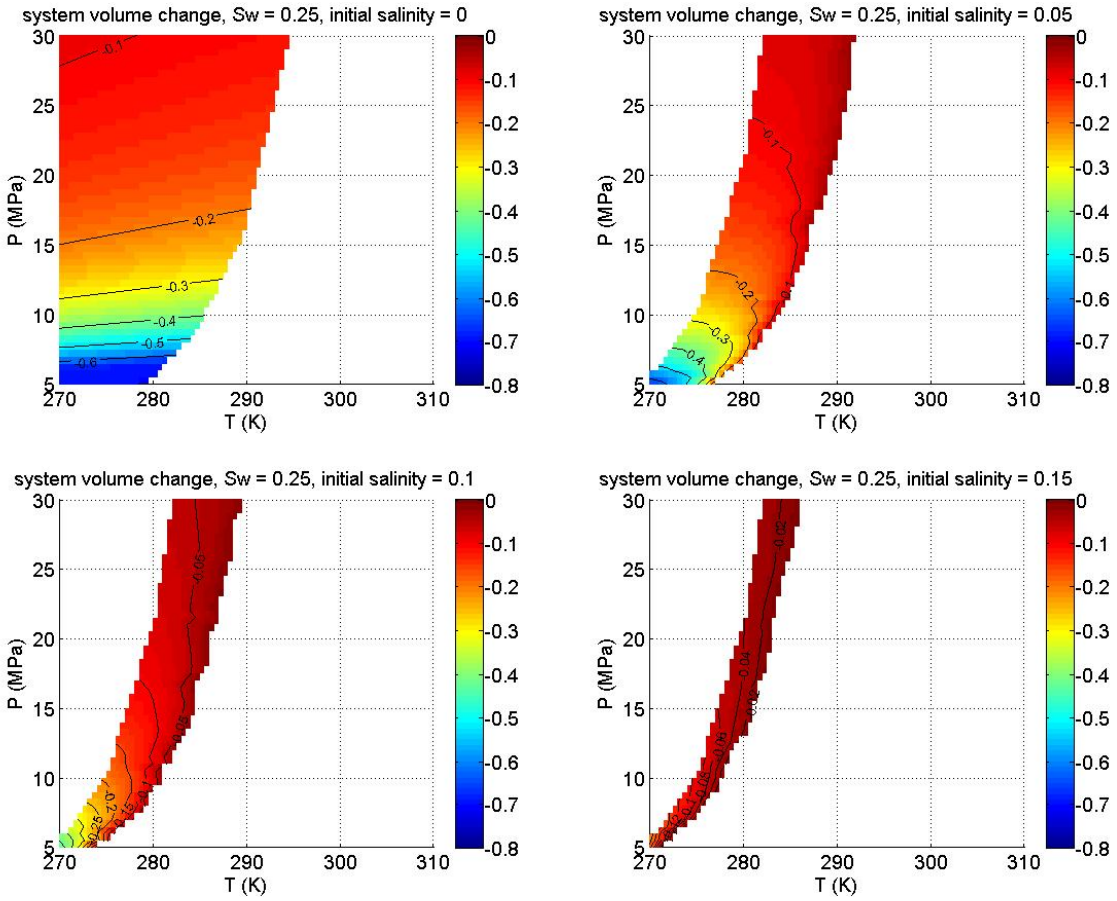

Figure 4.9: System volume reduction when initial $S_w = 0.25$. The color bar has negative signs. The calculation assumes the maximum conversion into hydrate, and neither additional methane nor water enters the volume.

At S_w = 0.25, the system volume decreases at all salinities (Figure 4.9). Figure 4.4 shows that S_{wc} = 0.25 is at the bottom of the *Sal* = 0 case, and is not present for the rest. The volume reduction at S_w = 0.25, at a specific T and P, is always less than the corresponding point when $S_w = S_{wc}$ (Figure 4.8). This is because the available water for hydrate formation is always insufficient to convert all the methane: after the maximum conversion to hydrate, there is coexistence of hydrate, aqueous phase and gas phase in the system.

The volume reduction decreases from high to low T and P combinations. In this case of insufficient water, the amount of hydrate is determined by the availability of water molecules, and therefore is a constant. The change of volume reductions at different T and P are due to the density variation of methane. At high T and P, methane density has a high value, so that the volume used to convert a specific amount of water is less than that at low T and P, where the density is relatively lower. The observation is similar with different initial salinity (*Sal*).

At a specific T and P, the volume reductions for different *Sal* changes significantly. The amount of available fresh water decreases with increasing *Sal*, and therefore produces less hydrate and less volume reduction.

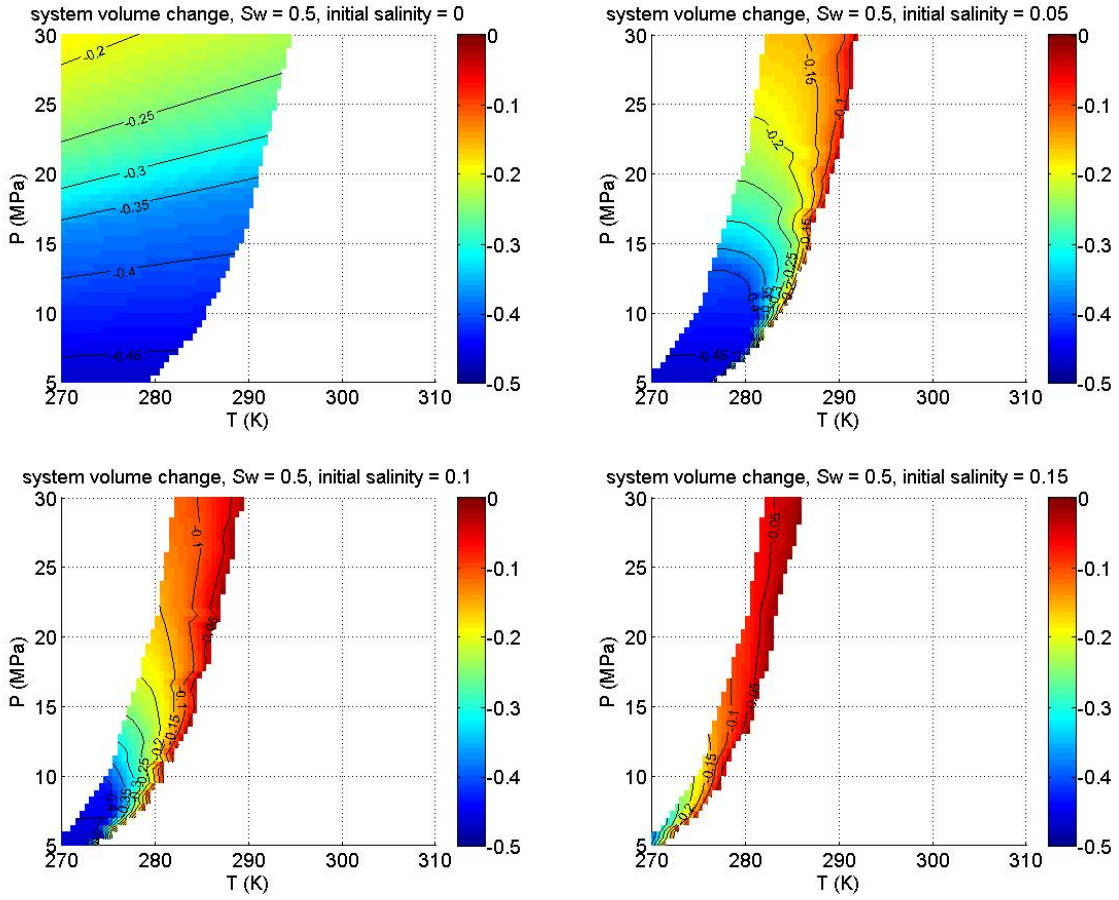

Figure 4.10: System volume reduction when $S_w = 0.5$. The color bar has negative signs. The calculation assumes the maximum conversion into hydrate, assuming that neither additional methane nor water enters the volume.

Figure 4.10 also shows the system volume reduction for all the salinities at $S_w = 0.5$. This saturation is labeled in red curve in Figure 4.4. S_{wc} is higher above the curve, indicating that $S_w = 0.5$ is not enough to convert all the methane into hydrate; however, below the curve S_{wc} is smaller than 0.5, so that fresh water is excess. The red curve is the boundary for excess water versus excess methane cases. Both cases suggest a volume reduction during the hydrate association from water and methane. It is similar to the case of $S_w = 0.25$ (Figure 4.9) that the volume reduction is greater at higher T and P, an effect

of the greater methane density variation at larger P. In this water excess case (below the red curve), the amount of hydrate is only controlled by the availability of methane. Methane with higher density is able to produce more hydrate, which compensates the volume reduction in the system and yields less volume reduction.

The volume reduction always has smaller magnitude when S_w differs from S_{wc}. Thus calculations of the effect of the volume change made at S_{wc} provide an upper bound on the actual behavior.

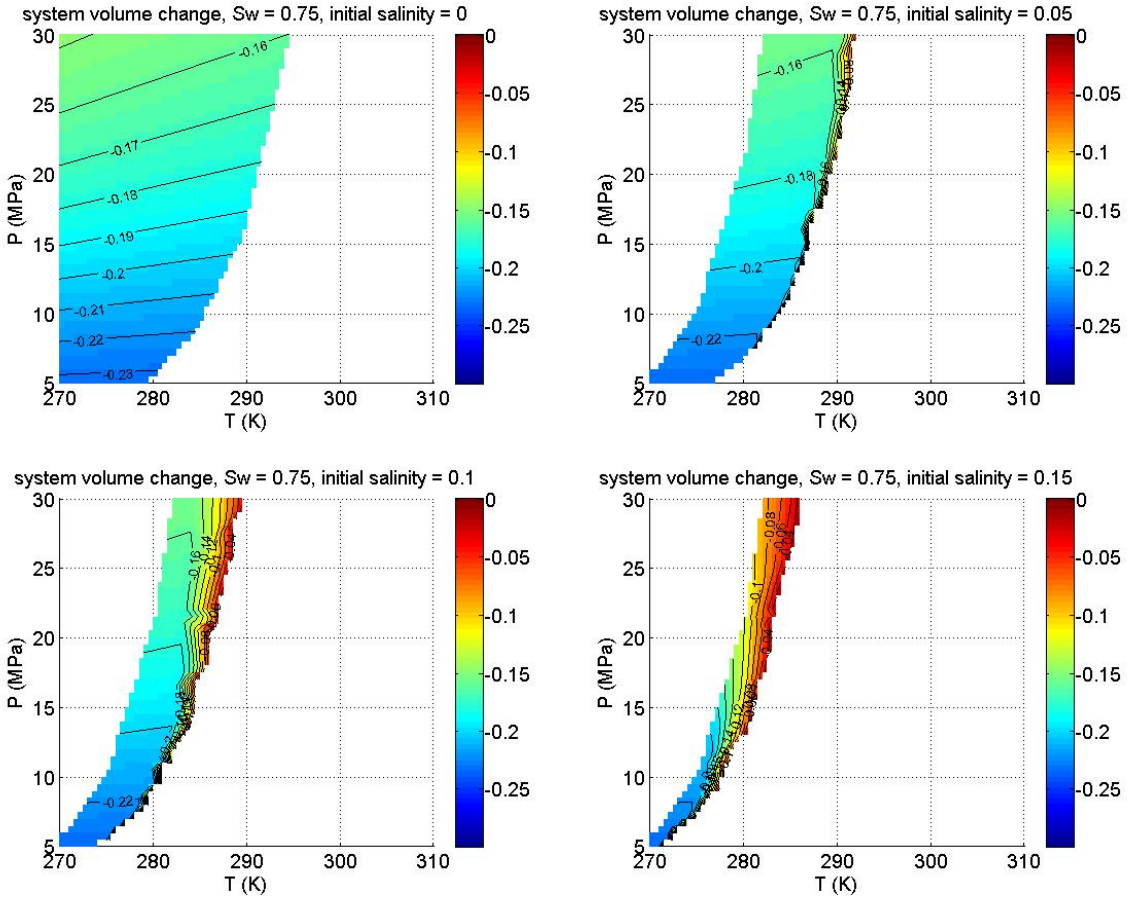

Figure 4.11: System volume reduction when $S_w = 0.75$. The color bar has negative signs. The calculation assumes the maximum conversion into hydrate, assuming that neither additional methane nor water enters the volume.

The last case we consider is when S_w = 0.75, a very high salty water saturation that is similar to the imbibition endpoint. At *Sal* = 0, fresh water is excess and methane gas becomes the limited component. The salinity effect becomes obvious as the volume reduction is almost zero close to the right boundary, but increases significantly as moving away from the boundary. We observe a relatively smaller volume reduction compared to the case of S_w = 0.25 and S_w = 0.5 at the same *T* and *P*.

The situation of S_w = 0.25 represents the wetting phase saturation at a drainage endpoint (the value might not be the same as drainage endpoint; however, the same analysis can be applied). S_w = 0.5 can be considered as the mid point of drainage/imbibition, when wetting and nonwetting phases are all connected with the bulk. S_w = 0.75 resembles the case of imbibition endpoint, where gas phase has been displaced by wetting phase down to its residual saturation; in this case S_{gr} would be 0.25. As S_w increases from 0.25 to 0.75, the amount of volume change is smaller. Thus converting fresh water and methane at drainage endpoint will cause a larger volume reduction than at intermediate saturations, and converting residual gas to hydrate will induce the smallest volume change. Even at residual saturations, however, the volume reduction could be 20% under typical reservoir conditions.

4.2.2 Limited methane, fixed water saturation

In this section, we consider a scenario that methane is limited, but not water. Water saturation is a fixed value This corresponds to the situation that water is always connecting to the bulk phase in the reservoir, while gas on the other hand is contained by the trap and seal, and isolated from the gas source. The hydrate formation is considered to be much slower than the salt ion diffusion in the water. Therefore, the salt ions will not

accumulate and inhibit the hydrate formation. Salinity is not a determinant in the calculation. Also we assume that the initial S_w remains constant as hydrate forms.

Critical water saturation

There is no critical water saturation based on the setting of unlimiting water supply.

Hydrate Saturation

Because of the unlimited water and because we assume the water saturation after hydrate formation is the same as the initial water saturation, the hydrate saturation is only determined by the amount of methane in the system.

Figure 4.12 shows the hydrate saturation computed from equation (4.28) at different salinities for initial S_w = 0.25. Because S_w is fixed as 0.25, the initial gas saturation S_g 0.75 determines the volume that will be occupied by hydrate, i.e. we will have S_h is less than or equal to 0.75. We labeled the contour of S_h = 0.75 as the red curve. When S_h is greater than 0.75, the volume occupied by hydrate will be greater than the volume originally occupied by methane, which leads to a system volume increase (since we assume S_w fixed). However below the red curve, hydrate volume is smaller than the methane volume, so that the system volume will decrease as methane is converted into hydrate. Hydrate saturations that exceed unity are obviously nonphysical but are included for generality. The meaning of this region is the same as for $S_h > 0.75$, namely that the system pore volume would have to increase to accommodate the hydrate.

All the cases in Figure 4.12 suggest that the system volume change from positive to negative as decreasing temperature and pressure. As water is unlimited and the

saturation is presumed constant, this behavior is the consequence of the variation of methane density. Smaller methane density creates less hydrate and thus decreases the system volume.

For the hydrate systems we are interested in (shallow sediments in permafrost regions), T and P have relatively smaller value (T from 273 K to 280 K, P from 6 MPa to 9 MPa), so that system volume expansion never takes place. It should be noted that although salinity does not affect the calculation in the following calculation, it does determine the right boundary of the region, that is, the boundary beyond which hydrate is not stable. Since we assume salinity does not accumulate in the water as hydrate is formed, hydrate saturation does not vary with proximity to the stability boundary.

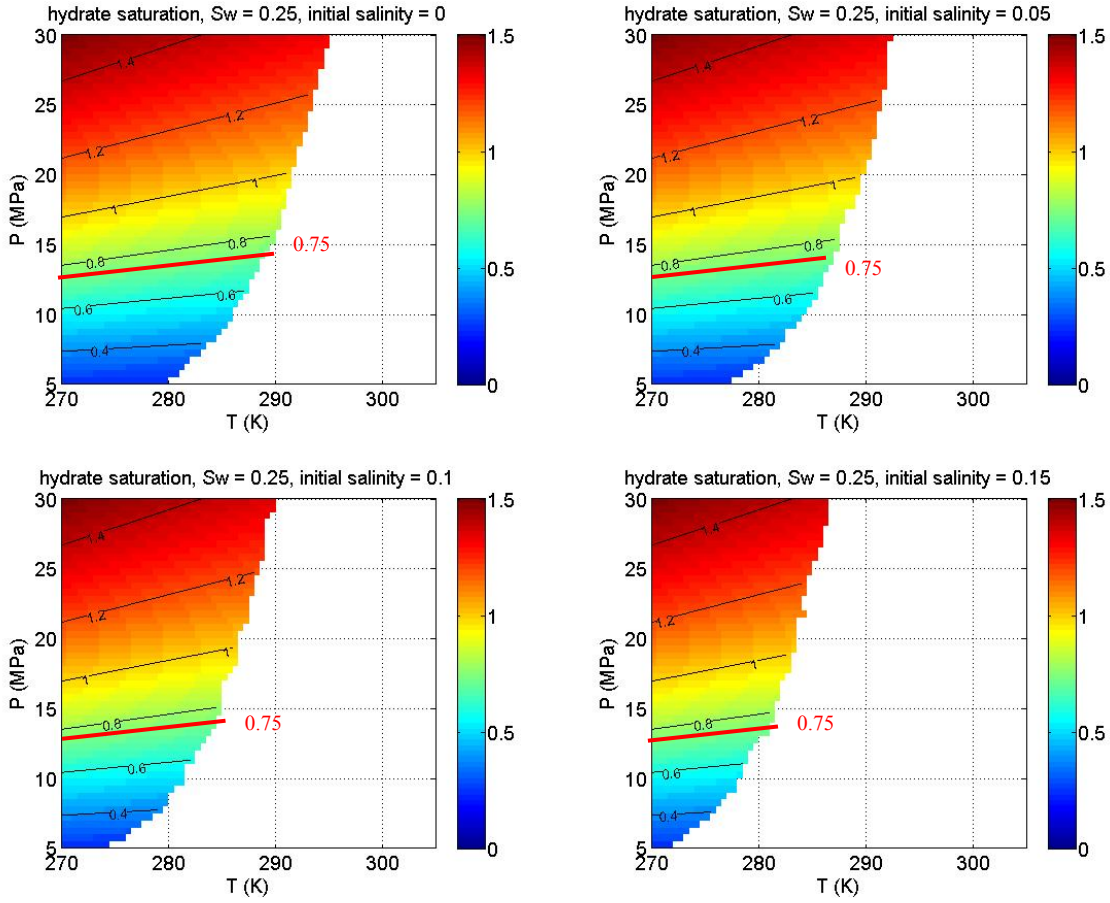

Figure 4.12: Hydrate saturation resulting from S_w held constant at 0.25, at four salinities. Water is assumed to be available without salinity buildup. There is no supply of methane from outside the system. The red line is the initial gas saturation (75%). Above this line system volume expands, and below this line is the opposite.

Figure 4.13 shows hydrate saturation resulting from initial S_w = 0.5 at four different salinities. The initial methane saturation S_g (=1-S_w) = 0.5, which is the labeled red curve. When hydrate saturation is greater than 0.5, it means the hydrate volume is greater than the initial methane volume. Consequently the system volume increases (by

assumption the water volume does not change). When hydrate saturation is smaller than 0.5, the opposite situation holds, that is, the system volume decreases.

The similar analysis can also be applied to explain Figure 4.14, where the initial S_w is 0.75. Here, the contour of S_w = 0.25 becomes the watershed for system volume increment or reduction: above that curve, system volume will increase; while below it will lead to system volume reduction.

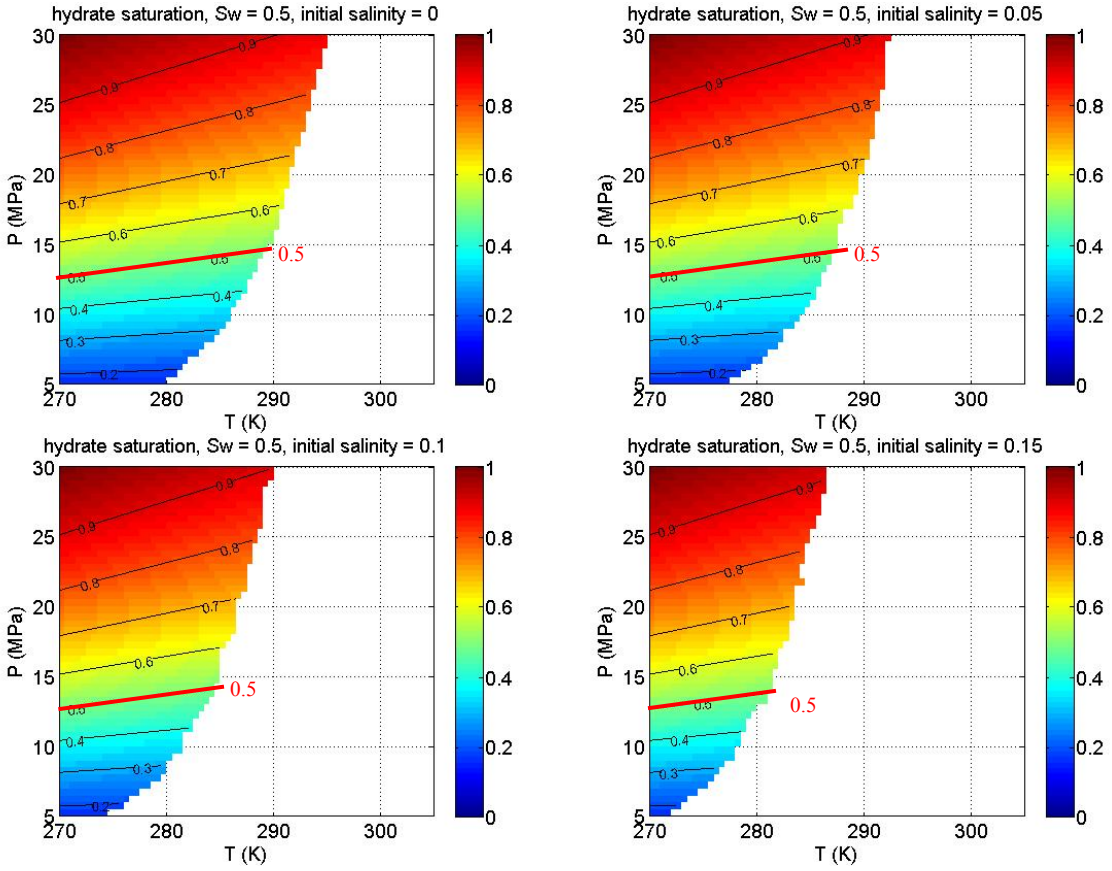

Figure 4.13: Hydrate saturation resulting from S_w held constant at 0.5, at four salinities. Water is assumed to be available without salinity buildup. There is no supply of methane from outside the system. The red line is the initial gas saturation (50%). Above this line system volume expands, and below this line is the opposite.

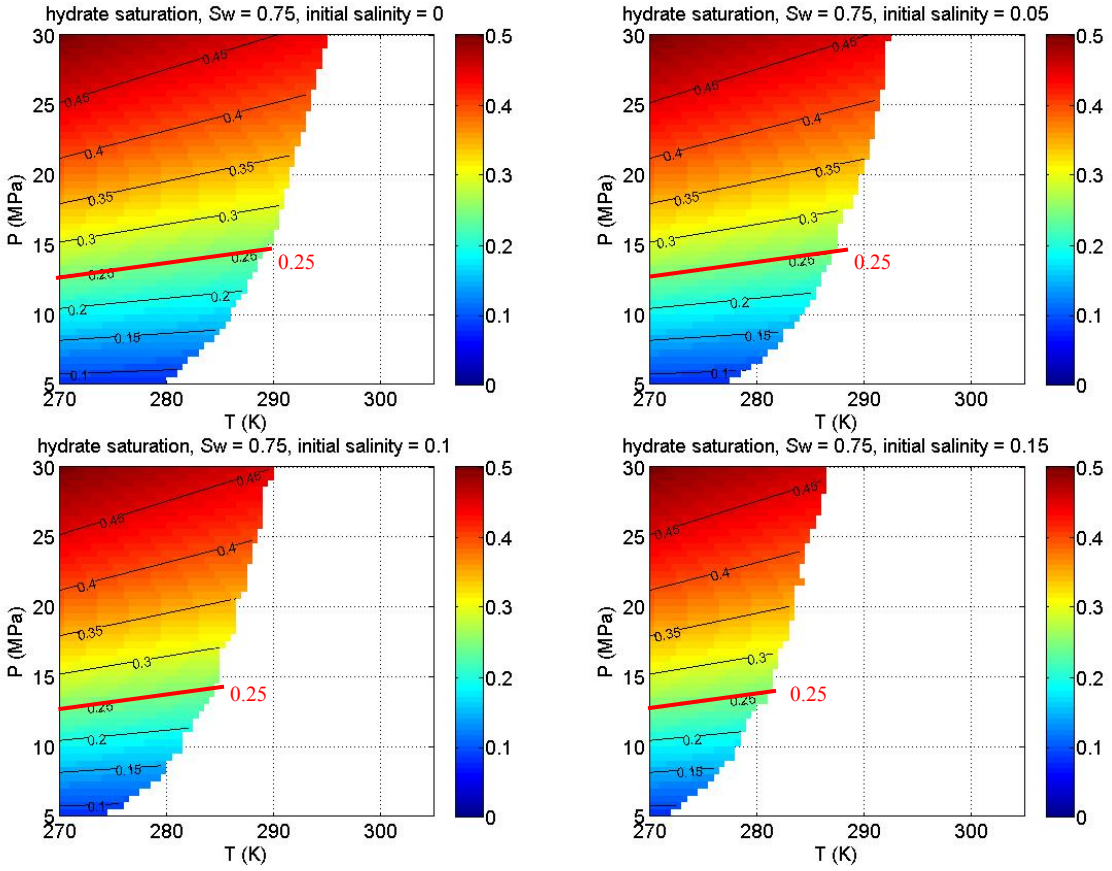

Figure 4.14: Hydrate saturation resulting from S_w held constant at 0.75, at four salinities. Water is assumed to be available without salinity buildup. There is no supply of methane from outside the system. The red line is the initial gas saturation (25%). Above this line system volume expands, and below this line is the opposite.

As in this case the hydrate saturation is totally determined by the amount of initial gas in the system, we observe a significant variation of hydrate saturation from Figure 4.12Figure 4.13 and Figure 4.14, at the same T, P and initial salinity. In this scenario where water is presumed to be available and held at a constant value, the hydrate saturation is only determined by the amount of methane in the system. In general, at higher P and lower T, the methane density becomes higher, and thus can form more hydrate.

System Volume change

Because S_{wc} is not defined in this scenario (that is, water saturation is held constant, and water is always available for making hydrate), system volume reduction at $S_w = S_{wc}$ and $S_w \neq S_{wc}$ is not relevant. Instead we analyze the system volume change based on the initial gas saturation from equation (4.29).

Figure 4.15 shows the system volume change with limited methane and unlimited water. When the contour value is 0, the volume of methane converted is equal to the volume of hydrate formed, and the system volume remains unchanged. This contour corresponds to the red curve of Figure 4.12, which indicates that all methane is converted into hydrate and fills the vacancies. Above this contour, the system volume increases as the methane density is greater than the critical density (122 kg/m^3, which is the methane molecule density in the hydrate lattice); while below the contour the system volume will decrease.

With increasing the initial salinity, the contour map does not change except for the GHSZ shrinkage to the upper left. As long as water can be supplied from outside the system, there is always sufficient fresh water to generate more hydrate. Consequently, hydrate saturation is not a function of initial salinity in this case. It is only controlled by the gas saturation, which is kept as a constant of 75% (1-S_w). This is the reason for the same system volume change for all the different initial salinities.

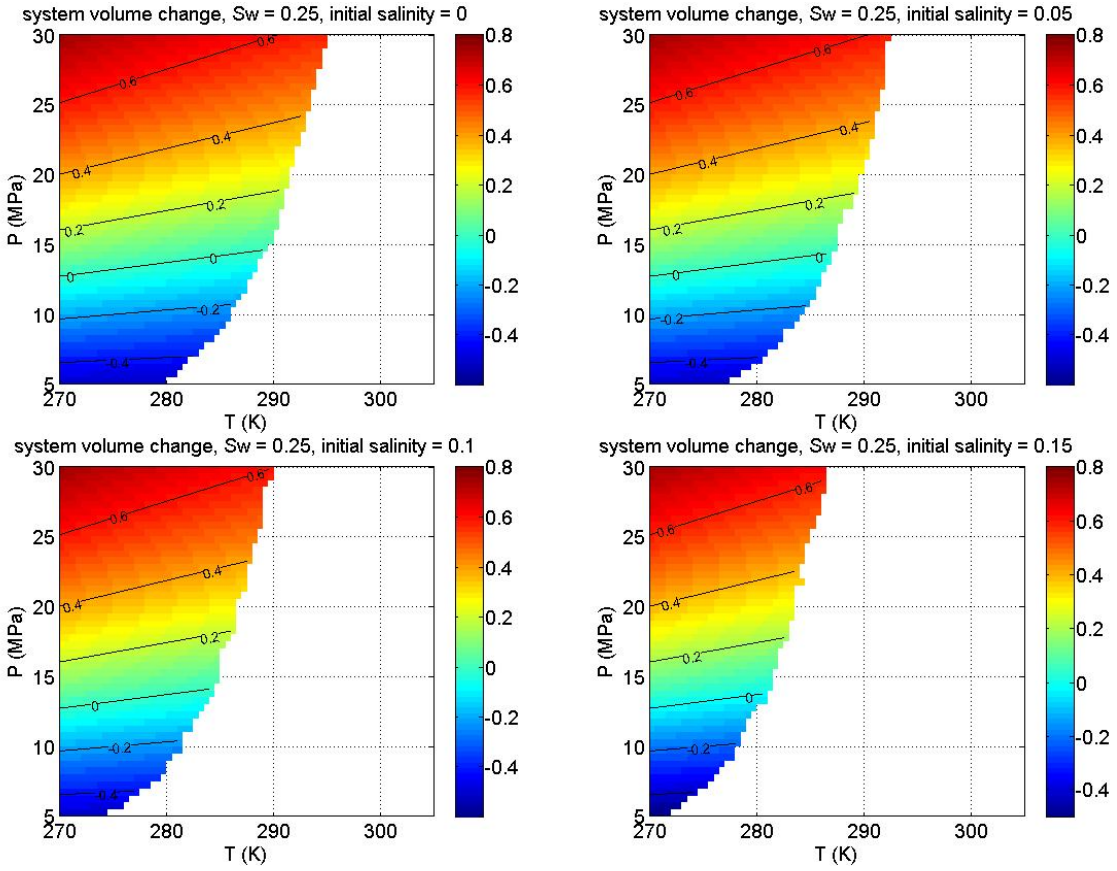

Figure 4.15: System volume change, S_w is held constant at 0.25. Water is assumed to be available without salinity buildup. There is no supply of methane from outside the system. Equation (4.29) is used for this calculation.

Figure 4.16 shows the system volume change at S_w = 0.5. Contour = 0 is at the same location as in Figure 4.15 and Figure 4.17, where the methane density is equal to the critical methane density (122 kg/m^3, as computed from equation (4.30)). The volume change can also be positive or negative, depending on the region is above or below contour = 0. Similar behavior can also be observed in Figure 4.17, where S_w = 0.75.

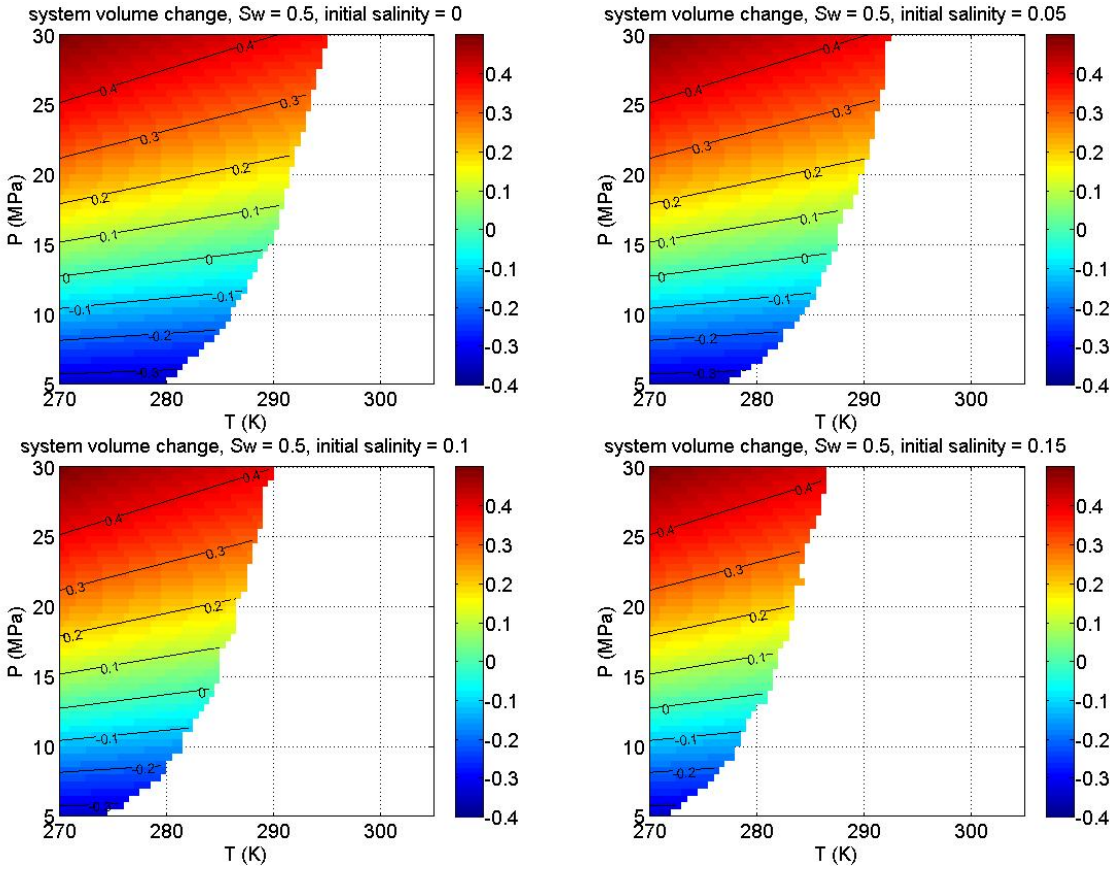

Figure 4.16: System volume change, S_w is held constant at 0.5. Water is assumed to be available without salinity buildup. There is no supply of methane from outside the system. Equation (4.29) is used for this calculation.

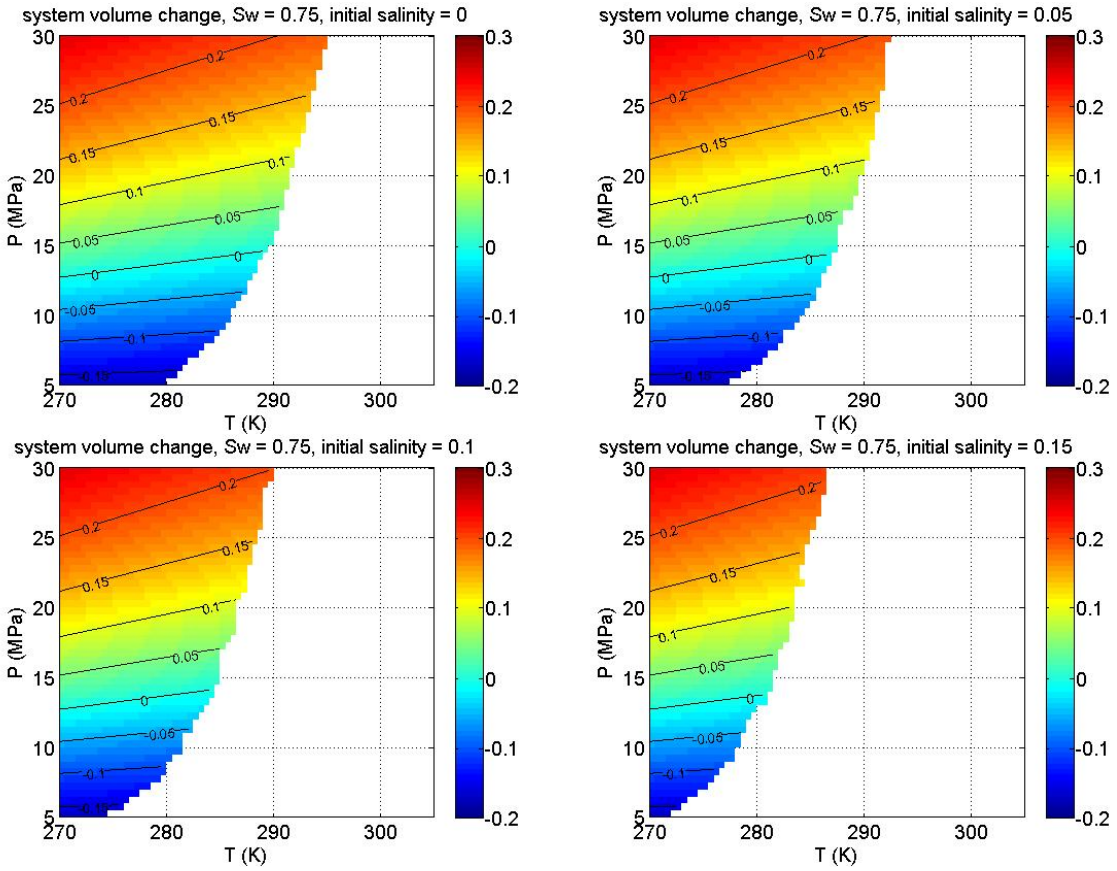

Figure 4.17: System volume change, S_w is held constant at 0.75. Water is assumed to be available without salinity buildup. There is no supply of methane from outside the system. Equation (4.29) is used for this calculation.

The comparison among Figure 4.15, Figure 4.16 and Figure 4.17 shows that the possible volume change (the absolute value) at a specific T and P decreases as S_w increases. Since the water volume is assumed constant, the volume change of the system is totally determined by the difference between methane and hydrate volumes. When S_g (1-S_w) decreases, less hydrate can be generated. Since more hydrate formation leads to more volume change, from Figure 4.15 to Figure 4.17 the system volume change decreases at the same T and P with decreasing the initial gas saturation.

4.2.3 Discussion

Although the scenarios proposed in this section are different – hydrate formation from limited water and methane vs. from limited methane but unlimited water – we reach a similar conclusion regarding the effect of initial saturations of gas and water phases. For both models, lower initial water saturation S_w leads to the greater volume change. Consequently the greatest need for accommodation, whether by grain movement or by fluid displacement, occurs at small S_w. This corresponds to the situation of hydrate formation after gas has invaded a sediment and displaced water down to the drainage endpoint.

An important qualitative difference also emerges from the models. In the limited water and methane scenario, the volume change is always negative, whereas in the limited methane and unlimited water scenario, the volume change can be negative or positive, depending on the methane density and hence upon T and P.

Under the assumption of the limited water and methane model, sediment compaction must take place to accommodate the volume change. If mechanical constraints prevent such compaction, *e.g.* if the sediment has already been deeply buried, then the fluid phase pressures will decrease. This will stop hydrate formation when the phase stability boundary is reached. Alternatively, the pressure changes will cause important changes in the grain-scale configuration of the fluids.

Under the assumption of limited methane/unlimited water model, the negative volume change that occurs at lower values of T and P would require sediment compaction. If this cannot occur because of mechanical constraints, the gas phase pressure would decrease. The aqueous phase pressure would remain constant because of the presumed connection to bulk aqueous phase. This breaks the original capillary

equilibrium and the fluid displacement will occur. We analyze this behavior in the next section of this chapter.

On the other hand, the positive volume change that occurs at larger values of pressure would require the sediment to expand. This could induce fractures, whose onset in the gas/water system is described in (Juanes and Bryant, 2009). However, such mechanism is not covered in this dissertation. More information can be found at (http://www.netl.doe.gov/technologies/oil-gas/FutureSupply/MethaneHydrates/projects/DOEProjects/MH_43067GasHydSediments.html)

4.3 HYDRATE SATURATION PREDICTION IN THE PORE SCALE – THE EFFECT OF GAS SATURATION FOOTPRINT

Our conceptual model suggests that hydrate formation took place at the base of gas hydrate stability zone (BGHSZ) when it descended over the geological time, either as sea level rose (above ocean sediments) or air temperature decreased (at the surface above Arctic sediments). The overall hydrate distribution at the field scale resulting from this type of conversion is determined by many factors. In section 4.1 and 4.2 we have discussed the effects of temperature, pressure and salinity on hydrate saturation. However, the models used in section 4.1 and 4.2 are based on a simple 1D box, while ignores the factors only happening in a real porous medium. An important one is the different capillary events, which determines the hydrate saturation at each layer of the reservoir. Another factor is the need to redistribute the free gas in the vertical direction, driven by the decline in pressure caused by hydrate formation (discussed in the next chapter). Here we propose two pore-scale models that would yield the maximum and minimum hydrate saturation in the porous medium. We illustrate the model with a 2D porous medium, for the purpose of better visualization and demonstration. Calculations are done in 3D geometries to produce necessary properties for the hydrate saturation prediction in the field scale.

4.3.1 Hydrate formation scenarios in the pore scale

We assume the following scenario for hydrate formation at the pore scale. The steps are discussed in more detail with schematics in subsequent sections.

1. The gaseous phase (pure methane) and aqueous phase (water with constant salinity) are at capillary equilibrium, so that methane/water interfaces are static.

Our model also assumes that both methane and water are connecting to the bulk volume, and thus neither of them would be exhausted (it is different from the settings in section 4.2). We consider the case that the salt ion diffusion rate is much larger than the hydrate formation rate, and therefore salinity does not inhibit the conversion.

2. The first layer of hydrate crystal forms along the interface between methane and water when the local temperature and pressure reach the phase equilibrium boundary (the hydrate-water/gas-water boundary).

3. Forming a layer of hydrate reduces the gaseous phase volume more than the aqueous phase, since volumetrically hydrate formation consumes more methane than water at typical hydrate stability conditions (P = 5 to 10 MPa, T = 273 to 283 K). Therefore, hydrate preferentially grows into the gaseous phase, which is consistent with the discussion in Section 4.1 and 4.2. In this fashion a layer of hydrate appears between gas and water, and the gas/water interface is replaced by a methane/hydrate interface, a thin hydrate layer, and a hydrate/water interface.

4. Continued growth of hydrate requires water to migrate from the aqueous phase in the sediment through microscopic defects (e.g. crystal defects within the hydrate, grain surface roughness, etc.) to the methane/hydrate interface.

5. The total vacancy (reduction in methane volume + reduction in water volume – increase in hydrate volume) generated when an incremental volume of hydrate forms is filled by aqueous phase. Depending upon the connectivity of the aqueous phase (between the interface where hydrate is forming and the bulk phase of formation water) and, more critically, upon the rate at which water can migrate through the existing hydrate in step (4), the rate of this filling may be faster or slower than the rate of hydrate formation at the interface.

In this model, hydrate saturation that accumulates at BGHSZ can vary between maximum and minimum values. If the water supply rate is much smaller than the hydrate formation rate, hydrate saturation will reach a maximum value. On the other hand if the water supply rate is much larger than the hydrate formation rate, hydrate saturation will reach the minimum value. The purpose of this section is to identify the two limiting scenarios, and give an insight into the hydrate formation in the porous medium.

LSMPQS is applied to determine the geometric configuration of the fluid interface during hydrate formation, and thus saturation. This technique employs no geometry simplification, and is capable of capturing the natural movement of fluid interfaces in great detail.

4.3.2 Hydrate saturation and distribution prediction in porous medium, Scenario A: water supply rate much smaller than hydrate formation rate

In this limiting case hydrate formation is controlled by the water availability. Thus the water supply rate controls the rate of hydrate formation. Figure 4.18 demonstrates this case in a small 2D domain, which is a simple granular medium with large open spaces. Such domain yields clear water/methane interface for the demonstration purpose. The gray disks are sand grains, blue regions correspond to the aqueous phase, green region is hydrate phase, and the red region is gas phase. The initial aqueous and gaseous phase distribution (A) is obtained by simulating a drainage endpoint with our LSMPQS simulation. The initial hydrate nucleation happens at the fluid/fluid interface, which consumes both water and methane (the salt ions are excluded from the hydrate, and are assumed to disperse at a rate much faster than the hydrate formation rate. Salinity is therefore not an inhibitor). The hydrate layer does not form as a single crystal. The microscopic defects within the layer of crystals allow water to imbibe through the

hydrate layer and form a thin layer of water at the hydrate surface (Figure 4.18B the zoom-in figure, notice the thin water layer (blue) on the gaseous phase (red)). Since hydrate formation is rapid compared to water supply, this water layer is quickly converted into hydrate. This further reduces the gaseous phase pressure (Figure 4.18B and C) and water again imbibes to the gas-hydrate interface. During this process, we assume that the curvature of hydrate layer maintains the curvature of capillary-equilibrium between gas and water, and therefore the hydrate invasion into the gaseous phase can be approximated as an imbibition process. That is, the movement of the gas/hydrate interface is calculated as though it were a gas/aqueous phase interface. The position of a gas/aqueous phase interface is readily computed by LSMPQS simulation. This stage of the hydrate formation (Figure 4.18B and C) is referred to as the stage 1.

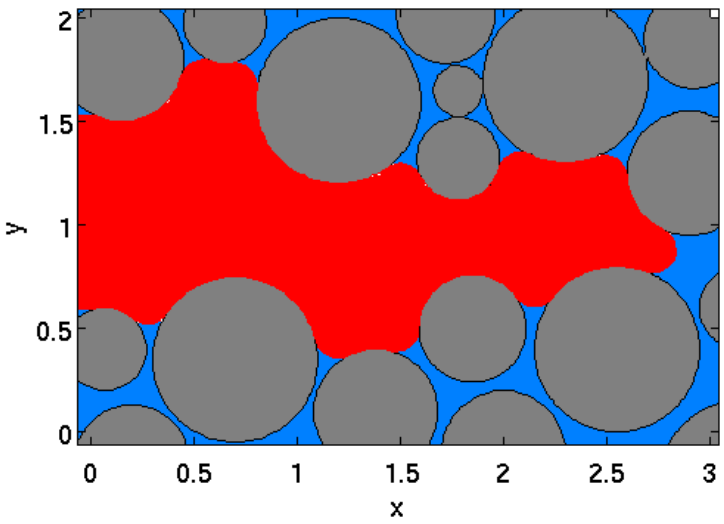

A. The initial methane (red) and water (blue) distribution in a granular medium (gray disks represent the grains). The distribution is in capillary equilibrium (satisfies Young-Laplace equation), obtained at the drainage endpoint by the LSMPQS simulation.

The colors of the interface are only for the demonstration purpose, and should not be associated with the colors of the phases.

Continued on next page

B. Stage 1, the incremental movements of methane/water interface due to hydrate formation (phases are not colored for a better visualization). This figure shows three sequential representative locations of interfaces during hydrate formation. The arrows indicate the directions that the interface moves and in which hydrate grows. The first layer of hydrate will form at the interface. Subsequent hydrate continues to grow into the gaseous phase.

A schematic (inset and zoom in below main figure) describes the mechanism by which water is supplied to maintain hydrate formation at the interface between methane and hydrate. Numerous tortuous conduits exist in the hydrate layer (green) because of the crystal defects. Water (blue) can therefore be sucked through the layer and coats the hydrate surface. When in contact with methane (red), new hydrate can form at the methane/water interface. This is the driving mechanism for hydrate "invasion" of the methane-occupied pores.

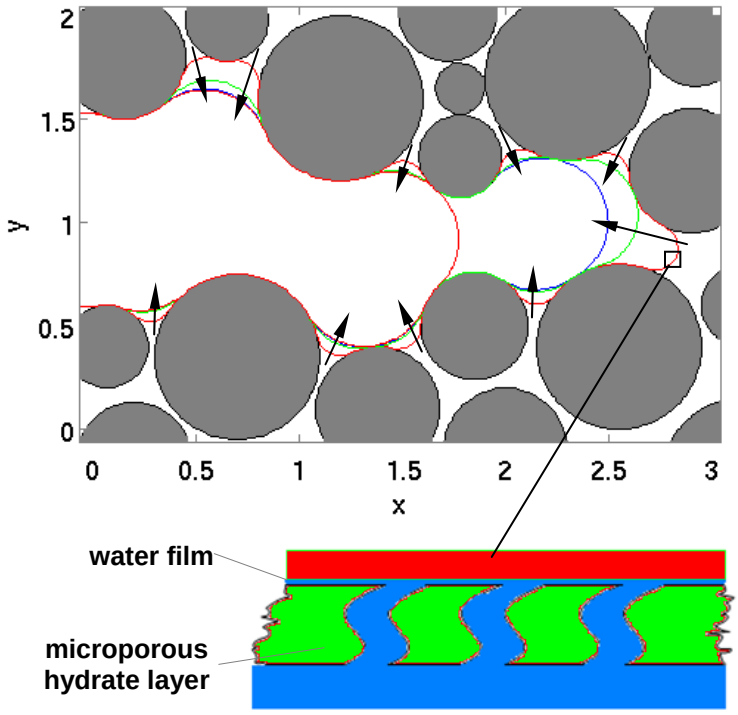

C. Hydrate distribution (green) when the interface (indicated by the arrow) is at the critical point. From this point, an infinitesimal decrement of capillary pressure will make the intereface unstable.

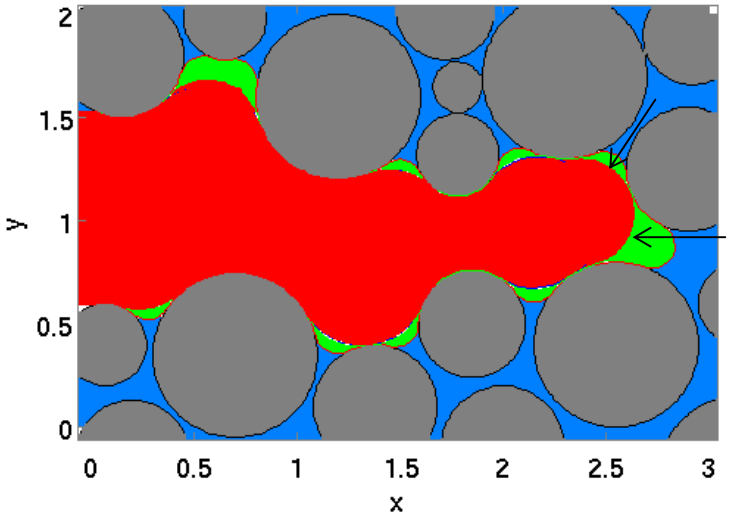

Continued on next page

D. Stage 2, the incremental movement of methane-water interface (from green to red interfaces; phases are not shown). The red curve is the capillary-equilibrium curve after an imbibition jump from the position indicated by the green curve, computed as if aqueous phase were displacing gas. Because the scenario considered here assumes that water can be supplied only very slowly, the jump cannot occur. Instead gradual incremental movement from green to red curves (blue curve is an example intermediate position) happens during this stage. The rapid formation of hydrate means that similar to B, hydrate grows from the water film on the methane/hydrate interface and gradually invades the gaseous phase.

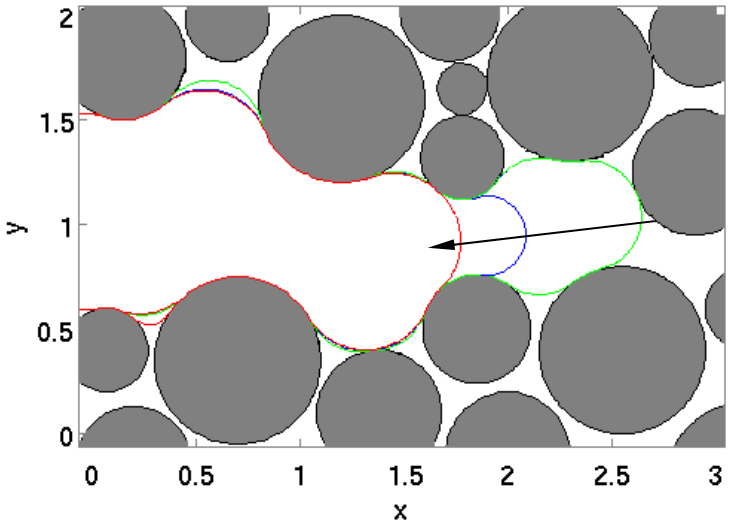

E. Hydrate distribution (green region) after stage 2. The total hydrate distribution is due to the hydrate formations in stages 1 and 2. Hydrate occupies the entire space that was taken up by methane before. That is, hydrate distribution replaces the initial methane gas distribution.

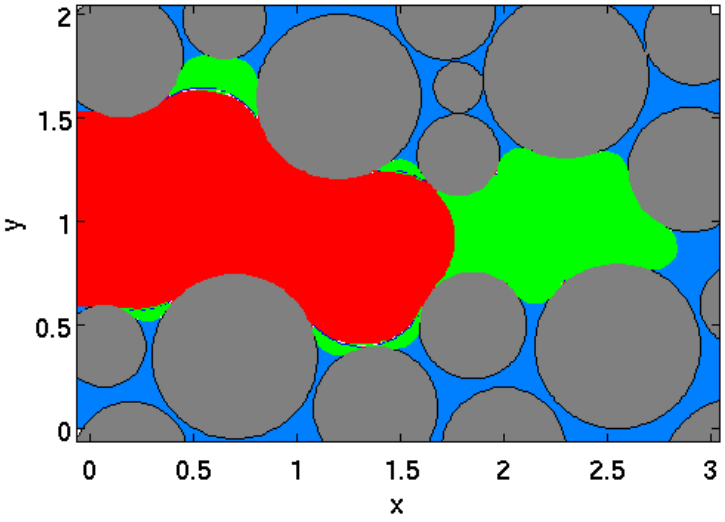

Continued on next page

F. Stages 1 and 2 repeat themselves cyclically, which allows the hydrate formation slowly invades the gaseous phase. The final hydrate distribution from the right figure (green is hydrate and blue is water) is identical with the initial methane distribution in A.

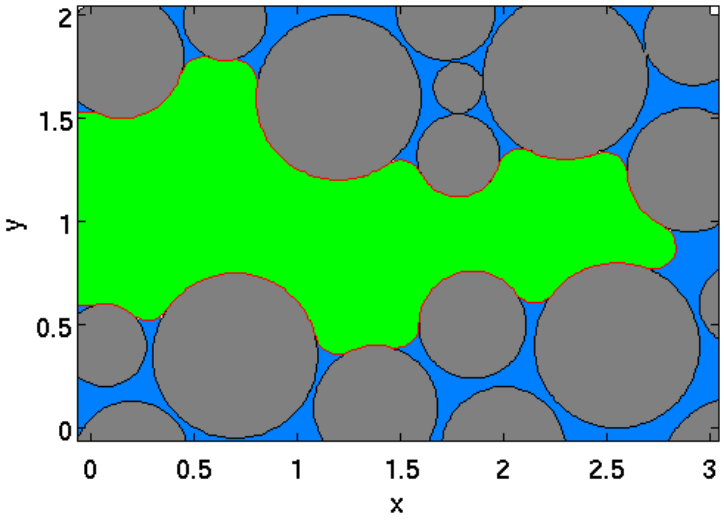

Figure 4.18: Schematics of scenario A that water supply rate is much smaller than hydrate formation rate. This gives the maximum hydrate saturation as hydrate replaces all the initially present gas.

The critical feature of this limiting case is that the gas/hydrate interfaces will gradually advance into the gas phase, so that adjacent interfaces eventually merge. This also means that separated gas/water interfaces merge as well, as water always coats the hydrate surface (Figure 4.18B the zoom-in figure) because of capillarity in the microporous hydrate. We have previously established that the point of merger of methane/water interfaces is unstable: in classical imbibition, the interface will jump to a new location. This is the Melrose condition for imbibing a pore. However when two methane/hydrate interfaces (also methane/water interfaces) merge, a spontaneous Melrose imbibition event is not possible, because the fluid (water) is converted to a solid (hydrate) as soon as it reaches the methane/hydrate interface, and thus no extra water is available for the imbibition jump. In other words, the limiting water supply disables imbibition events, and only the slow and incremental movement of interface is allowed (Figure 4.18D and E). This increment movement gives a similar pattern as for Figure

4.18B and C. That is, water is sucked through the hydrate layer and coats the hydrate surface as a thin layer, of which the water is later converted into hydrate and ions are dispersed. This gradual movement of hydrate finally allows the interface to move into the following pores. We refer to this (Figure 4.18D and E) as stage 2.

This incremental motion has an important implication: all the gas phase initially present is eventually converted to hydrate. Thus the final hydrate saturation has the same pore-scale "footprint" (occupies the same pores, throats, etc.) as the initial gas saturation.

These two stages have the same behavior but are driven by different forces. Stage 1 is controlled by the capillary equilibrium, which is independent of the water supply rate. Stage 2, which would exhibit an imbibition jump if both phases at the interface were fluids, happens only because the water supply rate is slower than the rate of hydrate formation at the methane/hydrate interface. These two stages happen cyclically.

This model allows for maximum hydrate saturation in the porous medium. Based on the assumption that hydrate grows into gaseous phase only, hydrate distribution fully repeat the footprint of the initial gas distribution (Figure 4.18F). The final hydrate saturation is equal to the initial gas saturation.

4.3.3 Hydrate saturation and distribution prediction in porous medium, Scenario B: water supply rate much larger than hydrate formation rate

This scenario has the similar stage 1 as in section 4.3.2: hydrate slowly invades the gaseous phase (Figure 4.19B and C). When the methane/water interface reaches the critical point at which two interfaces merge (the end of stage 1), the fluid behavior becomes different from 4.3.2. The assumption that water supply rate is much larger than the hydrate formation rate indicates that water supply is no longer a constraint of imbibition. At the critical point, a Melrose imbibition jump takes place due to the

unstable fluid/fluid interface, and invades gas-filled pores in an abrupt fashion. This is the conventional imbibition process, and can be modeled by LSMPQS technique.

In Figure 4.19C, imbibition jump of a methane/water interface takes place instead of the incremental movement. Consequently a large portion of the pore(s) will be filled by water. After the imbibition jump, a stable interface exists between methane and water. As stated by the assumption, hydrate grows only into the gaseous phase. Therefore, water invasion during the imbibition jump will not be converted into hydrate (Figure 4.19D and E). Hydrate resumes growth only on the new stable locations of the gas/water interface(s), and into the gaseous phase as before. After several steps of incremental movement of the gas/hydrate interface into the gaseous phase, a Melrose imbibition jump happens again. This sequence of events leads to a sandwich-like pattern, illustrated at the imbibition endpoint in Figure 4.19F: water droplets are encaged by hydrate shells in the entire porous medium.

A. The initial methane (red) and water (blue) distribution in a porous medium (gray disks represent the sand grains). The distribution is in capillary equilibrium (satisfies Young-Laplace equation), obtained from the drainage endpoint by the LSMPQS simulation.

The colors of the interface are only for the demonstration purpose, and should not be associated with the colors of the phases.

This is the same as Figure 4.18A.

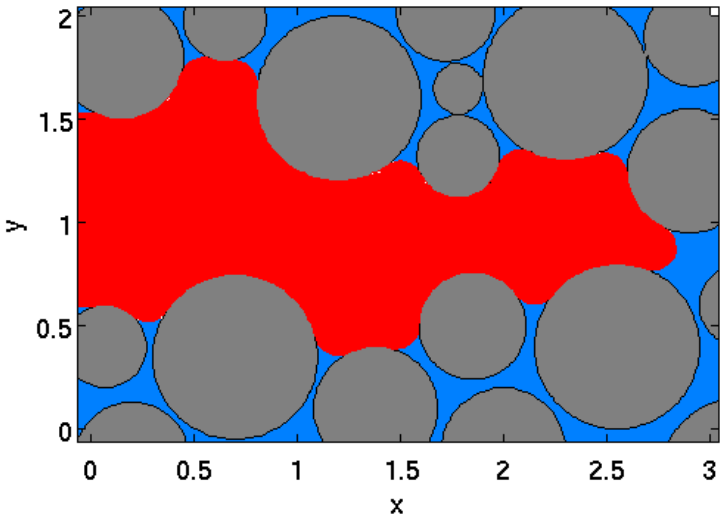

Continued on next page

B. Stage 1, the incremental movements of interface due to hydrate formation (from the red to blue interfaces). The arrow indicates the direction of methane/water interface movement and hydrate growth. The first layer of hydrate forms on the original methane/water interface. The zoom-in figure shows the mechanism that drives the hydrate growth. The micro defects in the hydrate layer allow water to imbibe into the gaseous phase and coat the surface of the hydrate. This thin film becomes the new nucleation cites for the hydrate association. This cyclic process (that is, water imbibes the gaseous phase and forms new hydrate, which further allows imbibition to happen) determines that hydrate grows into the gaseous phase.

This stage is the same as in Figure 4.18B.

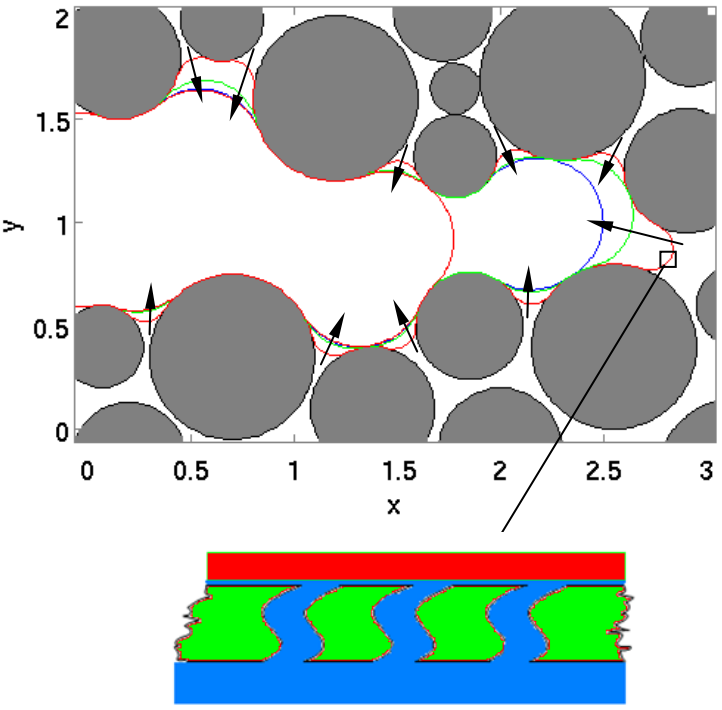

C. Hydrate distribution (green) when the methane/hydrate interface is at the critical point. In contrast to Figure 4.18C, following this step, a slight decrement of curvature will result in a jump of interface to the left (Melrose imbibition jump). This is because the separate water films at the surface of the hydrate merge to form a single methane/water interface, which is unstable.

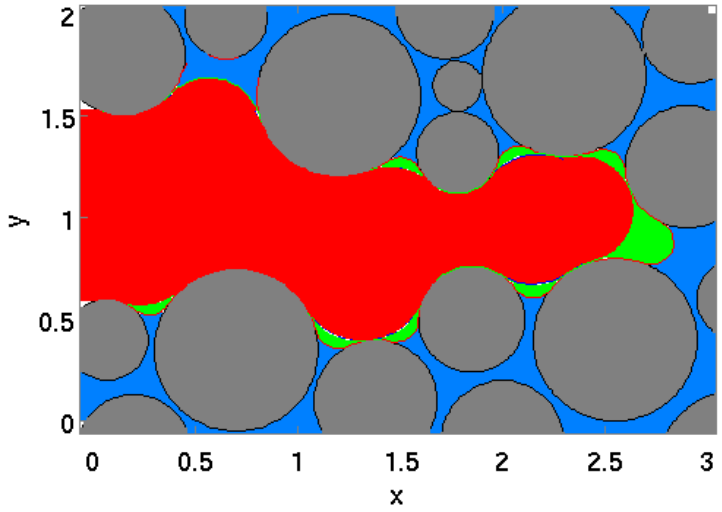

Continued on next page

D. Stage 2, the imbibition jump is an abrupt, instantaneous process. No intermediate steps, like the blue interface in Figure 4.18D, will be available. Thus the interface jumps as a gas/water interface to the next stable position, which is shown as the red curve.

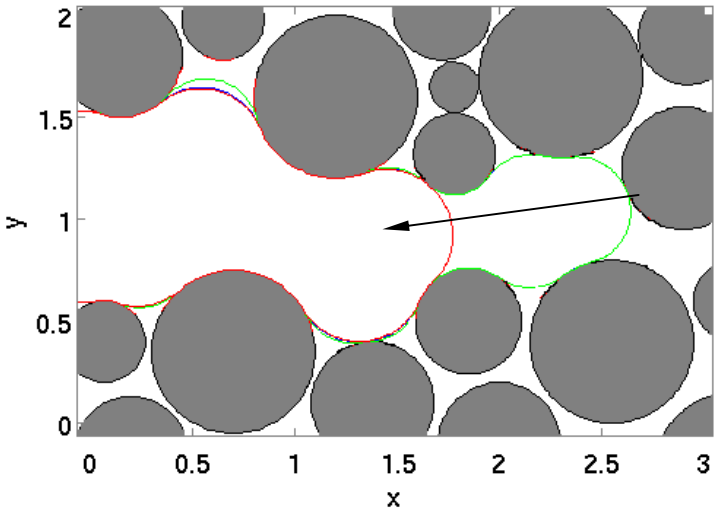

E. Imbibition jump sucks the water to fill the pore (blue). A new, stable location of the gas/water interface is reached at the end of the jump. Since this is a sudden process that gives no time for hydrate formation, water can be maintained between the two interfaces. New hydrate can form along the newly-formed interface (boundary between red and blue regions), and only grows into the gaseous phase (red).

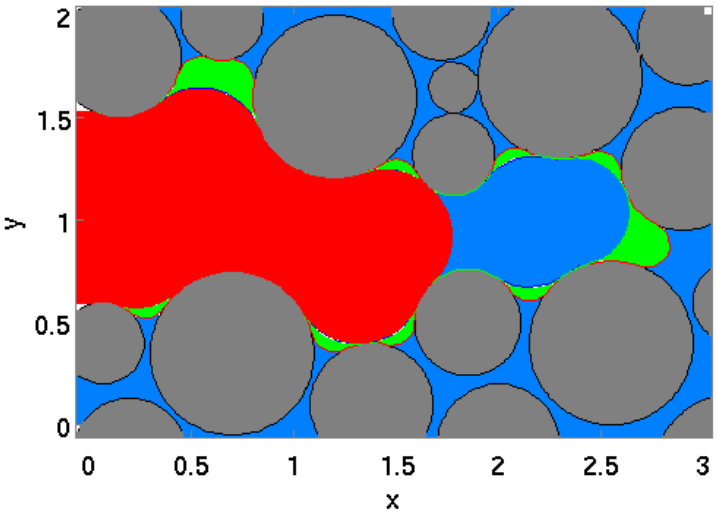

Continued on next page

F. Stages 1 and 2 repeat themselves cyclically. We only show here the final hydrate (green) and water (blue) distribution. Due to the cyclicity, the final distribution has a sandwich-like pattern: the water-filled pores are separated by hydrate shells of varying thickness. This gives the minimum hydrate saturation.

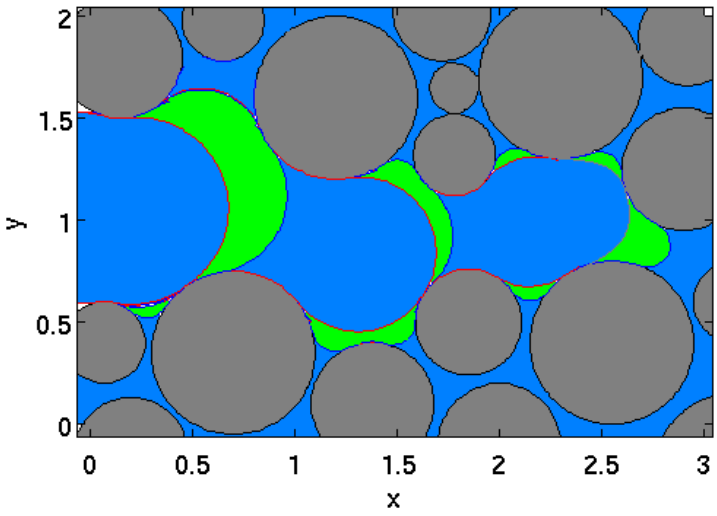

Figure 4.19: Schematics of Scenario B that water supply rate is much larger than the hydrate formation rate, which gives the minimum hydrate saturation. The color scheme is the same as in Figure 4.18.

It follows that this limiting case yields the minimum hydrate saturation. The original footprint of the gas phase is now occupied by water-filled pores and hydrate lenses of varying thickness.

These two scenarios suggest the upper and lower limits of the hydrate saturation that could possibly happen in the porous medium: hydrate saturation is equal to the original gas saturation (upper limit, demonstrated in Figure 4.18), and hydrate saturation is equal to the swept volume of the incremental movement (slow movement) of the interface (lower limit, demonstrated in Figure 4.19). However, the requirement for the occurrence of these cases is that both methane and water are sufficient for hydrate formation (note that we do not constrain the availability of either component in Scenarios A and B). The case of insufficient materials is discussed in section 4.2 of this chapter.

One important behavior missing from the above analysis is the nonwetting phase trapping. The above geometry has large open space, and therefore does not permit

trapping. In a real 3D geometry, nonwetting phase is trapped at the imbibition endpoint, and disconnected from the bulk phase.

Nonwetting phase trapping occurs due to two mechanisms. First, the continuous clusters of nonwetting phase are disconnected due to the imbibition happening in pores. Once the nonwetting phase loses its connection to the exit face (pores), it is trapped. Second, menisci at constraint geometries (for example, throats) merge at lower applied capillary pressure or curvature. This behavior snaps off the nonwetting phase in the pores, and thus traps it as well. Both of the mechanisms require the coalescence of separate menisci, that is, the Melrose event. A more detailed analysis can be found at (Gladkikh and Bryant, 2003).

Both mechanisms require the quick invasion of wetting phase into either pores or throats. Scenario 1 features a gradual invasion of hydrate, and there is no interface coalescence. Therefore, we do not consider nonwetting phase trapping in this scenario. Nonwetting phase is assumed always connecting to the bulk. With sufficient gas supply from other porous media, the hydrate saturation in Scenario A will be exactly the same as the initial gas saturation. On the other hand, Scenario B considers the possibility of Melrose jump. Therefore, nonwetting phase will be trapped at the imbibition endpoint. When hydrate formation by using the trapped gas is complete (in this case, no extra gas can be provided from other porous media), water comes in to fill the vacancy due to the hydrate formation. Much more water saturation, and correspondingly smaller final hydrate saturation, is obtained by using this scenario.

4.3.4 Hydrate saturation prediction in the porous medium – 2D and 3D granular medium case

To compute the upper limit of the hydrate saturation, only the methane/water saturations at the drainage endpoint are needed, since hydrate saturation is equal to the original methane saturation, given that sufficient amounts of gas and water. Such information can be obtained from either pore network or LSMPQS simulations. However, the lower limit of the hydrate saturation can only be determined from the imbibition simulation. This is because the volume of incremental movement and Melrose imbibition jump are needed to be identified. We use network modeling and LSMPQS for such purpose. Since LSMPQS captures the interface movement in great details, simulation based on this technique is used as the benchmark, while network modeling results are compared with LSMPQS, and later applied to larger samples.

LSMPQS simulation on a 2D granular medium is introduced to visualize different imbibition events: incremental movement and Melrose jump. A 3D granular medium containing about 100 randomly-positioned uniform spheres (a subset of Finney pack) is employed to determine the volumes of two events during imbibition simulation, , that is, the cumulative change in saturation associated with Melrose jumps, and the cumulative change in saturation associated with incremental movement of gas/brine interface. The Melrose jumps give the increase in water saturation and the incremental movements give the increase in hydrate saturation. The porosity of this unconsolidated granular medium is roughly 37%, which agrees well with the porosity of the sediments of the hydrate reservoirs in the permafrost regions, and therefore a good representation of a sediment. We later apply network modeling to study the case of much larger granular medium with 5000~7000 spheres. With the above analyses, we manage to obtain physically-based, and also reliable increments in saturation for the two types of events.

The criterion to differentiate incremental movement and Melrose jump

The key feature that differentiates the incremental movement and Melrose jump is that incremental movement is the gradual motion of fluid interface when the applied curvature is decreased slightly, while Melrose jumps causes the wetting phase to invade a volume abruptly. Physically, the incremental movements are reversible: the interface would return to its original location if the applied curvature were increased slightly, whereas the Melrose jumps are irreversible. Computationally, the gradual motion usually spans only several voxels and thus can be distinguished from Melrose jumps that span tens of, even hundreds of pores and hence hundreds of thousands of voxels. Consequently, these two types of fluid movement are identifiable from the simulation.

We use a 2D porous medium to demonstrate the idea (Figure 4.20). The domain is described by 1166 by 1006 cells, which gives enough resolution for the analysis. This domain contains randomly distributed disks with equal sizes. No length unit is assigned to the disks, so that every parameter in the calculation, including the applied curvature, is dimensionless. The upper and lower boundaries are sealed by using the flat surfaces, while the left and right boundaries are sealed by using the overlapping disks. Such treatment prevents the occurrence of multiple possibilities of interface attaching to the open boundary, and thus multiple solutions of the interface distributions at an applied curvature. This artifact often prevents getting the correct interface during the imbibition.

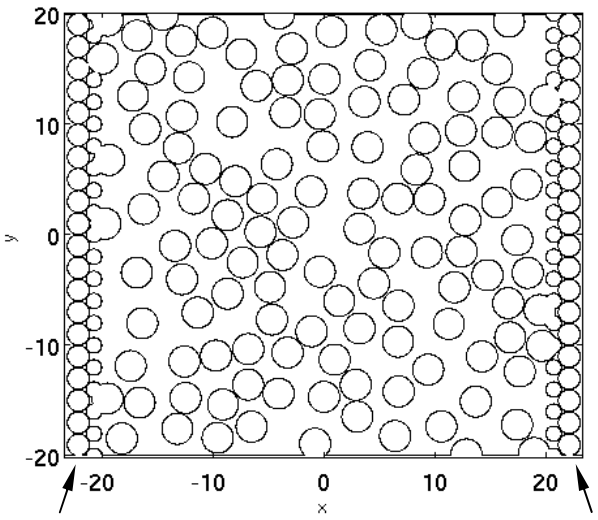

Figure 4.20: A 2D random disk pack. The disks have uniform size. We use smaller disks (indicated by the arrows) to seal the left and right boundaries. The upper and lower boundaries are sealed as well, by the flat surfaces. We use this domain only to demonstrate the criterion for differentiating events of incremental movement and Melrose jump.

We start drainage from the left boundary. At drainage endpoint (applied dimensionless curvature = 4.126), all possible wetting phase is displaced by nonwetting phase. Imbibition later starts from this fluid configuration. For the majority of the imbibition steps in this case, the incremental movement dominates the fluid/fluid displacement. We only focus on the steps where both Melrose jump and incremental movement coexist, so that a criterion to differentiate these two can be developed.

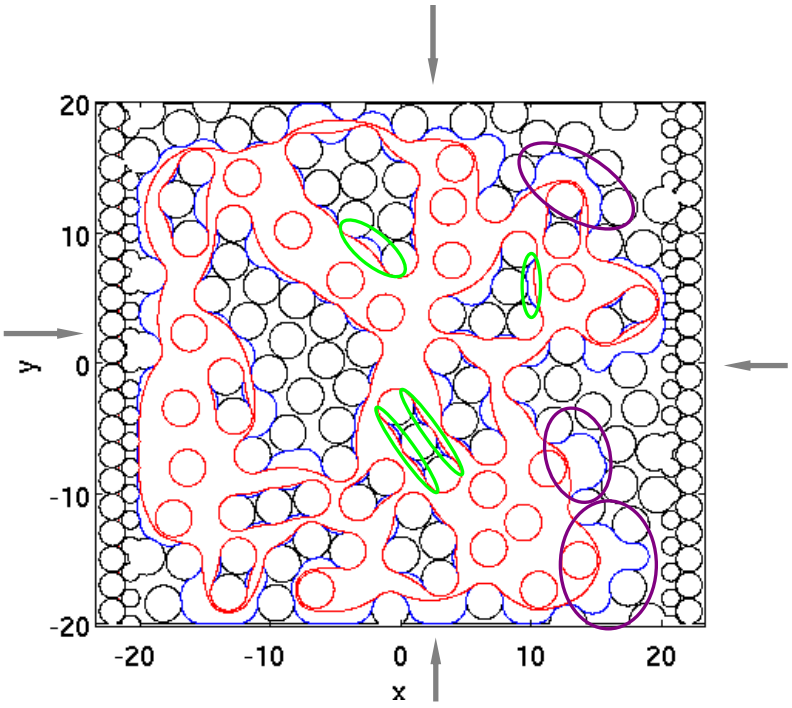

Figure 4.21: Fluid/fluid interface at step 9 (blue curve, applied dimensionless curvature = 0.626) and 10 (red curve, applied dimensionless curvature = 0.126) of imbibition. Several examples of incremental movement (green circle) and Melrose jump (purple circle) are also shown.

Figure 4.21 indicates the comparison of fluid/fluid interface between two consecutive steps. Our computational domain has tighter pore space close to the boundary than the center of the medium, which forces imbibition to occur from the boundary to the center (indicated by the gray arrow). Step 9 (the blue curve) shows that at applied dimensionless curvature = 0.626, the bulk wetting phase concentrate around the boundaries, while the nonwetting phase fills most of the pore space at the center. A further reduction of the applied curvature (step 10, also the imbibition endpoint) allows for wetting phase invasion, and gives the fluid/fluid interface shown in red curve.

The difference between the blue and red curves determines the incremental movement and Melrose jump. The incremental movement involves the movement of a single fluid/fluid interface, and some of the events are indicated by the green circles in

Figure 4.21. In the granular medium, most of them are the expansions of the pendular rings held between two neighboring grains. On the other hand, the Melrose jump is the sequence of the coalescence of two separate interfaces, and occurs in the scale of several pores. We indicate several of these events by using the purple circles: when the separate menisci merge, the newly-formed single meniscus becomes unstable and jumps to a stable location. Unlike the incremental movement, there are no intermediate stable locations for the jump.

The comparison between the purple and green circles suggests that for the individual events, the space swept by incremental movement is much smaller than the Melrose jump. This is a straightforward, and yet useful observation to develop a criterion: A threshold value is set to check the difference (the distance in the normal direction) between two curves. If the difference is greater than the threshold, we consider the event to be the Melrose jump, otherwise incremental movement.

Several problems rise with this treatment. One is that the arbitrary selection of the threshold value largely changes the ratio of incremental movement and Melrose jump. As shown in Figure 4.22, we color the regions of incremental movement to be green and the Melrose jump to be red. The left panel shows the results by using threshold = 0.5, that is, the distance between fluid/fluid interfaces at two sequential curvatures is 0.5 dimensionless length (a single cell is 0.04 unit in length). Any distance change greater than 0.5 is considered to be the Melrose jump, otherwise the incremental movement. It gives that Melrose jump (colored red) dominates the phase change between step 9 and 10, while incremental movement (colored green) only exists as the isolated expansion of the pendular rings. When increasing the threshold to 1 (the right panel), we observe more green regions. This is equivalent to a stricter rule to check Melrose jump: only the variation greater that 1 is considered to be a Melrose jump. For this larger threshold, our

estimated Melrose jump totally disappears in some blobs (yellow circle), and is smaller in the rest of the blobs (red circle). This comparison raises the concern that without a reasonable choice of the threshold value, the estimation of these two events might be subject to large error.

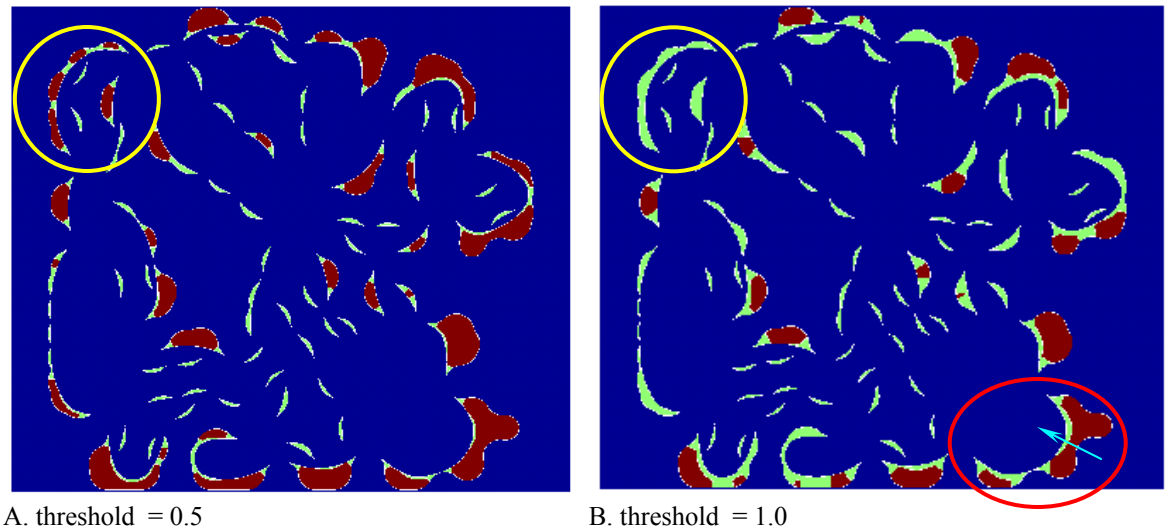

A. threshold = 0.5 B. threshold = 1.0

Figure 4.22: The distribution of incremental movement and Melrose jump between step 9 and 10. The blue region means no interface movement occurs between the two steps. This region includes grains and is filled by the same phase at both steps; no distinction is made regarding which phase occupies the blue region. Regions through which interface movement occurs are associated with a phase change and are colored in red and green we refer to these regions 'blobs'). The shape of these blobs is the same as those between two interfaces in Figure 4.21. Melrose jump is indicated by the red region, and incremental movement by the green region. The size of the computational cell is 0.04 in this calculation. Consequently, threshold = 0.5 corresponds to 12.5 cell variation in the simulation (A), while 1.0 means 25 cell variation (B).

Another problem is that the separation of the two events within the same blob is physically implausible. If two events can coexist in the same blob, it means that the interface can have two stable positions at the same applied curvature. In fact, from the red

circle of Figure 4.22B, the interface between the green region (incremental movement) and the blue region is the fluid/fluid interface at the applied curvature. The interface between red region (Melrose jump) and green region (incremental movement) is not a equilibrium place. Therefore physically this interface should not exist. This is an artifact of the computational criterion. We argue that in the individual blobs, only one type of events can take place. For example, in the red circle of Figure 4.22B only one event is possible. The blob should either be incremental movement only (green) or Melrose jump only (red).

The treatment to remove the artifact is that the entire blob is assigned to be Melrose jump if any Melrose jump takes place in this blob. We refer to this as the **reevaluation** process, which recalculates the distribution of the two events. Figure 4.23 shows the distribution of the two events after the reevaluation. A direct comparison with Figure 4.22 suggests that all the blobs that were filled in by both events are now only by Melrose jump. However, the blobs that were filled by incremental movement only do not change the status. The fraction of Melrose jump increases by using this treatment (the fraction of Melrose jump in the saturation unit is also referred to as S_{jump}; and the fraction of incremental movement is referred to as S_{incr}).

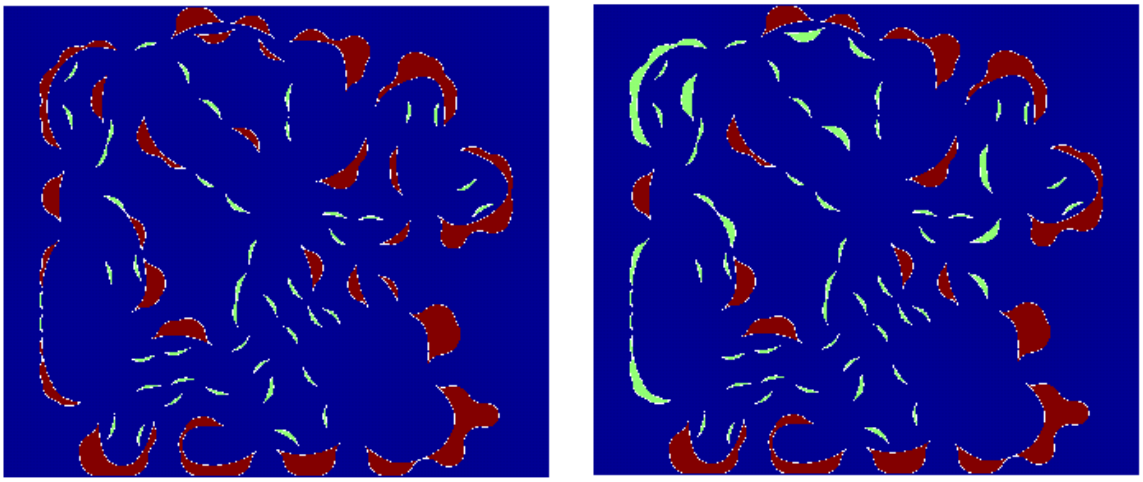

A. threshold = 0.5 B. threshold = 1.0

Figure 4.23: The distribution of Melrose jump and incremental movement, after the reevaluation process. The color scheme is the same as in Figure 4.22. The entire blob is assigned with either Melrose jump or the incremental movement. Compared to the distribution before the reevaluation (Figure 4.22), the fraction of Melrose jump (S_{jump}) increases and the fraction of incremental movement (S_{incr}) decreases.

The effect of different curvature steps

In the simulation process, the stable locations for the fluid/fluid interface are computed at each applied curvatures. A question needed to be answered is whether the same fluid distribution will be obtained if refining or coarsening the curvature steps. If the same fluid distribution is obtained at the same applied dimensionless curvatures based on two simulations with different step sizes of applied dimensionless curvatures, the simulation results are step-independent, and are reliable for the study of the different events.

We compare the fluid distribution computed by using two dimensionless curvature steps (0.5 and 0.05) for imbibition simulation. Figure 4.24 shows a step of imbibition for both simulation, at which the applied dimensionless curvature = 0.129. The

only observable differences between the predicted interfaces from two simulations are circled in the figure. Only a slight difference can be identified. For the rest part of the domain, two interfaces completely overlap (due to the color scheme used only the red interface can be seen). Such behavior indicates that changing the curvature step does not affect the occurrence of the events, nor the fluid distribution. Consequently, our analysis of the incremental movement and Melrose jump based on LSMPQS simulation is independent of the simulation steps applied.

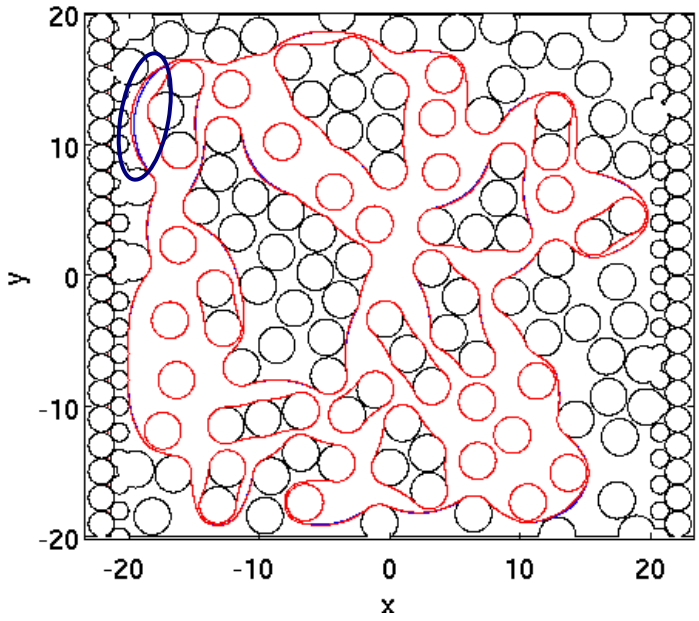

Figure 4.24: The comparison of the fluid/fluid interface between two simulations by LSMPQS. Simulation #1 (red curve) has curvature step of 0.5, and simulation #2 (blue curve, almost invisible) has the dimensionless curvature step of 0.05. We compare the fluid distribution at the same applied dimensionless curvature = 0.129. The two interfaces overlap at most parts, and the only differences are indicated by the blue circle.

3D granular medium

As stated in the two limiting cases, knowing the fraction of incremental movement and Melrose jump (S_{incr} and S_{jump}) determines the amount of hydrate that can possibly form inside the porous medium. An imbibition simulation in a 3D granular medium is therefore important for this purpose. Due to the restriction of the computational time, our granular medium is chosen to be a small sphere packing of about 100 spheres, whose porosity is 37%, similar to the sediments of the hydrate reservoir.

A threshold value is required to be developed in order to differentiate incremental movement from Melrose jump. Such value depends on the porous medium used for the simulation, and thus the value estimated from a 2D medium cannot be directly applied to a 3D domain. Drainage and imbibition are simulated, and the threshold value is determined based on the special features observed during the imbibition simulation.

Figure 4.25A gives the computational domain for the drainage and imbibition simulations. Only partial spheres exist on the boundaries because the pack is truncated to give a cubic computational domain. At the end of drainage, nonwetting phase dominates the pore bodies, and the wetting phase retreats to the surface of the grains, or the corners among the grains (Figure 4.25B).

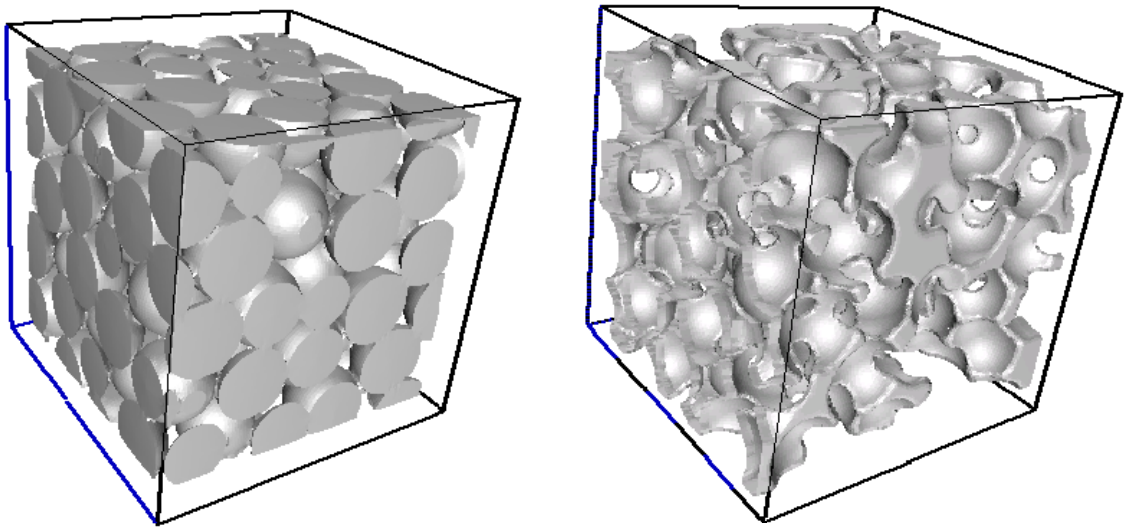

Figure 4.25: 3D granular medium (left panel) and the fluid/fluid interface and fluid/grain interface at the drainage endpoint (right panel). The fluid/grain interface has the shape of the spheres.

We monitor the phase change (from nonwetting to wetting) in every voxels of the computational domain during imbibition simulation. Between two consecutive steps, a change in the level set function from negative to positive means that nonwetting phase (negative) is displaced by wetting phase (positive). As level function variation between two steps can be measured by the change of the interface at the normal direction, we record such value in order to find a threshold to differentiate the two different events. S_{jump} and S_{incr} at different possible threshold values are shown in Figure 4.26.

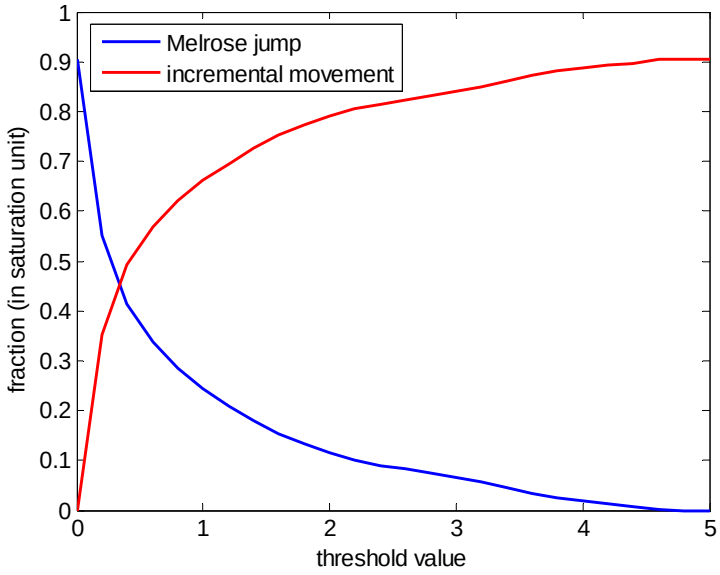

Figure 4.26: The fraction of Melrose jump and incremental movement at different threshold values for imbibition from the state of Figure 4.25B. The *y* axis is the saturation change due to either event. The *x* axis is the threshold value. It is equal to the distance of the level set functions at the normal direction between two consecutive steps. The threshold value is normalized by the sphere radius.

Figure 4.26 shows the comparison of incremental movement and Melrose jump at given threshold values. A dimensionless curvature step size of 0.2 is used in the simulation. The summation of these two curves always equals to the total wetting phase saturation change during the imbibition simulation, and in this case is equals to 90%. The 10% saturation (1-90%) indicates the void space that is not subject to phase change during the imbibition simulation, which is the summation of irreducible wetting (S_{wirr}) and residual nonwetting (S_{nwr}) phase saturations. At a given threshold value, we check phase change in every voxel, and determine if such change belongs to incremental movement or Melrose jump. All the voxels belonging to an event are summed up for all the imbibition steps and divided by the total amount of voxels of the void space, which

gives the fraction in saturation unit. In Figure 4.26, with increasing the threshold values, the fraction of Melrose jump decrease, since in order to be qualified as Melrose jump, the level set function of a voxel should have a greater variation than the threshold value. When the threshold value increases, the number of voxels qualified for this requirement reduces substantially.

Both curves in Figure 4.26 change gradually with the threshold values. This indicates no clear cut-off for the proper threshold value that would differentiate these two events from each other. This is somewhat surprising, because changing the threshold value should not affect how many regions are identified as Melrose jumps. This is because varying the threshold only varies the proportion of two events inside a region, as shown in Figure 2.22, in a gradual fashion. The same reevaluation process, as shown in Figure 2.23, should be applied to 3D case and give a reasonable prediction of the fractions of two events.

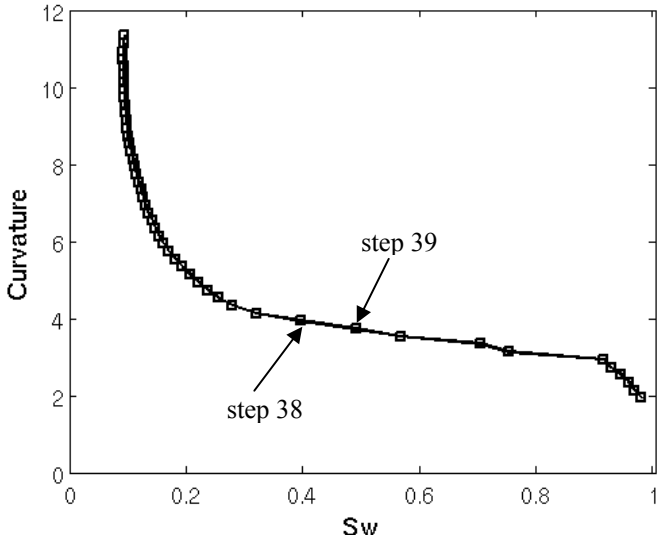

Figure 4.27: Imbibition curve of a subset of Finney Pack.

The 3D reevaluation process is the as 2D: if the Melrose jump exists in the blob, the entire blob is assigned to this event; if the entire blob has only incremental movement, the event does not change. Step 37 and 38 are at the imbibition percolation, where the level set function change involves both events. An example of the 3D simulation is shown in Figure 4.28. The yellow and red regions show the different imbibition events. For the demonstration purpose, we use an arbitrary threshold value 1 in this example. In the 3D case, the threshold value is also normalized by the sphere radius. Before the reevaluation (left panel), the yellow regions (incremental movement, smaller than the threshold value) dominate the domain. Only several red regions (Melrose jump, greater than the threshold value) exist, and share the same blobs with the yellow ones. The red regions expand after the reevaluation (right panel), and the yellow voxels that are adjacent to the red regions before become red. This indicates that blobs are shared by both events now are filled by Melrose jump only. The portion of the Melrose jump is largely increased after this treatment.

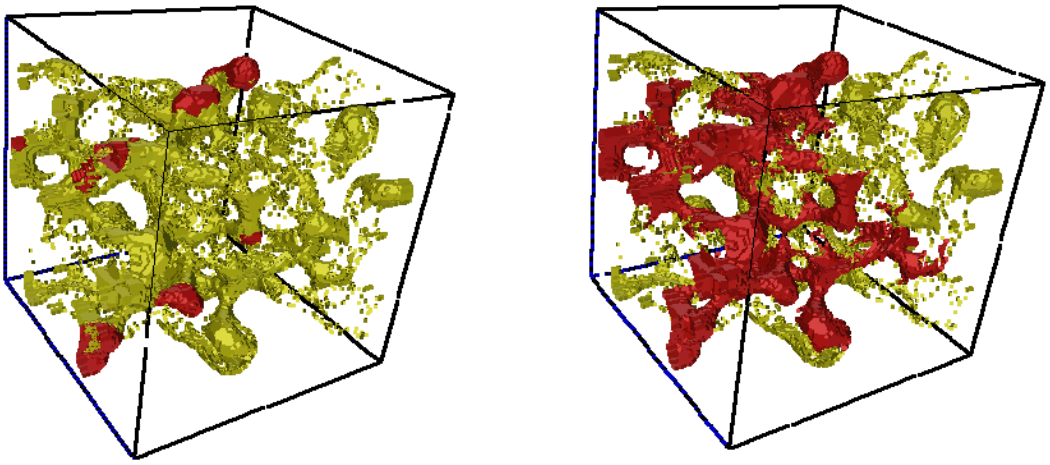

A. before reevaluation B. after reevaluation

Figure 4.28: The level set function variation between step 38 and 39 of LSMPQS imbibition simulation in a subset of Finney pack. The yellow and red blobs indicate the places where level set function variation is smaller than, and greater than 1, respectively.

We compare S_{jump} and S_{incr} at different threshold values with the original results (Figure 4.29). The reevaluation process largely increases the S_{jump}, and decreases S_{incr}. Stair-like behavior is observed instead compared to the smooth curves obtained before the reevaluation. This suggests the level set function variation is no longer continuous during the imbibition. For example, the biggest plateau occurs from 2.5 to 4 (threshold value, meaning the distance is 2.5 to 4 times of the grain radius), between which the fractions of two events are constant. This indicates that incremental movement happens less than a distance of 2.5, while Melrose jump happens greater than a distance of 4. Between 2.5 and 4 there is a gap and no events are captured.

Several small plateaus other than this one are observed as well. However, those plateaus are not strictly parallel to the x axis. That is, the variation of the threshold values still changes the fractions of the events. These plateaus do not establish a clear cut-off

value to differentiate two events. Only the one occurs between 2.5 and 4 gives a satisfactory cut-off value. Using this plateau we can set the threshold to be any value between 2.5 and 4, and therefore obtain S_{jump} is 27% and S_{incr} is 64%.

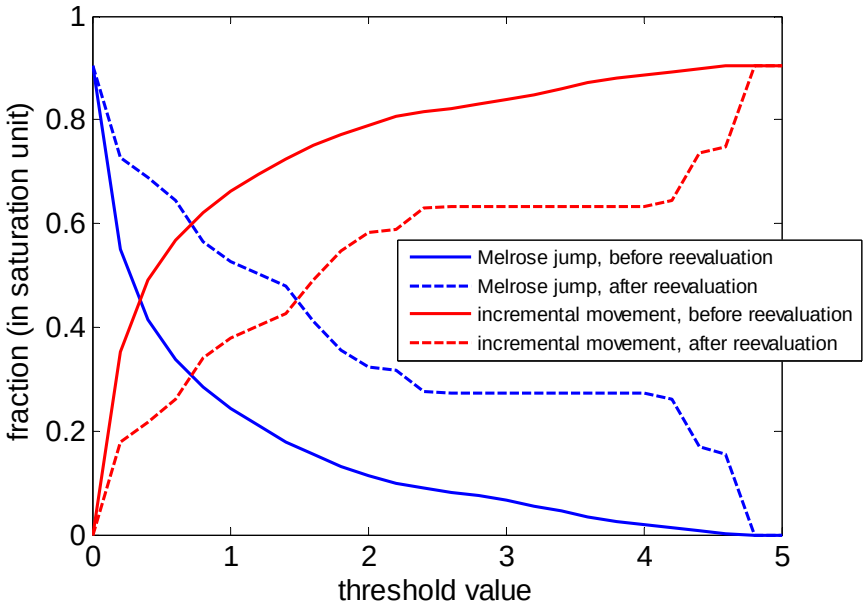

Figure 4.29: A comparison of the fractions before and after the reevaluation process. The x and y axes are the same as Figure 4.26.

The application of the above results is limited by 1) the sample size and 2) the step size of the imbibition simulation (in the above 3D example, a sample of only about 100 spheres is used). In LSMPQS simulation, the imbibition step size is limited by the mesh size of the domain. The imbibition step size needs to be large enough so that the interface movement between two subsequent steps is not smaller than the length of a single cell, so as to maintain the simulation accuracy. Moreover, LSMPQS is time-consuming (an entire imbibition simulation on the above 3D packing takes more than a day to finish). The simulation of imbibition in a significantly larger sample is therefore not feasible. To estimate the fraction of jumps and increments in larger samples, we use

the results from LSMPQS simulation for analysis, and also the results are used as a benchmark to justify the reliability of the network simulation.

We have justified the correctness of network modeling of drainage and imbibition from the pore-by-pore comparison with LSMPQS (Chapter 2). The justification allows us to use network simulation to model the different events during imbibition. Here we use conventional boundary conditions, which agree with the LSMPQS settings. In network modeling, between step n and n+1 of imbibition, the newly imbibed pores are labeled. We compute their distances to the pores that were already imbibed till step n. These distances are equivalent to the level set function difference between two steps. The blobs, which are the isolated clusters of newly imbibed pores, occur in the network simulation, similar to those in LSMPQS (Figure 4.28). For any threshold value, it is also possible that some pores within a single blob are associated with Melrose jump and other pores in the same blob are associated with incremental movement (Figure 4.22). As discussed previously, such behavior is nonphysical and should be corrected. The same procedure developed in LSMPQS simulation (reevaluation) is also used in this case: the events in a single blob are assigned to be Melrose jump if any part of the blob is originally filled by such event; while the blobs only filled by incremental movement are not subject to any change. We attempt to identify a similar pattern as in Figure 4.29: a plateau separates the imbibition events to be Melrose jump and incremental movement.

Four packings with different numbers of spheres are used to show the effect of packing size on S_{incr} and S_{jump} (Figure 4.30). The imbibition step used in the simulation is the same as in LSMPQS simulation. The critical curvature for imbibition is computed by using C_1 imbibition criterion (Equation (2.8)). First we simulate imbibition in the network model on the same subset of Finney pack used for the LSMPQS simulation in Figure 4.25, and obtain the results in Figure 4.30A. A comparison with Figure 4.29 therefore

would enable us to check the reliability of the network modeling for distinguishing the two kinds different imbibition events. Without the reevaluation treatment, smooth curves are observed for S_{incr} and S_{jump} as a function of threshold size. Employing reevaluation introduces several plateaus in the curve. Three noticeable plateaus are identified by the arrows in Figure 4.30A, which yields S_{jump} to be 13%, 21% and 25%, respectively. These values of S_{jump} correspond to the threshold ranging from 2.3 to 5. Compared with Figure 4.29, network modeling predicts a slightly smaller S_{jump} and threshold value. In network modeling, the true incremental movement is the expansion of menisci and pendular rings, and the fluid displace in a pore happens in a discrete fashion (that is, a pore is either filled by wetting or nonwetting phase). Thus strictly speaking, in the pore level all the events in network modeling are jumps. On the other hand, LSMPQS does not employ the concept of pores and throats. It is likely the 'pore' (defined in network model) is filled by two phases if the physical stability permits. These differences prevent us from getting the same results between the network modeling and LSMPQS. Nevertheless, a qualitative agreement is obtained between Figure 4.30A (S_{jump} and S_{incr} from network modeling) and Figure 4.29 (S_{jump} and S_{incr} from LSMPQS): Plateau(s) exist at threshold values between 2.5 to 4, and gives S_{jump} and $S_{incr.}$ S_{jump} from the network simulation have three values (13%, 21% and 25%), smaller than S_{jump} from LSMPQS, which is 27%.

From the above comparison between LSMPQS and network modeling, we argue that since network modeling follows the same imbibition sequence (Chapter 2), we are able to capture the correct Melrose jumps. Because the reminder of events must be incremental movement, we get the right answer even though our network is not explicitly accounting for any incremental events.

We then can use the network modeling to study the effects of sample size and simulation step size, both of which cannot be easily performed in LSMPQS. Samples of

three different sizes (packs with 1000, 5000, and 7000 spheres) are studied. The results are shown in Figure 4.30B, C, D.

Without reevaluation, smooth curves are observed. S_{jump} slowly decreases from (1-S_{wirr}-S_{nwr}) to 0 with increasing the threshold value, while S_{incr} slowly increases from 0 to (1-S_{wirr}-S_{nwr}). There is no distinct cut-off value that could differentiate these two events. The reevaluation treatment generates plateaus in all the packings, and they all start at the threshold value approximately equal to 4. This value is greater than that in Figure 4.29 and Figure 4.30A, showing that the packing size does affect the results. S_{jump} slightly increases from Figure 4.30A to the rest of the packing sizes (1000, 5000 and 7000 spheres). This is because the distance of jump is limited by the size of the packing. A bigger jump is expected with larger packing size, so that S_{jump} increases accordingly. When the packing size is big enough (for example 5000 spheres), S_{jump} becomes almost a constant (between 5000 spheres in Figure 4.30C and 7000 spheres in Figure 4.30D). The fraction at the plateau varies from 21% of the 1000-sphere packing (Figure 4.30B), to 25 % of the 7000-sphere packing (Figure 4.30D), all of which are smaller than the case of LSMPQS (Figure 4.29).

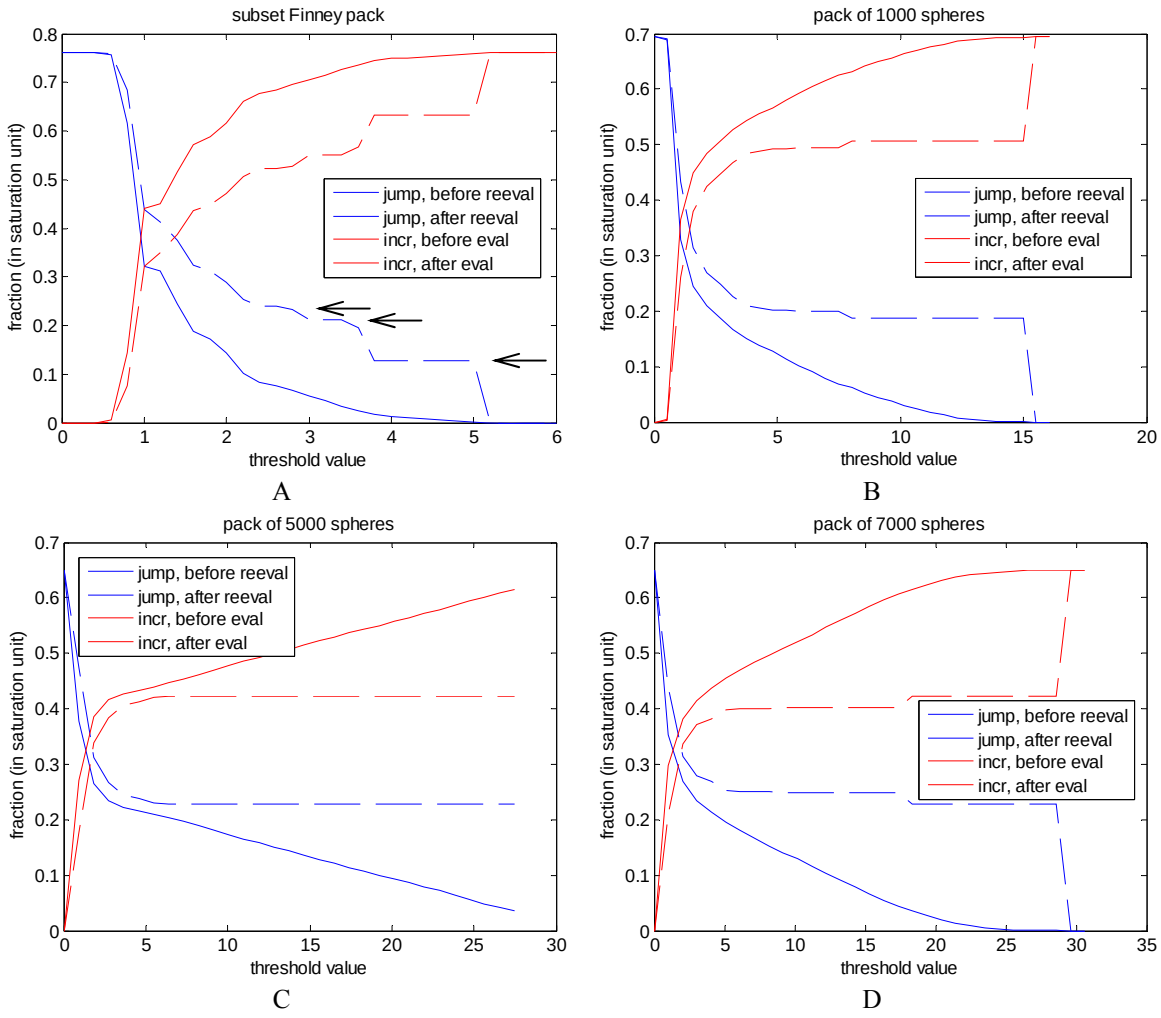

Figure 4.30: A comparison of S_{jump} and S_{incr} before and after the reevaluation for four sphere packings. The numbers of spheres in the pack are 100, 1000, 5000, and 7000, respectively. The *y* axis is the fractions of incremental movement and Melrose jump in saturation units. The *x* axis is the threshold value, which is the distance from the newly imbibed pores to the pores imbibed in the previous steps. It is normalized by the grain radius.

After the reevaluation, similar pattern are obtained for all the cases, where a plateau exists when the threshold value is greater than 5. Both models (network modeling and LSMPQS) suggest a clear cut-off saturation value that differentiates incremental

movement and Melrose jump. This suggests that although different packing size does have an effect on S_{jump}, S_{incr} and the threshold value, the basic behavior, i.e., a plateau that separates the two events, is the same for every case. However, all the simulations shows above are all based on a certain imbibition step size. This is a key parameter that might affect the results as well.

Step size effect

The fractions of incremental movement and Melrose jump might change at different imbibibition step sizes. During the imbibition simulation, for example, more volume change is associated with larger step sizes, and thus larger difference in level set function distance. This difference, if greater than the threshold value, is considered to be the Melrose jump. Therefore, increasing the step size increases the fraction of Melrose jump as well. On the other hand, if the step size is reduced, the level set function difference between two consecutive steps becomes smaller, and therefore increases the fraction of incremental movement. However, Melrose jump will never disappear no matter how small the step size is. This event is due to the physical instability of the menisci coalescence, and should not be affected by the algorithm parameters as step size. A correct prediction of S_{jump} and S_{incr} should be found from a proper step size.

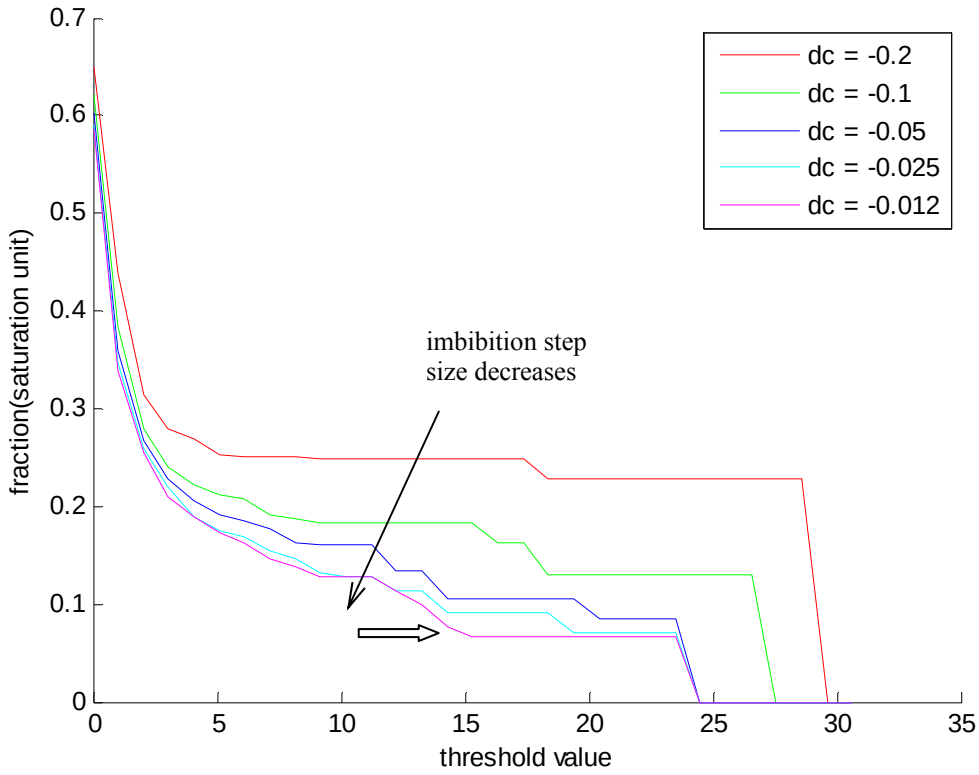

Figure 4.31: The fraction of Melrose jump at different imbibition step sizes. The results are from the network simulation based on a 7000-sphere packing.

Network model simulation is used to check the step size effect. Figure 4.31 shows the results for the 7000-sphere packing with five different dimensionless curvature step sizes (-0.2, -0.1, -0.05, -0.025 and -0.012). Only the fraction for Melrose jump is shown for clarity. S_{jump} decrease with reducing the step size, which agrees with our expectation described above. The difference between curves diminishes as the step size reduces. While a big difference is still observed between the curves of dc = -0.2 and -0.1, curves of dc = -0.025 and -0.012 almost overlap. The results indicate that steps smaller than 0.025 make no significant difference of S_{jump}, and therefore nor S_{incr}. As indicated by the hollow arrow, the first plateau is encountered as S_{jump} decreases with increasing the

threshold value. We consider S_{jump} at this plateau is the correct choice of the Melrose jump fraction, which is 7% saturation unit.

Boundary effect

All of the previous simulations are based on the conventional boundary conditions described in Chapter 2 and 3. Compared to the results with periodic boundary condition, the irreducible wetting phase saturation and residual nonwetting phase saturation are substantially different (Chapter 2).

Using periodic boundary condition affects the fractions of the two imbibition events in different ways. For Melrose jump, no significant effect is expected. This is because the periodic boundary condition primarily alters the fluid connectivity towards the drainage and imbibition endpoints, but does not affect the percolation. Most of the Melrose jump occurs at the percolation, so that its fraction is not influenced by the boundary condition. On the other hand, the incremental movement takes place typically at the drainage or imbibition endpoint, and therefore are affected by different boundary effect.

A simple approach is developed to estimate the S_{jump} and S_{incr} based on the periodic boundary condition. We assume S_{jump} based on the periodic boundary condition to be the same as on conventional boundary condition. This approximation ignores the small fraction of Melrose jump (also the saturation) taking place towards the drainage and imbibition endpoints, which are affected by different boundary conditions. Therefore, S_{incr} can be easily calculated as 1- S_{jump} - S_{wirr} - S_{nwr}. S_{wirr} and S_{nwr} are obtained from the drainage and imbibition endpoints based on periodic boundary condition.

4.3.5 Discussion

The models we have developed enable the quantification of Melrose jump and incremental movement. In Scenario A, incremental movement is the only event during imbibition, which give gives the hydrate saturation to be the initial gas saturation. In Scenario B, the volume of Melrose jump contributes only to the water saturation, but not hydrate saturation. Only the volume of incremental movement becomes hydrate saturation. S_{jump} is directly obtained from LSMPQS simulation, while S_{incr} is determined from S_{jump}, S_{wirr} and S_{nwr}. The latter two terms are affected by the boundary conditions that are employed. The calculated hydrate saturation (using equation (5.3) for Scenario A and equations (5.1) and (5.2) for Scenario B) is tabulated in Table4-1. This calculation is based on the fact that 1 unit of methane gas can only be converted into 1/3 unit of hydrate (T = 275 K and P = 6 MPa).

Table 4-1: Hydrate saturation from different pore level scenarios

Saturation	Scenario A. Water supply rate << hydrate formation rate, hence only incremental movement of gas/hydrate interface (Figure 4.18)		Scenario B. Water supply rate >> hydrate formation rate, hence both incremental movement and Melrose jump occur (Figure 4.19)	
	Conventional boundary condition	Periodic boundary condition	Conventional boundary condition	Periodic boundary condition
S_{wirr}[(1)]	8%	15%	8%	15%
S_{nwr}[(2)]	0	0	17%	32%
S_{jump}[(3)]	0	0	7%	7%
S_{incr} (=1-S_{wirr}-S_{nwr}- S_{jump})	92%	85%	68%	46%
S_h[(4)]	92%	85%	74%	57%

[(1)] S_{wirr} is the average value of irreducible wetting phase saturation in the drainage simulations of 60 packings, using network modeling.

[(2)] S_{nwr} is the average value of residual nonwetting phase saturation in the imbibition simulations of 60 packings, network modeling. For Scenario A, no Melrose jumps occur and thus we assume no trapping of nonwetting phase, thus S_{nwr} is 0.

[(3)] S_{jump} is computed by network modeling from a packing of 7000 spheres, based on the conventional boundary condition. This is described in Section 4.3.4.

[(4)] Hydrate saturation (S_h) includes the saturation change associated with volume of the incremental movement of the interface and the conversion from the residual gas saturation (S_{nwr}). The latter is determined by the in-situ pressure and temperature, and equation (5.1) is used for the conversion. Here we choose T = 275 K and P = 6 MPa.

Table 4-1 gives the possible hydrate saturation in the porous medium, for the assumptions described at the beginning of this section, namely there is no constraint of temperature, pressure, salinity, or the availability of gas and water. Because the calculations are at the pore scale, it is assumed that gas from far below the BGHSZ moves into the gas-filled pores as needed to maintain the gas phase pressure as hydrate forms. The hydrate saturation thus depends only on the nature of the movement of the gas/hydrate and/or gas/aqueous phase interface. It is only calculated from different

imbibition events, and based on the concept that the void space in the porous medium, which is occupied by gas and water, will be filled by only hydrate and water.

The results show that the periodic boundary condition predicts lower S_h than the conventional boundary condition. In this specific case, more than 17% difference is observed. The difference mainly rises from two sources: S_{wirr} and S_{nwr}. Hydrate cannot grow into the volume filled by irreducible water (one of the basic assumptions). Therefore, higher S_{wirr} leads to lower S_h. Moreover, when residual gas is converted into hydrate, a large vacancy is created. For example, for 1 unit volume of gas at T = 275 K and P = 6 MPa, only about 1/3 unit volume of hydrate is formed, the rest 2/3 unit will be filled with invaded water. Higher S_{wirr} and S_{nwr} would lead to lower hydrate saturation. With periodic boundary conditions, S_{wirr} and S_{nwr} have much higher values than with conventional boundary condition, and thus lead to much lower hydrate saturation.

With the same boundary condition but different scenarios, there is 28% hydrate saturation difference for the two scenarios. The difference is contributed from two different behaviors. First, S_{jump} contribute 7% water saturation. When Melrose jump exists, it quickly imbibes water into the porous medium, a rate too fast to let hydrate form. The water saturation of this type, known as S_{jump}, occupied the space that could possibly be used for the hydrate formation in the other scenario. Second, if no Melrose jump takes place (that is, Scenario A where only incremental movement occurs), there is no trapped gas during the hydrate formation (S_{nwr} in this case only shows the trapped gas phase saturation based on the conventional imbibition process). Hydrate occupies the entire volume of S_{nwr} in Scenario A. However in Scenario B, gas is trapped because of Melrose jump, and only about 1/3 of S_{nwr} will be filled by hydrate eventually.

By using the periodic boundary condition we feature the reservoir conditions, where the local porous medium is not affected by the reservoir boundary at a great

distance. The simulation based on the conventional boundary conditions allows the fluids to have a shorter and easier access to the boundaries, and traps less fluids. In other words, we argue more trapping should be present in the reservoir condition. Therefore, results from the periodic boundary condition are used for the hydrate distribution prediction in the reservoir size.

4.4 CONCLUSIONS

A 1D simple box model is proposed to investigate the hydrate saturation, remaining water saturation, and system volume variation owing to hydrate formation. The set of stoichiometric equations are developed and used to compute these values. Temperature, pressure, salinity, and the availability of methane and free water are studied individually.

For a gas-water-hydrate system, hydrate formation converts gas and water into hydrate. The phase change varies the system volume. The calculation suggests that the cases of both system volume (based on the definition, the system is short for the system of hydrate/gaseous/aqueous phase) increment and decrement are possible, given proper temperature and pressure combinations. However, natural hydrate reservoirs are typically within the region of the system volume reduction, which means that hydrate formation inevitably reduces the system volume and creates vacant spaces in the porous medium. Two possible consequences of the volume reduction arise: 1) fluids are sucked into the vacancy or 2) sediment compaction occurs. Only the first possibility is accounted for in the analysis, which is the driving force of the imbibition process during the hydrate formation, as we have developed in the latter part of this chapter.

Two types of systems are used to estimate the hydrate saturation: limited water and methane, and limited methane but unlimited water. At the low pressure and temperature regions (reservoirs under this condition include Mount Elbert and Mallik hydrate reservoirs), both cases predict lower hydrate saturation than the observation in the field, with all the available gas consumed. This suggests more gas should fill the vacant space from the other layers of the porous medium, and forms more hydrate. It is also unlikely that in nature water availability is limited. The first case featuring limited

gas and water gives even lower hydrate saturation (30%) than the second scenario with unlimited water, while the log measurement suggests more than 70% saturation in the Mount Elbert and Mallik sediments.

Based on this 1D model, we can draw the conclusion that the gas-water-hydrate system is an open system that allows for the movements of fluids in porous medium. Moreover, system volume reduction due to hydrate formation is confirmed from the calculation, which becomes the driving force to redistribute gas and water. This redistribution process, as we argue, resembles the imbibition process, and the hydrate formation associated with it is controlled by the imbibition events that occur: Melrose jump or incremental movement. Melrose events are assumed possible when the water supply rate is large relative to the rate of hydrate formation at the gas/hydrate or gas/water interface.

Two scenarios are proposed to estimate the hydrate saturation. Scenario A assumes water supply rate is much lower than the hydrate formation rate. This assumption allows the hydrate distribution to be the same with the initial gas distribution. This scenario also predicts the upper bound of the hydrate saturation in the porous medium. Scenario B assumes water supply rate is much higher than the hydrate formation rate. This gives two possible imbibition events: Melrose jump and incremental movement. We develop models to quantify the fractions (S_{jump} and S_{incr}) of these events in the imbibition process. Since Melrose jump occurs in a very fast fashion, hydrate is not able to form during this event. Water displaces gas in the porous medium, and stays in the form of aqueous phase. Incremental movement, on the other hand, takes place gradually, the rate of which is comparable to the hydrate formation rate. Hydrate forms during this process, with the volume equal to that of the displaced gas by water invasion. These two

events repeat cyclically during imbibition, and yield a characteristic hydrate distribution pattern at the pore scale in the porous medium.

Both network modeling and LSMPQS techniques are used to determine the fraction of the different imbibibition events. LSMPQS is capable of capturing the detailed interface movement in high accuracy. This enables us to visualize the events in both 2D and 3D domains, and calculates the fractions. Moreover, it is the benchmark result to justify our network model, where a reasonable agreement is obtained between the two simulations. The simulation based on different packing sizes suggests that the packing size has limited influence on the values of S_{jump} and S_{incr}. However, the decrement in applied dimensionless curvature does significantly alter the values of S_{jump} and S_{incr}. By reducing the step sizes, we manage to obtain a reliable estimate of these values, which helps the prediction of hydrate saturation based on Scenario B.

We conclude that Scenario A predicts the upper limit of hydrate saturation in the porous medium, while Scenario B gives the lower limit. The simulation based on periodic boundary condition predicts more trapping of gas than the one with conventional boundary condition. Trapping (either of wetting or nonwetting phases) reduces the amount of hydrate that can be formed, so the hydrate saturation based on the periodic boundary condition is lower than that on the conventional one. In the next chapter, we use the results from the simulation by using periodic boundary condition as it approximates the reservoir situation where local porous medium is not largely affected by the reservoir boundaries.

5. Hydrate distribution in a reservoir initially occupied by gas phase

Hydrate saturation and distribution in the porous medium are affected by temperature, pressure, salinity, as well as the initial methane and water saturations. We have investigated the influences of these factors in Chapter 4. One important parameter that cannot be investigated in the pore scale is the macroscopic fluid transportation. During hydrate formation, free methane and water need to be transported into the local porous medium in order to fill the vacancy that would otherwise be created. These newly transported methane and water become available for conversion to hydrate formation as well. The positive feedback leads to a much larger hydrate saturation than that predicted based on the scenario of a closed system (section 4.2 of Chapter 4). Consequently, the local hydrate saturation is also determined by the availability of methane and water supplies from other layers or surrounding aquifers.

The hypothesis examined here is that the field-scale hydrate distribution is a consequence of the behavior of pore-scale hydrate formation. In this chapter, the 1D sedimentological model of (Behseresht et al., 2009a) is used to predict the vertical hydrate saturation in the field scale. We assume a quasi-static system, where capillarity controls the fluid distribution and migration in the reservoir, and the pore-scale fluid distribution is upscaled to the field model using the macroscopic saturations of Table 4-1. The prediction by using this model is compared with the field observation from Mallik and Mount Elbert sites (both are in the Arctic regions). This model employs the study from both pore- and field- scales to give a better understanding of the hydrate distribution.

5.1 INTRODUCTION

Massive hydrate sites have been discovered worldwide. These sites include onshore continental sediments in Arctic regions (Mount Elbert and Mallik), and offshore deep water regions (Gulf of Mexico, Blake ridge, offshore South Carolina and Hydrate ridge, offshore Oregon). The hydrate reservoirs in the Arctic regions (Dallimore and Collett, 2005; Hunter et al., 2011) are usually the passive systems. No significant gas seepage is observed in these reservoirs, and the hydrate saturation is usually at very high value. On the other hand, reservoirs in the offshore deep water regions (MacDonald et al., 1994; Egeberg and Dickens, 1999; Torres et al., 2004) are very active system. These reservoirs are associated with massive hydrate formation and dissociation nowadays. Gas seepage is observed on the seafloor, and the hydrate saturation is in general lower than the hydrate reservoir in the arctic region (a quick introduction can be found at Section 1.3).

Seismic study is usually applied to investigate the hydrate distribution in large scales (Holbrook, 2001; Chevallier et al., 2005; Bauer et al., 2005; Cooper and Hart, 2002). Well logging technique is also a common and practical approach to estimate hydrate saturation in the field scale. Methods of resistivity log, density log, and NMR log are applied in order to cross-verify estimated hydrate saturations (Lee and Collett, 2008; Collett and Ladd, 2000; Katsube et al., 2005; Uchida et al., 2005). The most accurate method is by retrieving cores from the well, and measures the hydrate saturation from the chloride concentration, or isotope concentration (Stern et al., 2011; Lorenson et al., 2011; Lorenson et al., 2011; Torres et al., 2011). Although the accuracy of this method will be compromised due to the hydrate dissociation when lifting the core to the surface, it is most reliable tool to directly measure the hydrate saturation. However, it is an expensive

and time-consuming process, and therefore only a limited amount of core data is available to the public.

Models are also developed to study the methane hydrate distribution in the field scale. Compared to the numerous literatures concerning the reservoirs in the ocean sediments (Davie, 2003; Liu and Flemings, 2006; Garg et al., 2008; Marquardt et al., 2010; Liu and Flemings, 2007), to our best knowledge there is no model proposed to predict the hydrate saturation and distribution in the Arctic region. The research of the Arctic region still focuses on the petrophysical, geophysical, and geochemical descriptions of this type of hydrate system. The explanations tend to associate the hydrate distribution with lithologies. However, they do not address the observation that in some cases very little hydrate exists in the good lithologies, which should be the ideal environment for large hydrate saturation. The models we have developed in this dissertation provide an alternative approach to explain the hydrate distribution pattern in the Arctic region.

5.2 MODEL DESCRIPTION

We describe a 1D sedimentological model originally presented by (Behseresht et al., 2009a). Figure 5.1 gives the hydrate distribution in the Mallik gas hydrate field. The vertical hydrate distribution has a characteristic nonuniform pattern, where the high hydrate saturation layers are embedded between the low saturation zones. The hydrate saturation is relatively continuous in the lateral direction. Layers with similar hydrate saturation extend up to a hundred meters, which is much larger than the vertical length of each hydrate layer. This observation allows us to ignore the lateral variation of the hydrate distribution, and focus only on the vertical distribution. Consequently, a 1D model, which models the vertical hydrate distribution, is proposed.

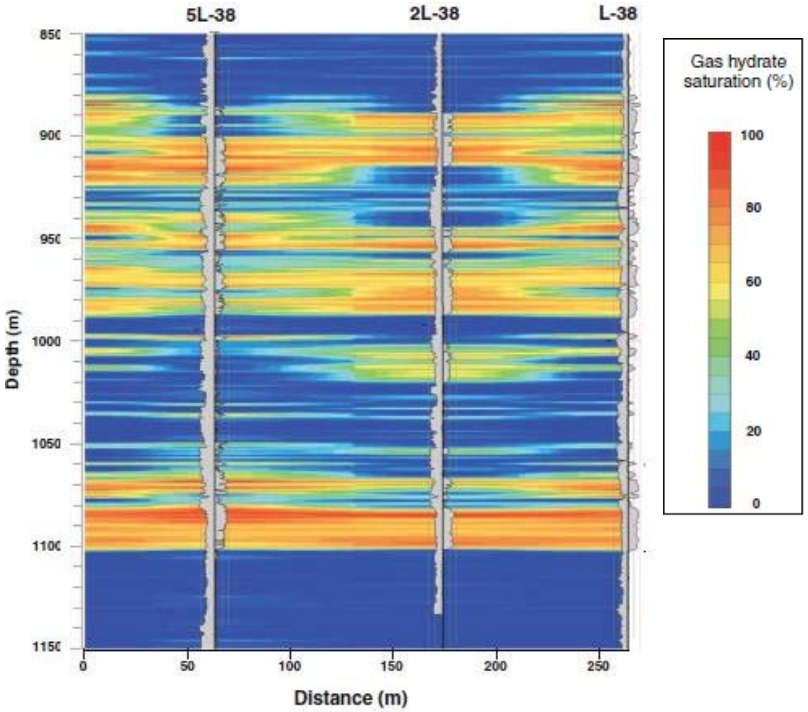

Figure 5.1: Hydrate distribution in the field scale, Mallik field, Mackenzie Delta on the coast of Beaufort Sea, northwest Canada. The *x* axis is the distance in the lateral direction. The hydrate distribution is inferred from the seismic and well logs in several exploration wells (5L-38, 2L-38, L-38). From (Dallimore and T.S. Collett, 2005)

We consider the following scenario. Reservoir sediments (with a depth of tens to hundreds of meters) sit on top of an aquifer. Each depth contains different grain size, so that the capillary entry pressure for the sediments varies along the depth. The reservoir is sealed on top by the cap rock, which has fine grains and large clay content (Figure 5.2).

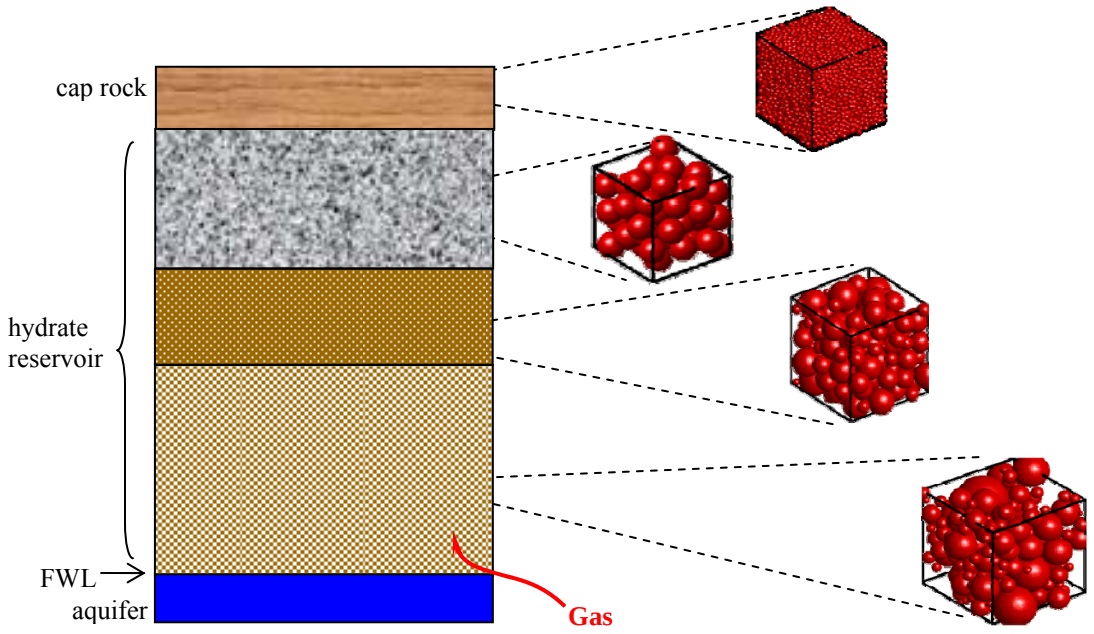

Figure 5.2: A schematic of the reservoir. Except for the cap rock layer, three different sediment layers are shown for demonstration. Different layers are with different grain size distributions. An aquifer locates below the reservoir. Before hydrate formation takes place (when BGHSZ is still above the cap rock) Gas migrates through the pathway (for example, fractures) to the reservoir from the deeper source rock over the geological time.

Over the geological time when the Base of Gas Hydrate Stability (BGHSZ) was far above the reservoir, free methane from the source rock migrated upwards, and accumulated in the reservoir sediments. The displacement of water by methane is determined by the competition between capillary pressure of the gaseous phase and capillary entry pressure of individual layers (capillary pressure P_c, and capillary entry pressure P_c^{entry}. Figure 5.3). The capillary pressure is zero at Free Water Level (FWL), and increases with height above FWL in an almost linear manner (the variation of the gas density due to temperature and pressure causes slight nonlinearity). The capillary entry pressure is the natural feature determined by the throat sizes, which are directly related to

the grain sizes and their distributition. When capillary pressure exceeds the capillary entry pressure, free gas enters the sediments and displaces the original fluid inside, in this case, water. This is the drainage process, and the final fluid distribution and saturation can be modeled by using the network modeling proposed in Chapter 2 and 3. On the other hand, when capillary pressure is smaller than capillary entry pressure, gas cannot invade the sediments. The cap rock has very fine grain size, and also contains significant amount of clay, which further reduces the throat sizes. This is the reason that the cap rock is capable of holding a column of free gas below it within the reservoir.

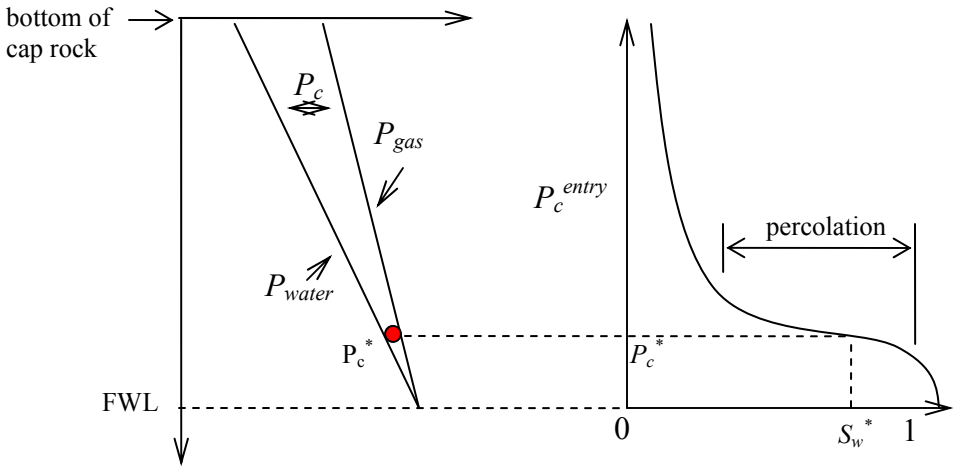

Figure 5.3: A demonstration of capillary pressure (P_c) and capillary entry pressure (P_c^{entry}), and how the comparison of these two values affects the fluid saturation in the porous medium. The capillary pressure is the pressure difference between water and gas, and increases upwards (left panel). The right panel shows the drainage curve, which gives the relationship between capillary entry pressure and the water saturation. At a point where the capillary pressure is P_c^* on the left panel, S_w^* can be determined from the drainage curve on the right panel.

Before hydrate formation, gas and water coexist in the system, and their saturations are determined by the capillarity (Figure 5.3). When the capillary pressure is much larger than the percolation threshold (as the upper part of Figure 5.3), gas can

displace water to its residual value, and reach the maximum gas saturation. During the percolation fluid saturation varies significantly with different capillary pressures (Figure 5.3). A transition zone exists between FWL, where gas saturation is zero, and the upper region of the reservoir where the maximum gas saturation is obtained.

For this gas reservoir, the transition zone can be ignored. For example, Figure 5.4 shows the median grain size distribution and the corresponding capillary entry pressure of Mount Elbert hydrate reservoir. The capillary entry pressure is obtained from the medium grain size, which is discussed in the next section. In this reservoir, the capillary entry pressure for most sediments is smaller than 0.05 MPa. On the other hand, the average methane density from 614 m to 672 m is 51 kg/m^3. Assuming the water density to be 1000 kg/m^3, we obtain the capillary pressure gradient to be (1000-51) × 9.8 = 0.009 MPa/m. On average it requires 5.5 m of gas column height for capillary pressure to overcome the capillary entry pressure (Figure 5.4 shows P_c (red line) from BGHSZ). Compared to the length of the gas column (58 m), the length of transition zone is relatively small (especially close to the bottom of the reservoir, where the capillary entry pressure is extremely low), and thus is negligible.

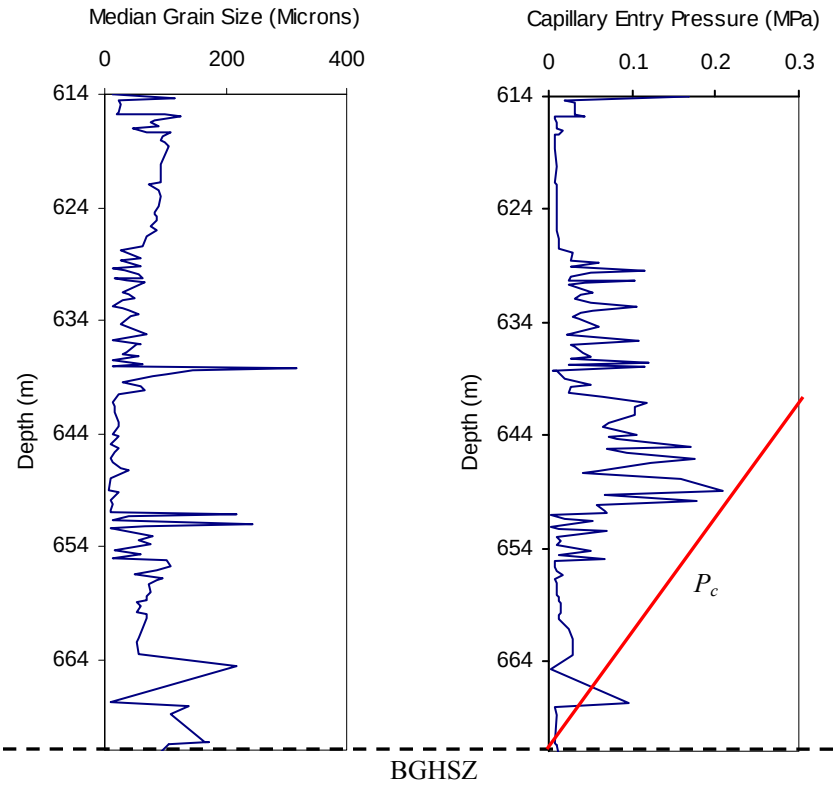

Figure 5.4: The average grain size distribution and the capillary entry pressure of the Mount Elbert hydrate reservoir. The capillary entry pressure is by assuming the throat size to be 1/3 of the grain size, and the interfacial tension between water and methane to be 0.075 N/m (this is the surface tension of water at 300 *K*. This value is a weak function of salinity and pressure)

As shown in Chapter 2, the different grain size distributions do not lead to large variation of the irreducible water saturation. This suggests that the maximum gas saturation at each depth only has insignificant difference, which can be ignored as a first order approximation. We therefore idealize the initial gas saturation has a uniform distribution in the vertical direction, from FWL at the bottom to the cap rock on top. We compare the conceptual and idealized gas saturation in Figure 5.5. Our model employs the idealized one.

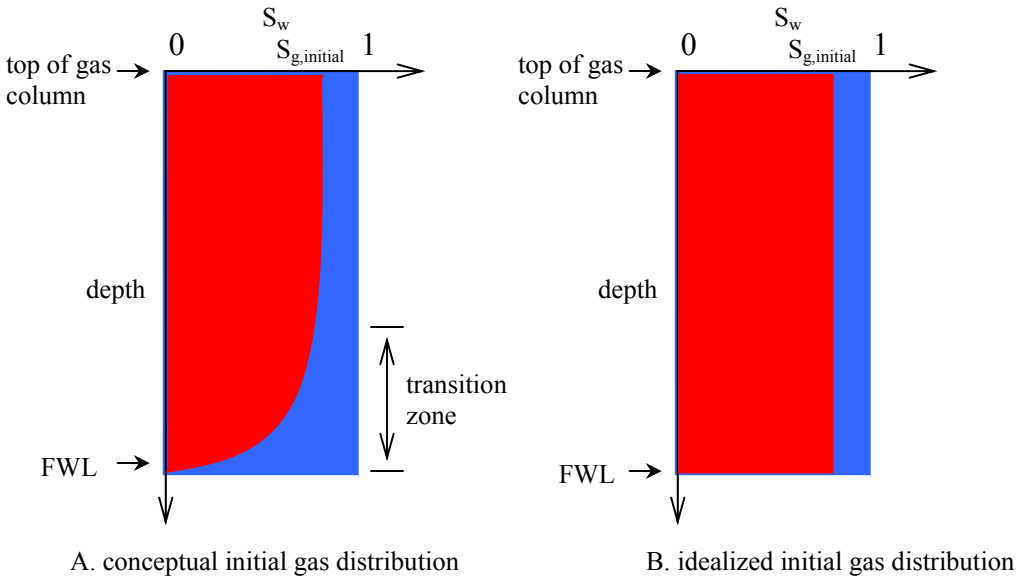

Figure 5.5: The conceptual and idealized initial gas distributions (red: gas; blue: water). Due to the low capillary entry pressure of the sediment and the high capillary pressure gradient between water and gas, we ignore the transition of gas saturation.

BGHSZ initially was above the gas column, and later began to move downwards due to temperature decrement. During this process, we do not allow gas communication with the deeper gas sources. This treatment makes gas the limiting phase. On the other hand, water is allowed to feed in from both below and above the gas column. On top of the gas column, the capillary seal has a very high capillary entry pressure, but similar permeability with the reservoir below (Figure 5.6 shows the example of Mount Elbert, the gray box shows the location of the capillary seal). This feature allows for the water invasion from the capillary seal into the reservoir, when hydrate formation creates vacancies in the porous medium (as shown in Section 4.2.2). An aquifer locates below the reservoir (below 670 m, shown in Figure 5.6), with good lithology and high permeability. Thus water invasion from the aquifer is also possible. Due to the setting of 1D model, water cannot invade from the horizontal surrounding of the reservoir.

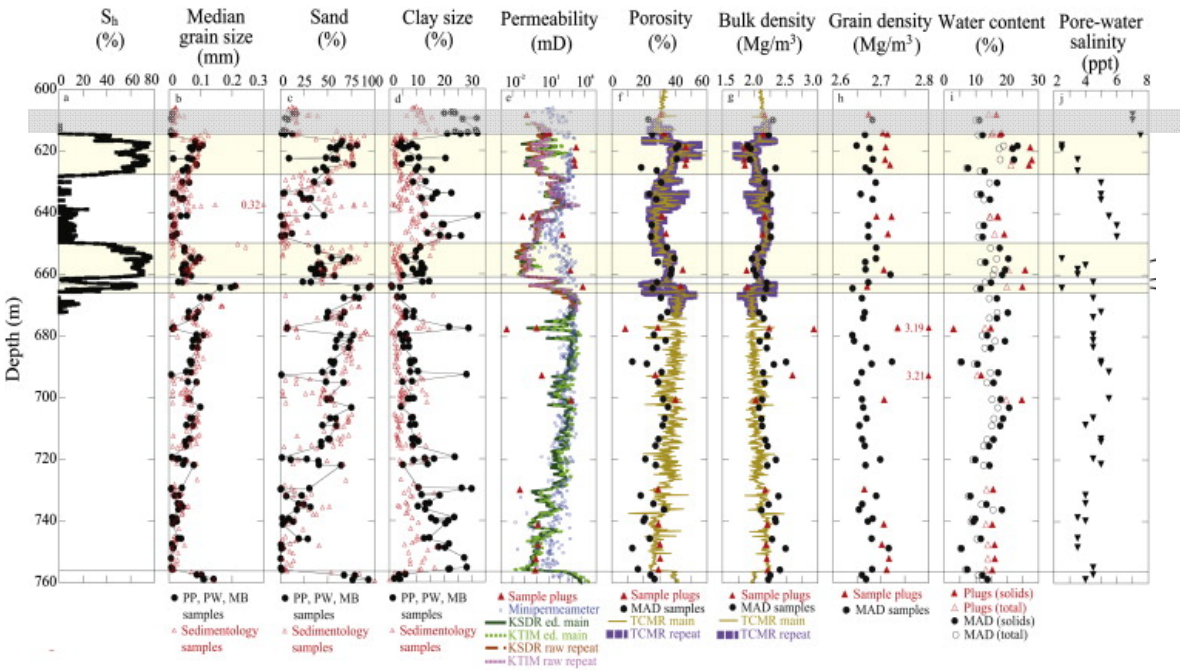

Figure 5.6: Some petrophysical and lithological properties from Mount Elbert hydrate reservoir.

When BGHSZ begins to descend and passes the reservoir, hydrate begins to form at BGHSZ, where the condition for temperature and pressure is satisfied for hydrate formation. It is believed that BGHSZ in the arctic region descends or ascends according to the glacial and interglacial periods, respectively (Torres et al., 2011). Depending on the depths of hydrate reservoir (for example, Mount Elbert locates at about 600 m, while Mallik locates at about 900 m), the hydrate formation for these two reservoirs might have taken place at different geological times (Majorowicz et al., 2008). The numerical model proposed by (Majorowicz et al., 2008) suggests that it is a general trend that BGHSZ has been descending over the past several million years. BGHSZ reached 600 m 2.5 Ma ago, and has stayed always below 600 m. Therefore, gas hydrate in Mount Elbert is likely to form 2.5 Ma ago. Although BGHSZ reached 900 m 1 Ma ago, the following cycles of

glaciation and interglaciation keeps forming and disassociating hydrate in the reservoir, until the last glaciation (~100,000 years ago) yields the hydrate profile we observe today.

The descending of BGHSZ is a slow process that usually takes hundreds of thousands of years to cover the entire depth of the reservoir (Majorowicz et al., 2008). Consequently, we assume that BGHSZ is static when hydrate formation takes place. This assumption decouples the complex and dynamic processes of BGHSZ movement and hydrate formation. After the hydrate formation was complete at BGHSZ, BGHSZ moved down to a deeper layer where gas and water still coexisted. The infinitesimal downwards movement of BGHSZ reflects the real behavior in the reservoir. But in our model, we divide such movement into tiny but representative steps.

As discussed in Chapter 4, the formation of hydrate creates vacant spaces. Therefore, fluids were drawn to fill the vacancy. Figure 5.7 shows a schematic of the hydrate formation at BGHSZ. The layer of green (hydrate) and white (vacancy) bars shows the layer at BGHSZ, where hydrate formation is taking place. The thickness of the layer is magnified for a better visualization. We assume that hydrate grows into the gaseous phase as gas is the limiting phase. Water, however, is connecting to the aquifer from above and below the gas column (water supply from the horizontal surrounding is not possible for this 1D model).

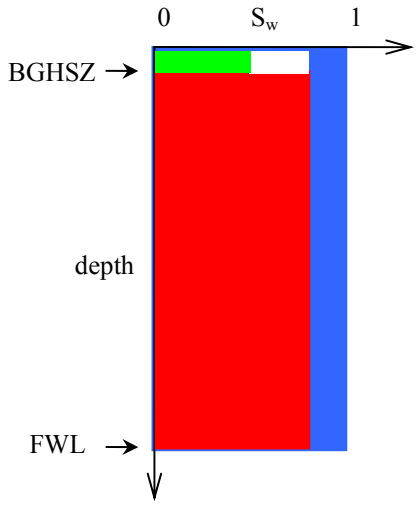

Figure 5.7: Hydrate formation as BGHSZ moves downwards. The volume of hydrate (green) is smaller than the volume of water and gas consumption. A large vacant space (white) is left in the porous medium to be filled by fluid phase(s).

The vacancy can be filled by either free gas or water, or both. The free gas can only come from the deepest depth of the reservoir where free gas is still available. That is, free gas first comes from the layers at the bottom of the gas column. After those layers are depleted of free gas, the next deepest layers still filled by free gas become the gas source. It is not possible for free gas to come from shallower layers while the deeper layers still contain free gas: if gas leaves from shallower layers, the local pressure reduces. As no water invasion can take place from the horizontal direction, only free gas from deeper layers can be sucked upward. The upward increment of gas movement is thus transferred layer by layer to the deepest layer where free gas is still available. At this depth, the pressure decrement due to the loss of free gas will be compensated by the water invasion, from the aquifer below.

We also consider the scenario that part of the vacancy is filled by water, which is transported from the cap rock on top of the original gas column. (Behseresht and Bryant,

2011) examined this scenario from the macroscopic point of view. Here the focus is upon the pore scale and how it influences the macroscopic behavior. The water movement involves the imbibition process through the micro defects of the hydrate layers, which has a very low permeability compared to that of the sediments, and might be a potential constraint to the water supply rate. In Chapter 4, section 4.3 we proposed two scenarios that consider this effect. Scenario B introduces a situation where the water supply rate is much larger than the hydrate formation rate, and thus Melrose imbibition jump takes place. During this event, water invades the gas-filled space instantaneously. This behavior gives noticeable water invasion, as shown in Figure 5.8A. When the water supply rate is much smaller than the hydrate formation rate, only the incremental movement can occur (Scenario A). Such slow movement provides just enough water to form new hydrate, and no extra water invades the vacancy (Figure 5.8B). Therefore, the vacancy in Figure 5.7 is occupied by both gas (red) and water (blue) in Scenario B, while only gas occupies the vacant space in the Scenario A (Figure 5.8A).

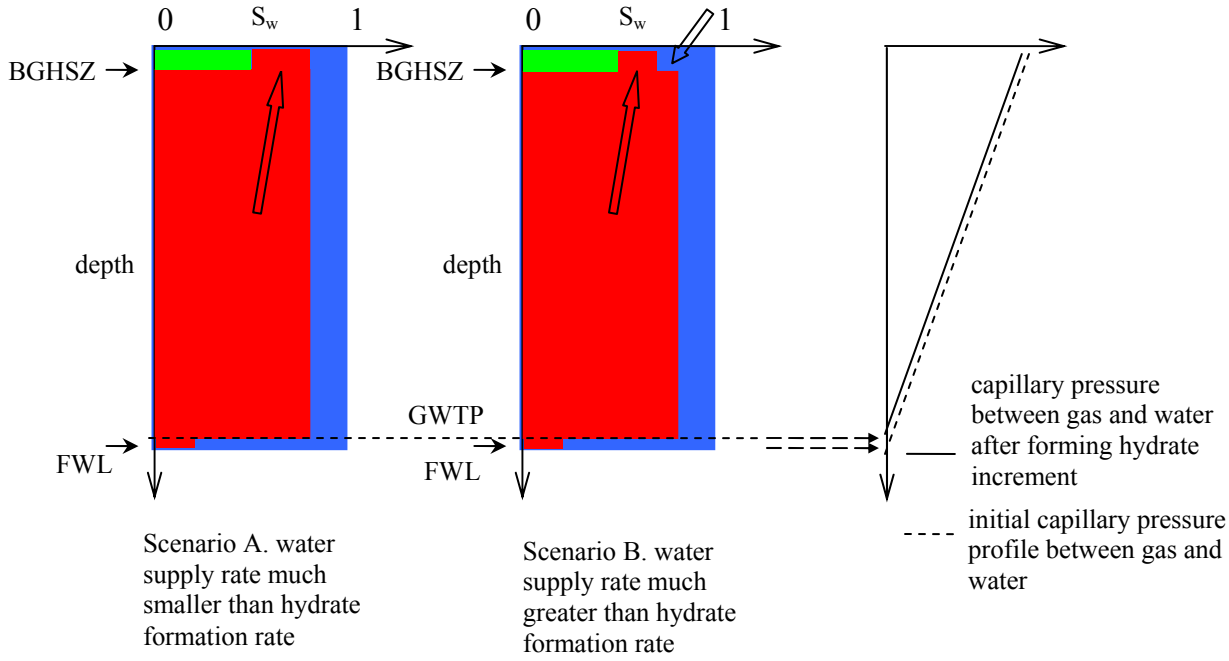

Figure 5.8: The comparison of the filling fluids for two pore-level scenarios described in Ch. 4. The left panel (A) shows that only gas invade the vacancy induced by hydrate formation (Figure 5.7) and the right panel (B) shows both water and gas invade the vacancy. Water at the bottom invades the gas reservoir from below, which also moves the Gas Water Transition Point (GWTP) upward. We assume the capillary pressure at the GWTP to be zero. The arrows show the either the upward migration of gas or the water invasion from the cap rocks.

When free gas from the bottom migrates upwards to fill the vacancy, water invasion takes place at the bottom. The imbibition process displaces gas to the residual value, which can be predicted from the imbibition simulation by our network modeling in Chapter 2. The GWTP (Gas Water Transition Point) defines the depth where gas no longer percolates the porous medium. Between GWTP and FWL, the gas saturation is at the residual value. The water invasion at the bottom raises the GWTP (we do not show GWTP in the previous figures, as it is very close to FWL), and shifts the capillary pressure between gas and water upwards (the right panel in Figure 5.8). Strictly speaking,

GWTP does not correspond to zero capillary pressure (by using the periodic boundary condition), only FWL does. However, as the sediments have relatively low capillary entry pressure, we assume GWTP indicates zero capillary pressure in our model.

The upward shift of capillary pressure profile between gas and water in effect induces imbibition at other layers of the reservoir. In this work we ignore this behavior as the capillary pressure is much higher than the capillary entry pressure. Therefore, a small decrease of the capillary pressure only leads to a small increase of the water saturation, which is negligible for this analysis. Close to GWTP where capillary pressure reduces to the similar value of capillary entry pressure, we expect a sharp transition. However, we assume a stair-like gas saturation profile instead as a first order approximation.

The water and gas that fill the vacant space cannot persist as the temperature and pressure of that layer provide a proper environment for hydrate formation. Water and gas are eventually converted into hydrate, which further creates vacant space and draws more gas and water. The positive feedback continues to draw water and gas from their individual sources and form more hydrate (water comes from the cap rock and gas comes from the lower layers still filled with gas). In Scenario B, the water invasion that goes into Melrose jumps at the pore scale is not converted into hydrate. In Scenario A, however, all the imbibed water is turned into hydrate. After the hydrate formation is complete, the hydrate saturation of Scenario A is higher than that of Scenario B (Figure 5.9).

Another difference between these two scenarios is that, as proposed by Chapter 4, gas trapping is considered in Scenario B, but not in Scenario A. This is because when Melrose jump takes place, the instantaneous invasion of water disconnects the gas clusters and therefore traps gas bubbles. The conversion of the trapped gas into hydrate would only draw water to fill the vacancy, as no free gas can be supplied from the bulk.

Such mechanism further increases the water saturation in Scenario B after hydrate formation is complete.

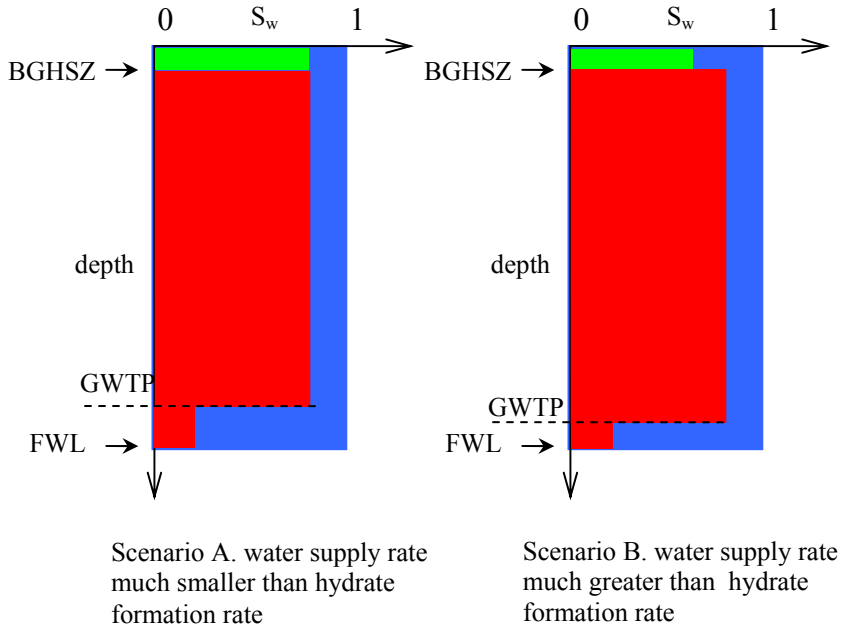

Figure 5.9: A schematic of the phase distribution after the hydrate formation is complete at BGHSZ.

For Scenario B, we apply a box model to show the calculation of hydrate saturation (Figure 5.10). The volume of the box is equal to the volume of the void space in a porous medium. Initially only gas and water fill the void space (Figure 5.10A). When gas is converted into hydrate completely, vacant space will be generated, and water invades part of the vacant space (Figure 5.10B). The vacant space will later be filled by the gas from other layers in the reservoir. Being contacted with water, gas is converted into hydrate. Vacant space is also generated, and part of it is filled by water invasion as well (Figure 5.10D). Figure 5.10B to D repeat cyclically until no more void space is available. The box is finally filled only by hydrate and water.

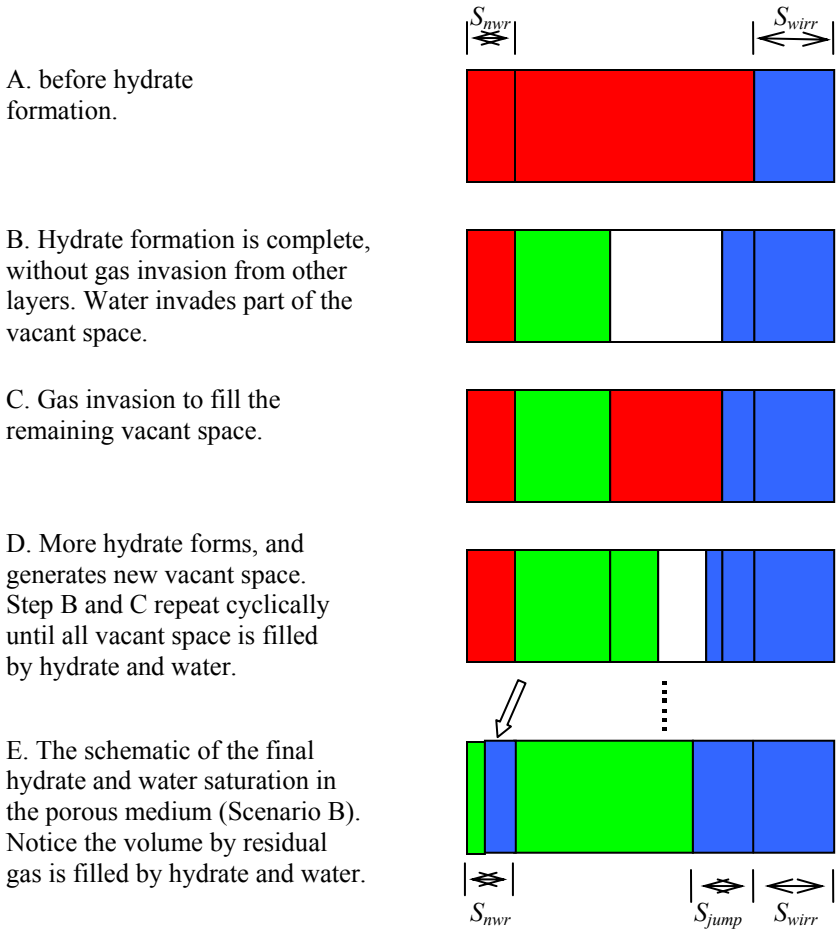

Figure 5.10: Schematics of the hydrate formation in a box model, based on Scenario B. Red region: methane gas; blue region: water; green region: hydrate.

Figure 5.10 suggests that, in Scenario B, the final hydrate saturation is the unity minus the summation of three water volumes: first, the irreducible water saturation from the initial gas-saturated reservoir. Second, the saturation unit of Melrose jump (S_{jump}). We obtain such value from chapter 4, where 7% S_{jump} is determined from the simulation based on a 7000-sphere packing. The last term comes from the water invasion due to hydrate formation inside the trapped gas bubbles. This is the water saturation indicated by

the hollow arrow in Figure 5.10E. This saturation (referred to as S^*) can easily be calculated from the residual gas saturation S_{nwr} obtained from Chapter 2.

$$S^* = S_{nwr}\left(1-\frac{\rho_g}{\rho_h}\frac{M_g + NM_w}{M_g}\right) \tag{5.1}$$

Therefore, the final hydrate saturation is calculated as

$$S_h = 1 - S^* - S_{jump} - S_{wirr} \tag{5.2}$$

The above equation is for Scenario B only. For Scenario A, we do not consider Melrose jump, and thus S_{jump} is equal to zero. Moreover, since there is no trapping, all the space that was filled up by the 'trapped' gas will be filled by hydrate eventually, which reduces S^* to zero as well. The hydrate saturation for this scenario can be calculated by the following equation.

$$S_h = 1 - S_{wirr} \tag{5.3}$$

As BGHSZ continues to move downwards, the processes described above repeat themselves in each thin layer of the reservoir, and fill the porous medium with hydrate and water. Meanwhile, free gas migrates upwards to fill the vacancy and reduces the gas saturation to the residual value at the GWTP. This causes GWTP to rise (Figure 5.9). Eventually the descending BGHSZ and ascending GWTP overlap at certain depth, at which point the entire reservoir is divided into the hydrate zone on top and water with residual gas zone at the bottom (Figure 5.11). The maximum hydrate saturation of Scenario B is lower than Scenario A, therefore yields a longer hydrate column, because of the fixed amount of gas original in the column.

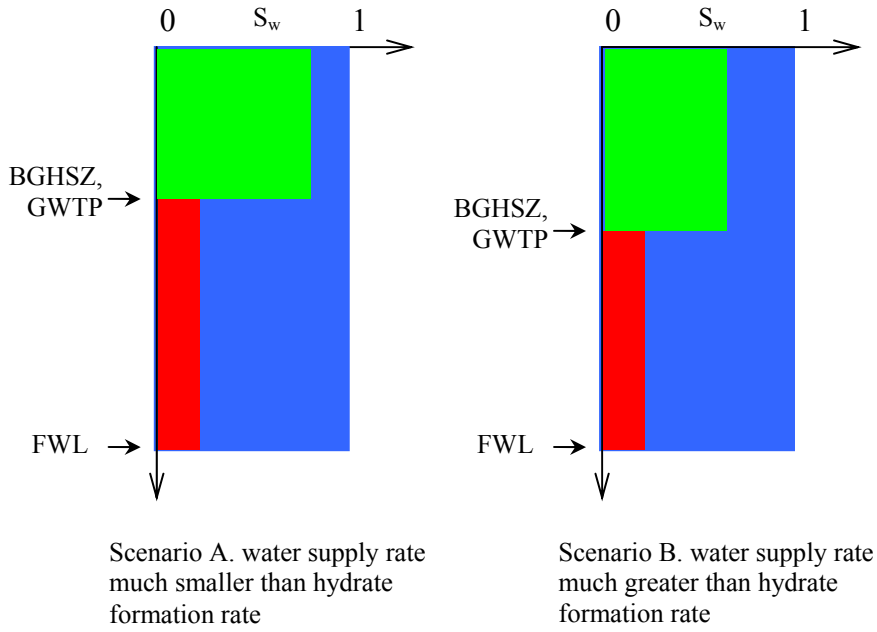

Figure 5.11: Phase distribution when BGHSZ and GWTP meet for both scenarios. The entire reservoir that is originally filled by gas and water is divided into two separate regions. Above BGHSZ, the region is mostly filled by hydrate. Below BGHSZ and GWTP water fills most pore spaces with residual gas trapped within.

The further downward movement of BGHSZ converts the residual gas into hydrate. No free gas is available so that only water imbibes to fill the vacant space. This process results in very low hydrate saturation, compared to the high saturation unit on top of the reservoir (Figure 5.12). The final hydrate distribution is obtained when BGHSZ moves below FWL. The pattern shows a combination of high and low hydrate saturation zones, which is totally different from the initial gas distribution of uniform saturation along the depth. The initial gas is totally redistributed: the upward migration of gas for new hydrate formation transports all free gas to the top of the reservoir, and reduces the gas saturation to the residual value at the bottom.

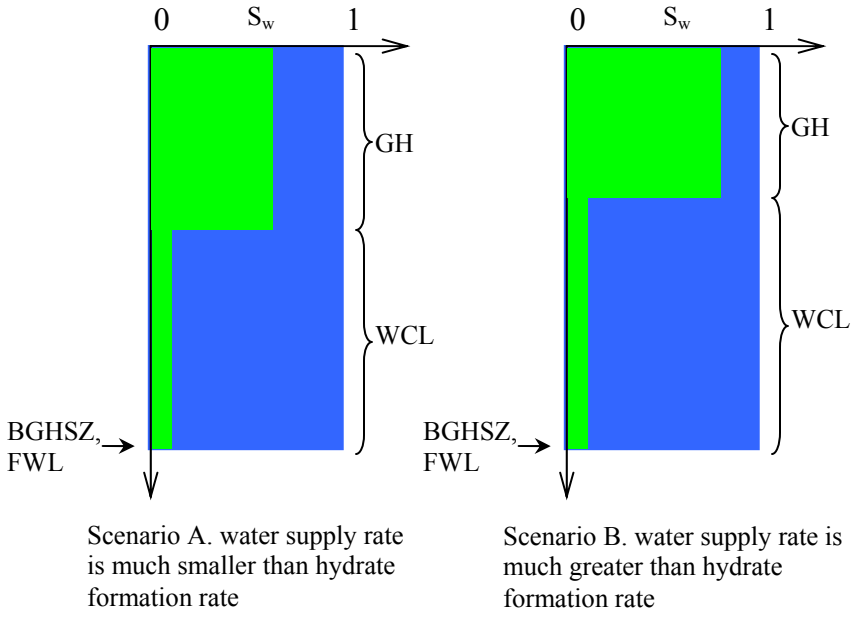

Figure 5.12: Hydrate distribution after BGHSZ moves to the bottom of the gas column. All gas is converted into hydrate. Due to the gas redistribution, the final hydrate profile includes the high saturation zone on top and low saturation zone. We refer to the high hydrate saturation unit as GH (Gas Hydrate) unit, and the other one as WCL (Water Contact Layer) unit.

This 1D model describes the hydrate formation and distribution in the reservoir scale, by combining the results from the pore network modeling. In the above analysis, we use one gas column for the demonstration. However, multiple gas columns along the depth might also exist in the reservoir. One possible reason is that the reservoir is separated into several compartments, and each compartment supports a single gas column, which has no communication with the others. The other reason that could yield multiple columns happens during the hydrate formation. When the capillary pressure decreases as GWTP rises (Figure 5.8), it might fall below the capillary entry pressure at certain depth. If this situation occurs, the gas column is disconnected into the upper and lower units.

Our calculation follows the model described above, which starts from the top of the reservoir, and then moves downwards. The gas column is equally divided into finite amount of layers. BGHSZ moves to the bottom of each layer in a discontinuous fashion. When BGHSZ is at the bottom of layer A, The hydrate formation in layer A occurs. The saturation of hydrate is determined by equation (2) and (3) for different scenarios. The global material balance is also checked to compute how much gas is required to fill the vacancy, and also the depth of GWTP at which the gas saturation is reduced to the residual value (Figure 5.9). BGHSZ moves to the next lower layer when the hydrate formation is complete in layer A. The same calculation is performed to determine hydrate saturation and GWTP.

When BGHSZ is lower than GWTP, hydrate forms only from the residual gas. No free gas is available to fill the vacancy. The final hydrate saturation is computed by the amount of residual gas. Eventually, these layers are filled by large amount of water and a small amount of hydrate.

5.3 CASE STUDY – MOUNT ELBERT GAS HYDRATE FIELD

Mount Elbert gas hydrate test well is drilled on the North Slope of Alaska (Figure 5.13). Cores are retrieved from 606.5 to 760.2 m, where two major gas hydrate-bearing zones are identified. The hydrate reservoir is below the base of permafrost, which locates at 536.4 m (Hunter et al., 2011). Modern BGHSZ is believed to be at around 900 m, far below the depth where hydrate is observed. The hydrate reservoir contains only solid hydrate and liquid water, and gas is not identified.

A great amount of data is collected from Mount Elbert well, including petrophysical (Winters et al., 2011), geochemical (Lorenson et al., 2011), and test production (Anderson et al., 2011) data. Those data help characterize and quantify the hydrate reservoir in both geological and engineering perspectives, and investigate the potential exploration and production capabilities. The hydrate distribution in the reservoir, along with the total hydrate reserve, is a critical factor that determines the production possibility. In Mount Elbert well, two major approaches are used to estimate the hydrate saturation in the sediments: well logs and lab-based core measurements. For example, resistivity log measures the resistivity of the sediments. The reading is directly correlated with the pore-throat connectivity of the porous medium. Given porosity and water salinity, the water saturation can be calculated by using Archie's equation. Moreover, by measuring the salinity of the fluids extracted from the cores, a simple calculation based on the material balance can be employed to estimate the hydrate saturation as well.

All these approaches are dependent on the direct measurements of the certain type of petrophysical and geochemical values. A model based on more fundamental knowledge, such as sedimentological information, is not yet available. However, such

model gives us an independent prediction of the hydrate distribution from the geological information, as well as the physics governing phase behavior and fluid transportation. Furthermore, data from well logging or core measurements are not required in this model. Therefore, the application of this model is not restricted by the availability of this information.

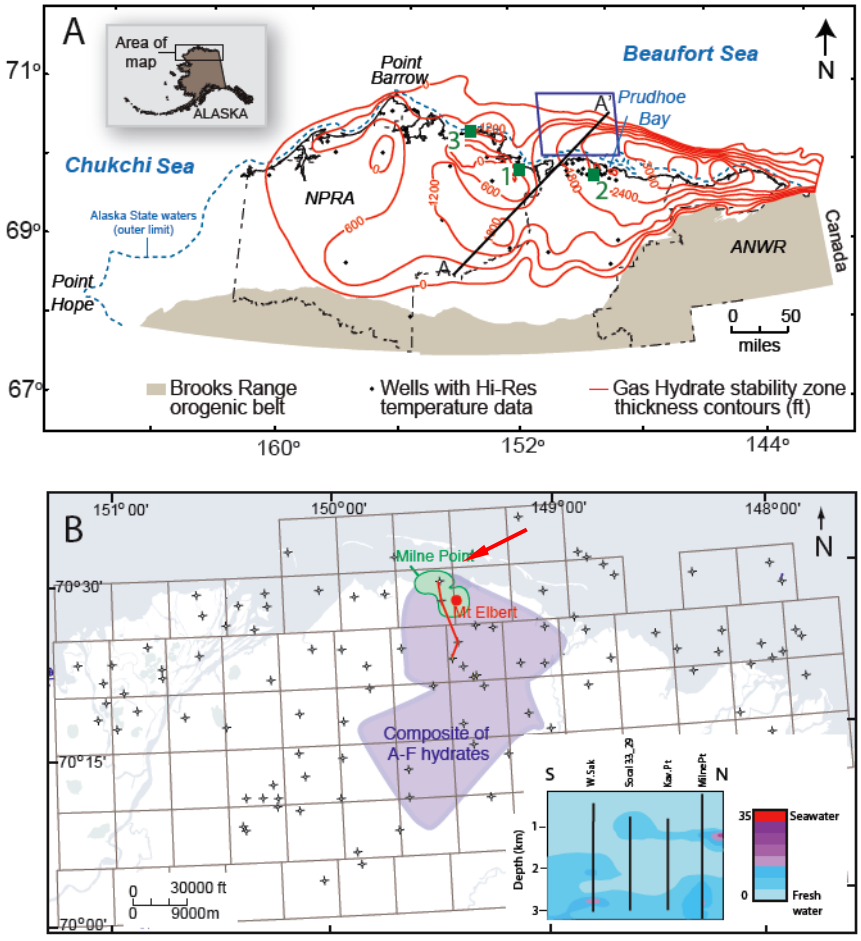

Figure 5.13: The map of Alaska North Slope (A), along with the extension and thickness of the hydrate stability zone. (B) shows the location where Mount Elbert test well is drilled. From (Torres et al., 2011)

The sediments in the reservoir are under normal overburden pressure. The porosity of the sediments ranges from 20% to 40% (Winters et al., 2011), owing to the different clay concentrations and grain size distributions. The model sediments with varied grain size distributions have a porosity ranging from 30% to 35% (Appendix A). Although we do not consider clay contents in the model sediments, we can still use this model sediment to represent the relatively clean lithologies in the reservoir. The pore network model derived from the model sediments is also applied to simulate the fluid movements during drainage and imbibition events.

One of the restrictions to apply different model sediments is the lack of the information of grain size distribution. (Winters et al., 2011) only reported a limited amount of grain size distribution at certain depths, which does not give us enough resolution to describe the entire reservoir. We therefore assume monodisperse in our simulation. As discussed in Chapter 2, different grain size distribution does not affect the initial gas saturation in the gas column. However, the residual gas saturation at imbibition endpoint is dependent on the grain size distribution: higher sorting index (wider grain size distribution) yields lower residual gas saturation, and thus gives more free gas in the porous medium. Therefore, more gas can be freely transported to BGHSZ, which fills the vacancy and generates hydrate.

We use the following equation to compute the capillary entry pressure of the sediments.

$$P_C^{entry} = \frac{2\sigma_{gw}}{R_{thr\_ins}} \tag{5.4}$$

where P_C^{entry} is the capillary entry pressure, σ_{gw} is the interfacial tension between gaseous and aqueous phases. R_{thr_ins} is the throat inscribed sphere, whose value can be determined by using these approximations:

$$R_{thr\_ins} = \begin{cases} \frac{1}{3} R_{grain} & clean\ sand \\ \frac{1}{6} R_{grain} & shaly\ sand \end{cases} \tag{5.5}$$

where R_{grain} is the average grain size of the sediment. Equation (5.5) is from (Behseresht et al., 2009a). The presence of clay and silt clogs the throats between sand grains and therefore results in smaller throat sizes and higher capillary entry pressure. With the above settings, the capillary entry pressure of the reservoir is computed and shown in Figure 5.14.

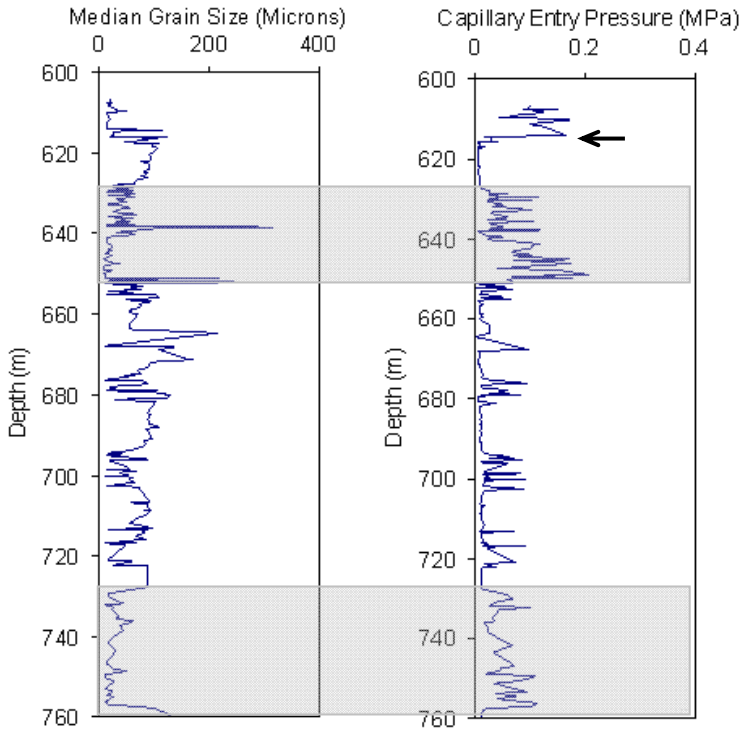

Figure 5.14: Median grain size and capillary entry pressure comparison along the depth, Mount Elbert test well.

Figure 5.14 gives the median grain size and capillary entry pressure (calculated from equation (5.4)) of the sediments from 606.5 to 760.2 m. The units of clean sands (thick layers with lower capillary entry pressure) are separated by the units of shaly sands

(thin layers with higher capillary entry pressure). Two abnormalities (indicated by the gray boxes) between 625 to 655 m and below 725 m, are observed, where thick layers of shaly units dominate the region. The upper one contains the highest capillary entry pressure (greater than 0.2 MPa), which becomes a potential barrier to separate the single gas column into two individual ones.

BGHSZ is at around 900 m. Above this depth, the environment permits hydrate formation. However, the observation gives no hydrate presence below 672 m (Lee and Collett, 2011). Two possible cases can be inferred from the observation: 1) no hydrate is present and the reservoir is totally saturated with water. This also means the initial gas column only extends to 672 m. 2). There is only very small hydrate saturation, generated from the residual gas in the reservoir. From the logging tools such small saturation cannot be identified. Therefore, the initial gas column can extend below 672 m; however in this case, the deepest extension of gas column cannot be determined from the available petrophysical and geochemical information. In this section, we only consider the former case.

No hydrate is observed above 614 m, which gives the upper bound of the initial gas column. It is believe that initial gas is trapped below the seal indicated by the arrow in Figure 5.14. Although it is an unconsolidated lithology at this depth, the high clay content might already block pores and throats, so that we could have underestimated the capillary entry pressure at that depth (indicated by the arrow in Figure 5.14). Also, we assume that no gas is present below 672 m. Therefore, the initial gas column existed between 614 and 672 m, with the Free Water Level (FWL) at 672 m. The capillary pressure between gas and water is also zero at that depth.

We assume the initial gas charge (that is gas invades the water-saturated sediments and displaces water) follows this scenario. The reservoir, ranging from

614~672 m, is divided into two units (Unit C and D). The barrier between these two regions is at 650 m, where the capillary entry pressure of the sediment is at the maximum value (Figure 5.15). At the time when BGHSZ was still above Unit D, gas generated from deeper reservoir migrated upwards and charged these two units. When the free gas reached the capillary barrier at 650 m, the capillary seal prohibited the further upward movement. Gas therefore accumulated first in the upper region of Unit C (Figure 5.15A), and expanded downwards. During the expansion, the capillary pressure at the top of Unit C increased as well. When the capillary pressure built up to exceed to capillary entry pressure of the barrier between Unit C and Unit D, gas was able to migrate upwards, and accumulated on top of Unit D (Figure 5.15B). When the gas charge continued, the entire Unit D was slowly filled by free gas from top to bottom. In the meantime, the length of gas column in Unit C did not change (Figure 5.15C). However, after Unit D was totally filled, gas can be used to fill C, so that the length of gas column in Unit C increased again. The final gas saturation profile gave a full gas column in both Unit C and D.

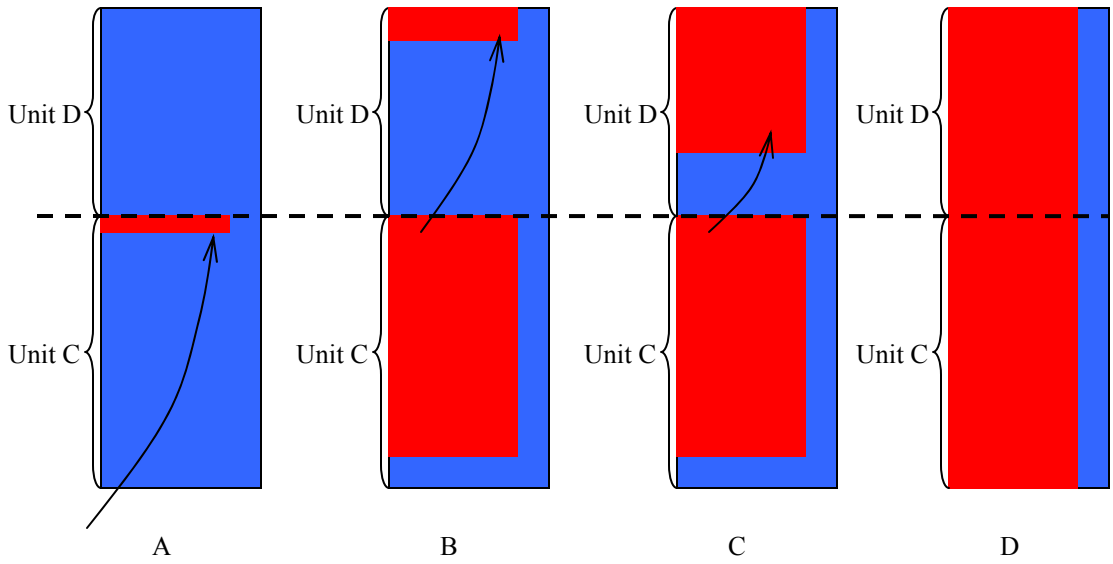

Figure 5.15: Initial gas charge in Mount Elbert hydrate reservoir. (A) the upward movement of free gas from deeper reservoir was stopped by the capillary barrier at 650 m (dashed line), so that gas accumulated and the gas column expanded downwards. (B) when the capillary pressure built up to exceed the entry pressure of the barrier, the upward migration restarted, and free gas began to fill the upper region of Unit D first, and expanded to the lower region (C). (D) both Unit C and D would eventually be filled up by gas.

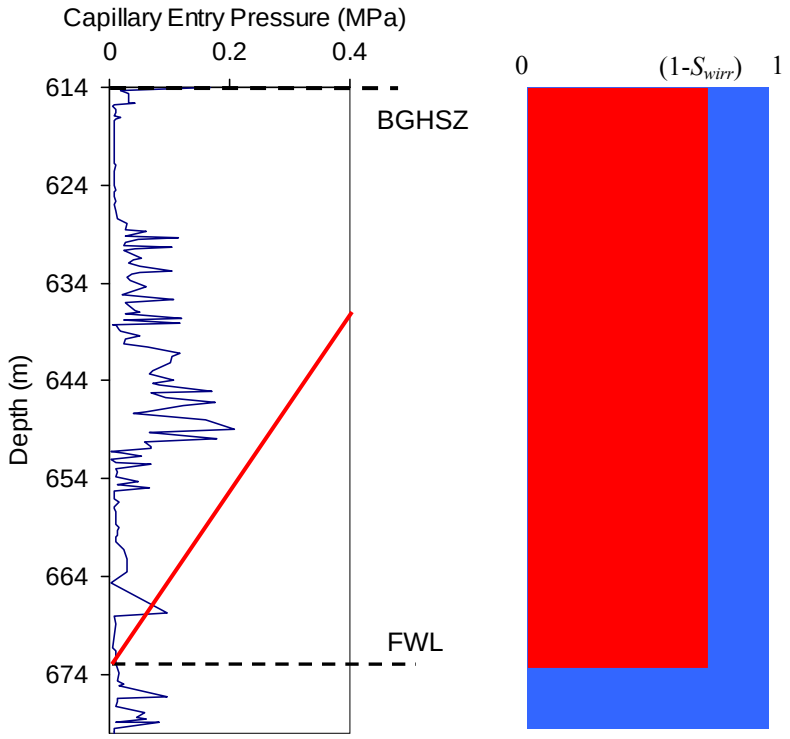

Figure 5.16. The comparison of the capillary pressure and capillary entry pressure of the sediments before BGHSZ moves downwards (left), and the initial gas column (red) in the reservoir (water in blue). At 614 m, we assume a capillary barrier that has an entry pressure of at least 0.7 MPa (not shown in the figure), which is high enough to overcome the capillary pressure between gas and water.

The initial gas saturation along the depth is replotted in Figure 5.16, along with the capillary pressure and the entry pressure of the sediments. Hydrate forms at BGHSZ when it begins to descend. As discussed previously, free gas from the bottom will transport upwards to fill the vacancies created by the hydrate formation. This shifts the capillary pressure upwards (from dashed to solid red line in Figure 5.17), and reduces the difference between capillary pressure and capillary entry pressure. When the capillary pressure falls below the capillary entry pressure at 650 m (indicated by the arrow), the communication inside the gas column might be hampered (Behseresht et al., 2009a).

Only a small amount of continuous gas clusters, if any, remain to connect the upper and lower parts of the gas column, so that the gas migration is largely restricted. We use a black line in the right panel of Figure 5.17 to demonstrate this capillary barrier. It is located at where the highest capillary entry pressure is (indicated by the black arrow). In the extreme case where no continuous gas clusters exist, the gas column is separated into upper and lower units. We refer to these two units as Unit C and D, which agree with the categorization in the literature (Lee and Collett, 2011; Anderson et al., 2011). It should be noted that in the literature, Unit C and D only contains the sediments with high hydrate saturation. In our definition, the unit contains the region beneath the hydrate-saturated sediments as well.

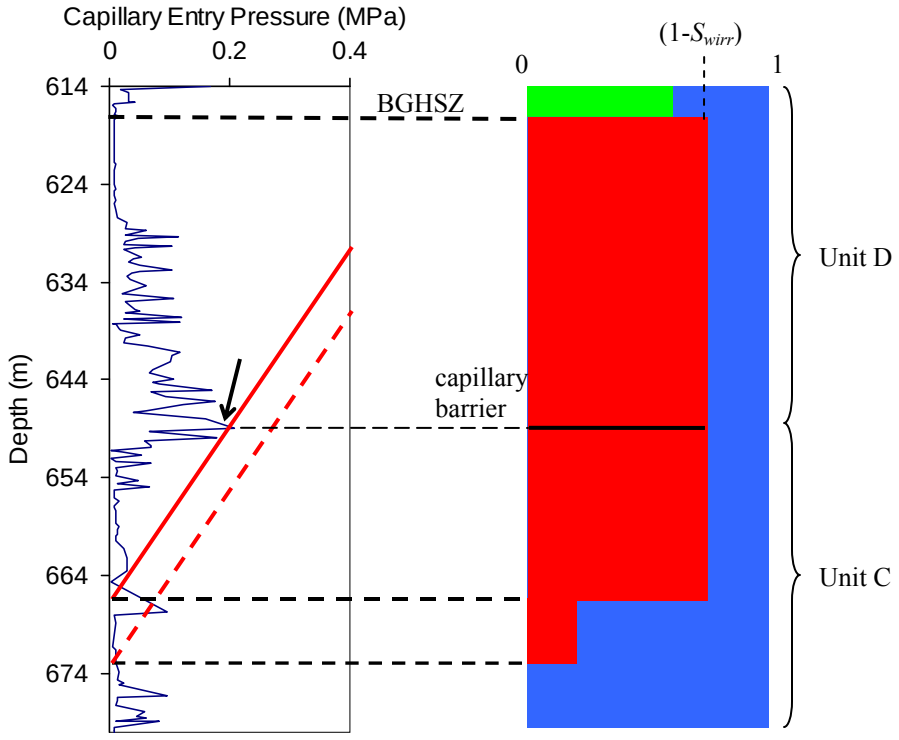

Figure 5.17: The communication inside the gas column is restricted when capillary pressure decreases (from dashed to solid red line), for example due to rising gas-water contact, and becomes smaller than the capillary entry pressure. The black line on the right panel shows the possible capillary barrier that could separate the gas column into Unit C and D.

When BGHSZ further moves downwards, based on the assumption no free gas in Unit C can be transported to fill the vacancy, as two gas units are separated by the capillary barrier. Instead, free gas from the bottom of Unit D (Figure 5.18A) is transported to fill the vacant space and generates more hydrate. Before BGHSZ reaches the capillary barrier, Unit C is almost intact. The only free gas it has lost is before the capillary pressure drops below the capillary entry pressure at the barrier. All the fluid transportation and phase conversion occur in Unit D.

When BGHSZ moves below the capillary barrier, the hydrate formation in Unit D is complete, and all available gas is converted into hydrate (Figure 5.18B). Subsequent hydrate formation and gas transportation only take place in Unit C, and follows the model described by Figure 5.9 to Figure 5.12. Unit D and C have the similar hydrate distribution pattern after the hydrate formation is complete.

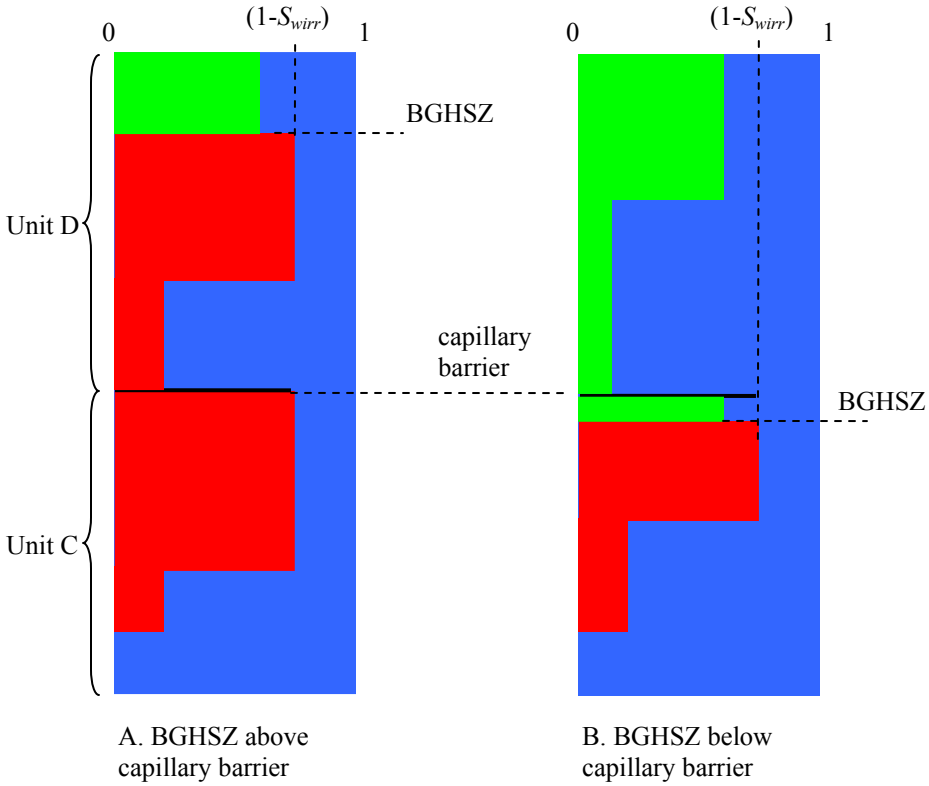

Figure 5.18: Two intermediate steps when BGHSZ is above (A) and below (B) capillary barrier. Almost all the free gas in (A) is supplied from the bottom of Unit D. In (B), the gas transportation is only within Unit C.

5.3.1 The effect of capillary barrier

The capillary barrier restricts the gas transportation between upper and lower units of the reservoir. Depending on the comparison between capillary pressure and capillary entry pressure, the effect of capillary barrier varies significantly. When capillary pressure is much greater than capillary entry pressure, the barrier is ignorable and gas can migrate from the lower to the upper unit. On the other hand, a much smaller capillary pressure than the capillary entry pressure does not support continuous gas clusters in the sediments, and thus disconnects the gas communication.

The quantification of this effect is nontrivial, which requires more information of the sediments, and the corresponding modification of the network models. For our purpose, we do not concern ourselves with such attempt; instead, two limiting cases are studied: 1) when there is no capillary barrier effect, and 2), the effect dominates the fluid migration. The latter case means gas column is separated into two units, and no communication is available between them.

We have proposed two different scenarios than would give different hydrate saturations in the porous medium, as shown in Chapter 4. In the current analysis, we assume that water invasion during the hydrate formation occupies 7% of the void space, a value that is obtained from the fraction of Melrose jump in Chapter 4. The initial gas saturation is 85% along the reservoir depth. This value is the average nonwetting phase saturation from the infinite acting network modeling of drainage (Chapter 2). Also the residual gas saturation is set to be 32% from the infinite acting network modeling of imbibition. The porosity at each depth of the reservoir is obtained from the lab measurements.

Unless otherwise specified, we set the water density to be 1000 kg/m^3. Methane hydrate has type I structure and has an average hydration number of 5.75 (Sloan, 2003).

This gives the methane hydrate density to be 910 kg/m^3 (Sloan and Koh, 2008). The methane density is computed by using the model presented by Soave, Redlich and Kwong (Sandler, 2006). With the above settings, the hydrate distribution in the field scale can be computed as follows.

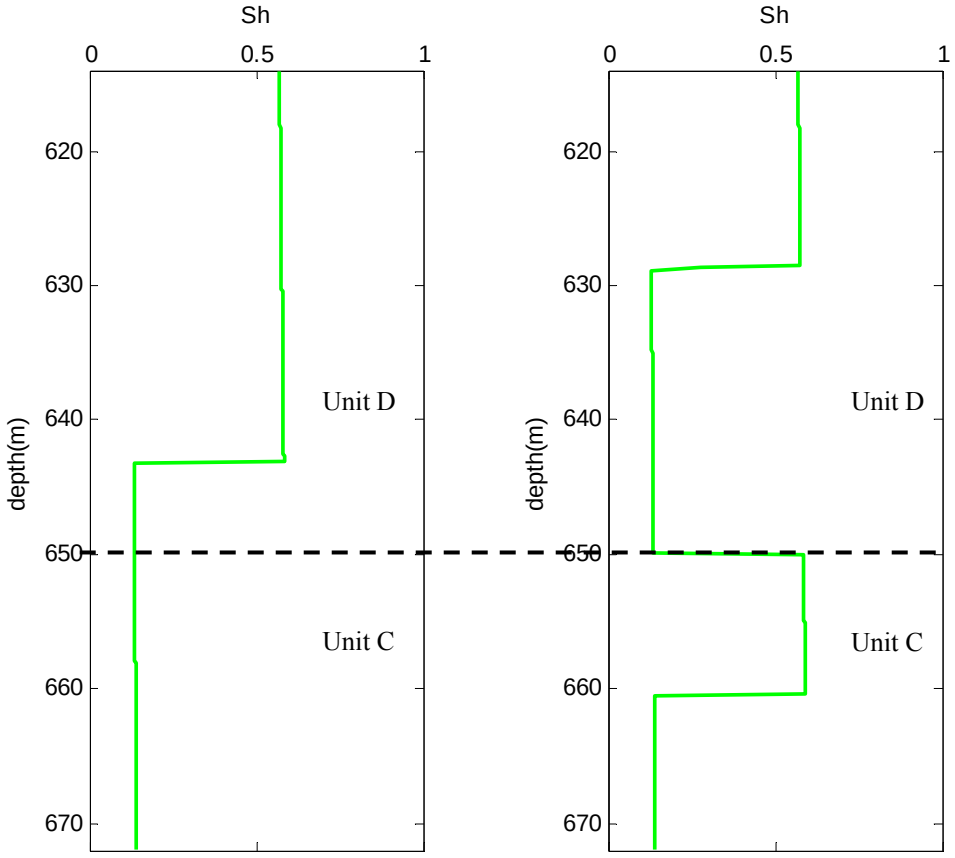

A. Unit C and D fully communicated

B. Unit C and D separated by the capillary barrier

Figure 5.19: Hydrate distribution in the field. The left panel (A) is the hydrate distribution without capillary barrier effect. Gas can freely transport inside the gas column, and fills the vacancy on top of the reservoir. The right panel (B) is the case when the capillary barrier completely separates the original column into Unit C and D (the barrier is indicated by the dashed line). Each unit draws the free gas from the bottom of itself to fill the vacancy, and therefore individually results in a similar pattern as (A).

Figure 5.19A shows the hydrate saturation without the capillary barrier. In this case, Unit C and D maintain good communication, so that the free gas from Unit C is able to migrate upwards to the vacancy in Unit D. Such process drains all the free gas in Unit C, and leaves only the residual gas. In Unit C, the hydrate saturation from the residual gas is less than 20%, while in Unit D, owing to the free gas from the entire gas column, a large column of sediment (from 614 to 640 m) is mostly filled with hydrate (S_h ≈ 58%). Only about 10 m beneath the hydrate-saturated region is filled by invaded water and hydrate converted from the residual gas.

The hydrate distribution with the capillary barrier has a different behavior (Figure 5.19B). Only the free gas from the bottom of individual units can be used to fill the vacancy created due to hydrate formation. The less availability of free gas, compared to the case of no capillary barrier (Figure 5.19A), yields shorter hydrate-saturated sediments (14 m) in Unit D.

A sharp transition of the hydrate saturation between the two units is observed at the unit boundary (650 m, also the location of capillary barrier). The hydrate saturation changes from 15% to 58% abruptly. Above this boundary, only the residual gas (32%) is used to generate hydrate, and thus yields a relatively small saturation. On the other hand, below this boundary there is a gas-saturated unit (Unit C). Due to the capillary barrier, gas is contained inside this unit. When BGHSZ reaches this depth, gas in this layer is converted to hydrate. Moreover, free gas from the bottom of Unit C also migrates to fill the vacancy and generates more hydrate. Such processes yield much higher hydrate saturation than the bottom of Unit D. In the lower region of Unit C, the hydrate saturation drops to small values due to the depletion of free gas in that region, which is similar to the case in Unit D.

Unit C and D have the similar pattern of hydrate distribution. Individually, this pattern is also similar to the case without capillary barrier (Figure 5.19A). This characteristic non-uniform distribution (high-low saturation regions repeat cyclically) indicates gas migration within the sediment as BGHSZ moves downwards. Furthermore, gas migration also results in water invasion from the bottom of gas column. Hydrate formation significantly consumes and redistributes gas and water in the system.

5.3.2 The comparison with the field data

Several approaches are employed to obtain a reasonable field estimate of the hydrate saturation in the reservoir condition. These approaches include the interpretations from density, resistivity, and acoustic logs (Lee and Collett, 2011), and also from core-derived chloride concentrations (Torres et al., 2011). These data are cross-verified, and thus are considered to reflect the real hydrate distribution in Unit C and D.

We assume the hydrate-gas interface movement during the hydrate formation resembles the gas-water interface movement at imbibition. As discussed in Chapter 4, if the water supply rate is much lower than the hydrate formation rate (Scenario A), only the incremental movement of the interface can take place. This event not only allows the hydrate formation to completely take up the volume of imbibition event, but also preclude the gas trapping at the imbibition endpoint, and therefore free gas can always invade to form more hydrate. This scenario yields the maximum hydrate saturation. When the water supply rate is much greater than hydrate formation rate (Scenario B), both Melrose jump and incremental movement occur. The abrupt occurrence of Melrose jump does not allow hydrate formation to take place. Instead, water is imbibed to fill the vacancy, without being converted into hydrate. Because of this event, gas trapping is

significant at imbibition endpoint. The trapped gas is disconnected from the bulk, and can only be converted into a limited amount of hydrate. Scenario B proposes that a large portion of the void space will be filled by imbibed water, and thus yields the minimum hydrate saturation. These two scenarios give the upper and lower bounds of the hydrate saturation that could form in the porous medium, provided sufficient gas and water. The comparison between the model predictions and field data would allow us to justify our model, as well as to study the underlying physics that controls the hydrate distribution.

We also account for the cases of capillary barrier. Two limiting cases are analyzed: 1) Unit C and D fully communicate (Figure 5.19A) and 2) two units have no communication at all (Figure 5.19B). The former case (referred to as case 1) ignores the effect of capillary barrier, and allows the gas migration freely from Unit C to D. For the latter case (referred to as case 2), however, the communication is hindered when the capillary pressure drops below the capillary entry pressure of the sediments. The remaining communication might be too small to give noticeable gas supply from Unit C. Therefore, two units behave similarly as the single, isolated gas columns. The comparison with the field data also tests these two cases.

In the model simulation, S_{wirr} and S_{nwr} are set to be 15% and 32%, respectively. Also for Scenario B, S_{jump} is 7%, from Chapter 4. These are average values from the drainage and imbibition simulations based on the periodic boundary condition. The porosity of the sediment varies with the lithologies. A sandy sediment has higher porosity compared to a shaly sediment. Porosities at different depths are obtained from (Winters et al., 2011). The densities of methane, water, and methane hydrate still use the same value as in the case of Figure 5.19.

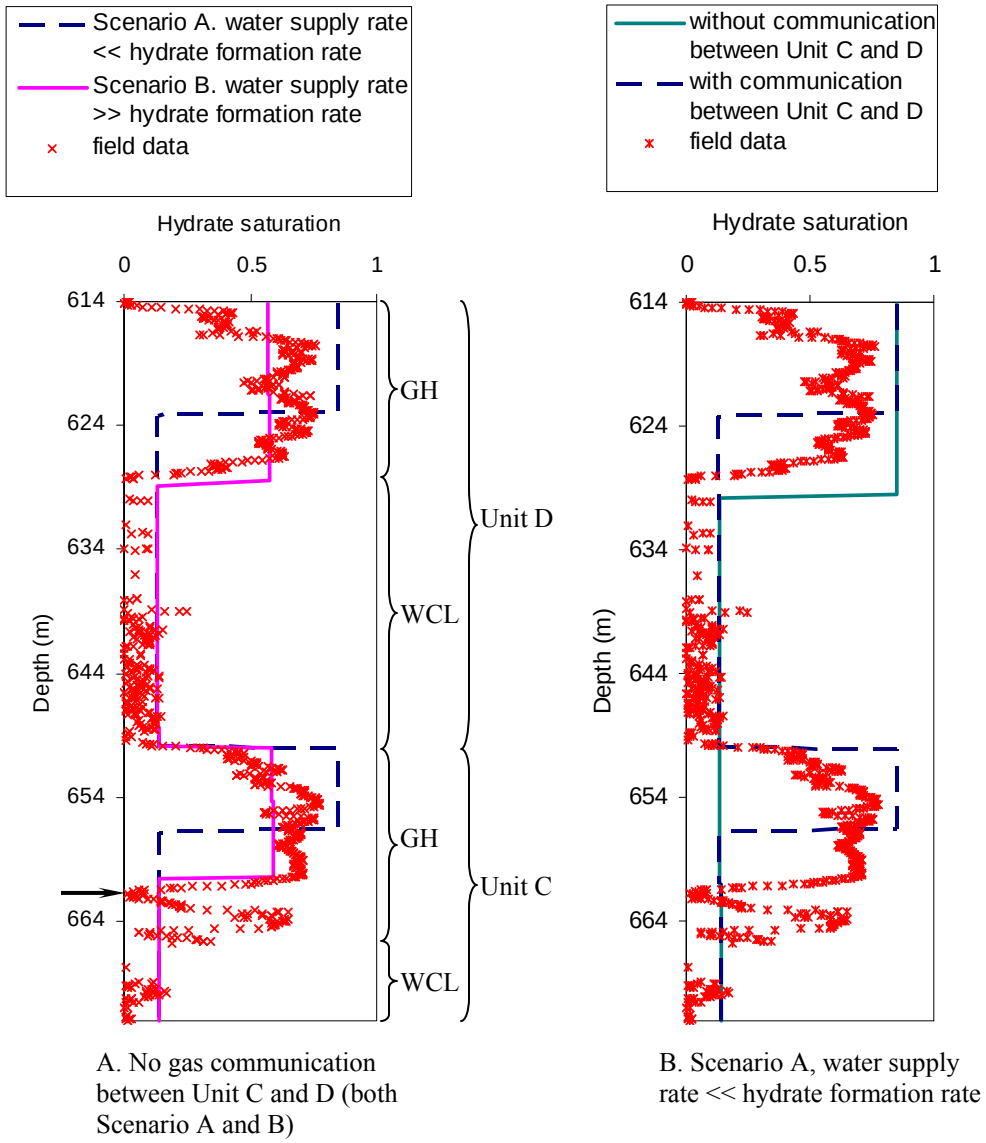

Figure 5.20: A comparison of the hydrate distribution in the reservoir between the model prediction and field data. The left panel assumes no communication between Unit C and D, and shows the hydrate distribution based on the two scenarios concerning the different water supply rate. The right panel assumes water supply rate is much smaller than hydrate formation rate, and shows the effect of communication of Unit C and D. Unit C and D are subdivided into GH (gas hydrate) and WCL (water contact layer) regions. This definition applies to both field and model predictions, although in the figure it is shown based on the field data.

Figure 5.20 shows the hydrate distributions of different scenarios, compared with field data. On the left panel, cases of different water supply rates are studied, with the assumption of no communication of gas between Unit C and D. When the water supply rate is much greater than the hydrate formation rate (scenario A, dashed blue line), only the incremental movement of gas-water interface exists during the hydrate formation process. Hydrate occupies the void space that is originally filled up by only gas. Water invasion in this scenario only provides necessary reactant to form hydrate, rather than filling the void space. Moreover, no gas trapping happens due to the slow incremental movement. Event at the imbibition endpoint, the gas that should be trapped in a conventional imbibition still connects to the bulk. Hydrate therefore can fill up the volume of all the original gas, and the hydrate saturation in the GH region becomes the same as the initial gas saturation in the sediment, which is 85%. This overestimates the saturation value from the field observation.

Hydrate formation in GH region of each unit drains the free gas from WCL region, and leaves behind only the residual gas in WCL region. When BGHSZ reaches WCL region, the residual gas (in the form of isolated gas blobs) is converted into hydrate. With the temperature and pressure in the Mount Elbert reservoir, 32% S_{nwr} yields about 10% S_h, the remaining 20% void space will be filled by water. Because the gas phase in Units C and D is assumed to not communicate, the same pattern of hydrate distribution is observed in both units, with higher saturation region (GH) on top and the lower saturation region (WCL) at the bottom.

When the water supply rate is greater than the hydrate formation rate (scenario B), another imbibition event (Melrose jump) occurs. This event happens very quickly that the imbibed water does not have enough time to be converted into hydrate. Compared to the incremental movement that allows hydrate formation, Melrose jump merely imbibes

water to fill the vacant space. In this scenario, the void space created owing to the hydrate formation will be filled by both hydrate (because of incremental movement) and water (because of Melrose jump), which gives relatively low hydrate saturation than Scenario A. Furthermore, gas trapping occurs at the imbibition endpoint. Melrose jump disconnects the gas bubbles from the bulk. One unit volume of bubbles results in only about 1/3 of the unit volume occupied by hydrate. Such behavior further increases the hydrate saturation difference to Scenario A, and gives the lower bound of hydrate saturation in the porous medium.

The maximum hydrate saturation predicted from Scenario B is about 58%, a much smaller value than Scenario A. With the same amount of initial gas in place, the lengths of the GH region for both scenarios are different. The length in Scenario B is much smaller than Scenario A, which is a reflection of the different maximum hydrate saturations.

The field data (red crosses) have the similar pattern, where GH region sits on top of WCL region. The highest hydrate saturation is around 80%, lower than 85% (scenario A) but much higher than 58% (scenario B). However, sediments with this saturation do not prevail in the entire GH region. In Unit D-GH the average hydrate saturation is about 57% and becomes 60% in Unit C-GH. These are the similar values to the model prediction by Scenario B. By using Scenario B, we also predict a very similar GH length to the field observation. The length of the GH region from the prediction shows 14 m of Unit D-GH and 10 m of Unit C-GH. The corresponding values from the field data are 14 m of Unit D-GH and 16 m of Unit D-GH. We obtain a satisfactory agreement in Unit D-GH for both average hydrate saturation and unit length; however, we significantly underestimate the length of Unit C-GH.

The comparison between Scenario A and the field data does not yield good agreements. The estimated hydrate saturation is much higher than, and also the estimated unit length is much smaller than, the field data. Such comparison suggests that the hydrate formation does not simply fills up gas-filled pores. It involves much more complex processes that contain water invasion as well (Melrose jump, Scenario B). Both of the incremental movement (hydrate filling) and Melrose jump (water filling) gives the final hydrate saturation. The good comparison between Scenario B and the field data confirms this conclusion.

We also notice that at Unit C-GH, there is a discontinuity at about 661 m (indicated by the black arrow in Figure 5.20A). A layer of sediment (4m) with high hydrate saturation lies below this depth. Our model fails to predict the hydrate distribution at this layer. The model estimation from Scenario B only predicts that Unit C-GH extends to 660 m, a depth that agrees well with the discontinuity. Below that depth, due to the assumed extent of the original accumulation of gas, the hydrate saturation drops to a very low value.

It is a common argument that hydrate saturation is a strong function of lithology: good lithology (clean sands with large grains) is the ideal environment for hydrate preservation (Rose et al., 2011; Winters et al., 2011), and therefore should be filled by large hydrate saturation. In Mount Elbert case, between 662 m to 672 m (the deepest depth where hydrate is observed) we observe a good lithology (Figure 5.4). However, sediments with large hydrate saturation only extend to 665 m. Between 665 m and 672 m, only a small amount of hydrate is observed (Figure 5.20). Based on our model prediction, we argue that such behavior is due to the size of the initial accumulation gas in the reservoir. Although lithology does play an important role in hydrate formation (for example, hydrate saturation is not uniform in the GH region, which reflects the lithology

effects), the availability of gas in the reservoir also determines the hydrate profile in the field.

Table 5-1: Comparison of the amount of hydrate between field data and prediction, Mount Elbert hydrate reservoir

Unit	Field data ($\times 10^3$ kg/m^2)	Prediction ($\times 10^3$ kg/m^2) Scenario A	Prediction ($\times 10^3$ kg/m^2) Scenario B
Unit C-GH	2.7	1.6	1.8
Unit D-GH	2.3	2.2	2.5

We tabulate the amount of hydrate (mass per unit pore volume times sediment thickness) in Table 5-1. We do not attempt to compare the amount of hydrate in WCL regions, since the saturation, which is estimated from the well log data, are not reliable when the value is below 10%. Our model prediction of the amount of hydrate increases from Scenario A to Scenario B. For Unit D-GH, a reasonable agreement is observed between the model prediction and field data. However, for Unit C-GH, both predictions underestimate the amount of hydrate by over 1/3. Since our hydrate prediction is from the isolated gas column that was originally formed in Unit C, the result indicates that the amount of gas in Unit C was insufficient from the very beginning. As there is no presence of hydrate below Unit C-WCL, the possibility might be that Unit C connects through fractures with the gas reservoir below. During hydrate formation, free gas migrates through these fractures and generates more hydrate in Unit C. As the gas in the fractures does not invade the sediments below Unit C-WCL, no hydrate is observed even though temperature and pressure are ideal for hydrate formation.

Whether or not Unit C and D maintain communication also strongly affects the hydrate distribution. We use only scenario A (water supply rate much smaller than hydrate formation rate) for the analysis (Figure 5.20B). With communication (solid green curve), only one region with high hydrate saturation exists in the reservoir, which extends

from 614 m to 630 m. Below this region, the hydrate saturation keeps at a small value (13%~14%) till the base of the reservoir. The prediction totally fails to account for the observation in Unit C-GH in the field data, which has 80% hydrate saturation. With the communication between Unit C and D, no capillary barrier can be established, and therefore no hydrate saturation can accumulate in Unit C-GH. Instead, no communication between Unit C and D is a reasonable assumption, and the prediction has a better agreement with the field data. This argument is also confirmed from Table 5-1, where the initial gas in Unit D is already sufficient to produce comsparable hydrate with the field data.

Figure 5.20 shows that the real hydrate saturation in the reservoir never maintains a constant value over a certain depth. Such behavior reflects the lithology variation in the reservoir (e.g. different clay contents), which is not considered in the network model: the clay-bound water is not displaceable, which decreases the initial gas saturation. Moreover, the presence of clay also might clog pores and throats, so that the capillarity-trapped water cannot be displaced as well. Therefore, even with the same total porosity, the initial gas saturation, and also the final hydrate saturation, varies with different clay contents. The zigzag profile of hydrate distribution from the field data is a reflection of this effect. Nevertheless, on average we obtain a similar profile between the field data and the prediction. This suggests that our models capture the physics underlying hydrate formation and distribution in the reservoir scale for this type of hydrate reservoir.

5.4 CASE STUDY – MALLIK GAS HYDRATE FIELD

The Mallik gas hydrate field is located on the coast of Beaufort Sea, northwest Canada (Figure 5.21). Most of the hydrate is found 300 to 700 m below the permafrost. Meanwhile, no active hydrate formation and gas migration processes are identified. In 2002, the Mallik Gas Hydrate Production Research Well program was initiated. From three test wells, massive data were collected. 63 research papers cover a great range of areas, including petrophysical, biochemical, geophysical and production studies (Dallimore and Collett, 2005). Among all the test wells, well 5L-38 is extensively studied. The hydrate saturation and distribution along the depth were estimated and crossed-verified from the interpretations of resistivity log (Collett and Lee, 2005), sonic log (Lee and Collett, 2005) and NMR (Kleinberg et al., 2005), and lab-based core analysis (Lu et al., 2005).

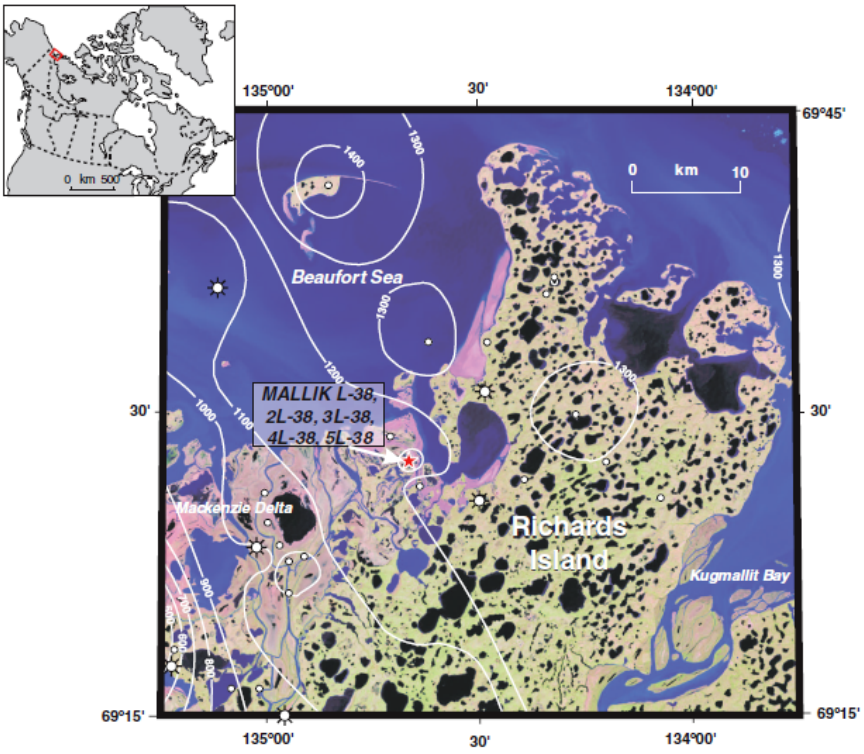

Figure 5.21: The location of Mallik gas hydrate reservoir. 2L-38, 3L-38, 4L-38 and 5L-38 indicates the wells drilled for the study. L-38 was drilled decades ago for the gas production. Contour lines show the depth of BGHSZ.

The hydrate distribution along the 5L-38 well has a nonuniform pattern as well, where the units with high hydrate saturation are separated by the units with low hydrate saturation (Figure 5.23 and Figure 5.24). The hydrate occurrence starts at 890 m and ends at 1110 m, though it is not present continuously. It occurs almost 300 m lower than Mount Elbert, therefore when gas was still present before the descending of BGHSZ, gas density in Mallik reservoir was higher than that of Mount Elbert reservoir, owing to the higher pore pressure. Therefore, a unit volume of gas would be converted to more hydrate than at Mount Elbert reservoir. BGHSZ is located at 1100 m. Below this depth, no hydrate is present. In this reservoir a total of 120 m of hydrate column is identified, much longer than Mount Elbert.

We subdivide the hydrate reservoir into different units. Our model still assumes the original gas column before hydrate formation. Figure 5.22 shows the in-situ chloride concentration along the depth of 5L-38. Three regions of distinct chloride concentrations can be identified, and the individual average chloride concentration is listed in Table 5-2. Between two neighboring units, the hydraulic communication is very limited, if any; otherwise, the chloride concentration would behave a more continuous fashion. Between Unit A and B, the lithology analysis shows that the sediments are clay and clayey silt, embedded by two thick coal beds (Matsumoto et al., 2005). Thick mudrock, along with a 0.4 m of coal bed, is the major lithology that differentiates Unit B and C (Uchida et al., 2005).

Table 5-2: The length of three stratigraphic units at Mallik and the corresponding average chloride concentration

Unit	Approximate range (meter)	Approximate Length (meter)	Chloride concentration (millimolar)
A	900 – 940	40	320
B	940 – 1010	70	450
C	1010 – 1100	90	500

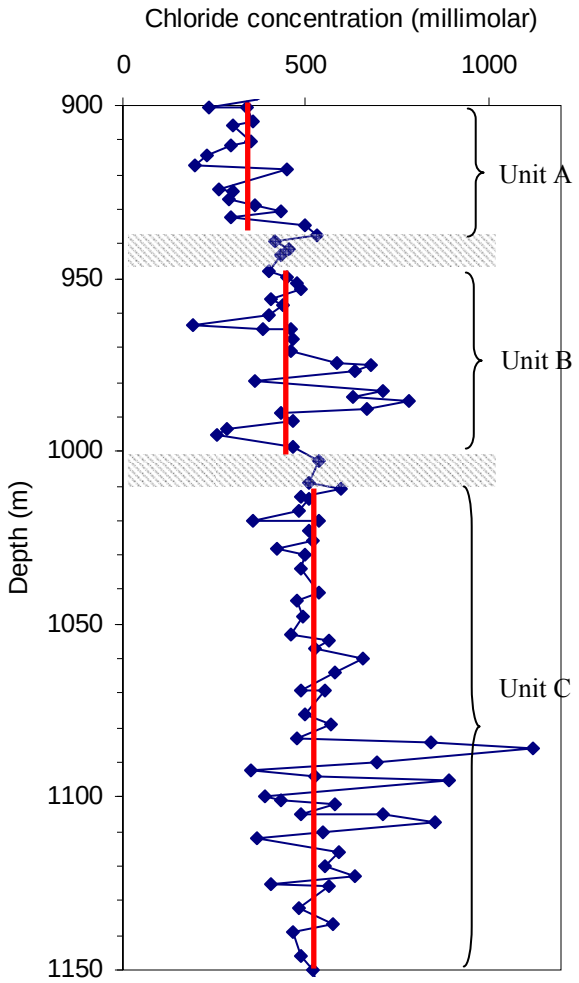

Figure 5.22: The chloride concentration profile along the depth of 5L-38. The results are calculated from the residual water, in-situ condition. Red lines give the average chloride concentration of each unit. Modified from (Matsumoto et al., 2005). The jumps between units suggest hydraulic isolation.

Another piece of evidence comes from the petrophysical data (Figure 5.23). At 941 m, near the base of Unit A, the median pore size and the gas permeability are all at their local minimum values. The main-mode pore size is about 0.5 μm (main-mode represents the dominant mode from the pore size distribution). Since mercury porosimetry was used for the pore size determination, 'pore size' in Figure 5.23 in fact

indicates throat size defined in this work. Therefore for 0.5 μm throat size, by assuming the interfacial tension between gas and water to be 0.075 N/m we calculate the capillary entry pressure of this sediment to be 0.6 MPa (it should be noted that this is a much higher value than the calculation based on the median grain size in Figure 5.24. The measurement in Figure 5.23 is more accurate, while Figure 5.24 gives a rough comparison of the capillary entry pressure of different units). Recalling that the capillary pressure gradient between gas and water at Mallik temperature and pressure is 0.009 MPa/m, it follows that 67 m of initial gas column must be established to overcome this capillary barrier. This length equals to the length of Unit B, which means that a full column of gas in Unit B will establish enough capillary pressure to barely exceed the capillary barrier at the base of Unit A.

At 1006 m, near the base of Unit B, the gas permeability is at the smallest value of the entire depth, and also the main-mode pore size is at its local minimum. The 'pore size' obtained from Figure 5.23 is about 0.2~0.3 μm. Based on the same analysis as above, we calculate that the capillary entry pressure at this depth (1006 m) ranges from 1 to 1.5 MPa, which corresponds to 111~167 m of gas column. This is close to the length of Unit C (95 m), considering our estimate of the 'pore size' from Figure 5.23 is only approximate. We thus presume that once continuous gas column is established in Unit C, the capillary pressure at the base of Unit B would be just sufficient to overcome the capillary entry pressure at 1006 m.

The capillary barrier between Unit B and C separates the good lithology (Unit B) from the bad (sand-poor) lithology (Unit C). Below the barrier, except for an abnormal point (~1020 m), the petrophysical properties at other depths (from 1006 to 1072 m) all indicate very tight sediments, with gas permeability about 0.5 mD. Along with the lithology description from (Uchida et al., 2005), we infer that water, either capillary-

bound or clay-bound, dominates this region. The gas saturation during charge only just exceeded the critical saturation in Unit C (this value is the minimum gas saturation that can maintain a continuous gas cluster to allow gas flow through the porous medium) to enable the gas migration pathway. Therefore, the upper part of Unit C allowed gas to migrate to the units above but was not drained to large gas saturation. This relatively small initial gas saturation explains the low hydrate saturation observed in this part of Unit C.

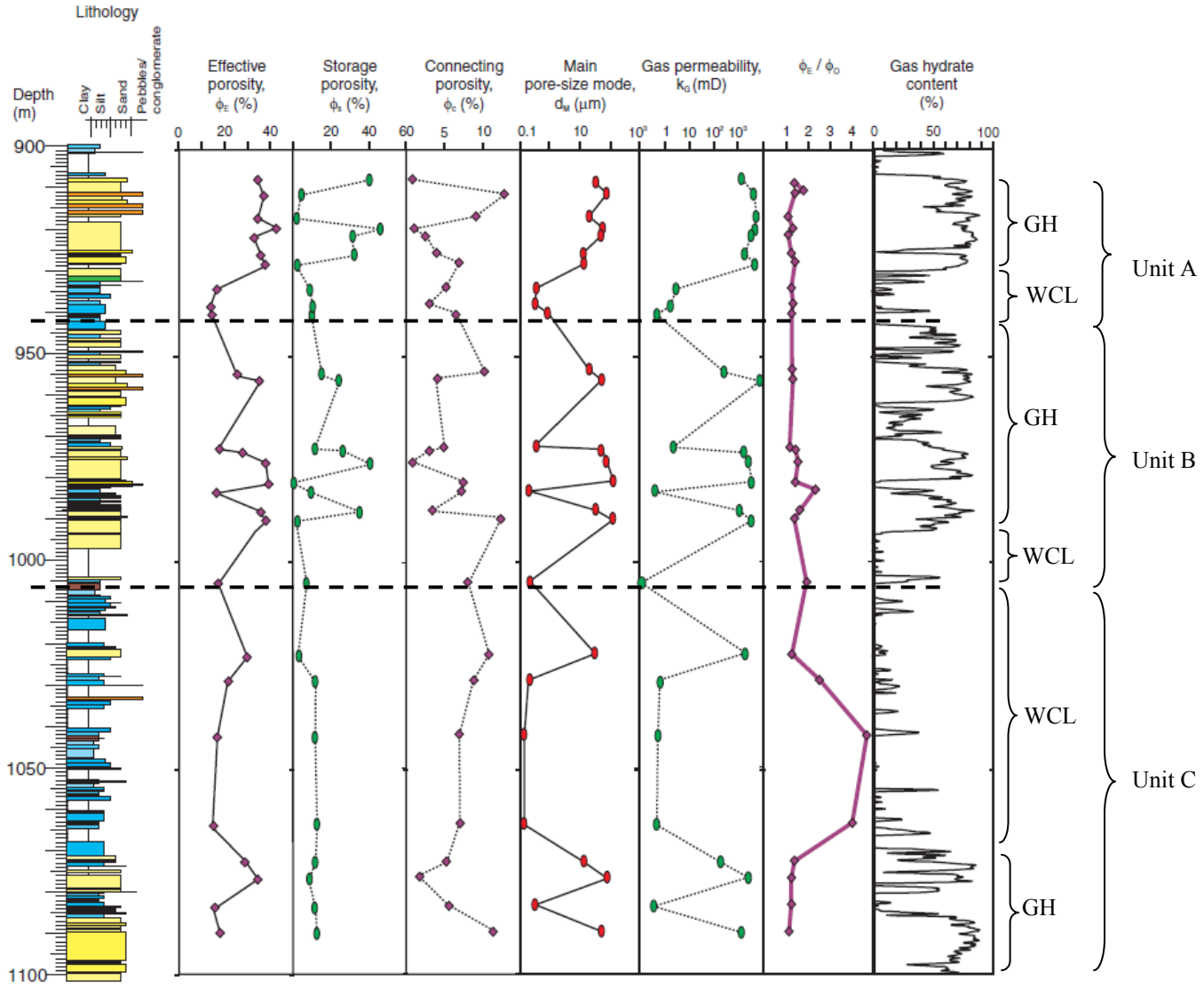

Figure 5.23: The petrophysical properties from the sediments of Mallik hydrate reservoir. The properties are based on the lab measurements on samples of recovered core. Similar to Mout Elbert reservoir, Mallik is divided into different units (Unit A, B and C), and different regions (GH and WCL regions) within each unit are also identified.

Neither the chloride concentration (Figure 5.22) nor the petrophysical properties (Figure 5.23) give enough resolution to give a clear separation of different units. To obtain unambiguous unit boundaries, the capillary entry pressure based on the average

grain size is calculated by using the method proposed in Equation (5.4) and (5.5), and shown in Figure 5.24. Figure 5.24 is only used for the identification of different regions of Mallik gas hydrate reservoir, not for quantitative values of entry pressures. In Mallik reservoir, due to the high content of shale, calculating the capillary entry pressure, especially at the shaly regions, is subject to large error. However, it still provides the relative comparison with the entry pressure in sandy sediments.

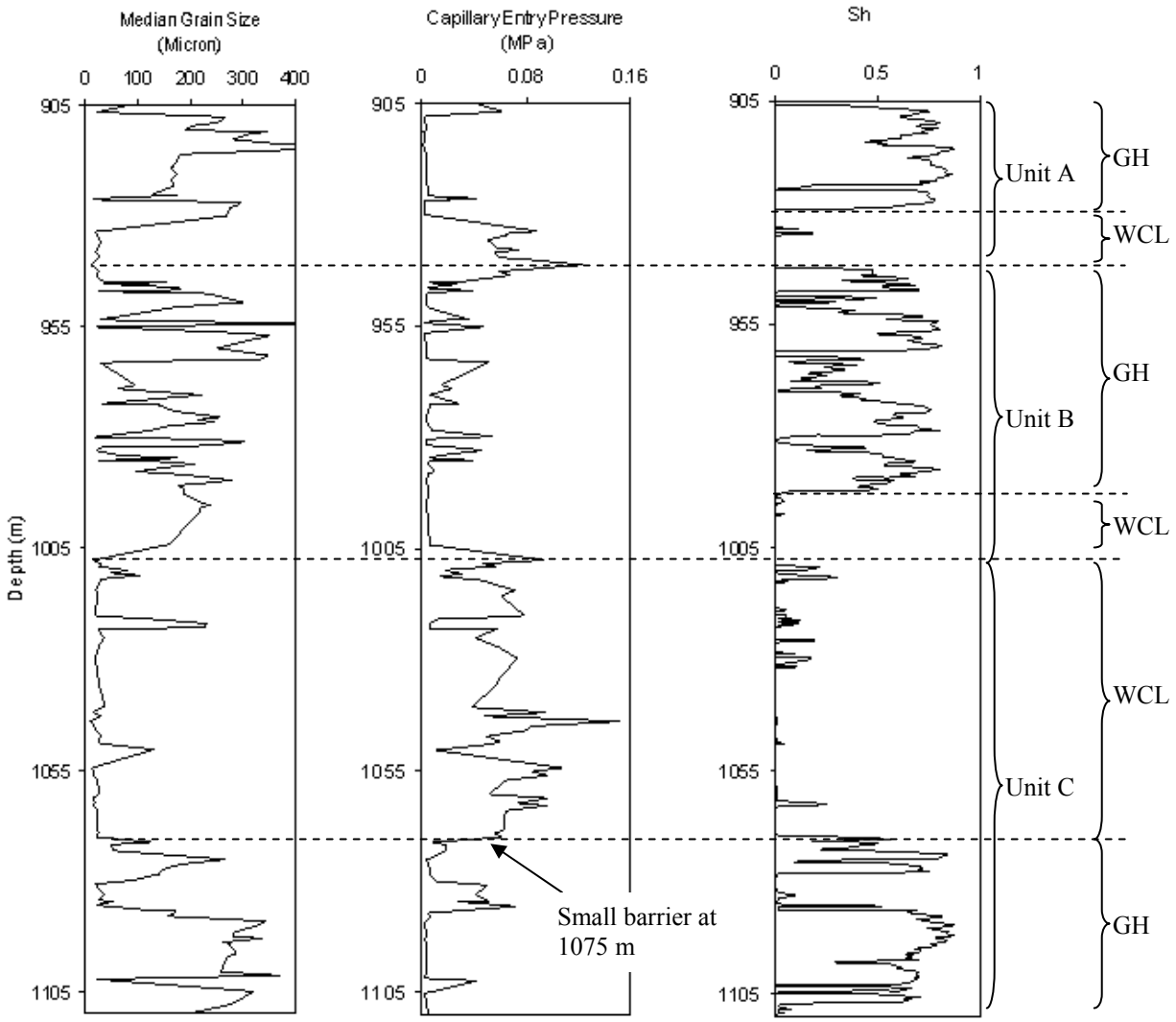

Figure 5.24: The identification of different reservoir units from the capillary entry pressure, by using equation (5.4) and (5.5), Mallik gas hydrate reservoir. This figure should only be used for the identification of different regions in Mallik gas hydrate reservoir, not for quantitative values of entry pressures.

We then subdivide the different units as shown in Figure 5.24. In this work we do not attempt to predict the hydrate distribution in Unit C because of the following reasons. First, the location of GWTP is not known from the available data. Consequently, the

length of the initial gas column in Unit C cannot be estimated, and without this information the model cannot predict the total amount of hydrate. Second, BGHSZ locates at 1100 m, a depth where hydrate saturation is still at very high level. This is a major difference with Mount Elbert, where BGHSZ is much deeper than the deepest observed hydrate. It is not clear whether more hydrate would form at Mallik if BGHSZ were to continue to move downwards, and how much free gas is left below this depth. Such uncertainties prevent us from giving a reasonable prediction of the hydrate distribution. However, based on the model we have developed, the hydrate-poor region (Unit C-WCL) is analyzed in this work.

To summarize the hypothesized initial distribution of gas saturation at Mallik, we assume the thermogenic gas from deeper sources migrated upwards through faults or fractures. The migrating gas first encountered capillary barriers at 1075 m (Figure 5.24 and Figure 5.25A), thereby filling Unit C-GH (Figure 5.25A, B). The drainage curve for the Unit C-GH sediments, Figure 5.26, permitted build up of large gas saturation there. When the capillary pressure built up and exceeded the entry pressure of WCL region, free gas began to migrate upwards into WCL, Figure 5.25B (Recall that in Figure 5.24, the capillary entry pressure of Unit C-WCL region and its distribution along the depth are not to scale. The estimate in Figure 5.24 is based on the simple calculation of Equation (5.4) and (5.5), and only reflects the relative entry pressure comparison between the good and bad lithologies). The drainage curves of Unit C-WCL have different characteristics than Unit C-GH and Unit B (good lithologies). Because of the wider grain size distribution and higher content of clay in Unit C-WCL, these sediments have higher entry pressure and much higher irreducible water saturation (Figure 5.26). Therefore, the gas column was incapable of fully draining Unit C-WCL, but was capable of maintaining the minimum saturation that would allow the gas transport. When Unit C was filled by gas

(95 m of gas column, with large saturation in Unit C-GH and small but connected saturation in Unit C-WCL), the gas phase capillary pressure at the base of Unit B was just enough to exceed the capillary entry pressure of that sediment, and thus free gas entered Unit B (Figure 5.25B).

This behavior is also demonstrated by comparing the schematic drainage curves for the lithologies of Unit B and C in Figure 5.26. The drainage curves for Unit B and Unit C-GH have a low entry pressure, and also a sharp percolation. These features arise because the sediments in these regions have larger grain size and relatively narrower grain size distribution than those in WCL region, whose drainage curves in Figure 5.26 have higher entry pressure and do not exhibit sharp percolation. Unit C-WCL also has larger irreducible water saturation at drainage endpoint. The capillary pressure at the base of Unit B (P_c^*, corresponding to 95 m of gas column in Unit C) was just sufficient to break the capillary barrier at that depth. Once free gas entered Unit B, it displaced water to the irreducible value in accordance with the drainage curve in these coarser-grained sediments (Figure 5.26).

The gas column continued to build up, until close to the base of Unit B. Because the capillary pressure at the base of Unit B was only just enough to allow gas enter Unit B, the capillary pressure at the top of Unit B corresponds only to the thickness of the gas accumulation in Unit B. As discussed above, in this situation the capillary pressure at the top of Unit B was just enough to exceed the capillary entry pressure at the base of Unit A. Figure 5.26 shows that P_c^{**} is the capillary pressure at the top of Unit B when the entire Unit B is filled by gas. When P_c^{**} overcomes the capillary entry pressure of the barrier, gas could easily fill Unit A because of its low percolation threshold. It then allowed gas to charge Unit A (Figure 5.25C). No grain size measurements are available above Unit A, so we presume the capillary barrier at the top of Unit A is enough to hold the gas column

in Unit A, which is about 35 m. At each layer except for Unit C-WCL, the initial gas saturation is set to be the constant (1-S_{wirr}), because the capillary pressure between water and gas required to enter the base of each unit is more than enough to drain water to the irreducible saturation in the sands below each capillary barrier (Figure 5.26).

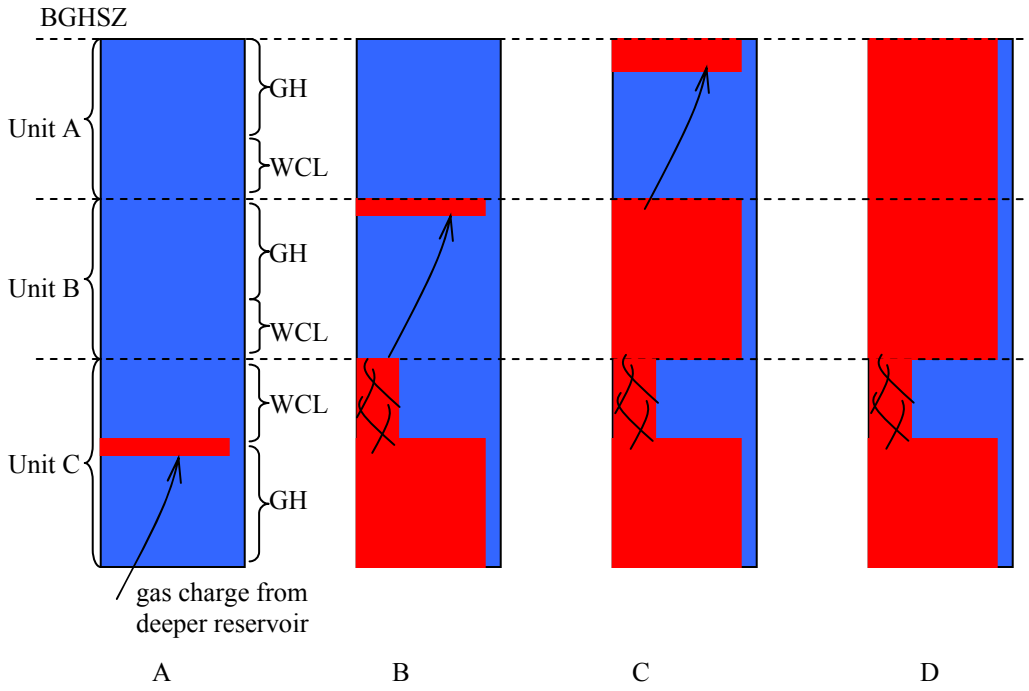

Figure 5.25: Initial gas charge in Mallik hydrate reservoir. (A) Gas invaded Unit C-GH from deeper gas reservoir. (B) Gas filled Unit C-GH from top to bottom. When the capillary pressure exceeded the capillary entry pressure of Unit C-WCL, gas migrated upwards through the pathways. However, the capillary pressure was not enough to allow gas to displace water to small saturations in Unit C-WCL. At Unit B, gas was contained under the capillary barrier between Unit A and B (dashed line). (C) When Unit B was filled up by gas, the capillary pressure barely exceeded the entry pressure of the barrier at the base of Unit A. Therefore, gas started to charge Unit A. The gas column accumulated at the top of Unit A and expanded downwards. (D) When gas charge was complete, Unit A, B and Unit C-GH were fully saturated with gas. Unit C-WCL had small gas saturation (the minimum value to maintain the gas transport).

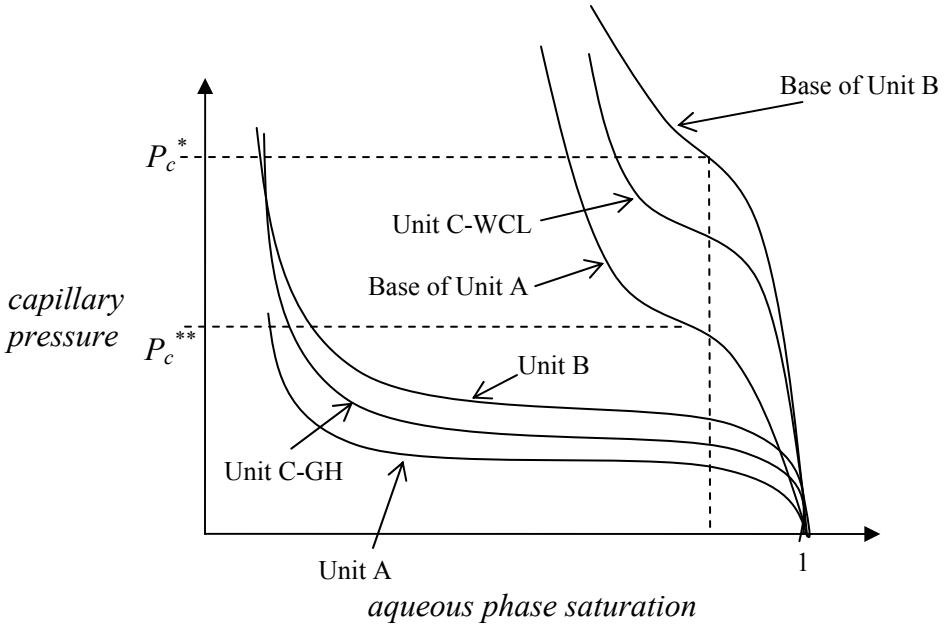

Figure 5.26: Capillary entry pressure at different regions of Unit A, B and C. P_c^* corresponds to the capillary pressure at the base of Unit B when 95 m gas column occupies Unit C. At this capillary pressure, S_w is still large in Unit C-WCL, while Units C-GH and B are drained to $S_{w,irr}$. P_c^{**} corresponds to the capillary pressure at the base of Unit A when 67 m gas column occupies Unit B. At this capillary pressure, Unit A will drain to $S_{w,irr}$.

A model is established to estimate the hydrate distribution from the initial gas columns. We focus on only Unit A and B, and Unit C is beyond our interest. Based on the analysis in Figure 5.25, we assume Units A and B are not connected and thus apply the model to them separately (Figure 5.27A). More precisely, it is assumed that the gas communication between A and B is barely available before hydrate formation, that is, the capillary pressure at the barrier between the two units only barely exceeds the capillary entry pressure of the barrier. When hydrate first forms at the top of Unit A-GH, the upward movement of gas will reduce the gas column height in Unit B. Thus the capillary pressure at the base of Unit A will immediately drops below the entry pressure, and

terminate the gas communication between Units A and B. The same phenomenon occurred within Unit C and D in Mount Elbert discussed in the previous section.

At this stage, BGHSZ is still above Unit A. We assume a Gas Water Transition Point (GWTP) lies at the bottom of each unit, which rises as the free gas from WCL region in each unit (Figure 5.27) moves upwards to fill the vacancy during hydrate formation

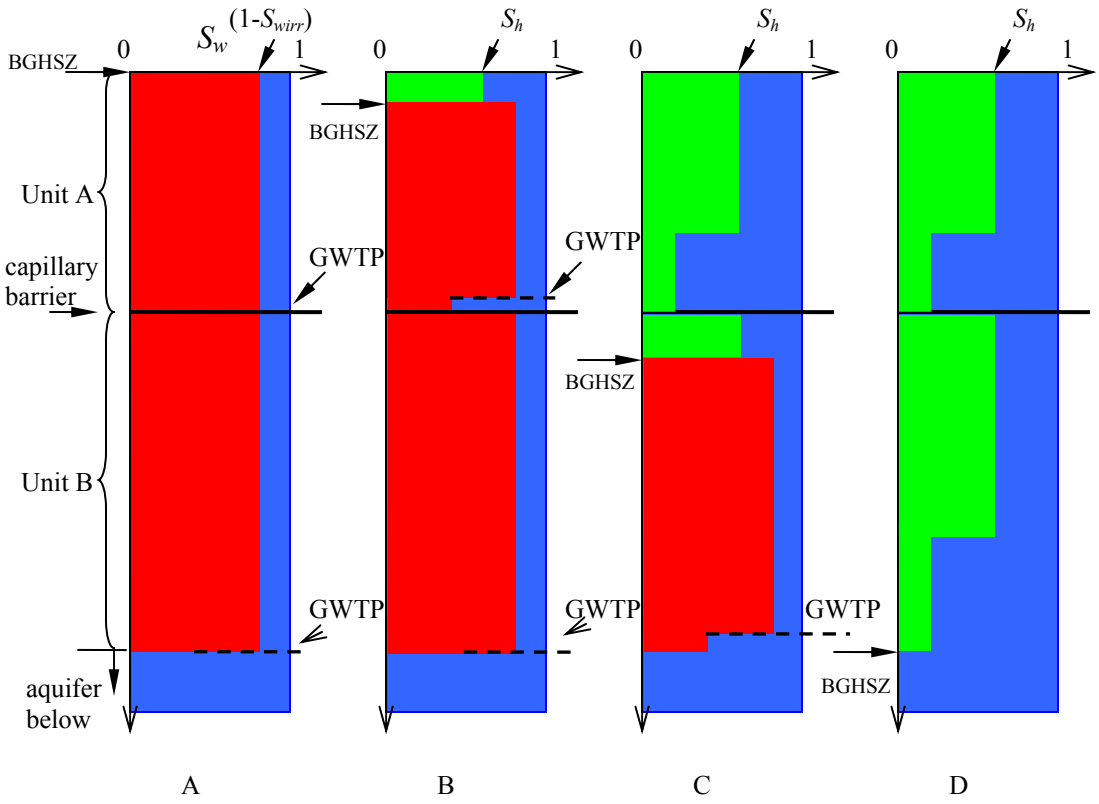

Figure 5.27: A schematic of hydrate formation in Units A and B. Figure A, B, C and D shows the distribution of hydrate, water and gas as BGHSZ moves downwards.

As BGHSZ descends, hydrate starts to form at BGHSZ. The scenario follows the discussion of Mount Elbert: hydrate formation generates vacant spaces, and the invading

gas and water to fill the vacant spaces also become the source for further hydrate generation. Two scenarios are considered, depending on the competition between water supply rate and hydrate formation rate, which yield upper and lower bounds of hydrate saturations. In the schematic of Figure 5.27B, we illustrate scenario B, that is, water supply rate is much greater than hydrate formation rate, so that water invasion by Melrose jump fills part of the void space. Free gas from the bottom of Unit A migrates to fill the void space, and allows for the water invasion happening below GWTP. During this process, the state of Unit B does not change. The capillary barrier at the base of Unit A prohibits the gas communication between the two units.

Gas in Unit A is converted into hydrate from the top down as BGHSZ moves downwards. Due to the gas redistribution within Unit A during the hydrate formation, the final hydrate distribution contains GH and WCL regions, similar to the case of Mount Elbert. The GH region has the maximum hydrate saturation, while WCL region only has the hydrate saturation that is converted from the residual gas. Figure 5.27C is an intermediate step after BGHSZ moves below the capillary barrier. The same hydrate formation process repeats in Unit B, and gives a final hydrate distribution as shown in Figure 5.27D.

The same procedure is used to predict the hydrate distribution for Scenario A. The comparison with the field data is shown in Figure 5.28. The hydrate density is set to be 910 kg/m^3 (Sloan, 2003), and the water density to be 1000 kg/m^3. The gas density is computed from the EOS by Soave, Redlich and Kwong (Sandler, 2006). The hydration number was measured by (Ripmeester et al., 2005), who give an average value of 6.1 over the depth. The porosity information is obtained at individual depth from (Winters et al., 2005).

On the left panel (Figure 5.28A) we consider Scenario A that water supply rate is much smaller than the hydrate formation rate. With this assumption, the model predicts hydrate saturation in the GH region to be 1-S_{wirr}, where S_{wirr} is the irreducible water saturation in the original gas saturated reservoir. In Unit A, the model prediction agrees with the maximum hydrate saturation observed in the field (85%). However, only several sublayers are observed to have such high saturation. Thus the model predicts less than 20 m thickness of Unit A-GH, while the field data show 25 m of this region. In Unit A-WCL, we predict roughly 20% hydrate saturation in Unit A-WCL. This value is obtained when residual gas saturation (S_{nwr} = 32%) is converted to hydrate. In the region, the field observation suggests zero hydrate saturation in almost the entire WCL region. As discussed in the Mount Elbert example, resistivity logs are not sensitive to small hydrate saturations, especially if the hydrate formed from residual gas. In this situation, the volume reduction during hydrate formation means that the hydrate is likely to exist as small blobs "floating" in pores. Therefore, we suggest that the model prediction is not necessarily inconsistent with the inferred saturation in the WCL regions of Units A and B.

The hydrate saturation from the field data has more variations in Unit B-GH. It varies between 30% to 85%, which is largely dependent on the facies. In general, maximum hydrate saturation occurs in the clean sands (for example, 950~960 m and 975~980 m, Figure 5.23), while silts with clay content have small hydrate saturation (for example, 962~965 m and 980~982 m, Figure 5.23) due to initial high water saturation associated with clay (Winters et al., 2005). The pore-scale model implemented here considers only clean lithology and thus predicts large, uniform hydrate saturation in Unit B-GH. The prediction exceeds the hydrate saturation from the field data and underestimates the thickness of GH region. By using Scenario A, we only predict 38 m of

Unit B-GH, while the field data give 53 m of this region. Below this region, the field data indicates zero hydrate saturation, where the model predicts 20% hydrate saturation.

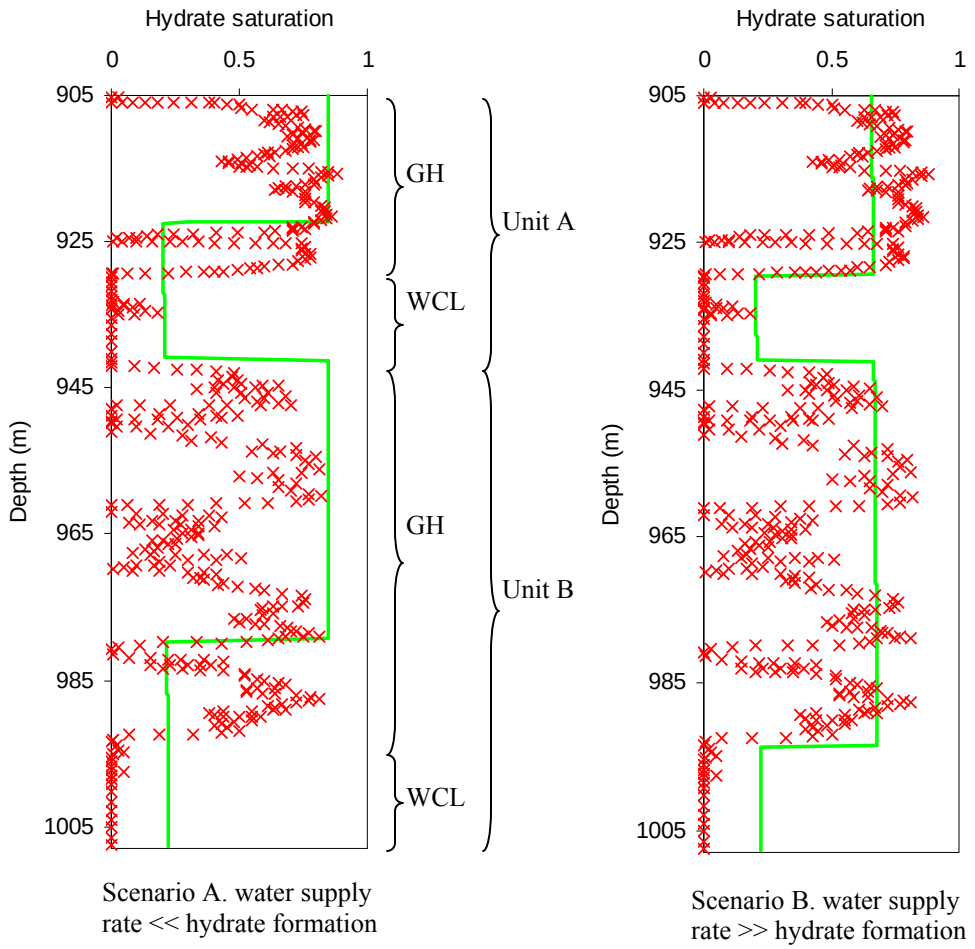

Figure 5.28: The comparison of model prediction (green curve) and field data (red crosses) of hydrate distribution in Mallik hydrate reservoir for the limiting cases of (left) very slow water supply (Scenario A) and (right) very fast water supply (Scenario B) during hydrate formation. GH and WCL regions designate the regions with high and low hydrate saturations, respectively, based on the field observation. The comparison suggests that the water supply rate was large compared to the rate of hydrate formation.

Consider now the hydrate saturation distribution predicted in scenario B. This scenario assumes water supply rate to be much greater than hydrate formation rate, and therefore allows for water invasion to occupy the vacant space generated by hydrate formation. As shown in Figure 5.28, the maximum hydrate saturation by this scenario is lower than scenario A, and provides a more satisfactory agreement with the field data. In Unit A-GH, the model prediction suggests 63%-65% hydrate saturation, which is the average saturation value from the field data. The model also yields 25 m of the GH region, same with the field observation. For Unit B-GH, our model fails to capture the zigzag feature of the hydrate distribution (because it neglects the variation in $S_{w,irr}$ with the lithology, as discussed above), and predicts an almost uniform saturation along the depth (S_h = 65% ~ 68%). The predicted thickness of Unit B-GH is almost the same as field data.

Our model predicts about 20% hydrate saturation in the WCL regions of both units. This value is much higher than the field data. However, as discussed previously, well log interpretation at low hydrate saturation might not be accurate, especially when that saturation is neither cementing nor pore-filling. The literature confirms such inaccuracy: below BGHSZ, log interpretation still suggests 1% - 4% hydrate saturation, which is nonphysical (Winters et al., 2005). Therefore, we argue that prediction and measurement in the WCL regions are not necessarily inconsistent, and quantitatively we compare the amount of hydrate only in the GH regions.

Table 5-3: Comparison of the amount of hydrate between field data and prediction, Mallik hydrate reservoir

Unit	Field data ($\times 10^3$ kg/m^2)	Prediction ($\times 10^3$ kg/m^2) Scenario A	Prediction ($\times 10^3$ kg/m^2) Scenario B
Unit A-GH	5.1	4.8	5.3
Unit B-GH	6.8	10.1	11.1

Table 5-3 shows a fairly good match in Unit A-GH between field data and model predictions (both scenarios); however, our model overestimates the amount of hydrate in Unit B-GH unit by 50%. The major discrepancy between two units raises the question of whether the correct assumptions are employed. Unit A-GH corresponds to clean lithologies with little presence of clay (Katsube et al., 2005). Therefore, our model prediction of the fluid saturation and distribution based on the model sediment agrees well with the reservoir condition, and thus yields satisfactory results. On the other hand, Unit B-GH has a large variation of the grain sizes along the depth (Figure 5.24). The small grain size region indicates the silt interbeds rich in clays (Katsube et al., 2005). Due to the complex clay structures in the porous medium, predicting the fluid saturation from this lithology by using the network modeling results from well-sorted to moderately sorted sediments might give a large error. For instance, the presence of clay might significantly reduce the throat size, or even block the throat. The effective porosity due to such effect will be largely reduced. The initial charge with gas phase will reach smaller initial gas saturations, and the connate water trapped inside non-connected pores cannot be displaced. Our model does not account for these effects and thus its prediction overestimates the initial gas saturation, and leads to a much larger total amount of hydrate.

We use a simple calculation to confirm the above argument. Figure 5.29 shows the imbibition curves starting from different drainage stages of a model sediment with 7000 monodisperse spheres. The blue curve is the usual one, which starts from the drainage endpoint. The other six curves (from 2 to 7) all start during the drainage percolation, at points for which the wetting phase saturation is larger than the irreducible value. These curves correspond at least qualitatively to the case where the clay content of the sediment causes the irreducible wetting phase saturation to increase. The results show that although the curvatures for imbibition percolation are similar for all the cases, the residual saturations of gas phase are different. When the wetting phase saturation at the beginning of imbibition increases from 10% (case 1, blue curve) to 92% (case 7, black curve), the residual nonwetting phase saturation decreases from 36% (case 1) to 4% (case 7). This saturation variation also changes the fraction of Melrose jumps, and therefore the final hydrate saturation.

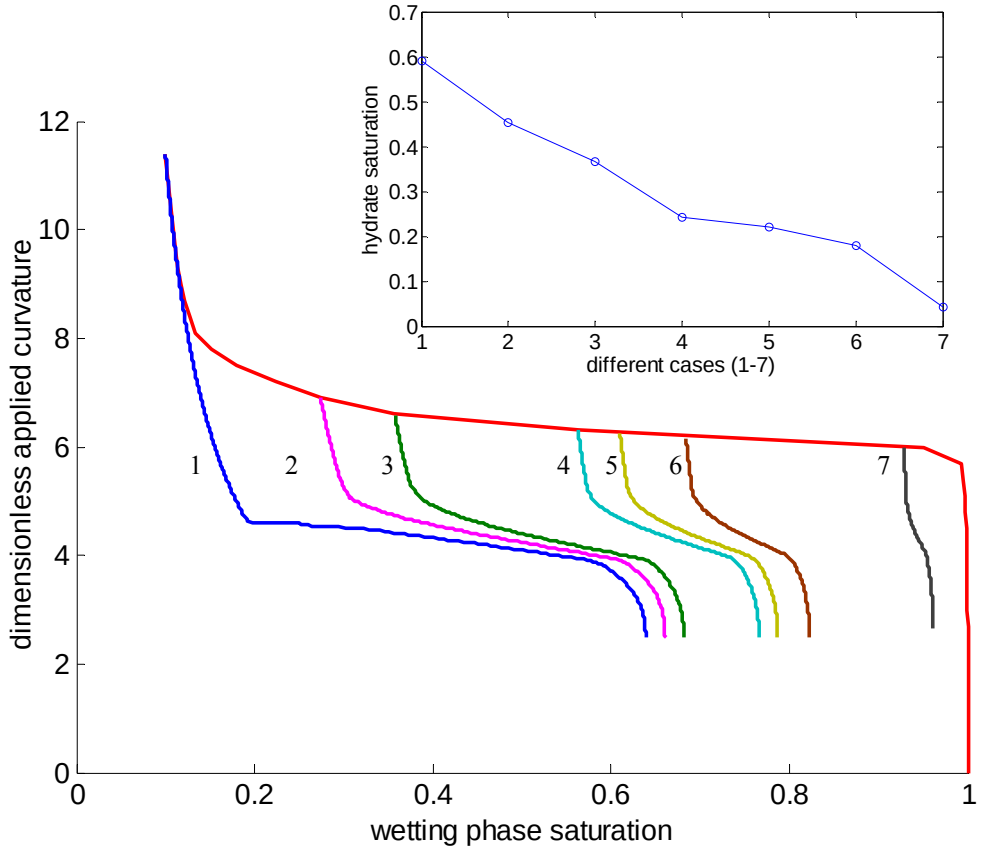

Figure 5.29: Imbibition curves from different stages of drainage; case 1 drains to irreducible S_w, and cases 2 – 7 drain to successively larger values of S_w. This is a network simulation based on 7000 equal sphere packing. The imbibition step size (dimensionless) is 0.012, which gives the correct fraction of Melrose jump and incremental movement. The figure in the upper right corner is the predicted hydrate saturation of different cases (1-7).

For the cases of 1 to 7 (Figure 5.29), we assume linear decrement of S_{jump} (from 7% to 0). We tabulate the values in Table 5-4. By using the same method of Table 4-1, we calculate hydrate saturation for different cases and show the values in the upper right corner of Figure 5.29 and Table 5-4. For example, we assume a change of 7 saturation units is associated with Melrose jumps (S_{jump} = 7%) for case 1. In case 1 (the

conventional imbibition), S_{incr} = 47% (that is, 54% (water invasion from $S_{w,irr}$ = 10% to 1 - S_{nwr} = 64% during imbibition) – 7%). 36 saturation units of residual saturation (S_{nwr}), will be converted into hydrate, yielding 12 saturation units of hydrate. Therefore case 1 gives 59% hydrate saturation (47% + 12%). In case 7 (assuming S_{jump} = 1%, and thus very little gas trapping (4%)), we obtain only 4.3% hydrate saturation. The hydrate saturation decreases consistently as the water saturation at the beginning of imbibition increases from case 1 to 7, showing that large hydrate saturation does not occur in sediments with higher initial water saturation (fine grains with high clay content).

Table 5-4: Fluid saturations for different cases

Case number	1	2	3	4	5	6	7
S_{jump} (linear decrement)	7.0%	6.0%	5.0%	4.0%	3.0%	2.0%	1.0%
S_{nwr} (from Figure 5.29)	36.0%	34.0%	32.0%	22.0%	21.0%	18.0%	4.0%
S_{wirr} (from Figure 5.29)	10.0%	26.0%	37.0%	57.0%	61.0%	68.0%	92.0%
S^* (Amount of hydrate converted from S_{nwr}, assuming 3 volume units of gas converts to 1 volume unit of hydrate)	12.0%	11.3%	10.7%	7.3%	7.0%	6.0%	1.3%
S_h (=1- S_{wirr}- S_{nwr}- S_{jump}+ S^*)	59.0%	45.3%	36.7%	24.3%	22.0%	18.0%	4.3%

The same analysis is also applicable to explain the gas-depleted region in Unit C. To maintain the continuous pathway for gas migration, Unit C-WCL only needs to have a critical gas saturation, which is just above 20%~30% (Gladkikh, 2005). This gives 70%~80% initial water saturation. From Figure 5.29, such high initial water saturation will give a very low hydrate saturation. The maximum hydrate saturation that can be obtained is when only incremental movement of the gas/water interface occurs (Scenario A). In this scenario, we could obtain 10%~20% hydrate saturation. Laboratory experiments (Liu et al., 2008; Hu et al., 2008) indicate that both resistivity and acoustic

velocities are a weak function of hydrate saturation for small saturations. Thus this low value predicted by the model is likely to be within the error of well logging estimates. Moreover, hydrate exists in the form of lenses because of the incremental movement, which does not alter the petrophysical properties of the porous medium significantly (for example, electrical resistivity). We argue that Unit C-WCL only contains very low saturation of hydrate, which is difficult to discern from well logs.

It is a common observation that in the Arctic hydrate system (for example, Mount Elbert and Mallik reservoirs), hydrate distribution has a nonuniform pattern, where high saturation regions are separated by the low saturation regions. It is usually argued that the distribution is highly associated with the lithologies. A good reservoir lithology (clean, uniform and larger grains) usually leads to high hydrate saturation, where a bad reservoir lithology leads to the opposite situation. Although this is true in a lot of cases, contradictions are also observed. Between 995 m and 1005 m of the Mallik reservoir, clean sands with large grain size are identified (Figure 5.24). Moreover, this region is in the ideal environment for hydrate formation, because BGHSZ is at 1110 m. However, little hydrate is discovered at the region. This raises the question of whether the lithology is the only controlling factor that determines the hydrate distribution. Based on our analysis, we argue that this behavior is the consequence of the fluid redistribution during the hydrate formation, and also because of the insufficient gas originally in the reservoir. In the model we consider a closed system without extra gas supply from outside the gas reservoir. By using Scenario B, we predict a satisfactory length of GH region for both Unit A and B. Especially for Unit B, the model results give a low hydrate saturation region (WCL region) between 1000 m and 1005 m. This is the result due to the depletion of free gas in the region, and thus yields very low hydrate saturation.

5.5 DISCUSSION

5.5.1 The effect of salinity

In the previous calculation of this chapter we assume that salt ion diffusion rate is much faster than hydrate formation rate, so that salt will not inhibit hydrate formation. In this section we consider a limiting case, where salt ion cannot be diffused at all. The salt ions excluded from the hydrate formation accumulate in the remaining water, and might possibly become an inhibitor for further hydrate formation.

In Mount Elbert hydrate reservoir, the background water salinity is 0.47 wt%, which is much lower than the general sea water salinity (about 3 wt %). (Torres et al., 2011) suggests the water salinity in Mount Elbert is close to that of the current fresh water, consistent with the meteoric water precipitation in the past 110 Ma. Since the hydrate formation might take place 2.5 Ma ago (Majorowicz et al., 2008), it was likely to be fresh water in Mount Elbert during the formation. For Scenario A, we start from S_{wirr} = 15%, and obtain 85% hydrate saturation. The total saturation of water required to generate this saturation of hydrate is 77.3%, calculated from the hydrate and water densities, which are 910 kg/m^3 and 1000 kg/m^3. If we assume that the initially present and the incoming water had salinity the same as the modern value of 0.47 wt%, then salt ions excluded from 77.3% water will remain in 15% irreducible water when hydrate formation completes. Assuming zero diffusion of the ions this would increase the salinity from 0.43 wt% to 2.6 wt% during hydrate formation. For Scenario B, the same procedure can be applied, and the salinity in the water is computed and tabulated in the following table.

Table 5-5: Water salinity without salt ion diffusion, Mount Elbert hydrate reservoir

Scenarios	Hydrate saturation (S_h)	Water saturation ($S_w = 1-S_h$)	Initial water salinity (weight percentage)	Water salinity after hydrate formation (weight percentage)
Scenario A	85%	15%	0.43%	**2.6%**
Scenario B	58%	42%	0.43%	**1.0%**

Figure 5.30 shows the maximum salinity under which hydrate can be stable in Mount Elbert and Mallik reservoirs. For Mount Elbert, hydrate is stable until the water salinity reaches up to 8 wt%, which is much higher than the maximum salinity we can predict by assuming no salt ion diffusion (Table 5-5). Therefore for both scenarios in Mount Elbert case, salt accumulation does not inhibit hydrate formation.

In Mallik hydrate reservoir, the background water salinity is 2.3 wt% (Matsumoto et al., 2005), which is close to the salinity of the sea water. The oxygen and hydrogen records show that the water salinity at hydrate formation could either come from the mixing of river water and sea water, or from the previous dilution due to the hydrate dissociation (Tomaru et al., 2005). However to our best knowledge there is no information of water salinity at the time when hydrate formed. Therefore, it is an assumption that the current salinity is similar to the value at hydrate formation. Based on the above analysis, we can also calculate the salinity after water formation. The results are tabulated in Table 5-6.

Table 5-6: Water salinity without salt ion diffusion, Mallik hydrate reservoir

Scenarios	Hydrate saturation (S_h)	Water saturation ($S_w = 1-S_h$)	Initial water salinity (weight percentage)	Water salinity after hydrate formation (weight percentage)
Scenario A	85%	15%	2.3%	**15.3%**
Scenario B	58%	42%	2.3%	**5.5%**

Figure 5.30 shows the temperature and pressure range of Mallik reservoir (temperature from 280 to 285 K, pressure from 8 to 10 MPa). For Scenario A, the water

salinity increases to 15.3 wt% after hydrate formation is complete, so that the entire reservoir is in a region where hydrate is unstable (the curve of 15.3 wt% salinity is not shown in the figure, but is close to the curve of 16 wt% salinity, the Mallik reservoir (red box) is below the curve, indicating that the hydrate is unstable). This observation suggests that for Scenario A, 85% hydrate saturation cannot be obtained without salt ion diffusion. Scenario B, on the other hand, only has 5.5 wt% salinity. The entire reservoir is therefore in the region where hydrate is stable, even though no salt ion diffusion occurs. Salt ion accumulation does not inhibit hydrate formation in Scenario B.

The comparison suggests that in Scenario A the hydrate saturation should be smaller than 85%. We thus would gain a similar profile with that of Scenario B (lower hydrate saturation, but longer length of GH region), and better comparison with the field observation.

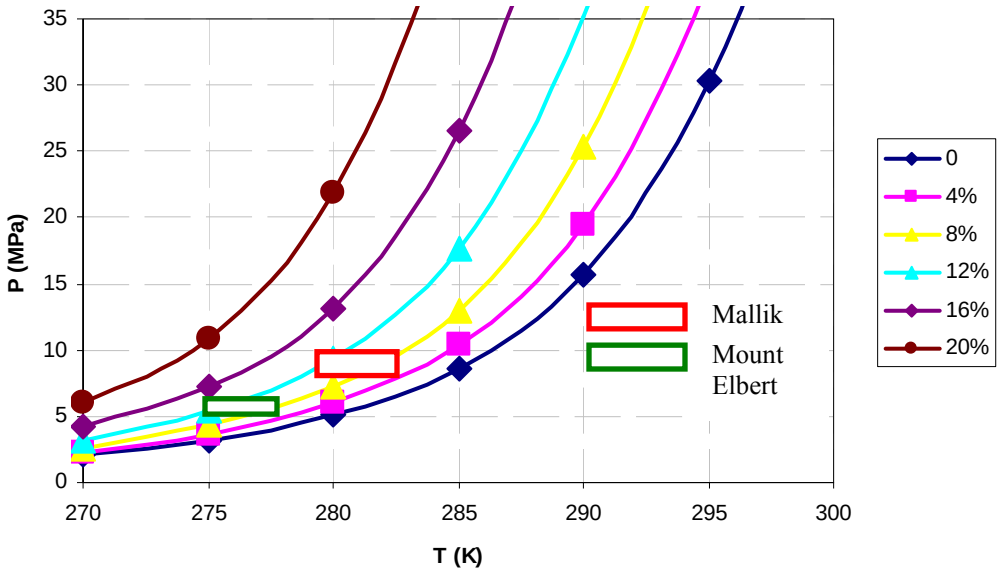

Figure 5.30: GHSZ variation as a function of pressure, temperature and salinity. At each salinity, above the curve hydrate is stable, while below the curve hydrate is unstable. The pressure and temperature range of Mount Elbert and Mallik reservoirs are shown.

5.5.2 The direction of hydrate growth in the porous medium

In this work we study a gas/water two-phase system. Hydrate formation first takes place at the interface between gas and water, and then by assumption, grows into the gaseous phase. Such assumption is made based on the observation from the experiment, where hydrate intends to grow into the limiting phase (and in our case, because gas column is isolated from the deep gas source, gas becomes the limiting phase).

Here we discuss another possibility. That is, hydrate grows into the aqueous phase instead of the gaseous phase. Based on the density comparison, 15% irreducible water saturation will be converted into only 16.5% hydrate saturation, leaving the rest of the pore space to be filled by gas ($S_{g,f}$ = 83.5%). This result does not match the field observation from two aspects. First, the hydrate saturation in the GH region, for both reservoirs, is more than 50%. Thus the prediction of 16.5% is much lower than the field observation. Second, from the field observation only hydrate and water coexist, and no free gas is present. These two observations invalidate this assumption that hydrate grows into the aqueous phase.

5.5.3 Water supply from above the reservoir

Figure 5.6 shows that the capillary seal on top of the reservoir is made of clay and silt. This lithology gives a high capillary entry pressure to contain the gas column in the reservoir below, but sufficient permeability to allow water invasion. In this section, we consider an extreme scenario that the permeability of the capillary seal is very low. Thus even when BGHSZ moves into the reservoir, no water is available to make hydrate (Figure 5.31A, the residual water is not used to form hydrate) and gas will remain.

In this case no hydrate can form during the descending of BGHSZ until BGHSZ reaches the aquifer below the reservoir (Figure 5.31B). Hydrate starts to form from the base of the reservoir as water can be provided from the aquifer below. When vacancy is created, no free gas can be supplied from the shallower layers of the sediments, as in those sediments water invasion is not possible. Therefore, the vacancy can only be filled by water invasion from the aquifer. The hydrate saturation can be computed from the initial gas saturation in the porous medium. For example, in Mount Elbert, 1 unit volume of gas will form about 1/3 unit volume of hydrate, and the rest of the void space will be filled by water. Therefore, for the situation of initial gas saturation equal to 85%, 28% hydrate saturation is obtained. This value is much less than the model prediction that assumes water invasion from above the reservoir (Section 5.3) and the field observation.

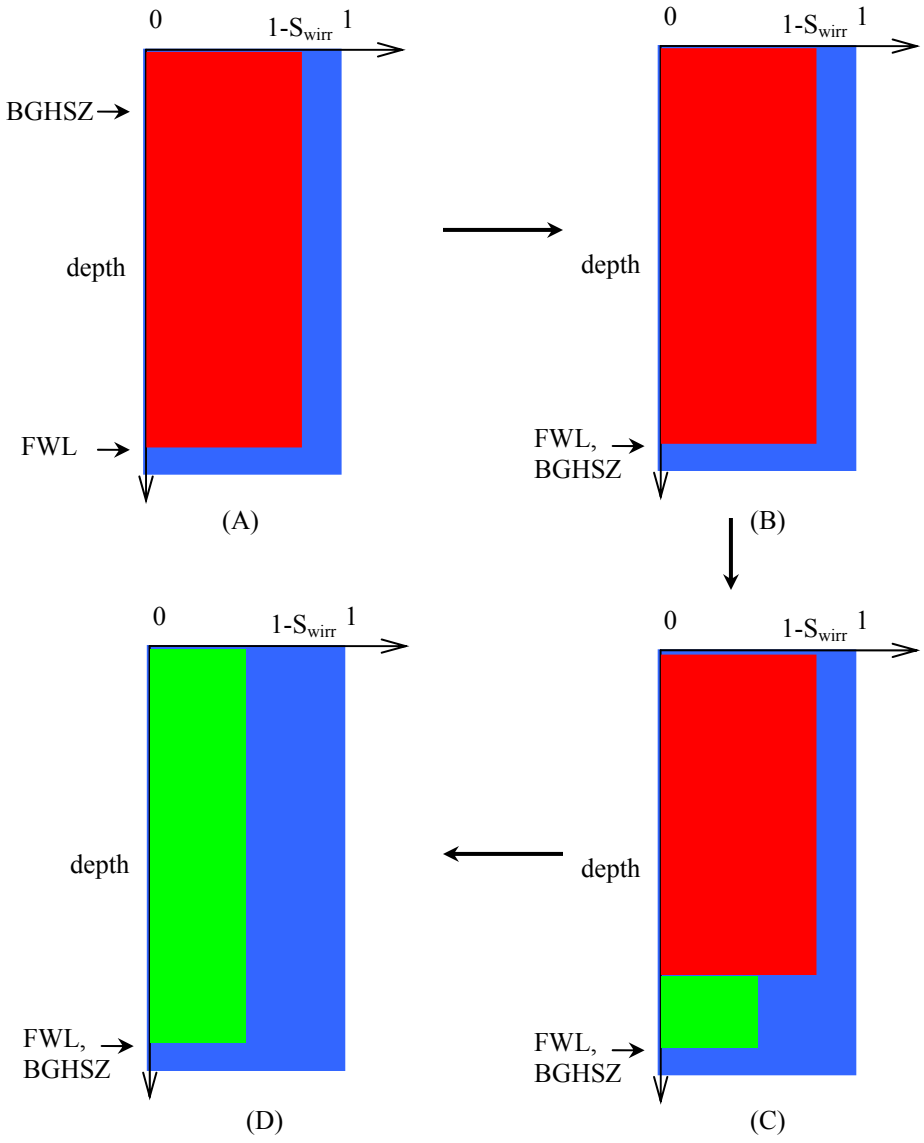

Figure 5.31: Hydrate formation and distribution with no water supply from above the reservoir.

Hydrate formation starts from the base of the reservoir, and is controlled by the availability of water. The upward migration of water allows hydrate formation to move upwards. Because no gas redistribution occurs in the reservoir (the gas redistribution in Section 5.2, 5.3 and 5.4 are possible because water invasion takes place from both above

and below the reservoir), hydrate saturation is uniform along the depth (Figure 5.31D). This saturation profile is different from the field observations (Figure 5.20 and Figure 5.28). We conclude that it must have been possible for water to be supplied from above the reservoir during BGHSZ descent.

5.5.4 Connection between gas column and deep gas source

In Section 5.2 to 5.4, it is an assumption that gas column, after it is fully charged, disconnects from the deep gas source. The entire gas column is isolated, and thus the total amount of hydrate is only determined by the amount of gas in the gas column.

In this section we qualitatively analyze the case when free gas still migrates into the gas column as BGHSZ descends. With more free gas available, a longer GH region will be obtained than those predicted in Section 5.2 and 5.3. For an extreme case where the gas supply from deep gas source is fast enough to fill the vacancy created by the hydrate formation, a uniform gas profile is expected along the depth. The hydrate saturation is determined by different scenarios developed in Chapter 4. For example in Mount Elbert gas reservoir, hydrate saturation could be 85% (Scenario A) or 58% (Scenario B).

Figure 5.20 and Figure 5.28 show that the model by using Scenario B yields GH region length that is comparable to the field observation. Assuming the connection with the deep gas source increases the GH region length, and thus gives less agreement. Therefore, it is more reasonable to assume isolated gas column in the reservoir when BGHSZ begins to descend.

5.6 CONCLUSIONS

In this chapter, we integrate a pore-scale network model with a field-scale sedimentological model, and predict the hydrate distribution in Arctic hydrate reservoirs. The model predictions are later compared with the field observation from two different reservoirs.

The sedimentological model is based on the hypothesis that the reservoir was initially filled by gas, the saturation of which is determined from the drainage simulation by using network modeling. At this stage, BGHSZ was above the gas reservoir. The descending BGHSZ provides environment for hydrate formation within the reservoir. During this process, gas and water are redistributed in not only the local porous medium, but also the entire reservoir. The complex behaviors give the final hydrate distribution a characteristic nonuniform pattern, which agrees with the field observation.

Two scenarios developed in Chapter 4 are employed to determine the local hydrate saturation in the porous medium. Scenario A (water supply rate << hydrate formation rate) requires the minimum water invasion, which is used to stoichiometrically convert gas to hydrate. This scenario gives the highest hydrate saturation of 85%. Scenario B (water supply >> hydrate formation rate) allows for the maximum water invasion, and thus leads to a lower hydrate saturation (58% in Mount Elbert and 68% in Mallik). The water invasion in this scenario is due to Melrose jumps during hydrate formation, filling the vacancy created by the conversion of the trapped gas to hydrate, and to supply the stoichiometric requirement of water for the gas conversion to hydrate. For the comparison with both field cases (Mount Elbert and Mallik hydrate reservoirs), the hydrate saturation predicted by Scenario A (85%) exceeds the maximum hydrate saturation observed in the field, while the prediction of Scenario B (58% for Mount Elbert and 68% for Mallik) are close to the average value of the GH regions.

The comparison of the thickness of the GH interval suggests Scenario B has a better prediction. For both reservoirs, Scenario B predicts a very close result with the field observation. Moreover, the comparison of the amount of hydrate in the GH region also indicates that Scenario B has a more satisfactory result than Scenario A. We therefore argue that the hydrate formation mechanism in the porous medium agrees with the description of Scenario B. That is, the gas/water or gas/hydrate interface movement follows the imbibition process. Hydrate forms at the gas/hydrate interface during the incremental movement, which is also the major behavior in the imbibition process. When the other behavior, Melrose jump, occurs, water displaces gas from the sediment, increasing S_w without changing S_h. Although the saturation change due to Melrose jump is only 7%, this behavior traps a large amount of gas at the imbibition endpoint. The hydrate formation inside the trapped gas bubbles triggers additional water invasion to fill the vacancy. This argument is consistent with the data of Mount Elbert and Mallik hydrate reservoirs.

A WCL region lies beneath each GH region for both model prediction and field observation. From the model, the occurrence of this region is due to the hydrate formation from residual gas. For Mount Elbert case, converting residual gas saturation yields 10% hydrate saturation, while for Mallik case, 20% hydrate saturation is obtained because the higher pressure in Mallik reservoir increases gas density and thus more hydrate can be formed given the same gas saturation as in Mount Elbert. Importantly, some of these WCL regions contain good reservoir lithologies, where clean sands with large grain size are capable of holding large hydrate saturations. This contradicts the conventional wisdom that associates high hydrate saturation with good reservoir quality. The analysis of this chapter suggests that free gas migrates upwards to form hydrate in the GH regions, leaving only residual gas to form hydrate in the deeper layers. The

reasonable agreement with the field observation justifies this argument. We provide a supplementary explanation for the hydrate distribution: although it is largely affected by lithology, the redistribution of gas and water during hydrate formation also play a significant role.

6. Conclusions and future work recommendations

6.1 CONCLUSIONS

The mechanisms governing methane hydrate formation and distribution in the subsurface are still open to scientific debates, especially in the hydrate reservoir under permafrost in the arctic regions. One explanation attributes the hydrate distribution to the quality of lithology. It argues that the good lithology (that is, clean sand) correspond to higher hydrate saturation. However, abnormalities are observed from the field, where clean sands exhibit little or no hydrate accumulation, even though hydrate is found both above and beneath these sands. The hypothesis of this work is that the hydrate formation and distribution are controlled by more fundamental mechanisms. A key to understanding these mechanisms is the hypothesis that Arctic accumulations of hydrate are originally conventional reservoirs of thermogenic gas that were converted as the base of gas hydrate stability zone (BGHSZ) descended through the reservoir.

The field-scale behavior is the accumulative effect of the events in a much smaller scale (pore scale). In the initial gas reservoir with proper temperature and pressure, we assume hydrate forms at the gas/water interface and grows into the gaseous phase (Chapter 4, section 4.3). Hydrate formation creates void space (Chapter 4, section 4.1 and 4.2), in the sense that the volume of hydrate is smaller than the volume of gas that is consumed, if pressure and temperature are kept constant. Fluids from elsewhere in the sediment column must be drawn to fill the void space and maintain pore pressure. Such process brings more reactants (gas and water) into the hydrate stability zone, thus enabling more hydrate to form. The positive feedback redistributes water and gas in the field scale. On the other hand, the amount of gas that can be used to fill the void space is also determined by the availability of gas in the entire reservoir (water in our case is an

unlimiting phase, and thus is always available). If gas is insufficient to fill the void space, water imbibes in and the sediment is saturated by water instead of hydrate. Hydrate formation and distribution involves complex, correlated pore- and field-scale behaviors. Consequently, models on these two scales are developed.

We apply two approaches to study gas/water distribution and hydrate formation in the pore scale: LSMPQS (Level Set Method Progressive Quasi Static Algorithm) and network modeling. The former captures the basic physics governing the fluid displacement in the porous medium, and requires no simplification of the pore-scale geometry. Thus we use this method as a benchmark to verify network modeling. Due to the simplifications employed in network modeling, it is less accurate in predicting the fluid displacement, but is capable of dealing with much larger porous medium with manageable amount of time, compared to LSMPQS.

We start by comparing the drainage and imbibition results by network modeling with those by LSMPQS (Chapter 2), in a model sediment. Both simulations are based on the conventional boundary conditions. We argue that the macroscopic comparison of the drainage and imbibition curves (pressure vs. saturation) is not an adequate check of the correctness of network modeling, since the curves are only the cumulative results of individual pores and do not reveal the fluid occupation status of each pore (pore filling status). A pore-by-pore comparison technique is developed to compare the filling status of individual pores at each step of drainage and imbibition simulations. A subset of Finney pack of monodisperse spheres is employed as the porous medium, which contains 109 pores. The pore-by-pore comparison suggests that drainage and imbibition events for these two simulations, although happening at slightly different applied curvatures, follow the same sequences. We also observe that the comparison of imbibition has less agreement than drainage. This is mainly due to the fact that the occurrence of imbibition

events in a single pore is determined by the configuration of menisci, which gives multiple possible imbibition critical curvatures. Our newly-developed C_1 imbibition criterion only captures the most likely critical pore-level event, while ignores the others. Overall, both the microscopic and macroscopic comparisons give a satisfactory agreement with LSMPQS, showing that network modeling is capable of predicting the correct drainage and imbibition events.

The pore-by-pore comparison technique is also applied to test the drainage and imbibition results of network modeling in sedimentary rocks (Chapter 3). Three digitized sandstone samples (Fontainebleau, Berea and Castlegate) are used, and *3DMA-Rock* is applied to generate the pore-throat network from the topological information. Our rudimentary network model in this case gives a less satisfactory agreement than in the Finney pack. There is still strong evidence that drainage events for these two simulations follow the same sequence but at different applied curvatures. However for imbibition, larger discrepancies between the two simulations are observed, although the macroscopic capillary curves match well. This also proves that the macroscopic agreement does not require microscopic consistency. The only way to check the correctness of a network simulation of drainage and imbibition is by checking the pore level events. As the experimental data are not available at individual pore level in sedimentary rocks, pore-by-pore comparison of network model and LSMPQS provides a unique technique for such purpose.

The good agreement with LSMPQS enables us to apply the periodic boundary condition on the network modeling (Chapter 3). This boundary condition eliminates the imposition of the usual boundary conditions on networks (typically, one face of the network is assumed open to an invading fluid, and the displaced fluid leaves the network through the opposing face). These conditions are not representative of the reservoir

situation. Results from drainage and imbibition simulations in the periodic networks agree with field observations of residual phase saturations and thus are employed in the field-scale sedimentological model for the prediction of hydrate formation and distribution.

Hydrate formation in the porous medium is hypothesized to follow the pore-scale pathway of conventional imbibition (Chapter 4, Section 4.3). Of the two imbibition events (incremental movement of the interface and Melrose jump (discontinuous interface movement)), hydrate formation only takes place during the former event, and occupies the volume traversed by the interface motion. In the latter event, aqueous phase fills the volume traversed by the interface, and hydrate formation begins anew at the new gas/water interface location. Two limiting cases are studied here. If water supply rate is much smaller than the hydrate formation rate (referred to as Scenario A), only the incremental movement can occur in the imbibition process. This yields the maximum hydrate saturation. On the other hand, if water supply rate is much larger than the hydrate formation rate (referred to as Scenario B), both types of imbibition events take place. This scenario results in the minimum hydrate saturation. The frequency of each type of event and the corresponding change in phase saturation associated with each event are derived from the network simulation in a much larger sample. This requires identification of a threshold for distinguishing a jump, and algorithms for this purpose were developed and applied at every step of imbibition simulations.

We study the volume change (the volume of gas used for hydrate formation less the volume of hydrate) associated with hydrate formation by using our stoichiometric thermodynamic model proposed in Chapter 4, Section 4.1 and 4.2. The calculation indicates that the hydrate volume is smaller than the volume of gas that is consumed (valid for $P < 13$ MPa, $T < 290$ K, Figure 4.15). Therefore, hydrate formation in the

reservoirs creates vacancy in the porous medium, and imbibes fluids from other layers and change the profile of fluid distribution.

A 1D sedimentological model is proposed to study the hydrate saturation in the field scale. In this model, methane gas from deep gas source migrates upwards through the conduits and fills the reservoir. The initial gas saturation in the reservoir is assigned from the drainage simulation of network modeling based on the periodic boundary condition. During reservoir charge, BGHSZ was still above the reservoir. When gas charge was complete, we assume the gas column in the reservoir no longer communicated with the deep gas source and thus no free gas could enter the reservoir. BGHSZ descended after gas charge was complete, and thereby converted accumulated gas into hydrate. The hydrate formation process is studied from two limiting imbibition scenarios. Both scenarios assume that gas is available to fill a portion of the void space created by hydrate formation. To do this, free gas must migrate upwards from lower portion of the accumulation. Water invasion into these lower layers must accompany gas migration, and this reduces the gas saturation to the residual value. The latter value is obtained from the imbibition simulation of network modeling based on the periodic boundary condition. Therefore, the upper region of the reservoir (referred to as GH region) is saturated with hydrate, the saturation of which depends on whether the water supply rate is small (Scenario A) or large (Scenario B); the lower region of the reservoir (referred to as WCL region) contains limited amount of hydrate that is converted from the residual gas. This behavior leads to a characteristic nonuniform hydrate distribution pattern.

The comparison with the field data from two hydrate reservoirs in the Arctic (Mallik in Canada's Northwest Territories and Mount Elbert on Alaska's North Slope) suggests that water supply rate was much greater than the hydrate formation rate during

BGHSZ descent. Scenario B not only gives a good agreement of average hydrate saturation in the GH region with the field data, but also correctly calculates the thickness of the GH region. Moreover, unlike the rule of thumb that attributes the nonuniform hydrate distribution only to the quality of lithology (hydrate fills sand but is not found in silt or clay), we conclude such pattern is a consequence of fluid redistribution induced by hydrate formation. This explains the existence of hydrate-poor regions with good lithology which are observed at both Mallik and Mount Elbert reservoirs: the inevitable migration of gas in the reservoir as BGHSZ descended determines which regions exhibit small hydrate saturation.

6.2 FUTURE WORK RECOMMENDATION

The less satisfactory comparison between network modeling and LSMPQS in the sedimentary rock samples (Chapter 3) raises the question that the current rudimentary network model does not yet captures the essential physics for the fluid movement and displacement in the real rock. We therefore recommend a further development of the current network model for the real rock. For example, we can use a triangular throat cross-section instead of the current circular one. This treatment would allow us to hold wetting phase at the corners, as well as to consider the snap-off events. Our ERdrainage and ERimbibition criteria deserve more development as well. The current approach does not consider the menisci.

The hydrate saturation and distribution prediction from our current model has a good agreement with the field observations. However, the reservoir data we use are all from the sediments in arctic region, below the permafrost. The other environment in which hydrates are commonly found, ocean sediment, is not yet taken into consideration.

The same model as proposed in this work might still be able to be applied to this environment, that is, gas charge occurred before BGHSZ moved downwards; and the descending of BGHSZ converted gas and water into hydrate from the top to the base of the reservoir. However, the current observation suggests that gas influx is a common phenomenon in these reservoirs. Therefore, the model should consider gas invasion into the reservoir during hydrate formation at BGHSZ. This becomes a major challenge for our model application. However, should we fail to predict the hydrate distribution in the ocean sediments, the attempt is still valuable: it could prove that the mechanisms governing the hydrate distribution in these two types of reservoirs are necessarily different, which also gives us a better understanding of the hydrate system at different locations.

The field-scale model assumes BGHSZ slowly moves downward and converts gas and water into hydrate. Another possibility is a fixed BGHSZ. Gas migrates into GHSZ and forms hydrate. This conceptual model is applied to the case of ocean sediments, but has not been used to explain the hydrate distribution in the arctic regions. It is intriguing to know whether or not this is a general model for all the hydrate systems.

Appendix A. A summary of properties of 76 packings (model sediments)

	Grain sizes (arbitrary units)				Porosity (fraction)	Sorting Index		Notes*
Packing No.	Minimum Radius	Maximum radius	Mean radius	Standard deviation		Number fraction basis	Volume or weight fraction basis	
1	0.32	2.58	2.18	0.11	0.37	1.04	1.04	LN
2	1.84	2.64	2.18	0.11	0.36	1.03	1.03	LN
3	1.80	2.60	2.18	0.11	0.37	1.03	1.03	LN
4	0.32	2.59	2.18	0.11	0.35	1.03	1.03	LN
5	1.82	2.52	2.15	0.11	0.41	1.03	1.03	LN
Average	1.22	2.59	2.17	0.11	0.37	1.03	1.03	
6	1.50	3.22	2.17	0.22	0.36	1.07	1.07	LN
7	1.50	3.08	2.16	0.22	0.36	1.07	1.07	LN
8	1.48	2.99	2.17	0.22	0.36	1.07	1.07	LN
9	1.47	3.06	2.16	0.22	0.37	1.07	1.07	LN
Average	1.49	3.09	2.16	0.22	0.36	1.07	1.07	
10	0.96	4.12	2.12	0.42	0.35	1.14	1.14	LN
11	0.93	4.64	2.12	0.43	0.34	1.14	1.14	LN
12	1.07	4.49	2.11	0.42	0.35	1.14	1.14	LN
13	0.99	4.27	2.11	0.43	0.35	1.14	1.14	LN
Average	0.99	4.38	2.11	0.43	0.35	1.14	1.14	
14	4.24E-03	7.05	1.90	0.80	0.32	1.31	1.32	LN
15	3.44E-03	6.44	1.90	0.79	0.35	1.31	1.31	LN
16	3.91E-01	6.38	1.91	0.78	0.33	1.31	1.29	LN
17	7.81E-03	7.01	1.90	0.79	0.32	1.31	1.30	LN
18	1.59E-03	7.62	1.91	0.79	0.32	1.31	1.29	LN
Average	8.17E-02	6.90	1.90	0.79	0.33	1.31	1.30	
19	1.86E-03	11.30	1.31	1.16	0.29	1.72	1.48	LN; Trn
20	2.39E-03	10.16	1.31	1.17	0.25	1.72	1.54	LN; Trn
21	7.85E-03	11.26	1.31	1.15	0.30	1.72	1.53	LN; Trn
22	1.17E-03	11.17	1.30	1.16	0.30	1.69	1.53	LN; Trn
Average	3.32E-03	10.97	1.31	1.16	0.29	1.71	1.52	
23	3.45E-05	11.31	0.69	1.25	0.31	3.11	1.32	LN; Trn
24	1.63E-05	11.19	0.71	1.26	0.30	3.12	1.38	LN; Trn
25	3.80E-05	11.28	0.70	1.25	0.37	3.16	1.30	LN; Trn
26	1.44E-05	12.16	0.72	1.23	0.32	3.07	1.46	LN; Trn
Average	2.58E-05	11.49	0.71	1.25	0.33	3.11	1.37	
27	8.10E-06	18.29	0.30	1.07	0.31	3.63	1.38	LN; Trn
28	2.04E-06	21.32	0.30	1.04	0.29	3.77	1.37	LN; Trn
29	6.94E-06	22.46	0.31	1.04	0.32	3.95	1.41	LN; Trn
Average	5.69E-06	20.69	0.31	1.05	0.31	3.79	1.39	

30	1.24E-03	11.93	1.01	1.20	0.29	2.00	1.50	LN; Trn
31	6.31E-04	11.99	1.04	1.22	0.32	2.00	1.56	LN; Trn
32	5.70E-04	12.34	1.02	1.21	0.30	2.03	1.48	LN; Trn
33	4.21E-05	12.57	1.07	1.22	0.31	1.94	1.51	LN; Trn
34	5.47E-04	11.63	1.03	1.19	0.34	2.01	1.49	LN; Trn
Average	6.06E-04	12.09	1.03	1.21	0.31	2.00	1.51	
35	4.62E-04	9.67	1.63	1.03	0.30	1.51	1.40	LN
36	1.89E-03	9.70	1.61	1.04	0.30	1.50	1.43	LN
37	1.35E-03	9.30	1.59	1.04	0.27	1.49	1.46	LN
38	3.98E-03	9.41	1.60	1.05	0.27	1.51	1.44	LN
Average	1.92E-03	9.52	1.60	1.04	0.29	1.50	1.43	
39	1.97	2.40	2.19	0.07	0.34	1.02	1.02	N
40	1.97	2.41	2.19	0.07	0.35	1.02	1.02	N
41	1.95	2.39	2.17	0.07	0.38	1.02	1.02	N
42	1.97	2.40	2.19	0.07	0.37	1.02	1.02	N
Averages	1.97	2.40	2.18	0.07	0.36	1.02	1.02	
43	1.07	3.20	2.14	0.35	0.36	1.12	1.10	N
44	1.07	3.20	2.14	0.35	0.36	1.12	1.10	N
45	1.07	3.20	2.14	0.36	0.35	1.12	1.11	N
46	1.07	3.20	2.14	0.35	0.37	1.12	1.11	N
Averages	1.07	3.20	2.14	0.35	0.36	1.12	1.10	
47	5.64E-05	4.01	2.01	0.68	0.34	1.27	1.17	N
48	4.20E-05	4.01	2.01	0.66	0.33	1.25	1.17	N
49	3.59E-05	4.03	2.01	0.67	0.34	1.25	1.18	N
50	3.22E-05	4.04	2.02	0.66	0.33	1.25	1.17	N
Averages	4.16E-05	4.02	2.01	0.67	0.34	1.26	1.17	
51	1.27E-03	4.59	1.85	0.90	0.32	1.42	1.21	N
52	1.10E-03	4.51	1.85	0.91	0.34	1.42	1.21	N
53	5.94E-04	4.44	1.86	0.89	0.35	1.40	1.21	N
54	2.94E-03	4.59	1.86	0.90	0.32	1.42	1.20	N
Averages	1.48E-03	4.53	1.86	0.90	0.33	1.42	1.21	
55	6.34E-04	5.00	1.73	1.04	0.32	1.60	1.23	N
56	3.30E-04	5.06	1.71	1.05	0.31	1.64	1.22	N
57	1.56E-03	5.07	1.71	1.05	0.35	1.62	1.22	N
58	8.76E-04	5.08	1.71	1.05	0.34	1.65	1.23	N
59	1.09E-03	5.01	1.70	1.05	0.33	1.63	1.22	N
Averages	8.98E-04	5.04	1.71	1.05	0.33	1.63	1.22	
60	3.81E-03	4.56	1.84	0.91	0.32	1.43	1.21	N
61	4.85E-03	4.82	1.77	1.00	0.31	1.53	1.22	N
62	4.93E-03	4.85	1.76	1.00	0.35	1.53	1.23	N
63	4.47E-04	4.81	1.76	1.00	0.33	1.53	1.22	N
64	2.51E-03	4.82	1.77	0.99	0.33	1.51	1.22	N
65	4.94E-03	4.88	1.76	1.00	0.34	1.54	1.23	N
Averages	3.58E-03	4.79	1.78	0.98	0.33	1.51	1.22	
66	3.31E-03	5.36	1.60	1.15	0.33	1.89	1.24	N
67	1.88E-04	5.38	1.61	1.14	0.32	1.85	1.24	N
68	2.30E-03	5.44	1.60	1.15	0.33	1.94	1.23	N

69	2.37E-03	5.43	1.60	1.14	0.33	1.91	1.24	N
70	2.43E-04	5.32	1.59	1.14	0.33	1.90	1.25	N
Averages	1.68E-03	5.39	1.60	1.14	0.33	1.90	1.24	
71	2.88E-04	5.46	1.54	1.19	0.33	2.12	1.23	N
72	2.93E-03	5.47	1.53	1.20	0.33	2.20	1.23	N
73	2.86E-04	5.49	1.52	1.20	0.32	2.27	1.24	N
74	2.52E-03	5.64	1.53	1.20	0.33	2.18	1.24	N
75	8.97E-04	5.65	1.53	1.19	0.33	2.13	1.26	N
76	7.35E-04	5.52	1.53	1.20	0.32	2.23	1.24	N
Averages	1.28E-03	5.54	1.53	1.20	0.32	2.19	1.24	

* LN: log-normal distribution; N: normal distribution; Trn: the actually distribution of sphere sizes in the packing is truncated

Appendix B. Network modeling of drainage and imbibition by conventional boundary condition

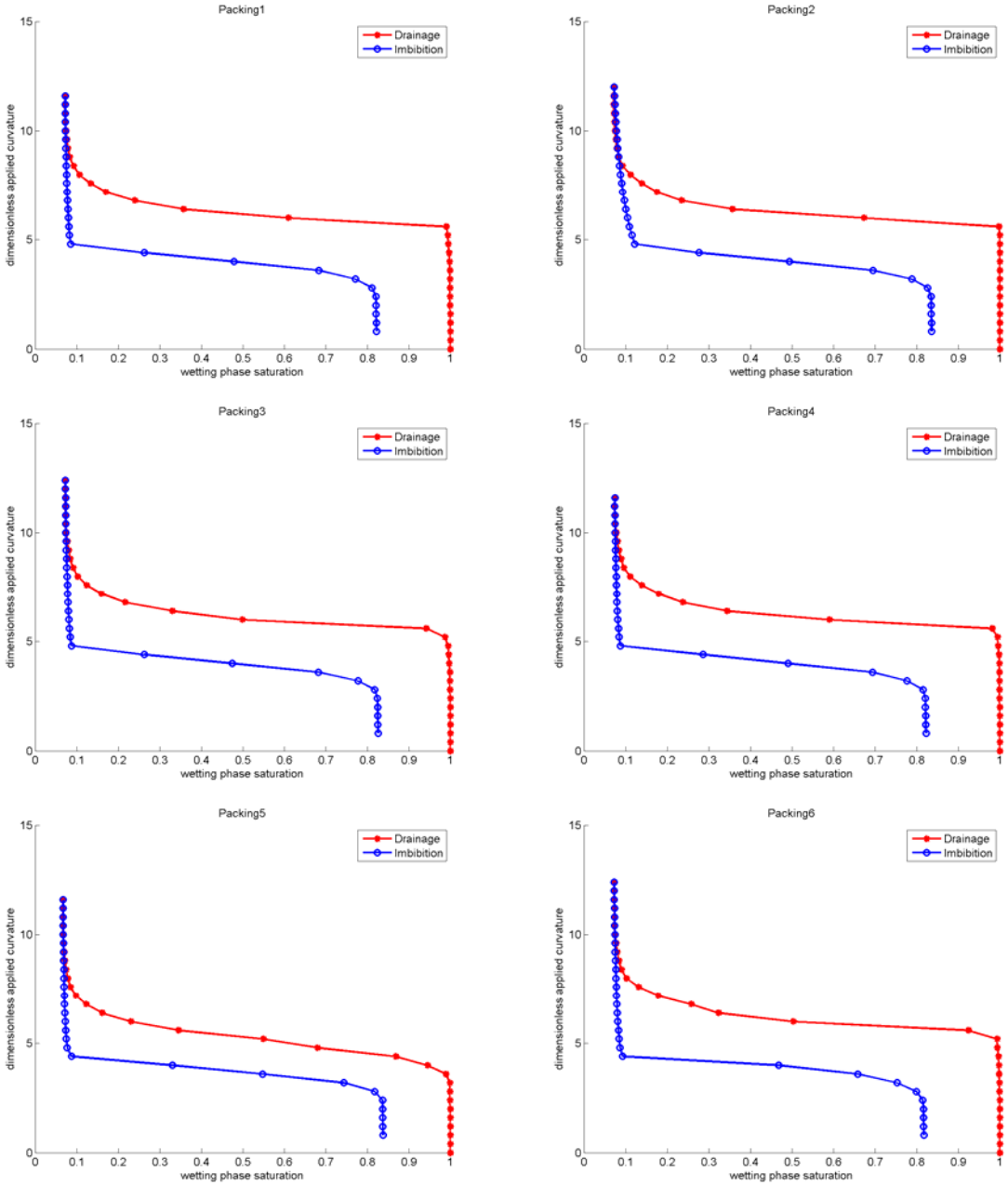

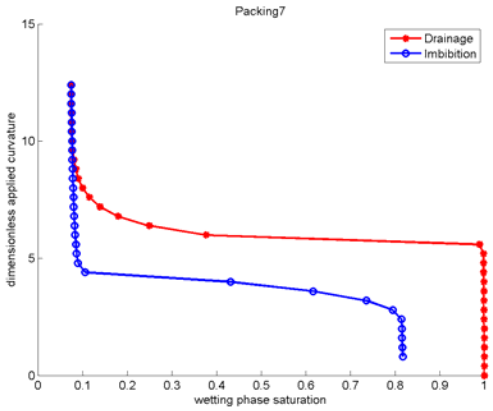
Packing7
Drainage
Imbibition
dimensionless applied curvature
wetting phase saturation

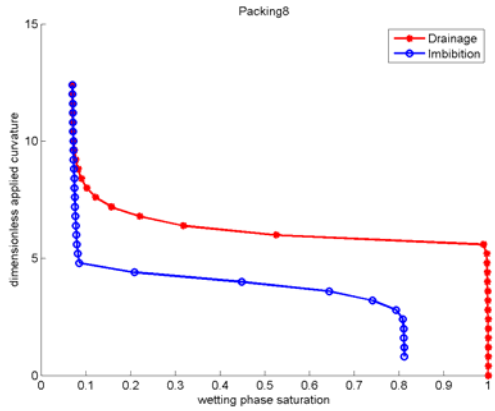
Packing8
Drainage
Imbibition
dimensionless applied curvature
wetting phase saturation

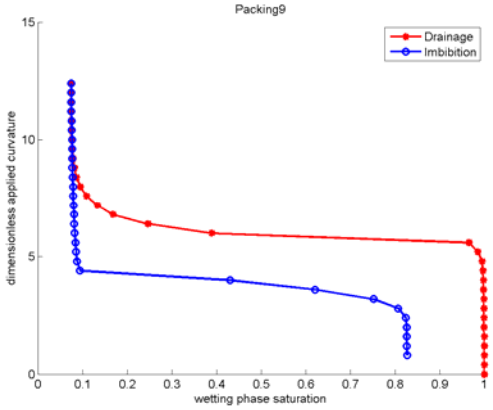
Packing9
Drainage
Imbibition
dimensionless applied curvature
wetting phase saturation

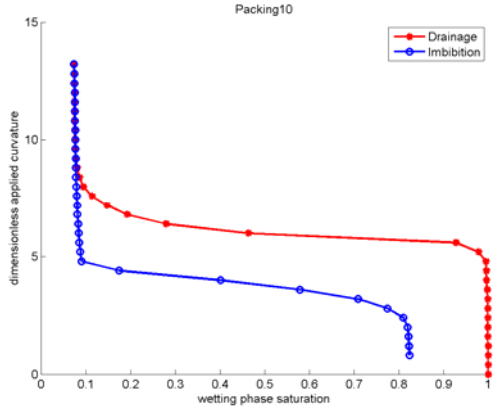
Packing10
Drainage
Imbibition
dimensionless applied curvature
wetting phase saturation

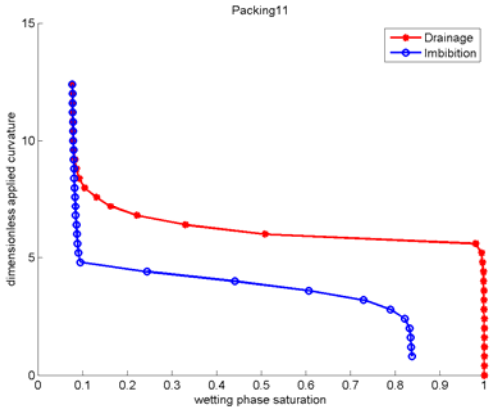
Packing11
Drainage
Imbibition
dimensionless applied curvature
wetting phase saturation

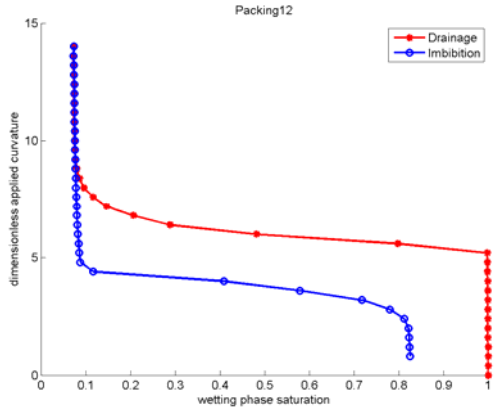
Packing12
Drainage
Imbibition
dimensionless applied curvature
wetting phase saturation

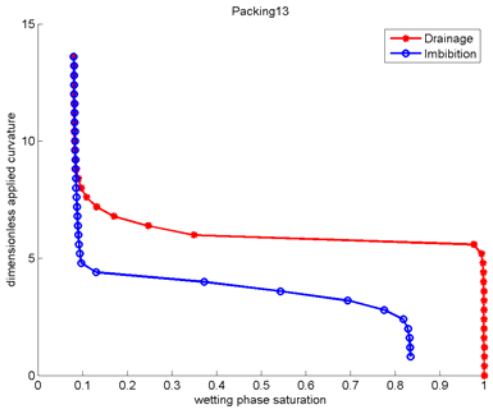
Packing13
Drainage
Imbibition
dimensionless applied curvature
wetting phase saturation

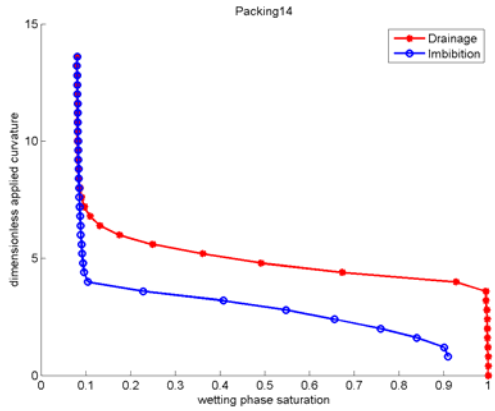
Packing14
Drainage
Imbibition
dimensionless applied curvature
wetting phase saturation

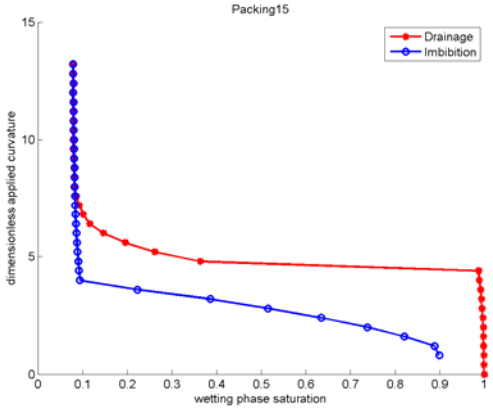
Packing15
Drainage
Imbibition
dimensionless applied curvature
wetting phase saturation

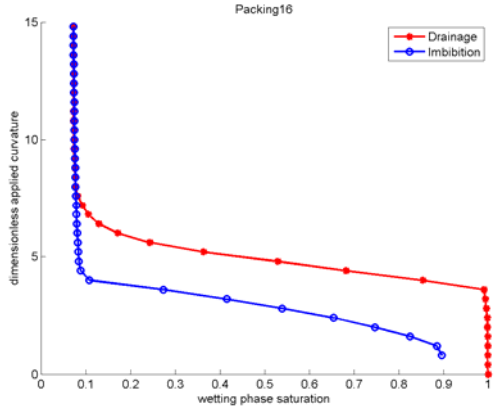
Packing16
Drainage
Imbibition
dimensionless applied curvature
wetting phase saturation

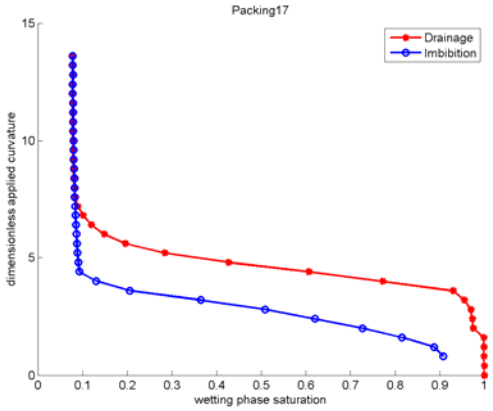
Packing17
Drainage
Imbibition
dimensionless applied curvature
wetting phase saturation

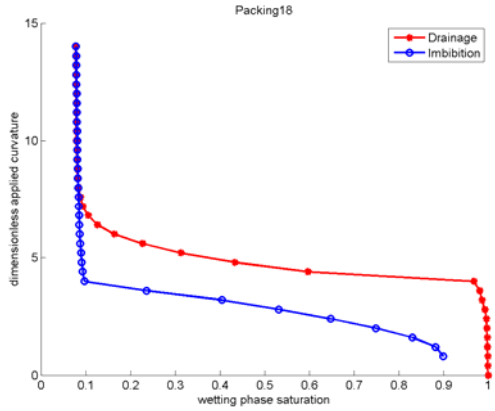
Packing18
Drainage
Imbibition
dimensionless applied curvature
wetting phase saturation

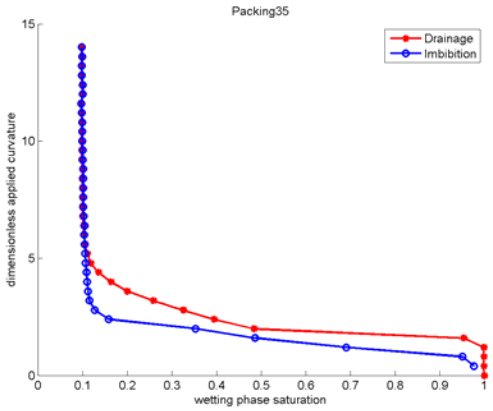
Packing35
Drainage
Imbibition
dimensionless applied curvature
wetting phase saturation

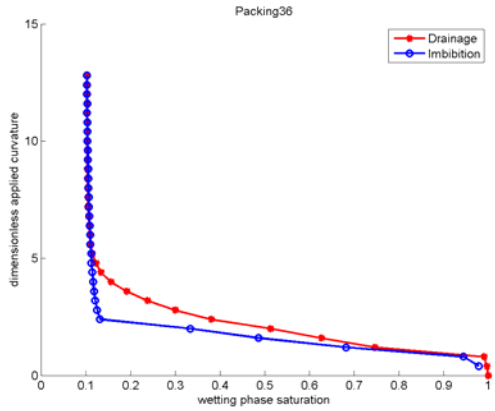
Packing36
Drainage
Imbibition
dimensionless applied curvature
wetting phase saturation

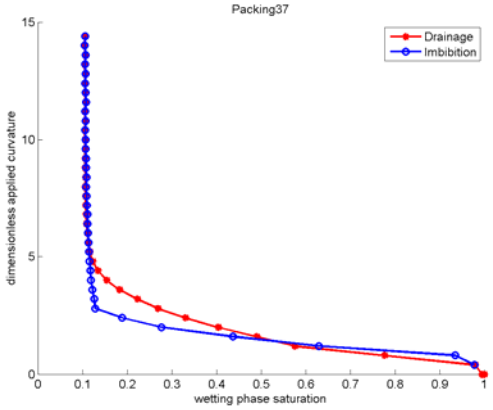
Packing37
Drainage
Imbibition
dimensionless applied curvature
wetting phase saturation

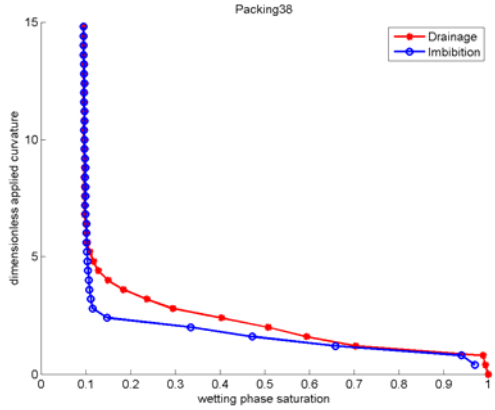
Packing38
Drainage
Imbibition
dimensionless applied curvature
wetting phase saturation

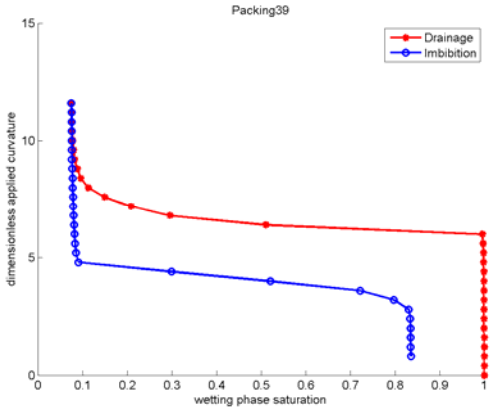
Packing39
Drainage
Imbibition
dimensionless applied curvature
wetting phase saturation

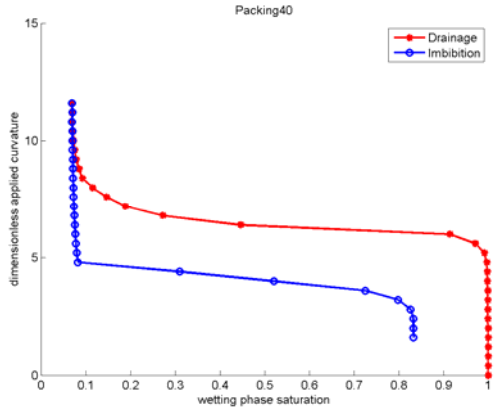
Packing40
Drainage
Imbibition
dimensionless applied curvature
wetting phase saturation

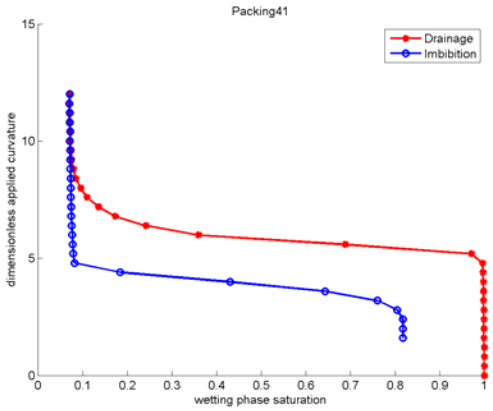
Packing41
Drainage
Imbibition
dimensionless applied curvature
wetting phase saturation

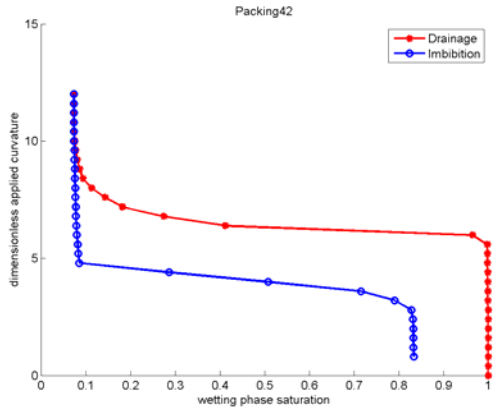
Packing42
Drainage
Imbibition
dimensionless applied curvature
wetting phase saturation

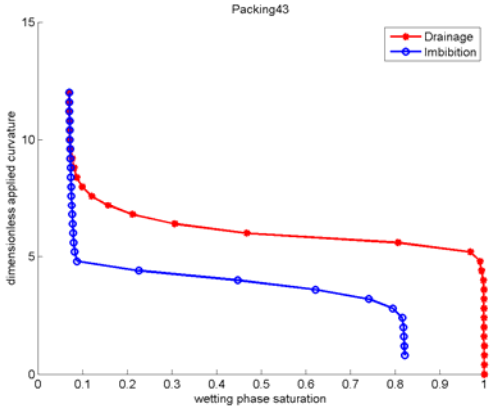
Packing43
Drainage
Imbibition
dimensionless applied curvature
wetting phase saturation

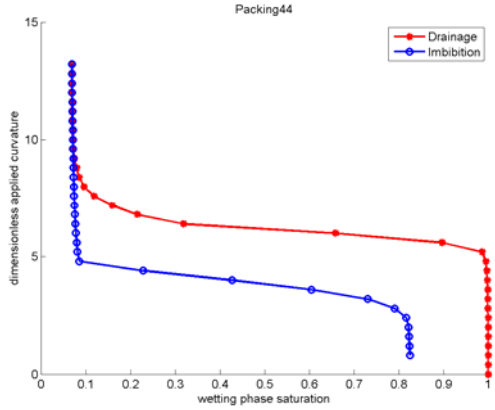
Packing44
Drainage
Imbibition
dimensionless applied curvature
wetting phase saturation

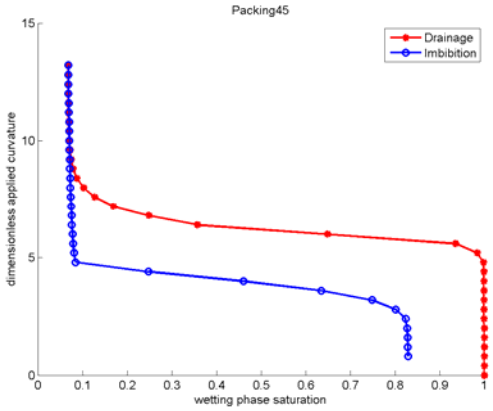
Packing45
Drainage
Imbibition
dimensionless applied curvature
wetting phase saturation

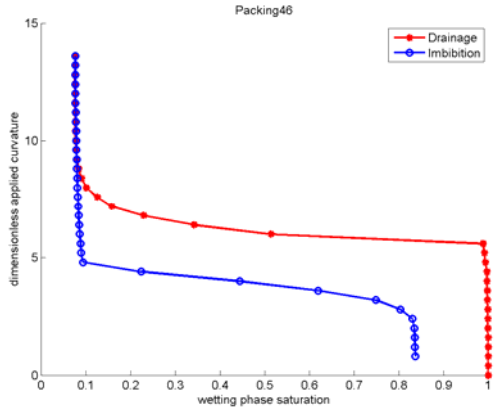
Packing46
Drainage
Imbibition
dimensionless applied curvature
wetting phase saturation

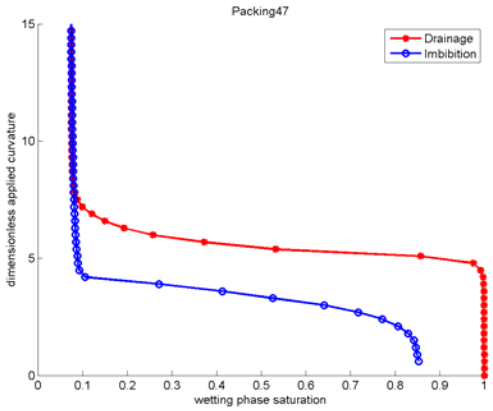
Packing47
Drainage
Imbibition
dimensionless applied curvature
wetting phase saturation

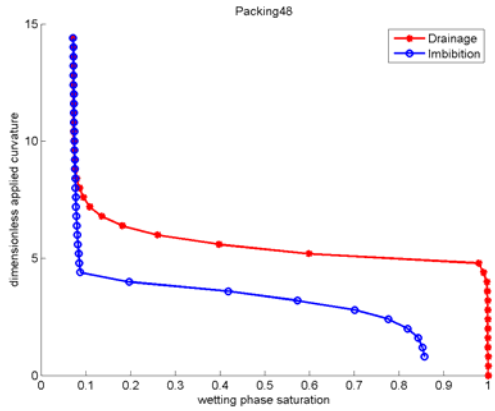
Packing48
Drainage
Imbibition
dimensionless applied curvature
wetting phase saturation

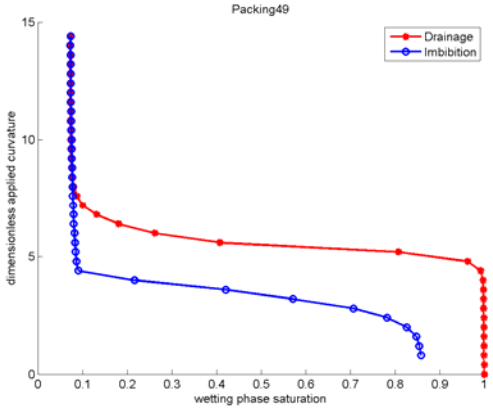
Packing49
Drainage
Imbibition
dimensionless applied curvature
wetting phase saturation

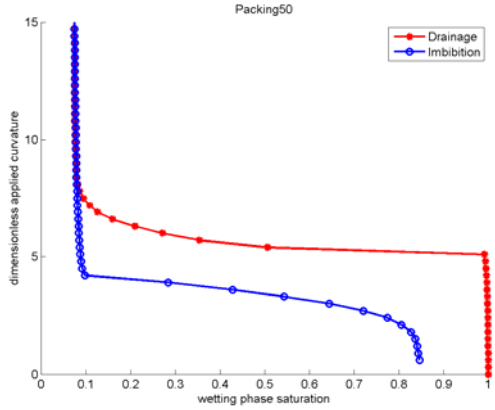
Packing50
Drainage
Imbibition
dimensionless applied curvature
wetting phase saturation

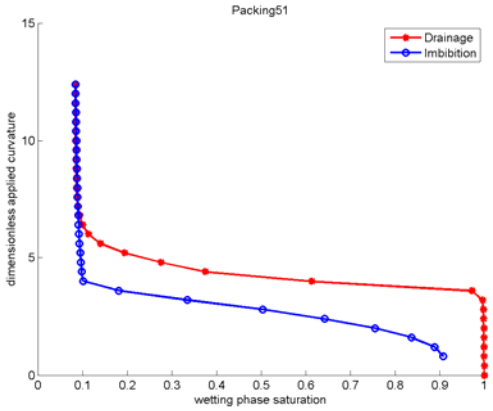
Packing51
Drainage
Imbibition
dimensionless applied curvature
wetting phase saturation

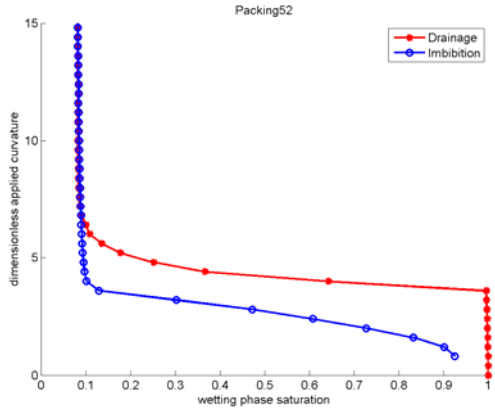
Packing52
Drainage
Imbibition
dimensionless applied curvature
wetting phase saturation

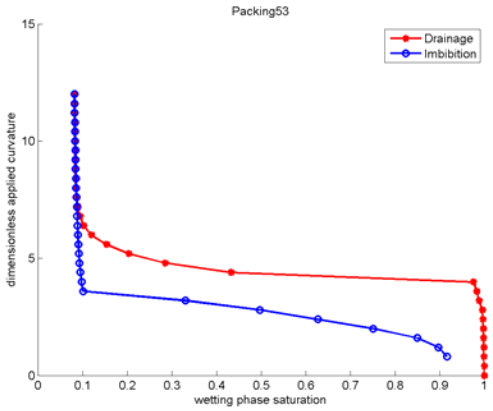
Packing53
Drainage
Imbibition
dimensionless applied curvature
wetting phase saturation

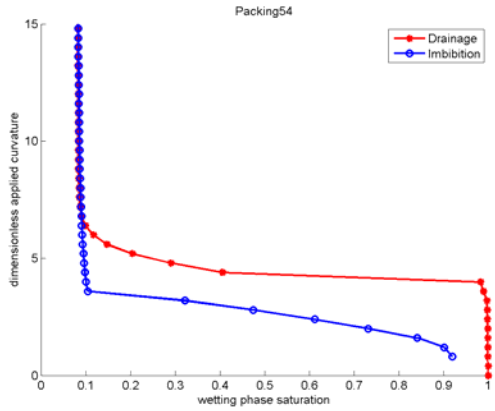
Packing54
Drainage
Imbibition
dimensionless applied curvature
wetting phase saturation

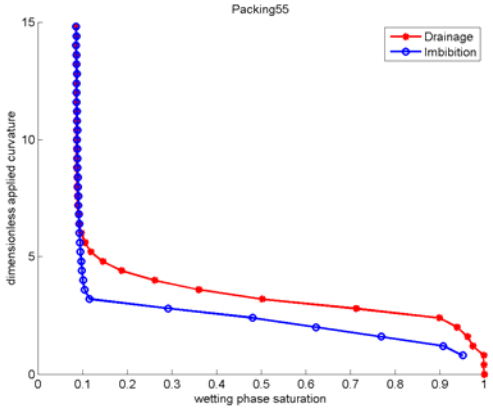
Packing55
Drainage
Imbibition
dimensionless applied curvature
wetting phase saturation

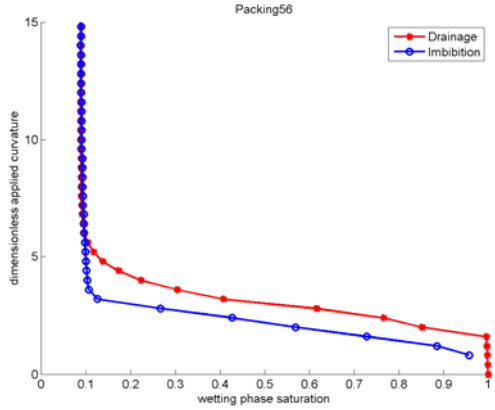
Packing56
Drainage
Imbibition
dimensionless applied curvature
wetting phase saturation

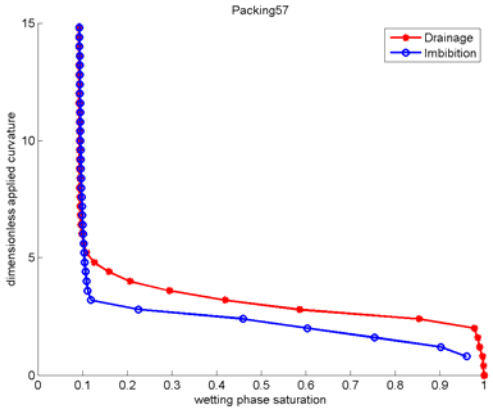
Packing57
Drainage
Imbibition
dimensionless applied curvature
wetting phase saturation

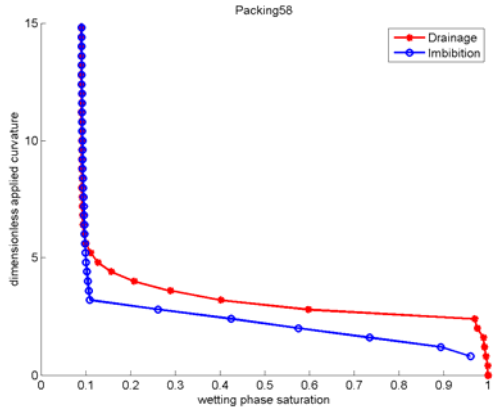
Packing58
Drainage
Imbibition
dimensionless applied curvature
wetting phase saturation

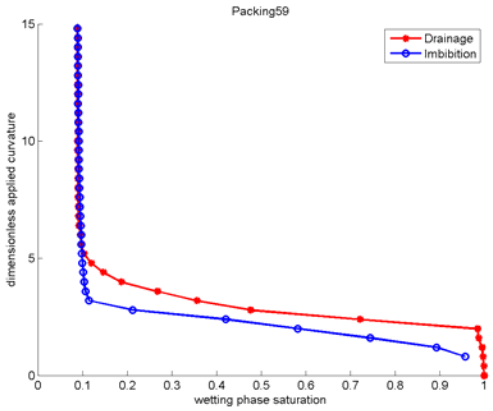
Packing59
Drainage
Imbibition
dimensionless applied curvature
wetting phase saturation

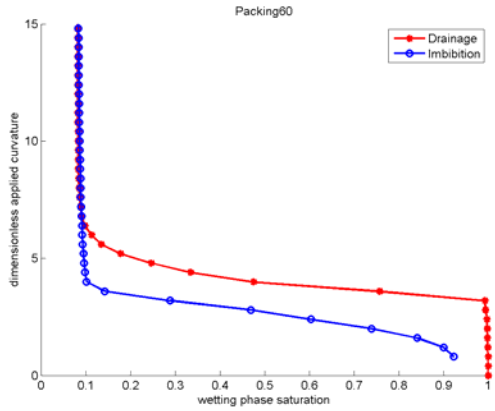
Packing60
Drainage
Imbibition
dimensionless applied curvature
wetting phase saturation

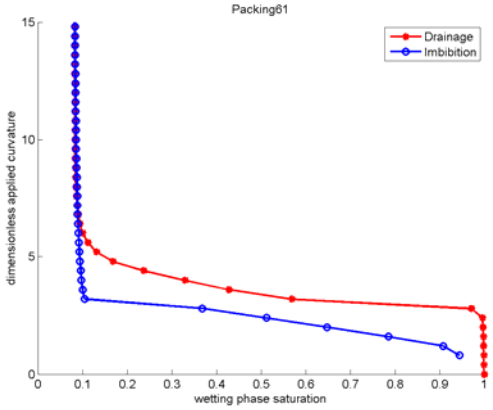
Packing61
Drainage
Imbibition
dimensionless applied curvature
wetting phase saturation

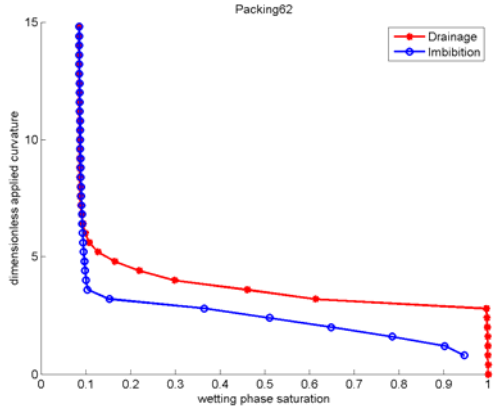
Packing62
Drainage
Imbibition
dimensionless applied curvature
wetting phase saturation

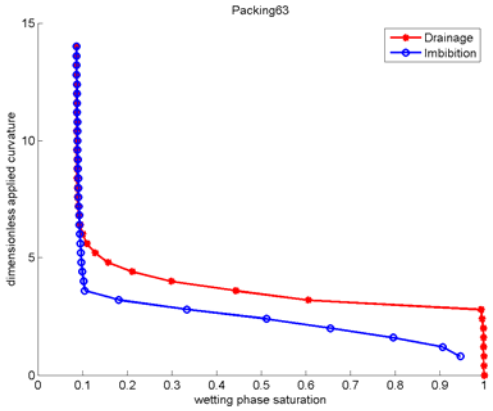
Packing63
Drainage
Imbibition
dimensionless applied curvature
wetting phase saturation

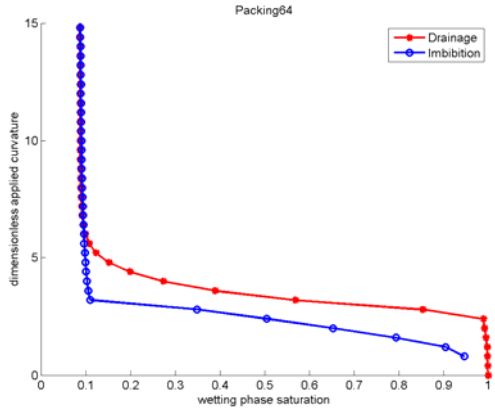
Packing64
Drainage
Imbibition
dimensionless applied curvature
wetting phase saturation

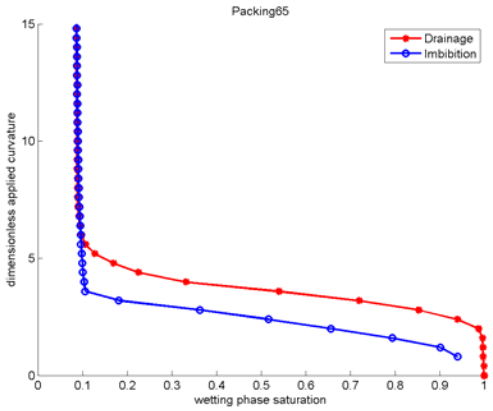
Packing65
Drainage
Imbibition
dimensionless applied curvature
wetting phase saturation

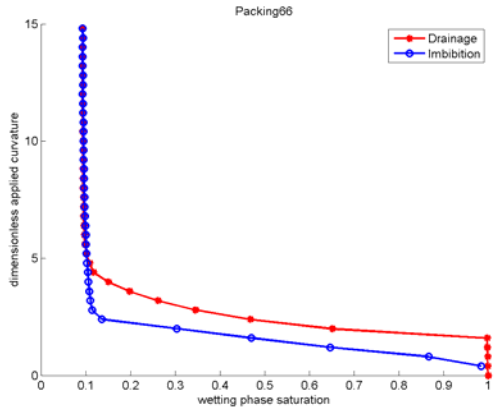
Packing66
Drainage
Imbibition
dimensionless applied curvature
wetting phase saturation

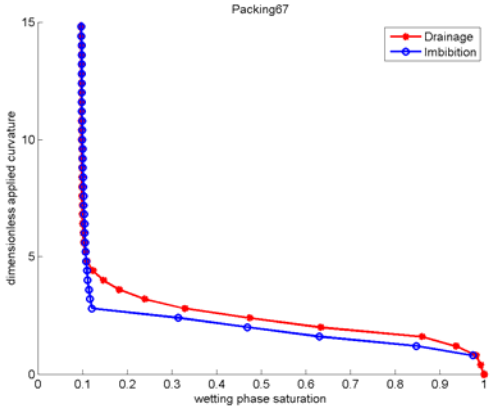
Packing67
Drainage
Imbibition
dimensionless applied curvature
wetting phase saturation

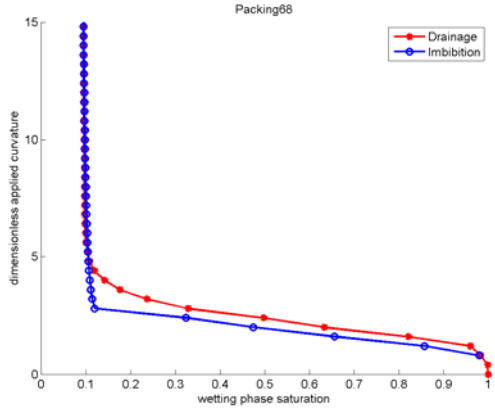
Packing68
Drainage
Imbibition
dimensionless applied curvature
wetting phase saturation

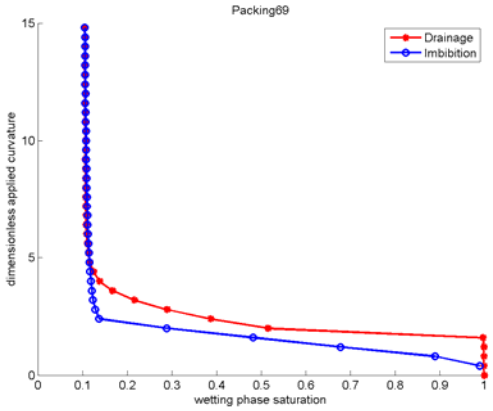
Packing69
Drainage
Imbibition
dimensionless applied curvature
wetting phase saturation

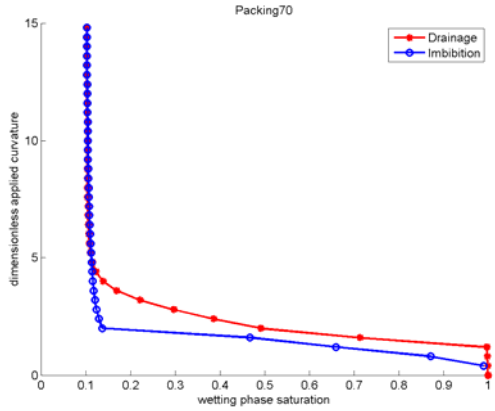
Packing70
Drainage
Imbibition
dimensionless applied curvature
wetting phase saturation

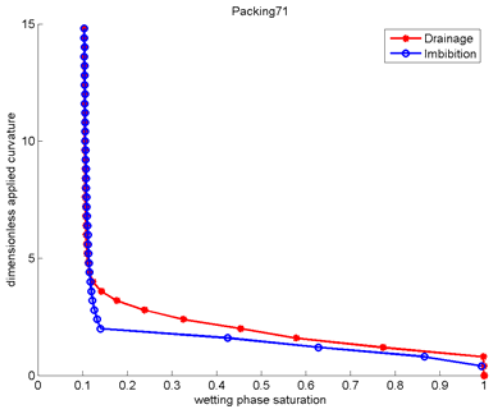
Packing71
Drainage
Imbibition
dimensionless applied curvature
wetting phase saturation

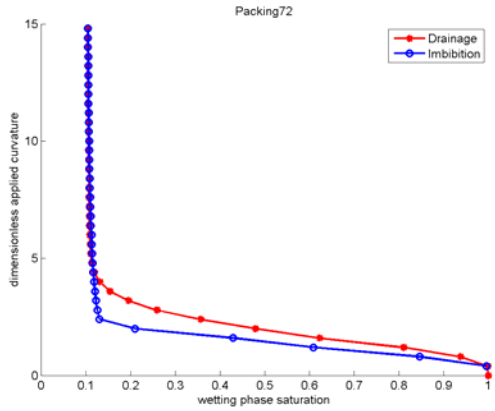
Packing72
Drainage
Imbibition
dimensionless applied curvature
wetting phase saturation

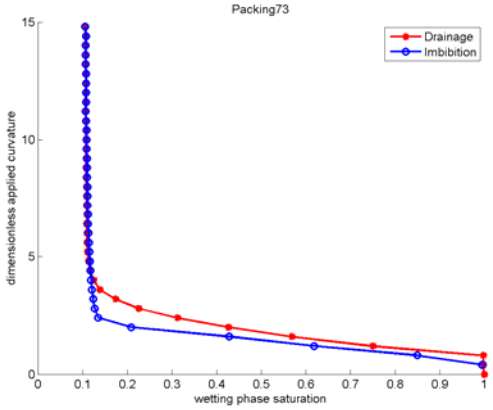
Packing73
Drainage
Imbibition
dimensionless applied curvature
wetting phase saturation

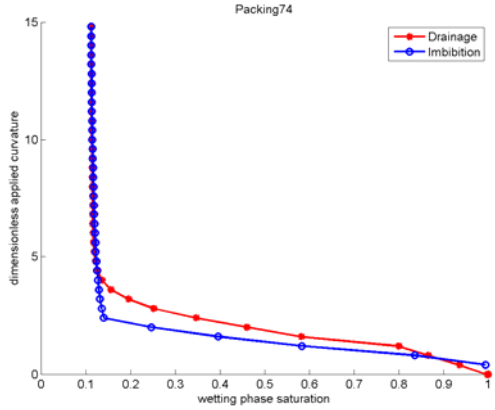
Packing74
Drainage
Imbibition
dimensionless applied curvature
wetting phase saturation

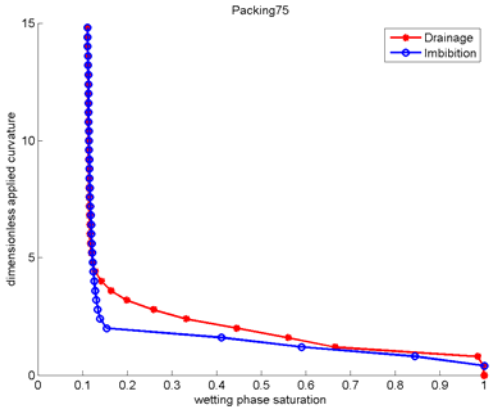
Packing75
Drainage
Imbibition
dimensionless applied curvature
wetting phase saturation

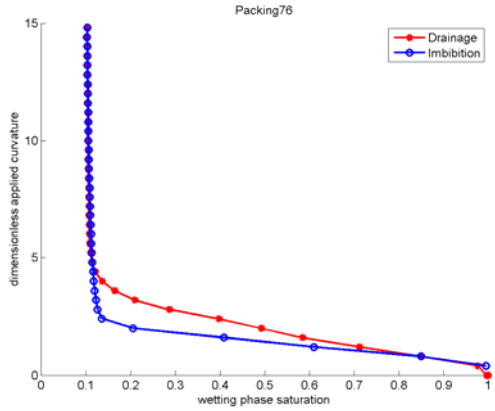
Packing76
Drainage
Imbibition
dimensionless applied curvature
wetting phase saturation

Appendix C. Network modeling of drainage and imbibition by periodic boundary condition

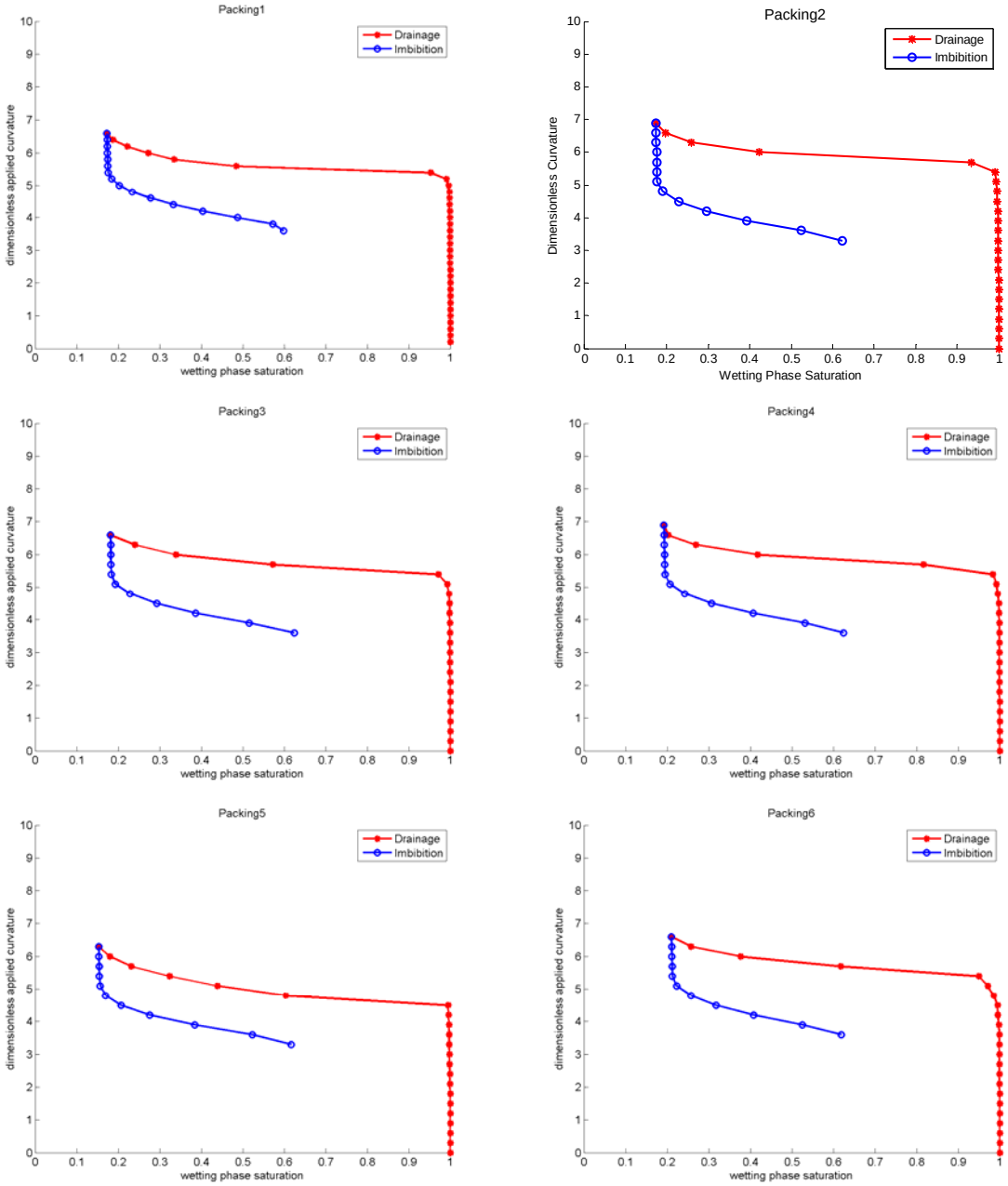

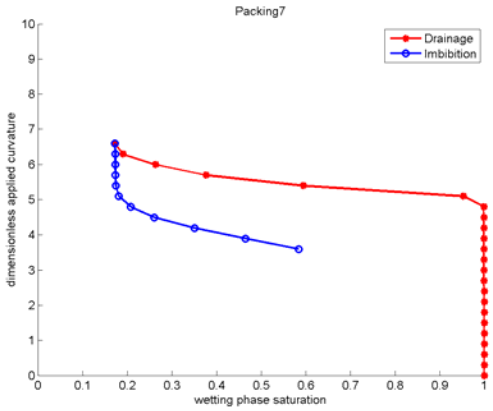
Packing7
Drainage
Imbibition
dimensionless applied curvature
wetting phase saturation

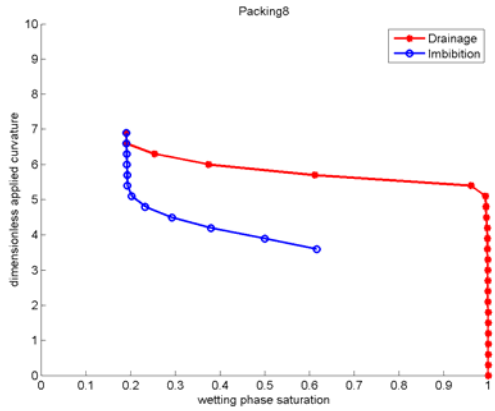
Packing8
Drainage
Imbibition
dimensionless applied curvature
wetting phase saturation

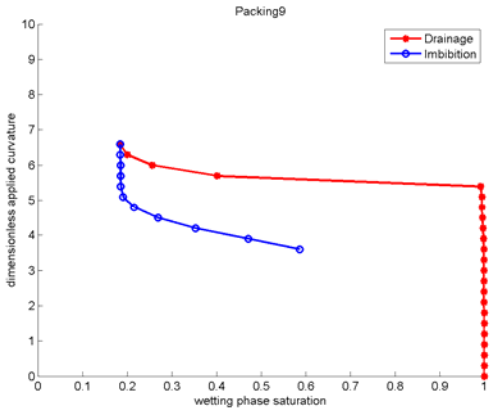
Packing9
Drainage
Imbibition
dimensionless applied curvature
wetting phase saturation

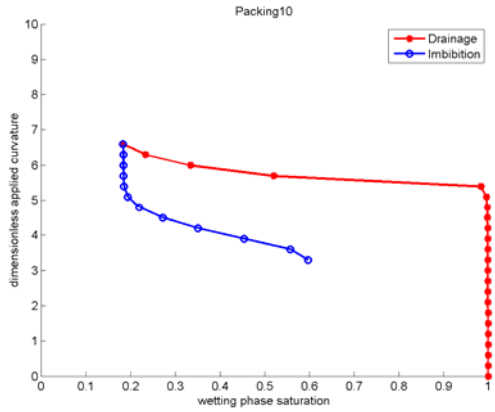
Packing10
Drainage
Imbibition
dimensionless applied curvature
wetting phase saturation

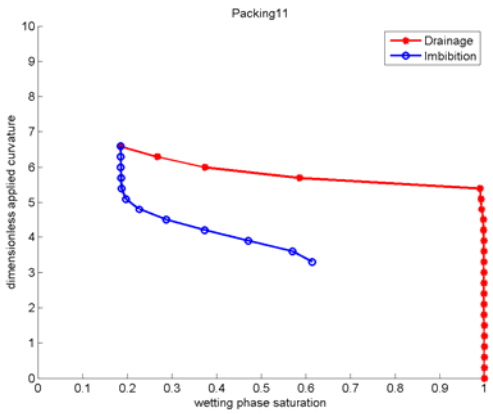
Packing11
Drainage
Imbibition
dimensionless applied curvature
wetting phase saturation

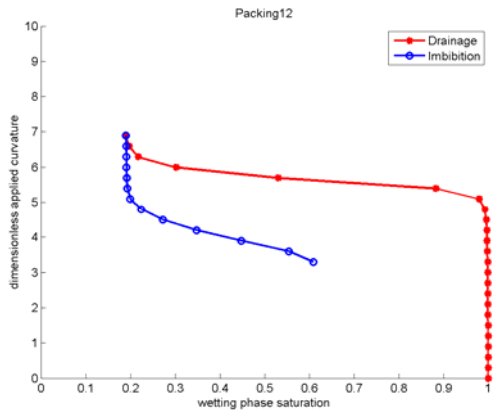
Packing12
Drainage
Imbibition
dimensionless applied curvature
wetting phase saturation

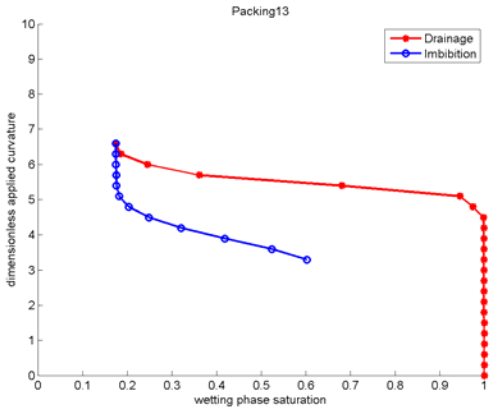
Packing13
Drainage
Imbibition
dimensionless applied curvature
wetting phase saturation

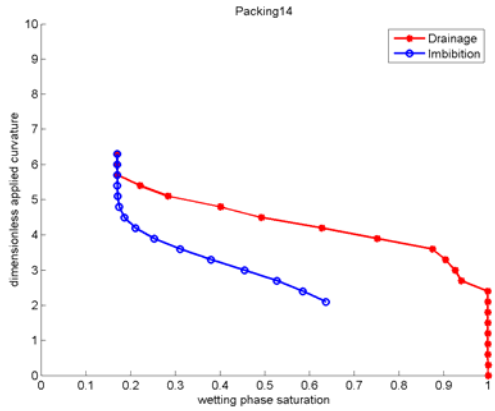
Packing14
Drainage
Imbibition
dimensionless applied curvature
wetting phase saturation

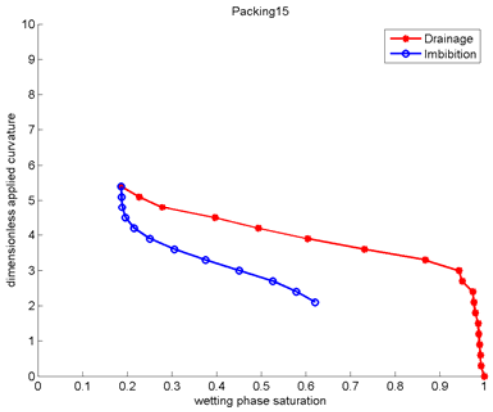
Packing15
Drainage
Imbibition
dimensionless applied curvature
wetting phase saturation

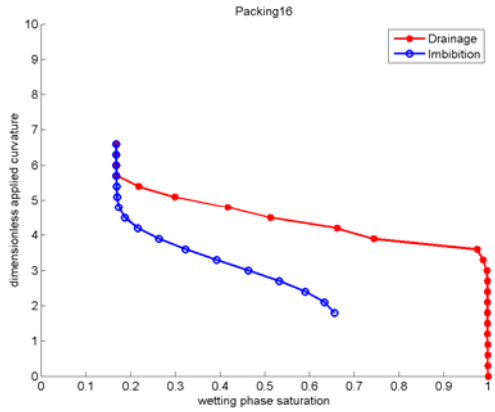
Packing16
Drainage
Imbibition
dimensionless applied curvature
wetting phase saturation

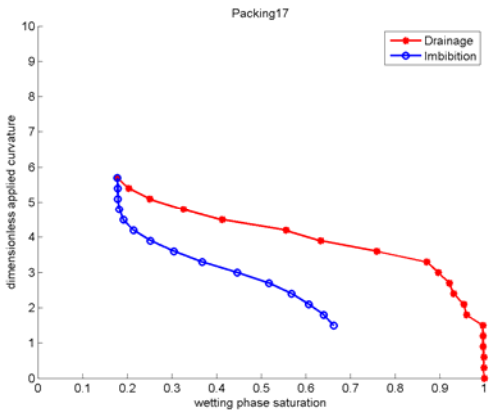
Packing17
Drainage
Imbibition
dimensionless applied curvature
wetting phase saturation

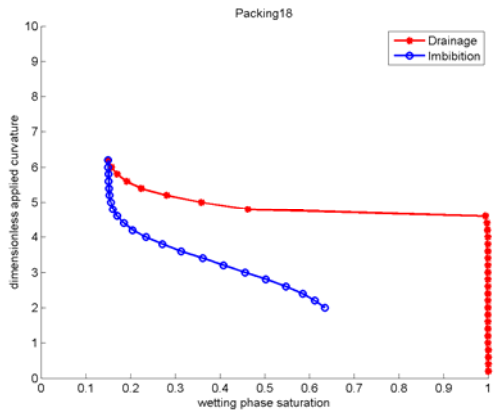
Packing18
Drainage
Imbibition
dimensionless applied curvature
wetting phase saturation

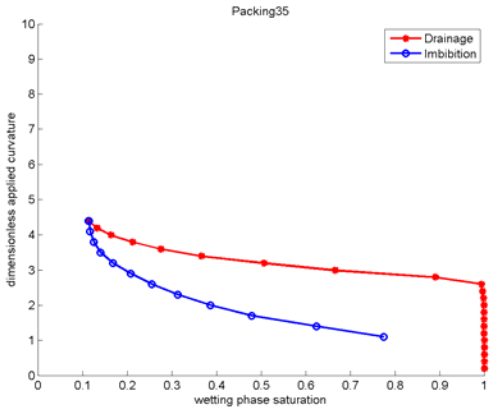
Packing35
Drainage
Imbibition
dimensionless applied curvature
wetting phase saturation

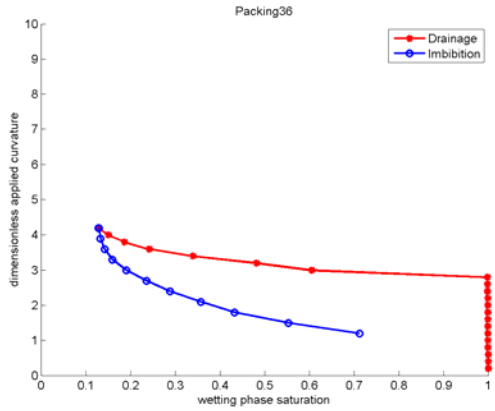
Packing36
Drainage
Imbibition
dimensionless applied curvature
wetting phase saturation

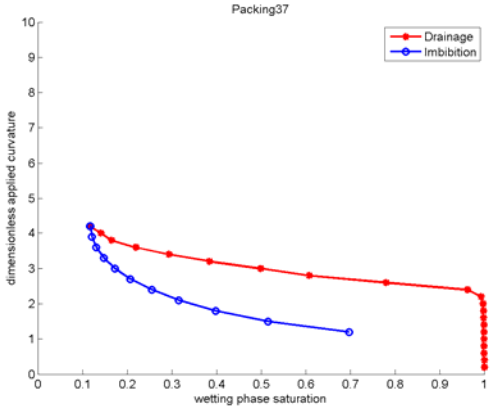
Packing37
Drainage
Imbibition
dimensionless applied curvature
wetting phase saturation

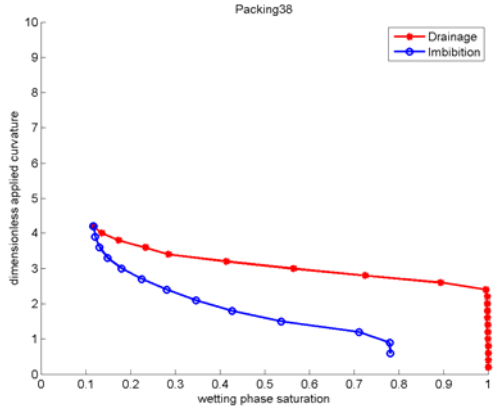
Packing38
Drainage
Imbibition
dimensionless applied curvature
wetting phase saturation

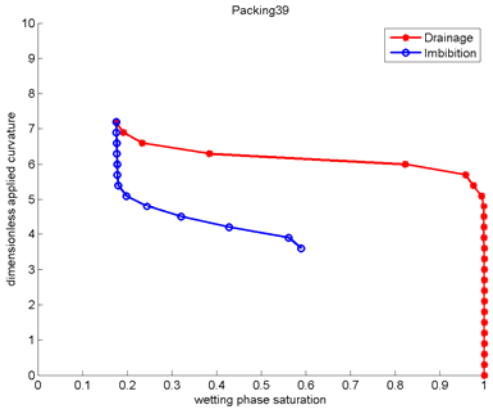
Packing39
Drainage
Imbibition
dimensionless applied curvature
wetting phase saturation

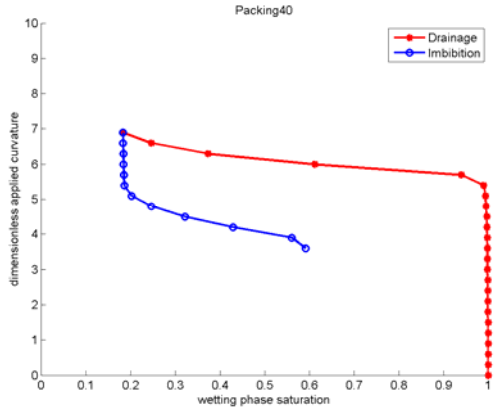
Packing40
Drainage
Imbibition
dimensionless applied curvature
wetting phase saturation

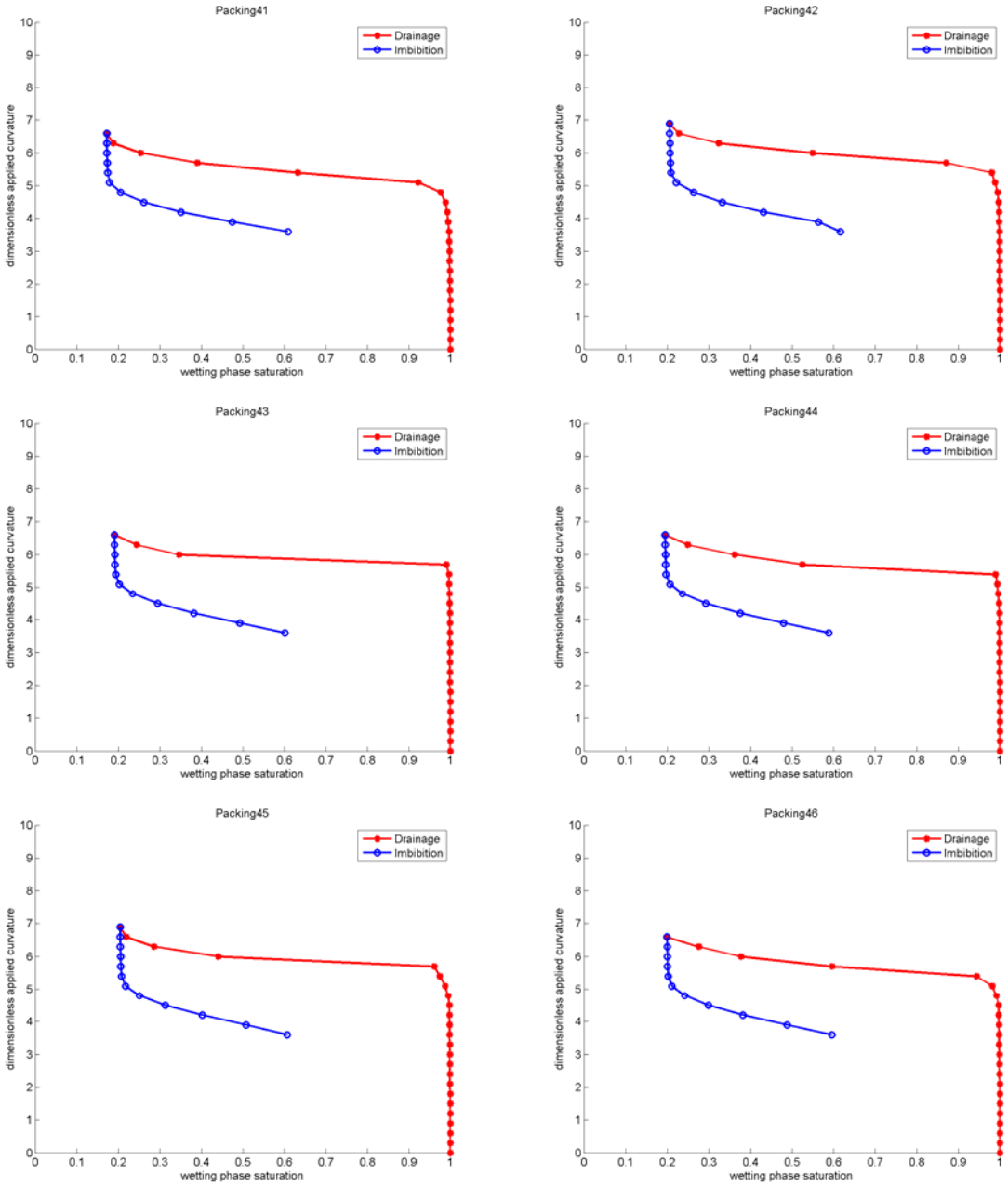
Packing41
Drainage
Imbibition
dimensionless applied curvature
wetting phase saturation
Packing42
Drainage
Imbibition
dimensionless applied curvature
wetting phase saturation
Packing43
Drainage
Imbibition
dimensionless applied curvature
wetting phase saturation
Packing44
Drainage
Imbibition
dimensionless applied curvature
wetting phase saturation
Packing45
Drainage
Imbibition
dimensionless applied curvature
wetting phase saturation
Packing46
Drainage
Imbibition
dimensionless applied curvature
wetting phase saturation

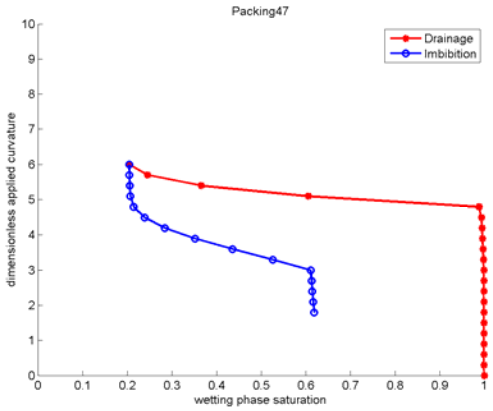
Packing47
Drainage
Imbibition
dimensionless applied curvature
wetting phase saturation

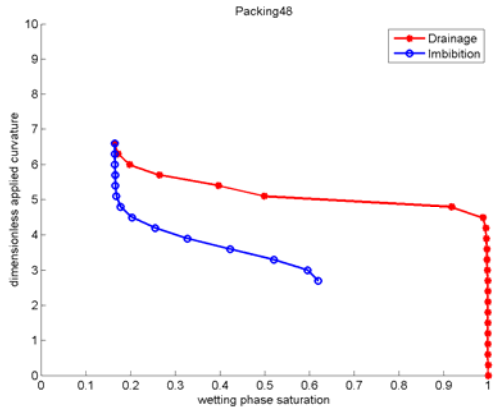
Packing48
Drainage
Imbibition
dimensionless applied curvature
wetting phase saturation

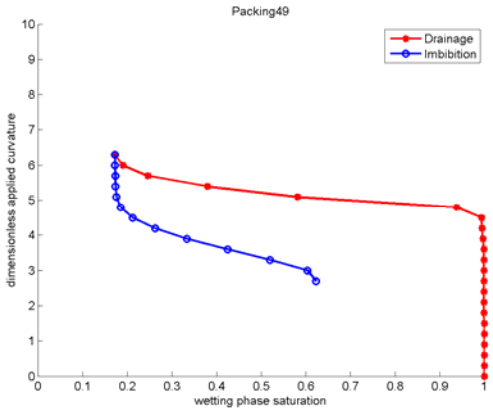
Packing49
Drainage
Imbibition
dimensionless applied curvature
wetting phase saturation

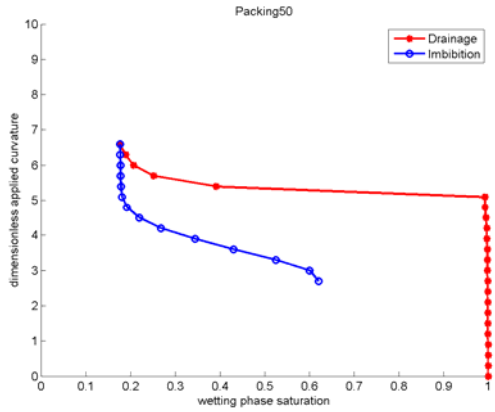
Packing50
Drainage
Imbibition
dimensionless applied curvature
wetting phase saturation

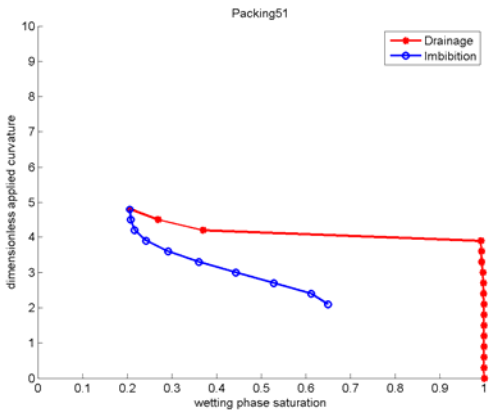
Packing51
Drainage
Imbibition
dimensionless applied curvature
wetting phase saturation

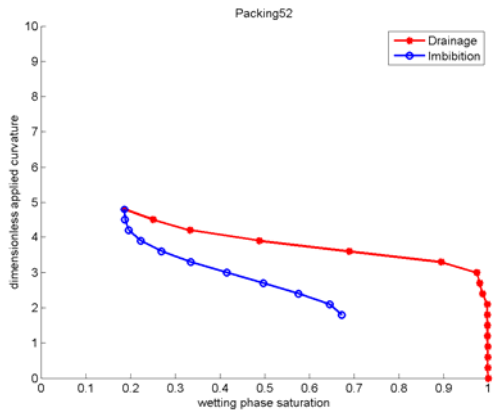
Packing52
Drainage
Imbibition
dimensionless applied curvature
wetting phase saturation

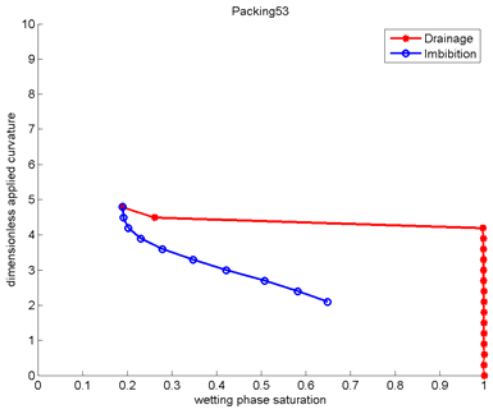
Packing53
Drainage
Imbibition
dimensionless applied curvature
wetting phase saturation

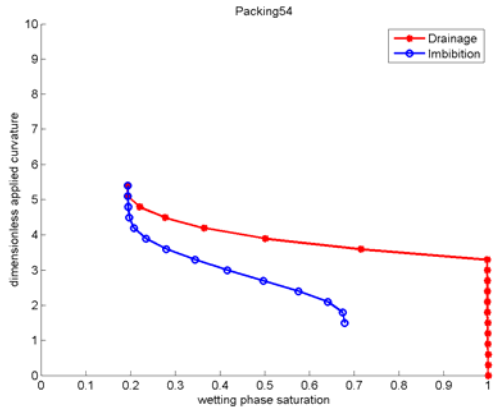
Packing54
Drainage
Imbibition
dimensionless applied curvature
wetting phase saturation

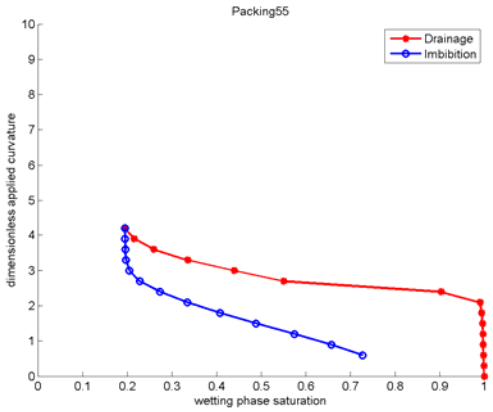
Packing55
Drainage
Imbibition
dimensionless applied curvature
wetting phase saturation

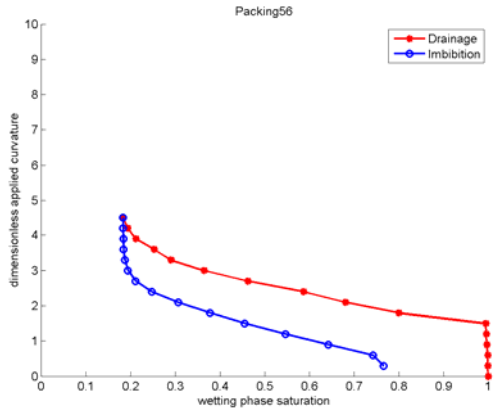
Packing56
Drainage
Imbibition
dimensionless applied curvature
wetting phase saturation

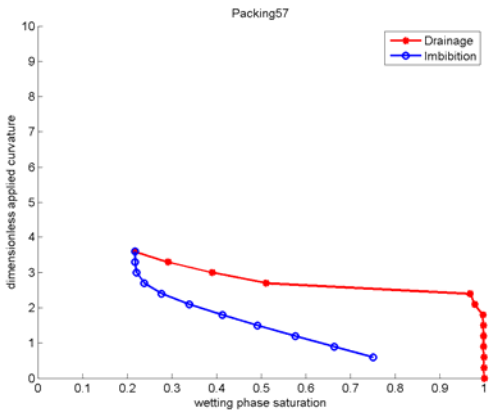
Packing57
Drainage
Imbibition
dimensionless applied curvature
wetting phase saturation

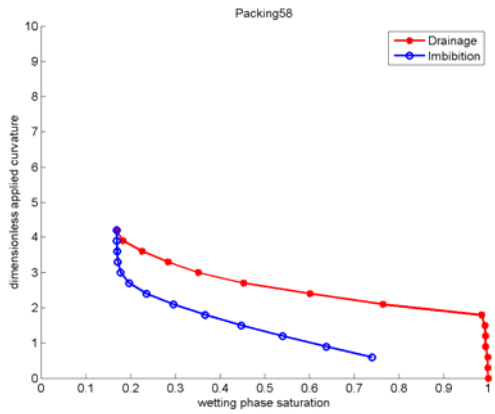
Packing58
Drainage
Imbibition
dimensionless applied curvature
wetting phase saturation

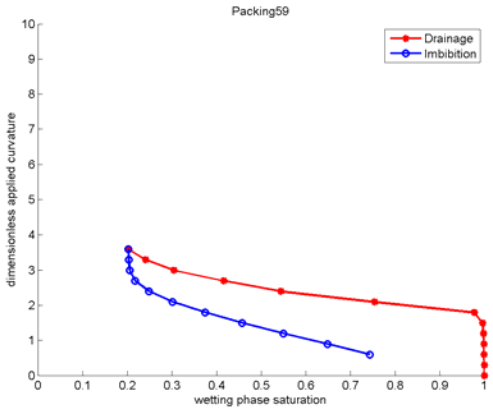
Packing59
Drainage
Imbibition
dimensionless applied curvature
wetting phase saturation

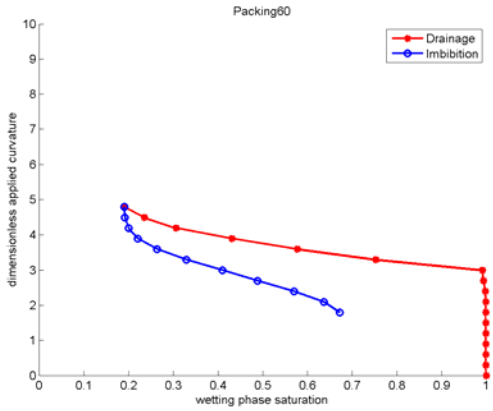
Packing60
Drainage
Imbibition
dimensionless applied curvature
wetting phase saturation

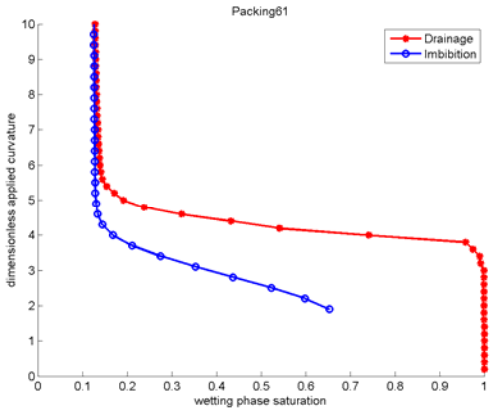
Packing61
Drainage
Imbibition
dimensionless applied curvature
wetting phase saturation

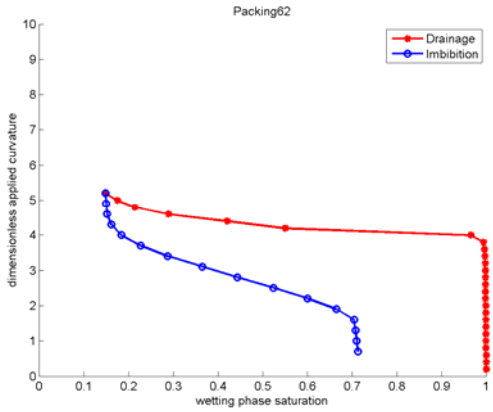
Packing62
Drainage
Imbibition
dimensionless applied curvature
wetting phase saturation

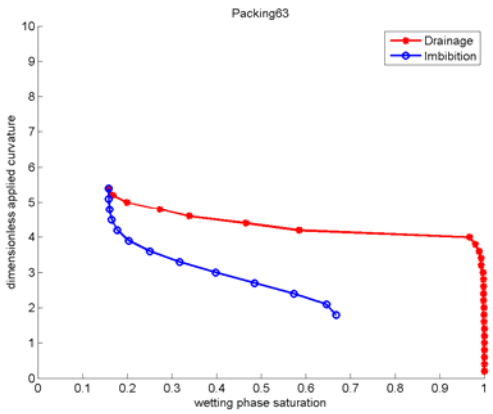
Packing63
Drainage
Imbibition
dimensionless applied curvature
wetting phase saturation

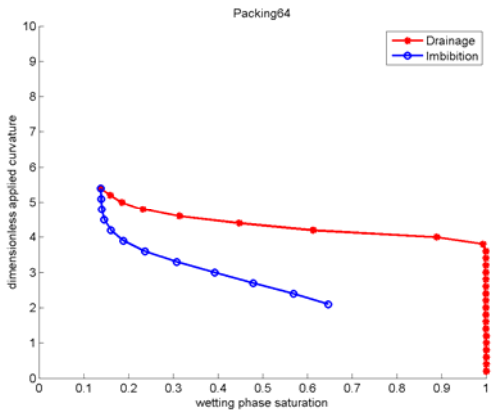
Packing64
Drainage
Imbibition
dimensionless applied curvature
wetting phase saturation

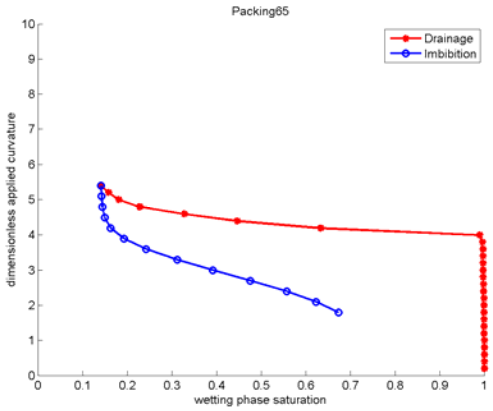
Packing65
Drainage
Imbibition
dimensionless applied curvature
wetting phase saturation

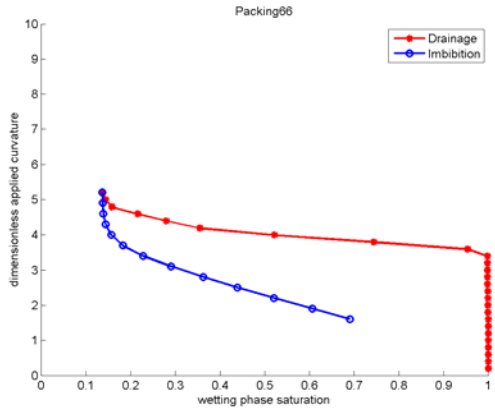
Packing66
Drainage
Imbibition
dimensionless applied curvature
wetting phase saturation

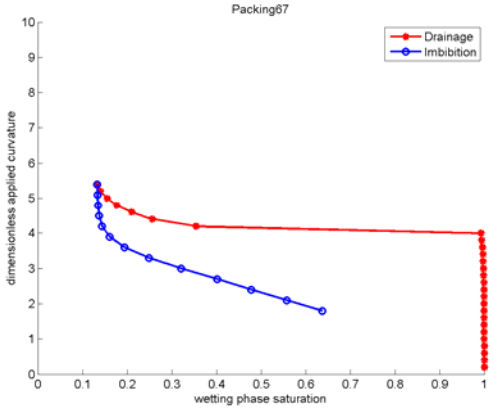
Packing67
Drainage
Imbibition
dimensionless applied curvature
wetting phase saturation

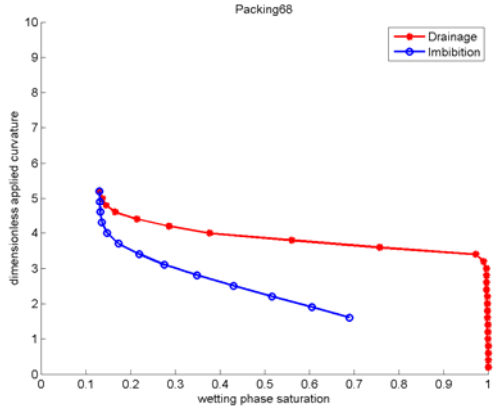
Packing68
Drainage
Imbibition
dimensionless applied curvature
wetting phase saturation

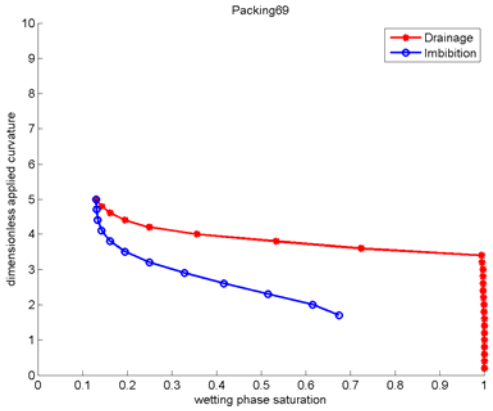
Packing69
Drainage
Imbibition
dimensionless applied curvature
wetting phase saturation

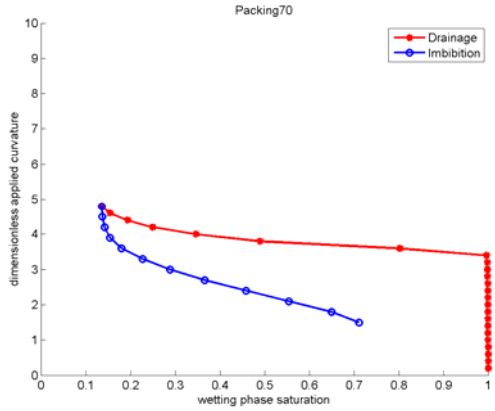
Packing70
Drainage
Imbibition
dimensionless applied curvature
wetting phase saturation

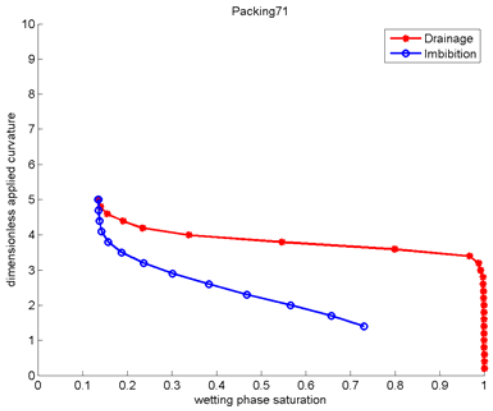
Packing71
Drainage
Imbibition
dimensionless applied curvature
wetting phase saturation

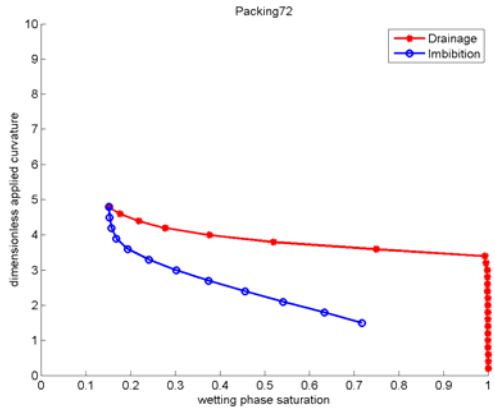
Packing72
Drainage
Imbibition
dimensionless applied curvature
wetting phase saturation

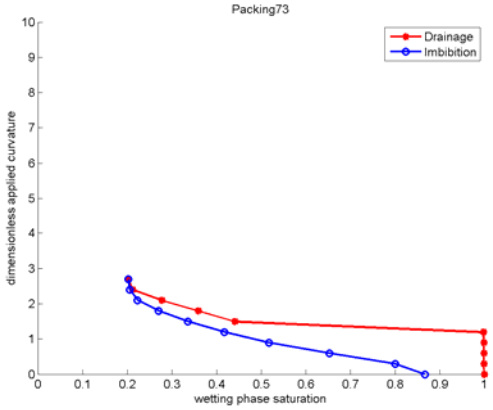
Packing73
Drainage
Imbibition
dimensionless applied curvature
wetting phase saturation

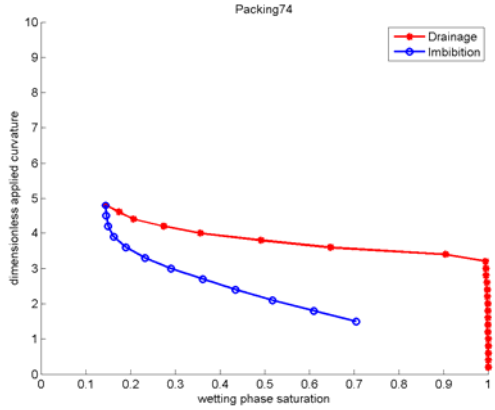
Packing74
Drainage
Imbibition
dimensionless applied curvature
wetting phase saturation

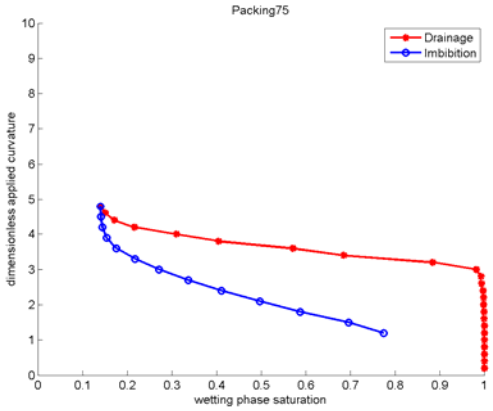
Packing75
Drainage
Imbibition
dimensionless applied curvature
wetting phase saturation

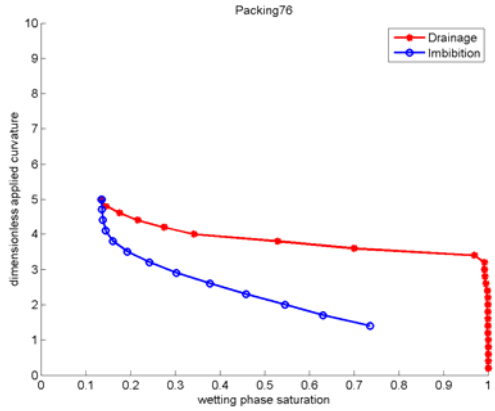
Packing76
Drainage
Imbibition
dimensionless applied curvature
wetting phase saturation

Reference

Aker, E., JØrgen MÅlØy, K., Hansen, A., and Batrouni, G., 1998, A Two-Dimensional Network Simulator for Two-Phase Flow in Porous Media: Transport in Porous Media, v. 32, no. 2, p. 163-186.

Al-Gharbi, M., and Blunt, M., 2005, Dynamic network modeling of two-phase drainage in porous media: Physical Review E, v. 71, no. 1, p. 016308.

Al-Raoush, R., and Willson, C., 2005, A pore-scale investigation of a multiphase porous media system: Journal of Contaminant Hydrology, v. 77, no. 1-2, p. 67-89.

Anderson, B., Hancock, S., Wilson, S., Enger, C., Collett, T., Boswell, R., and Hunter, R., 2011, Formation pressure testing at the Mount Elbert Gas Hydrate Stratigraphic Test Well, Alaska North Slope: Operational summary, history matching, and interpretations: Marine and Petroleum Geology, v. 28, no. 2, p. 478-492.

Anderson, B., Kurihara, M., White, M., Moridis, G., Wilson, S., Pooladi-Darvish, M., Gaddipati, M., Masuda, Y., Collett, T., Hunter, R., Narita, H., Rose, K., and Boswell, R., 2011, Regional long-term production modeling from a single well test, Mount Elbert Gas Hydrate Stratigraphic Test Well, Alaska North Slope: Marine and Petroleum Geology, v. 28, no. 2, p. 493-501.

Anderson, R., Llamedo, M., Tohidi, B., and Burgass, R., 2003, Characteristics of clathrate hydrate equilibria in mesopores and interpretation of experimental data: The Journal of Physical Chemistry B, v. 107, no. 15, p. 3500-3506.

Archer, D., 2007, Methane hydrate stability and anthropogenic climate change: Biogeosciences Discussions, v. 4, no. 2, p. 993-1057.

BáEz, L., and Clancy, P., 1994, Computer simulation of the crystal growth and dissolution of natural gas hydrates: Annals of the New York Academy of Sciences, v. 715, no. 1, p. 177-186.

Baldwin, C.A., Sederman, A.J., Mantle, M.D., Alexander, P., and Gladden, L.F., 1996, Determination and Characterization of the Structure of a Pore Space from 3D Volume Images: Journal of Colloid and Interface Science, v. 181, no. 1, p. 79-92.

Bangs, N., Hornbach, M., Moore, G., and Park, J., 2010, Massive methane release triggered by seafloor erosion offshore southwestern Japan: Geology, v. 38, no. 11, p. 1019-1022.

Bauer, A., Pratt, R., Weber, M., Ryberg, T., Haberland, C., and Shimizu, S., 2005, Mallik 2002 cross-well seismic experiment: project design, data acquisition, and modelling studies: Geological Survey of Canada, Scientific results frmo the Mallik 2002 Gas hydrate Production Research Well Program, Mackenzie Delta, Northwest Territories, Canada.

Behseresht, J., 2008, Infinite-acting physically representative networks for capillarity-controlled displacements: The University of Texas at Austin.

Behseresht, J. Peng, Y., Bryant S., Winters. W., 2009a, Sedimentological control on arctic gas-hydrate-bearing deposits. AGU fall meeting. San Fransisco, California.

Behseresht, J., Bryant, S., and Sepehrnoori, K., 2009b, Infinite-acting physically representative networks for capillarity-controlled displacements: SPE Journal, v. 14, no. 4, p. 568-578.

Behseresht, J., Bryant, S., 2011, Sedimentological control on saturation distriubtion in arctic gas-hydrate-bearing deposits. Proceedings of 7th ICGH, Edinburgh, Scotland.

Bloomenthal, J., 1988, Polygonization of implicit surfaces: Computer Aided Geometric Design, v. 5, p. 341–355.

Blunt, M., 2001, Flow in porous media -- pore-network models and multiphase flow: Current Opinion in Colloid & Interface Science, v. 6, no. 3, p. 197-207.

Bohrmann, G., Kuhs, W., Klapp, S., Techmer, K., Klein, H., Murshed, M., and Abegg, F., 2007, Appearance and preservation of natural gas hydrate from Hydrate Ridge sampled during ODP Leg 204 drilling: Marine Geology, v. 244, no. 1-4, p. 1-14.

Bohrmann, G., and Torres, M., 2006, Gas hydrate in marine sediments, *in* Marine Geochemistry, Springer, p. 481-512.

Bourbie, T., and Zinszner, B., 1985, Hydraulic and Acoustic Properties as a Function of Porosity in Fontainebleau Sandstone: Journal of Geophysical Research, v. 90, no. B13, p. 11524.

Bryant, S., and Blunt, M., 1992a, Prediction of relative permeability in simple porous media: Physical Review A, v. 46, no. 4, p. 2004-2011.

Bryant, S., Cade, C., and Mellor, D., 1993, Permeability prediction from geologic models: AAPG Bulletin, v. 77, no. 8, p. 1338-1350.

Bryant, S., and Johnson, A., 2003, Wetting phase connectivity and irreducible saturation in simple granular media: Journal of Colloid and Interface Science, v. 263, no. 2, p. 572-579.

Bryant, S., Mellor, D., and Cade, C., 1993, Physically representative network models of transport in porous media: AIChE Journal, v. 39, no. 3, p. 387-396.

Causin, E., Rochon, J., and Marzorati, D., 1990, Field measurements of remaining Oil saturation, *in* Proceedings of SPE/DOE Enhanced Oil Recovery Symposium.

Chevallier, J., Trehu, A., Bangs, N., Johnson, J., and Meyer, H., 2005, Seismic sequence stratigraphy and tectonic evolution of Southern Hydrate Ridge, *in* Proceedings of the Ocean Drilling Program, Scientific Results.

Clennell, M.B., Hovland, M., Booth, J.S., Henry, P., and Winters, W.J., 1999, Formation of natural gas hydrates in marine sediments 1. Conceptual model of gas hydrate growth conditioned by host sediment properties: Journal of Geophysical Research, v. 104, no. B10, p. PP. 22,985-23,003.

Collett, T., Johnson, A., Knapp, C., and Boswell, R., 2010, Natural gas hydrate: A review, *in* Natural gas hydrate --- Energy resource potential and associated geologic hazards, American Association of Petroleum Geologists, p. 146-219.

Collett, T., and Ladd, J., 2000, Detection of gas hydrate with downhole logs and assessment of gas hydrate concentrations (saturations) and gas volumes on the Blake Ridge with electrical resistivity log data., *in* Proceddings of the Ocean Drilling Program, Scientific Results, College Station, TX, p. 391-402.

Collett, T., and Lee, M., 2005, Electrical-resistivity well-log analysis of gas hydrate saturations in the JAPEX/JNOC/GSC et al. Mallik 5L-38 gas hydrate production rsearch well: Scientific results frmo the Mallik 2002 Gas hydrate Production Research Well Program, Mackenzie Delta, Northwest Territories, Canada.

Cook, A., Goldberg, D., and Kleinberg, R., 2008, Fracture-controlled gas hydrate systems in the northern Gulf of Mexico: Marine and Petroleum Geology, v. 25, no. 9, p. 932-941.

Cooper, A., and Hart, P., 2002, High-resolution seismic-reflection investigation of the northern Gulf of Mexico gas-hydrate-stability zone: Marine and Petroleum Geology, v. 19, no. 10, p. 1275-1293.

Dai, J., Snyder, F., Gillespie, D., Koesoemadinata, A., and Dutta, N., 2008, Exploration for gas hydrates in the deepwater, northern Gulf of Mexico: Part I. A seismic approach based on geologic model, inversion, and rock physics principles: Marine and Petroleum Geology, v. 25, no. 9, p. 830-844.

Dai, J., Banik, N., Gillespie, D., and Dutta, N., 2008, Exploration for gas hydrates in the deepwater, northern Gulf of Mexico: Part II. Model validation by drilling: Marine and Petroleum Geology, v. 25, no. 9, p. 845-859.

Dallimore, S., and Collett, T., 2005, Mallik 2002 - GSC Bulletin 585:Scientific results from the Mallik 2002 gas hydrate production well program

Davie, M., 2003, A steady state model for marine hydrate formation: Constraints on methane supply from pore water sulfate profiles: Journal of Geophysical Research, v. 108, no. B10.

Davie, M., and Buffett, B. A numerical model for the formation of gas hydrate below the seafloor: Journal of Geophysical Research, v. 106, no. B1, p. 497-514.

Deans, H., and Majoros, S., 1980, The single-well chemical tracer method for measuring residual oil saturation: Rice University,

Dickens, G., 2003, Rethinking the global carbon cycle with a large, dynamic and microbially mediated gas hydrate capacitor: Earth and Planetary Science Letters, v. 213, no. 3-4, p. 169-183.

Dickens, G., 2001, The potential volume of oceanic methane hydrates with variable external conditions: Organic Geochemistry, v. 32, no. 10, p. 1179-1193.

Dickens, G., and Quinby-Hunt, M., 1994, Methane hydrate stability in seawater: Geophysical Research Letters, v. 21, no. 19, p. 2115-2118.

van Dijke, M., and Sorbie, K., 2003, Pore-scale modelling of three-phase flow in mixed-wet porous media: multiple displacement chains: Journal of Petroleum Science and Engineering, v. 39, no. 3-4, p. 201-216.

Dong Lee, J., Susilo, R., and Englezos, P., 2005, Methane-ethane and methane-propane hydrate formation and decomposition on water droplets: Chemical Engineering Science, v. 60, no. 15, p. 4203-4212.

Dullien, F., Zarcone, C., Macdonald, I., Collins, A., and Bochard, R., 1989, The effects of surface roughness on the capillary pressure curves and the heights of capillary rise in glass bead packs: Journal of Colloid and Interface Science, v. 127, no. 2, p. 362-372.

Egeberg, P., and Dickens, G., 1999, Thermodynamic and pore water halogen constraints on gas hydrate distribution at ODP Site 997 (Blake Ridge): Chemical Geology, v. 153, no. 1-4, p. 53-79.

Erwin, D., 1993, The great Paleozoic crisis: life and death in the Permian: Columbia University Press.

Everett, D.H., 1961, The thermodynamics of frost damage to porous solids: Transactions of the Faraday Society, v. 57, p. 1541.

Fatt, I., 1956a, The network model of porous Media I. dapillary pressure characteristics: Transactions of the Society of Mining Engineers, v. 207, p. 144-159.

Fatt, I., 1956b, The network model of porous media II. dynamic properties of a single size tube network: Transactions of the Society of Mining Engineers, v. 207, p. 160-163.

Fatt, I., 1956c, The network model of porous media III. dynamic properties of networks with tube radius distribution: Transactions of the Society of Mining Engineers, v. 207, p. 164-181.

Finney, J., 1968, Random packings and the structure of the liquid state: University of London.

Flannery, B., Roberge, H., and D'Amico, K., 1987, Three-dimensional x-ray microtomography: Science, v. 237, no. 4821, p. 1439-1444.

Garg, S., Pritchett, J., Katoh, A., Baba, K., and Fujii, T., 2008, A mathematical model for the formation and dissociation of methane hydrates in the marine environment: Journal of Geophysical Research, v. 113, no. B1.

Gladkikh, M., 2005, A priori prediction of macroscopic properties of sedimentary rocks containing two immiscible fluids [PhD dissertation]: The University of Texas at Austin.

Gladkikh, M., and Bryant, S., 2005, Prediction of imbibition in unconsolidated granular materials: Journal of Colloid and Interface Science, v. 288, no. 2, p. 526-539.

Gladkikh, M., and Bryant, S., 2003, Prediction of interfacial areas during imbibition in simple porous media: Advances in Water Resources, v. 26, no. 6, p. 609-622.

Haines, W., 1930, Studies in the physical properties of soil: Journal of Agriculture Science, v. 20, p. 97.

Handa, Y., 1990, Effect of hydrostatic pressure and salinity on the stability of gas hydrates: The Journal of Physical Chemistry, v. 94, no. 6, p. 2652-2657.

Hirai, S., Okazaki, K., Araki, N., Yazawa, H., Ito, H., and Hijikata, K., 1996, Transport phenomena of liquid CO2 in pressurized water flow with clathrate-hydrate at the interface: Energy Conversion and Management, v. 37, no. 6-8, p. 1073-1078.

Holbrook, S., Hoskins, H., Wood, W., Stephen, R., and Lizarralde, D., 1996, Methane Hydrate and Free Gas on the Blake Ridge from Vertical Seismic Profiling: Science, v. 273, no. 5283, p. 1840 -1843.

Holbrook, W., 2001, Seismic studies of the Blake Ridge: Implications for hydrate distribution, methane expulsion, and free gas dynamics: Geophysical Monograph, v. 124, p. 235-256.

Hunter, R., Collett, T., Boswell, R., Anderson, B., Digert, S., Pospisil, G., Baker, R., and Weeks, M., 2011, Mount Elbert Gas Hydrate Stratigraphic Test Well, Alaska North Slope: Overview of scientific and technical program: Marine and Petroleum Geology, v. 28, no. 2, p. 295-310.

Husebø, J., Ersland, G., Graue, A., and Kvamme, B., 2009, Effects of salinity on hydrate stability and implications for storage of CO2 in natural gas hydrate reservoirs: Energy Procedia, v. 1, no. 1, p. 3731-3738.

Hu G., Ye, Y., Zhang, J., Diao, S., Wang, J., 2008, Study on acoustic properties during gas hydrate formation and dissociation in sediments. Proceedings of 6th ICGH, Vancouver, Canada.

Hyndman, R., and Spence, G., 1992, A Seismic Study of Methane Hydrate Marine Bottom Simulating Reflectors: Journal of Geophysical Research, v. 97, no. B5, p. PP. 6683-6698.

Hyndman, R., Yuan, T., and Moran, K., 1999, The concentration of deep sea gas hydrates from downhole electrical resistivity logs and laboratory data: Earth and Planetary Science Letters, v. 172, no. 1-2, p. 167-177.

Jerauld, G., and Salter, S., 1990, The effect of pore-structure on hysteresis in relative permeability and capillary pressure: Pore-level modeling: Transport in Porous Media, v. 5, no. 2, p. 103-151.

Jiang, H., Jordan, K., and Taylor, C., 2007, Molecular Dynamics Simulations of Methane Hydrate Using Polarizable Force Fields: The Journal of Physical Chemistry B, v. 111, no. 23, p. 6486-6492.

Juanes, R., and Bryant, S., 2009, Coupled gas/water/sediment dynamics with rigid hydrate films: U.S. Department of Energy - NETL, Mechanisms leading to co-existence of gas and hydrate in ocean sediments.

Judd, A., Hovland, M., Dimitrov, L., Garcia Gil, S., and Jukes, V., 2002, The geological methane budget at Continental Margins and its influence on climate change: Geofluids, v. 2, no. 2, p. 109-126.

Kagan, M., and Pinczewski, W., 2000, Menisci in a diamond-shaped capillary: Journal of Colloid and Interface Science, v. 230, no. 2, p. 452-454.

Kang, Q., 2004, Lattice Boltzmann model for crystal growth from supersaturated solution: Geophysical Research Letters, v. 31, no. L21604.

Katsube, T., Sallimore, S., Jonasson, I., Connell-Madore, S., Medioli, B., Uchida, T., Wright, J., and Scromeda, N., 2005, Petrophysical characteristics of gas-hydrate-bearing and gas-hydrate-gree formations in the JAPEX/JNOC/GSC et al. Mallike 5L-38 gas hydrate production research well: Geological Survey of Canada, Scientific results frmo the Mallik 2002 Gas hydrate Production Research Well Program, Mackenzie Delta, Northwest Territories, Canada.

Katsuki, D., Ohmura, R., Ebinuma, T., and Narita, H., 2006, Formation, growth and ageing of clathrate hydrate crystals in a porous medium: Philosophical Magazine, v. 86, no. 12, p. 1753-1761.

Katsuki, D., Ohmura, R., Ebinuma, T., and Narita, H., 2007, Methane hydrate crystal growth in a porous medium filled with methane-saturated liquid water: Philosophical Magazine, v. 87, no. 7, p. 1057-1069.

Kennett, J., 2002, Methane hydrates in Quaternary climate change: The clathrate gun hypothesis: American Geophysical Union.

Kleinberg, R., Flaum, C., and Collett, T., 2005, Magnetic resonance log of JAPEX/JNOC/GSC et al. Mallik 5L-38 gas hydrate production research well: gas hydrate saturation, growth habit, and relative permeability: Geological Survey of Canada, Scientific results frmo the Mallik 2002 Gas hydrate Production Research Well Program, Mackenzie Delta, Northwest Territories, Canada.

Kneafsey, T., Tomutsa, L., Moridis, G., Seol, Y., Freifeld, B., Taylor, C., and Gupta, A., 2007, Methane hydrate formation and dissociation in a partially saturated core-scale sand sample: Journal of Petroleum Science and Engineering, v. 56, no. 1-3, p. 108-126.

Knudsen, H., and Hansen, A., 2002, Relation between pressure and fractional flow in two-phase flow in porous media: Physical Review E, v. 65, no. 5.

Krull, E., and Retallack, G., 2000, {delta}13C depth profiles from paleosols across the Permian-Triassic boundary: Evidence for methane release: Geological Society of America Bulletin, v. 112, no. 9, p. 1459-1472.

Kumar, M., 2009, Multiphase flow in reservoir cores using digital core analysis [PhD dissertation]: Australian National University.

Kurihara, M., Sato, A., Funatsu, K., Ouchi, H., Masuda, Y., Narita, H., and Collett, T., 2011, Analysis of formation pressure test results in the Mount Elbert methane hydrate reservoir through numerical simulation: Marine and Petroleum Geology, v. 28, no. 2, p. 502-516.

Kvenvolden, K., 1988, Methane hydrate -- A major reservoir of carbon in the shallow geosphere?: Chemical Geology, v. 71, no. 1-3, p. 41-51.

Kvenvolden, K., 2002, Methane hydrate in the global organic carbon cycle: Terra Nova, v. 14, no. 5, p. 302-306.

Kvenvolden, K., Ginsburg, G., and Soloviev, V., 1993, Worldwide distribution of subaquatic gas hydrates: Geo-Marine Letters, v. 13, no. 1, p. 32-40.

Lee, M., and Collett, T., 2005, Assessment of gas hydrate concentrations estimated from sonic logs in the JAPEX/JNOC/GSC et al. Mallik 5L-38 gas hydrate research production well: Geological Survey of Canada, Scientific results frmo the Mallik 2002 Gas hydrate Production Research Well Program, Mackenzie Delta, Northwest Territories, Canada.

Lee, M., and Collett, T., 2011, In-situ gas hydrate hydrate saturation estimated from various well logs at the Mount Elbert Gas Hydrate Stratigraphic Test Well, Alaska North Slope: Marine and Petroleum Geology, v. 28, no. 2, p. 439-449.

Lee, M., and Collett, T., 2008, Integrated analysis of well logs and seismic data to estimate gas hydrate concentrations at Keathley Canyon, Gulf of Mexico: Marine and Petroleum Geology, v. 25, no. 9, p. 924-931.

Lee, T., Kashyap, R., and Chu, C., 1994, Building skeleton models via 3-D medial surface axis thinning algorithms: Graphical Models and Image Processing, v. 56, no. 6, p. 462-478.

Lekvam, K., and Ruoff, P., 1997, Kinetics and mechanism of methane hydrate formation and decomposition in liquid water. Description of hysteresis: Journal of Crystal Growth, v. 179, no. 3-4, p. 618-624.

Lichtenberger, G., 1991, Field applications of interwell tracers for reservoir characterization of enhanced oil recovery pilot areas, *in* Proceedings of SPE Production Operations Symposium.

Lindquist, W., 2008, 3DMA-Rock----A software package for automated analysis of rock pore structure in 3D computed microtomography images.

Lindquist, W., Lee, S., Coker, D., Jones, K., and Spanne, P., 1996, Medial axis analysis of void structure in three-dimensional tomographic images of porous media: Journal of Geophysical Research, v. 101, no. B4, p. PP. 8297-8310.

Lindquist, W., and Venkatarangan, A., 1999, Investigating 3D geometry of porous media from high resolution images: Physics and Chemistry of the Earth, Part A: Solid Earth and Geodesy, v. 24, no. 7, p. 593-599.

Liu, X., and Flemings, P., 2007, Dynamic multiphase flow model of hydrate formation in marine sediments: Journal of Geophysical Research, v. 112, no. B3.

Liu, X., and Flemings, P., 2006, Passing gas through the hydrate stability zone at southern Hydrate Ridge, offshore Oregon: Earth and Planetary Science Letters, v. 241, no. 1-2, p. 211-226.

Liu Y., Zhang, W., Liu, Y., Ren, S., 2008, Experimental characterization and modeling of acoustic velocity and electrical resistance in hydrate bearing sediments. Proceedings of 6th ICGH, Vancouver, Canada.

Lorensen, W., and Cline, H., 1987, Marching cubes: A high resolution 3D surface construction algorithm, *in* ACM SIGGRAPH Computer Graphics, ACM, New York, NY, USA, p. 163–169.

Lorenson, T., Claypool, G., and Dougherty, J., 2008, Natural gas geochemistry of sediments drilled on the 2005 Gulf of Mexico JIP cruise: Marine and Petroleum Geology, v. 25, no. 9, p. 873-883.

Lorenson, T., Collett, T., and Hunter, R., 2011, Gas geochemistry of the Mount Elbert Gas Hydrate Stratigraphic Test Well, Alaska North Slope: Implications for gas hydrate exploration in the Arctic: Marine and Petroleum Geology, v. 28, no. 2, p. 343-360.

Lorenson, T., Collett, T., and Hunter, R., 2011, Gas geochemistry of the Mount Elbert Gas Hydrate Stratigraphic Test Well, Alaska North Slope: Implications for gas hydrate exploration in the Arctic: Marine and Petroleum Geology, v. 28, no. 2, p. 343-360.

Lu, H., Dutrisac, R., Ripmeester, J., and Uchida, T., 2005, Measurement of gas hydrate saturation in sediment cores recovered from the JAPEX/JNOC/GSC et al. Mallik 5L-38 gas hydrate production research well: Geological Survey of Canada, Scientific results frmo the Mallik 2002 Gas hydrate Production Research Well Program, Mackenzie Delta, Northwest Territories, Canada.

Lund, P., Shindo, Y., Fujioka, Y., and Komiyama, H., 1994, Study of the pseudo-steady-state kinetics of CO2 hydrate formation and stability: International Journal of Chemical Kinetics, v. 26, no. 2, p. 289-297.

MacDonald, I., Guinasso, N., Sassen, R., Brooks, J., Lee, L., and Scott, K., 1994, Gas hydrate that breaches the sea floor on the continental slope of the Gulf of Mexico: Geology, v. 22, no. 8, p. 699-702.

Majorowicz, J., Osadetz, K., and Safanda, J., 2008, Onset and stability of gas hydrates under permafrost in an environment of surface climatic change - past and future, *in* Vancouver, Canada.

Man, H., and Jing, X., 1999, Network modelling of wettability and pore geometry effects on electrical resistivity and capillary pressure: Journal of Petroleum Science and Engineering, v. 24, no. 2-4, p. 255-267.

Mani, V., and Mohanty, K., 1997a, Pore-Level Network Modeling of Three-Phase Capillary Pressure and Relative Permeability Curves, *in* Proceedings of SPE Annual Technical Conference and Exhibition.

Marquardt, M., Hensen, C., Piñero, E., Wallmann, K., and Haeckel, M., 2010, A transfer function for the prediction of gas hydrate inventories in marine sediments: Biogeosciences, v. 7, no. 9, p. 2925-2941.

Maslin, M., Owen, M., Betts, R., Day, S., Dunkley Jones, T., and Ridgwell, A., 2010, Gas hydrates: past and future geohazard?: Philosophical Transactions of the Royal Society A: Mathematical, Physical and Engineering Sciences, v. 368, no. 1919, p. 2369 -2393.

Mason, G., and Mellor, D., 1995, Simulation of Drainage and Imbibition in a Random Packing of Equal Spheres: Journal of Colloid and Interface Science, v. 176, no. 1, p. 214-225.

Mason, G., and Morrow, N., 1991, Capillary behavior of a perfectly wetting liquid in irregular triangular tubes: Journal of Colloid and Interface Science, v. 141, no. 1, p. 262-274.

Matsumoto, R., Tomaru, H., Chen, Y., and Clark, I., 2005, Geochemistry of the interstitial waters of the JAPEX/JNOC/GSC et al. Mallik 5L-38 gas hydrate production research well: Geological Survey of Canada, Scientific results frmo the Mallik 2002 Gas hydrate Production Research Well Program, Mackenzie Delta, Northwest Territories, Canada.

Mayer, R., and Stowe, R., 1965, Mercury porosimetry--breakthrough pressure for penetration between packed spheres: Journal of Colloid Science, v. 20, no. 8, p. 893-911.

Melrose, J., 1965, Wettability as related to capillary action in porous media: SPE Journal, v. 5, no. 3, p. 259-271.

Milkov, A., Claypool, G., Lee, Y., Xu, W., Dickens, G., and Borowski, W., 2003, In situ methane concentrations at Hydrate Ridge, offshore Oregon: New constraints on the global gas hydrate inventory from an active margin: Geology, v. 31, no. 10, p. 833-836.

Mochizuki, T., and Mori, Y., 2006, Clathrate-hydrate film growth along water/hydrate-former phase boundaries--numerical heat-transfer study: Journal of Crystal Growth, v. 290, no. 2, p. 642-652.

Mogensen, K., and Stenby, E., 1998, A Dynamic Two-Phase Pore-Scale Model of Imbibition: Transport in Porous Media, v. 32, p. 299-327.

Mori, Y., 2001, Estimating the thickness of hydrate films from their lateral growth rates: application of a simplified heat transfer model: Journal of Crystal Growth, v. 223, no. 1-2, p. 206-212.

Mori, Y., and Mochizuki, T., 1997, Mass transport across clathrate hydrate films -- a capillary permeation model: Chemical Engineering Science, v. 52, no. 20, p. 3613-3616.

Moridis, G., 2004, Numerical Studies of Gas Production From Class 2 and Class 3 Hydrate Accumulations at the Mallik Site, Mackenzie Delta, Canada: SPE Reservoir Evaluation & Engineering, v. 7, no. 3.

Moridis, G., Collett, T., Dallimore, S., Satoh, T., Hancock, S., and Weatherill, B., 2004, Numerical studies of gas production from several CH4 hydrate zones at the Mallik site, Mackenzie Delta, Canada: Journal of Petroleum Science and Engineering, v. 43, no. 3-4, p. 219-238.

Motealleh, S., 2009, Mechanistic study of menisci motnion within homogeneously and heterogeneously wet porous media [PhD dissertation]: The University of Texas at Austin.

Motealleh, S., Bryant, S., Gladkikh, M., Bespalov, M., and Herrick, D., 2007, Grain-scale modeling of electrical resistivity of 'shaly sands', *in* 2007. Society of Petrophysicists & Well Log Analysts, Austin.

Nengkoda, A., Budhijanto, B., Supranto, S., Prasetyo, I., Purwono, S., and Sutijan, S., 2010, Production Behaviour of Gas Hydrate Under Hot Sea Water Injection: Laboratory Case Study, Canadian Unconventional Resources and International Petroleum Conference.

Ohmura, R., Matsuda, S., Uchida, T., Ebinuma, T., and Narita, H., 2005, Clathrate hydrate crystal growth in liquid water saturated with a guest substance: Observations in a methane + water System: Crystal Growth & Design, v. 5, no. 3, p. 953-957.

Øren, P., Bakke, S., and Arntzen, O., 1997, Extending Predictive Capabilities to Network Models, *in* Proceedings of SPE Annual Technical Conference and Exhibition.

Osher, S., and Sethian, J., 1988, Fronts propagating with curvature-dependent speed: Algorithms based on Hamilton-Jacobi formulations: Journal of Computational Physics, v. 79, no. 1, p. 12-49.

Osher, S., and Fedkiw, R., 2002, Level set methods and dynamic implicit surfaces: Springer.

Padden, M., Weissert, H., and de Rafelis, M., 2001, Evidence for Late Jurassic release of methane from gas hydrate: Geology, v. 29, no. 3, p. 223-226.

Patzek, T., 2001, Verification of a complete pore network simulator of drainage and imbibition: SPE Journal, v. 6, no. 2, p. 144-156.

Paull, C., Brewer, P., Ussler, W., Rehder, G., and Clague, D., 2003, An experiment demonstrating that marine slumping is a mechanism to transfer methane from seafloor gas-hydrate deposits into the upper ocean and atmosphere: Geo-Marine Letters, v. 22, no. 4, p. 198-203.

Paull, C., Dallimore, S., Blasco, S., Lorenson, T., Melling, H., Medioli, B., Nixon, F.M., and McLaughlin, F., 2007, Origin of pingo-like features on the Beaufort Sea shelf and their possible relationship to decomposing methane gas hydrates: Geophysical Research Letters, v. 34, p. 5 PP.

Paull, C., Lorenson, T., Dickens, G., Borowski, W., Ussler, W., and Kvenvolden, K., 2006, Comparisons of In Situ and Core Gas Measurements in ODP Leg 164 Bore Holes: Annals of the New York Academy of Sciences, v. 912, no. 1, p. 23-31.

Pearson, J.R.A., and Tardy, P.M.J., 2002, Models for flow of non-Newtonian and complex fluids through porous media: Journal of Non-Newtonian Fluid Mechanics, v. 102, no. 2, p. 447-473.

Peng, B., Dandekar, A., Sun, C., Luo, H., Ma, Q., Pang, W., and Lichtenberger, G., 2007, Hydrate Film Growth on the Surface of a Gas Bubble Suspended in Water: The Journal of Physical Chemistry B, v. 111, no. 43, p. 12485-12493.

Pooladi-Darvish, M., and Hong, H., 2011, Use of formation pressure test results over a hydrate interval for long-term production forecasting at the Mount Elbert Gas Hydrate Stratigraphic Test Well, Alaska North Slope: Implications of uncertainties: Marine and Petroleum Geology, v. 28, no. 2, p. 535-545.

Princen, H., 1969, Capillary phenomena in assemblies of parallel cylinders : II. Capillary rise in systems with more than two cylinders: Journal of Colloid and Interface Science, v. 30, no. 3, p. 359-371.

Princen, H., 1970, Capillary phenomena in assemblies of parallel cylinders : III. Liquid Columns between Horizontal Parallel Cylinders: Journal of Colloid and Interface Science, v. 34, no. 2, p. 171-184.

Prodanovic, M., 2009, LSMPQS Software: http://users.ices.utexas.edu/~masha/lsmpqs/index.html

Prodanovic, M., and Bryant, S., 2006, A level set method for determining critical curvatures for drainage and imbibition: Journal of Colloid and Interface Science, v. 304, no. 2, p. 442-458.

Prodanovic, M., and Bryant, S., 2008, Resolving Meniscus Movement Within Rough Confining Surfaces Via the Level Set Method, *in* In Focus on Water Resource Research, Nova Science Publishers, p. 237-262.

Prodanovic, M., Bryant, S., and Karpyn, Z., 2008, Investigating matrix-fracture transfer via a level set method for drainage and imbibition, *in* Proceedings of SPE Annual Technical Conference and Exhibition,

Prodanovic, M., Lindquist, W., and Seright, R., 2007, 3D image-based characterization of fluid displacement in a Berea core: Advances in Water Resources, v. 30, no. 2, p. 214-226.

Prodanovic, M., Lindquist, W., and Seright, R., 2006, Porous structure and fluid partitioning in polyethylene cores from 3D X-ray microtomographic imaging: Journal of Colloid and Interface Science, v. 298, no. 1, p. 282-297.

Ripley, B.D., 2004, Spatial Statistics: Wiley-Interscience.

Ripmeester, J., Lu, H., Moudrakovski, I., Dutrisac, R., Wilson, L., Wright, F., and Dallimore, S., 2005, Structure and composition of gas hydrate in sediment recoverd from JAPEX/JNOC/GSC et al. Mallik 5L-38 gas hydrate production research well, determined by X-ray diffraction and Raman and solid-state nulcear magnetic resonance spectroscopy: Geological Survey of Canada, Scientific results frmo the Mallik 2002 Gas hydrate Production Research Well Program, Mackenzie Delta, Northwest Territories, Canada.

Rose, K., Boswell, R., and Collett, T., 2011, Mount Elbert Gas Hydrate Stratigraphic Test Well, Alaska North Slope: Coring operations, core sedimentology, and lithostratigraphy: Marine and Petroleum Geology, v. 28, no. 2, p. 311-331.

Ruppel, C., Boswell, R., and Jones, E., 2008, Scientific results from Gulf of Mexico Gas Hydrates Joint Industry Project Leg 1 drilling: Introduction and overview: Marine and Petroleum Geology, v. 25, no. 9, p. 819-829.

Sandler, S., 2006, Chemical, biochemical, and engineering thermodynamics: John Wiley & Sons, Inc.

Schicks, Spangenberg, E., Steinhauer, J.K., Giese, R., Erzinger, J., Haeckel, M., Bigalke, N., Savy, J., Kossel, E., Deusner, C., and Wallmann, K., 2010, Natural Gas Hydrates: Development and Test of Innovative Methods for Gas Production From Hydrate-Bearing Sediments, *in* Calgary, Alberta, Canada.

Seright, R., Liang, J., Lindquist, W., and Dunsmuir, J., 2003, Use of X-ray computed microtomography to understand why gels reduce relative permeability to water

more than that to oil: Journal of Petroleum Science and Engineering, v. 39, no. 3-4, p. 217-230.

Shindo, Y., Fujioka, Y., Takeuchi, K., and Komiyama, H., 1995, Kinetics on the Dissolution of C02 into Water from the Surface of CO2 Hydrate at High Pressure: International Journal of Chemical Kinetics, v. 27, p. 569-575.

Singh, M., and Mohanty, K., 2003, Dynamic modeling of drainage through three-dimensional porous materials: Chemical Engineering Science, v. 58, no. 1, p. 1-18.

Sisk, C., Diaz, E., Walls, J., Grader, A., and Suhrer, M., 2010, 3D visualization and classification of pore structure and pore filling in gas shales, *in* Proceedings of SPE Annual Technical Conference and Exhibition,

Sloan, E., 2003, Fundamental principles and applications of natural gas hydrates: Nature, v. 426, no. 6964, p. 353-363.

Sloan, E., and Koh, C., 2008, Clathrate hydrates of natural gases: CRC Press.

Stern, L., Lorenson, T., and Pinkston, J., 2011, Gas hydrate characterization and grain-scale imaging of recovered cores from the Mount Elbert Gas Hydrate Stratigraphic Test Well, Alaska North Slope: Marine and Petroleum Geology, v. 28, no. 2, p. 394-403.

Sultan, N., 2007, Excess Pore Pressure and Slope Failures Resulting From Gas-Hydrates Dissociation and Dissolution, *in* Proceedings of Offshore Technology Conference,

Sun, R., and Duan, Z., 2007, An accurate model to predict the thermodynamic stability of methane hydrate and methane solubility in marine environments: Chemical Geology, v. 244, no. 1-2, p. 248-262.

Teng, H., Kinoshita, C., and Masutani, S., 1995, Hydrate formation on the surface of a CO2 droplet in high-pressure, low-temperature water: Chemical Engineering Science, v. 50, no. 4, p. 559-564.

Tohidi, B., Anderson, R., Clennell, M., Burgass, R., and Biderkab, A., 2001, Visual observation of gas-hydrate formation and dissociation in synthetic porous media by means of glass micromodels: Geology, v. 29, no. 9, p. 867-870.

Tomaru, H., Matsumoto, R., Chen, Y., and Clark, I., 2005, Evolution of a gas hydrate system as recorded by oxygen and hydrogen isotopes of the interstitial waters of the JAPEX/JNOC/GSC et al. Mallik 5L-38 gas hydrate production research well: Geological Survey of Canada, Scientific results frmo the Mallik 2002 Gas hydrate Production Research Well Program, Mackenzie Delta, Northwest Territories, Canada.

Torres, M., Collett, T., Rose, K., Sample, J., Agena, W., and Rosenbaum, E., 2011, Pore fluid geochemistry from the Mount Elbert Gas Hydrate Stratigraphic Test Well, Alaska North Slope: Marine and Petroleum Geology, v. 28, no. 2, p. 332-342.

Torres, M., Wallmann, K., Tréhu, A., Bohrmann, G., Borowski, W., and Tomaru, H., 2004, Gas hydrate growth, methane transport, and chloride enrichment at the southern summit of Hydrate Ridge, Cascadia margin off Oregon: Earth and Planetary Science Letters, v. 226, no. 1-2, p. 225-241.

Tréhu, A., Flemings, P., Bangs, N., Chevallier, J., Gràcia, E., Johnson, J., Liu, C., Liu, X., Riedel, M., and Torres, M., 2004, Feeding methane vents and gas hydrate deposits at south Hydrate Ridge: Geophysical Research Letters, v. 31, p. 4 PP.

Turner, M., Knüfing, L., Arns, C., Sakellariou, A., Senden, T., Sheppard, A., Sok, R., Limaye, A., Pinczewski, W., and Knackstedt, M., 2004, Three-dimensional imaging of multiphase flow in porous media: Physica A: Statistical Mechanics and its Applications, v. 339, no. 1-2, p. 166-172.

Uchida, T., Tsuji, T., Takahashi, T., Okui, T., and Minagawa, H., 2005, Petrophysical properties and sedimentology of gas-hydrate-bearing sediments in the JAPEX/JNOC/GSC et al. Mallik 5L-38 gas hydrate production research well: Geological Survey of Canada, Scientific results frmo the Mallik 2002 Gas hydrate Production Research Well Program, Mackenzie Delta, Northwest Territories, Canada.

Valvatne, P., and Blunt, M., 2004, Predictive pore-scale modeling of two-phase flow in mixed wet media: Water Resources Research, v. 40, no. W07406.

Valvatne, P., Piri, M., Lopez, X., and Blunt, M., 2005, Predictive pore-scale modeling of single and multiphase flow: Transport in Porous Media, v. 58, no. 1, p. 23-41.

Vogel, H., and Roth, K., 2001, Quantitative morphology and network representation of soil pore structure: Advances in Water Resources, v. 24, no. 3-4, p. 233-242.

Winters, W., Walker, M., Hunter, R., Collett, T., Boswell, R., Rose, K., Waite, W., Torres, M., Patil, S., and Dandekar, A., 2011, Physical properties of sediment from the Mount Elbert Gas Hydrate Stratigraphic Test Well, Alaska North Slope: Marine and Petroleum Geology, v. 28, no. 2, p. 361-380.

Winters, W., Dallimore, S., Collett, T., Medioli, B., Matsumoto, R., Katsube, T., and Brennan-Alpert, P., 2005, Relatinoships of sediment physcial properties from the JAPEX/JNOC/GSC et al. Mallik 5L-38 gas hydrate production research well: Geological Survey of Canada, Scientific results frmo the Mallik 2002 Gas hydrate Production Research Well Program, Mackenzie Delta, Northwest Territories, Canada.

Winters, W., Dugan, B., and Collett, T., 2008, Physical properties of sediments from Keathley Canyon and Atwater Valley, JIP Gulf of Mexico gas hydrate drilling program: Marine and Petroleum Geology, v. 25, no. 9, p. 896-905.

Wood, W., Hart, P., Hutchinson, D., Dutta, N., Snyder, F., Coffin, R., and Gettrust, J., 2008, Gas and gas hydrate distribution around seafloor seeps in Mississippi

Canyon, Northern Gulf of Mexico, using multi-resolution seismic imagery: Marine and Petroleum Geology, v. 25, no. 9, p. 952-959.

Xu, W., and Ruppel, C., 1999, Predicting the occurrence, distribution, and evolution of methane gas hydrate in porous marine sediments: Journal of Geophysical Research, v. 104, p. 5081-5095.

Zachos, J., 2001, Trends, Rhythms, and Aberrations in Global Climate 65 Ma to Present: Science, v. 292, no. 5517, p. 686-693.

Zatsepina, O., and Buffett, B., 1997, Phase equilibrium of gas hydrate: Implications for the formation of hydrate in the deep sea floor: Geophysical Research Letters, v. 24, no. 13, p. 1567-1570.

Zhao, H., Macdonald, I., and Kwiecien, M., 1994, Multi-orientation scanning: A necessity in the identification of pore mecks in porous media by 3-D computer reconstruction from serial section data: Journal of Colloid and Interface Science, v. 162, no. 2, p. 390-401.

Vita

Yao Peng was born in 1983, in Ya'an, Sichuan Province, China. He received a Bachelor and a Mater degree in Engineering Mechanics, from Tsinghua University in 2005 and 2007, respectively. He later pursued a PhD degree in Petroleum Engineering from the University of Texas at Austin, with the supervision of Drs. Steven L. Bryant and Maša Prodanović from 2007 to 2011.

Permanent email address: cliffrunner@gmail.com

This dissertation was typed by the author.